Local Earthquake Tomography at the Central Pacific margin of Costa Rica

Dissertation
zur Erlangung des Doktorgrades
der Mathematisch-Naturwissenschaftlichen Fakultät
der Christian-Albrechts-Universität
zu Kiel

vorgelegt von
Ivonne Aden-Arroyo

Kiel, 2008

Cover photo: street signal warning drivers about a “zone of geological instability in the next 500 meters” close to Parrita village, Central Pacific region of Costa Rica.

Referent: Prof. Dr. Ernst Flüh
Korreferent: Prof. Dr. Jan Behrmann
Tag der mündlichen Prüfung: 10. Juli 2008

Zum Druck genehmigt: Kiel, ...
Der Dekan

Abstract

The Central Pacific area of Costa Rica is a convergent erosional margin, characterized by a high seismicity rate, coincident with the subduction of rough-relief ocean floor. It has generated earthquakes with magnitude up to seven in the past along the subduction megathrust and the inner-forearc faulting. This study uses the records from a temporal seismological network, consisting of on- and offshore stations, installed for a period of six months in this segment of the Middle American margin. The aim was to obtain a model of the 3-D velocity structure of the margin and to characterize the seismicity of the shallow part (< 70 km depth) of the subduction zone, with the focus on the seismogenic zone. A subset of well locatable events was selected to calculate a minimum 1-D model for the P-wave velocity. This model served as initial reference model for the subsequent 3-D inversion in a Local Earthquake Tomography, performed by inverting P- and S-wave traveltimes from 595 selected earthquakes. Several tools for resolution assessment were applied. Additionally, first-motion, double-couple focal mechanisms were determined for earthquakes originated at the plate interface, the subducting slab and the overriding plate.

The results reflect the complexity associated to subduction of ocean-floor morphology and the transition from normal to thickened subducting oceanic crust. The subducting slab is imaged as a high-velocity perturbation with a conspicuous band of low velocities (LVB) on top, encompassing the intraslab seismicity deeper than ~30 km. The LVB is locally thickened beneath the margin slope by the presence of at least two subducted seamounts. There is a general eastward widening of the LVB over a relatively short distance, accentuated by a low-velocity anomaly beneath the continental shelf, interpreted as a relative big seamount or plateau. The thickening of the subducting crust closely coincides with the onset of an inverted forearc basin onshore and the appearance of an aseismic low-velocity anomaly beneath the inner forearc. The latter is located in a sector where differential uplift of blocks of the subaerial forearc has been described, suggesting tectonic underplating of eroded material against the base of the upper plate crust. Alternatively, the low velocities could be induced by an accumulation of upward migrating fluids. Other observed velocity perturbations are attributed to various processes taking place at different depths, such as slab hydration through bend faulting at the trench and outer rise, tectonic erosion and slab dehydration.

In the west part of the studied area, the interplate seismicity is clearly distinguished as tightly-packed clustering, dipping ~16-19° between 15 and 25 km depth, beneath the continental shelf. The updip limit of the interplate seismicity closely coincides with temperatures of 150°C and an increase in the P-wave velocities along the plate boundary, and it closely follows the border of the continental shelf. These observations fit within a recently proposed hydrogeological model for erosional margins, which attributes the onset of stick-slip behaviour in the plate interface to a decrease in the abundance of the fluids released by early dehydration reactions in the subducted sediments; escape of overpressured fluids is propitiated by upward percolation through a fractured upper plate. The thickness and mechanical coherence of the upper plate also influence the start of the seismic behavior. Locally, the presence of subducted seamounts and the associated margin disruption updip of the seismogenic zone could shift the onset of seismicity trenchward. As commonly observed in regions with relatively weak plate coupling, higher seismicity rates

concur with the presence of seamounts in the seismogenic zone: in this case, the seamount that originated a Mw-7.0 earthquake in 1990 and the above mentioned seamount or plateau revealed by this study. Furthermore, seismic swarms known as “burst”-type were detected by the experiment in these two subareas as well. They are possibly originated by repetitive rupture of the same small relief patches at the seamounts. If interpretation of the anomaly as a big seamount or plateau is correct, it could act as an asperity in the seismogenic zone, able to generate large earthquakes. The downdip limit of the interplate seismicity seems to be thermally controlled, but the available data is not conclusive. In the east part of the studied area, the interplate seismicity becomes scarce and distributes in clusters.

Intraslab earthquakes were detected from the outer rise down to depths greater than 100 km. The highest rates coincide with subduction of thickened crust, where they distribute all over the width of the LVB. If slab dehydration enables seismicity, as widely accepted, and hydration of thickened oceanic crust at the outer rise-trench area is much reduced due to impaired bending ability, then hydration at alternative tectonic scenarios seems to play an important role for seismogenesis.

The upper plate seismicity is limited trenchward by the margin wedge. Burst-type seismic swarms were also detected in the overriding plate. The focal mechanisms are in good agreement with previous models of upper plate internal deformation. The low-velocity anomaly at the base of the crust in the inner forearc, seems to promote seismicity in its surroundings by high-friction with the overriding plate, and could be linked to a Mw-6.4 earthquake that caused extensive civil damage along the coast in 2004.

Zusammenfassung

Der zentrale pazifische Kontinentalrand vor Costa Rica ist ist eine konvergente und erosive Plattengrenze, die gekennzeichnet ist durch eine hohe Seismizität, welche wiederum einhergeht mit der Subduktion von stark ausgeprägter Meeresbodenmorphologie. Diese Plattengrenze sowie Störungen innerhalb des angrenzenden Forearcs haben in der Vergangenheit Erdbeben bis zu einer Magnitude 7 hervorgebracht. Die vorliegende Arbeit wertet die Aufzeichnungen eines temporären seismologischen Netzwerkes bestehend aus Land- und Ozeanbodenstationen aus, welches für einen Zeitraum von 6 Monaten in diesem Bereich des mittelamerikanischen Kontinentalrandes installiert wurde. Ziel der Auswertung ist die Erstellung eines 3-D Geschwindigkeitsmodells dieser Plattengrenze sowie eine genaue Charakterisierung der Seismizität der oberen Tiefenbereiche (<70km Tiefe) dieser Subduktionszone, insbesondere die Charakterisierung der Seismizität innerhalb der seismogenen Zone. Mittels einer Auswahl gut lokalisierbarer Beben wurde zunächst ein Minimum 1-D Tiefen Modell für P-Wellengeschwindigkeiten erstellt. Dieses Modell diente im weiteren Verlauf als Start- sowie Referenzmodell für die anschließende 3-D Inversion innerhalb der Lokalen Erdbeben Tomographie, bei der P- und S-Wellen Laufzeiten von 595 ausgewählten Beben invertiert wurden. Unterschiedliche Arten von Auflösungstests wurden dabei durchgeführt. Zusätzlich wurden Herdflächenlösungen (first-motion, double-couple focal mechanisms) für Erdbeben entlang der Plattengrenze, innerhalb der subduzierten Platte sowie innerhalb der überfahrenden Platte bestimmt.

Die Komplexität der Ergebnisse spiegelt zum einen die Subduktion der ausgeprägten Meeresbodenmorphologie und zum anderen den Übergang von normaler zu verdickter ozeanischer Kruste wieder. Die subduzierte ozeanische Platte wird als eine positive Geschwindigkeitsperturbation abgebildet, welche im oberen Bereich durch ein auffälliges Band von aneinander gereihten Niedriggeschwindigkeitsanomalien (LVB) gekennzeichnet ist. Die Wadati-Benioff Erdbeben liegen alle innerhalb dieses LVB. Das LVB ist im Bereich unterhalb des Kontinentalhanges stellenweise verdickt, was auf die Anwesenheit von zwei subduzierten unterseeischen Bergen (Seamounts) zurückzuführen ist. Es ist überdies eine generelle Verdickung des LVB nach Osten hin festzustellen, welche durch das Vorhandensein einer ausgeprägten Niedriggeschwindigkeitsanomalie unterhalb des Kontinentalschelfs noch verstärkt wird, welche als ein subduzierter großer Seamount oder als ein subduziertes ozeanisches Plateau interpretiert wird. Die Verdickung der subduzierten ozeanischen Kruste geht an Land einher mit dem Auftreten eines angehobenen Forearc Beckens sowie eines aseismischen Bereiches niedriger Geschwindigkeiten unterhalb des inneren Forearcs. Letzterer befindet sich in einem Gebiet, von dem relative Hebungsprozesse einzelner Blöcke bereits in der Literatur beschrieben sind und auf tektonische Akkretion (Underplating) von erodiertem Material an der Untergrenze der überfahrenden Platte hindeuten. In einem alternativen Szenario könnten diese niedrigen Geschwindigkeiten auch auf eine Ansammlung von aufwärts migrierenden Fluiden hinweisen. Weitere beobachtete Geschwindigkeitsanomalien können auf verschiedene Vorgänge in unterschiedlichen Tiefen zurückgeführt werden, wie z.B. auf die Hydratisierung der abtauchenden Platte durch biegungsinduzierte Dehnungsbrüche im Bereich des Tiefseegrabens und des äußeren Hochs, auf tektonische Erosion sowie auf Entwässerungsvorgänge innerhalb der abtauchenden Platte.

Im westlichen Abschnitt des Untersuchungsgebietes weist die Seismizität zwischen den Platten eine klar abgegrenzte Häufung auf, die im Bereich des kontinentalen Schelfs unter

~16-19° Einfallswinkel zwischen 15 km und 25 km Tiefe verläuft. Die obere Grenze der Seismizität fällt annähernd zusammen mit der 150°C Isotherme sowie einem Anstieg der Vp Geschwindigkeiten im Modell entlang der Plattengrenze; lateral folgt der Verlauf dem der Grenze des kontinentalen Schelfs. Diese Beobachtungen stützen das kürzlich eingeführte hydrogeologische Modell für erosive Plattenränder, welches den Beginn des Haft-Gleitverhaltens der Plattengrenze auf eine Reduzierung der Fluidmenge zurückführt, die durch die Entwässerung der subduzierten Sedimente freigesetzt wird; die Entweichung dieser Fluide erfolgt unter Überdruck durch die Bruchflächen innerhalb der darüberliegenden Platte. Dabei beeinflusst sowohl die Mächtigkeit als auch die mechanische Kontinuität der Oberplatte den Beginn der Seismizität. Wo vorhanden können subduzierte Seamounts und damit einhergehende Störungen in der Oberplatte die obere Grenze der seismogenen Zone zum Tiefseegraben hin verschieben. Wie gemeinhin in Gebieten mit schwach ausgeprägter Kopplung zwischen den Platten beobachtet werden kann, so wird auch in dieser Arbeit eine Erhöhung der Seismizität mit der Existenz von subduzierten Seamounts in Zusammenhang gebracht; dies gilt gleichermaßen für den subduzierten Seamount, der auch für das Mw 7.0 Erdbeben von 1990 verantwortlich gemacht wird, wie für den in dieser Arbeit erstmals entdeckten großen subduzierten Seamount bzw. Plateau. Außerdem wurden innerhalb dieser zwei Gebiete jeweils Erdbebenschwärme vom sog. “burst”-Typ lokalisiert. Diese sind mit hoher Wahrscheinlichkeit auf sich wiederholende Bruchvorgänge zurückzuführen, die vom kleinräumigen Relief des Seamounts ausgehen. Wenn die Interpretation der Geschwindigkeitsanomalie als ein subduzierter großer Seamount bzw. als ein subduziertes ozeanisches Plateau korrekt ist, dann könnten diese Gebilde als Unebenheiten innerhalb der seimogenen Zone das Potenzial haben, große Erdbeben auszulösen. Die untere Grenze der Seismizität zwischen den Platten scheint thermisch bestimmt zu sein, jedoch weisen die zugrunde liegenden Daten Unschlüssigkeiten auf. Im östlichen Bereich des Messgebietes ist Seismizität nur sehr vereinzelnd auflösbar und innerhalb weniger Gebiete konzentriert.

Erdbeben innerhalb der abtauchenden ozeanischen Platte können vom äußeren Hoch bis in Tiefen von 100 km nachgewiesen werden. Die höchsten Seismizitätsraten treten im Bereich der subduzierten verdickten ozeanischen Kruste auf, wo sie sich über die gesamte Breite der LVB verteilen. Wenn, wie gemeinhin angenommen, die Entwässerung der abtauchenden Platte die Entstehung der Seismizität ermöglicht, jedoch die Hydratisierung der verdickten ozeanischen Kruste im Bereich des äußeren Hochs und des Tiefseegrabens auf Grund eingeschränkter Biegungsfähigkeit stark reduziert ist, müssen alternative tektonische Szenarien die Hydratisierung ermöglichen, um das beobachtete Seismizitätsmuster zu erklären.

Die beobachtete Seismizität innerhalb der oberen Platte ist seewärts begrenzt durch den Margin Wedge. Erdbebeschwärme des “burst”-Typs wurden ebenfalls in der überfahrenden Platte lokalisiert. Die dazugehörigen Herdflächenlösungen bestätigen frühere Modellvorstellungen zur internen Deformation der oberen Platte. Die Niedriggeschwindigkeitsanomalie an der Krustengrenze im Bereich des inneren Forearcs stellt dabei anscheinend einen Bereich erhöhter Reibung mit der überfahrenden Platte dar und kann räumlich dem Mw 6.4 Erdbeben von 2004 zugeordnet werden, welches erhebliche Schäden an der Küste verursacht hat.

Contents

Chapter 1

Introduction

Subduction zones are the regions of the planet where slabs of lithosphere created at middle-ocean ridges dive into the mantle, providing most of the force needed to drive the plates. They are the dominant physical and chemical system of the Earth's interior and its largest recycling system (Stern 2002). Subduction zones have been compared with an industrial plant, the "subduction factory", where the raw materials entering the process are the components of the oceanic plate, including sediments, trench-fill from down-slope mass wasting and serpentinized oceanic mantle; these materials eventually "produce" melting, volatiles and continental crust.

The subducting slab is progressively dehydrated by compaction, diagenesis and metamorphic reactions, which control depth-dependent fluid release. Fluid output in the forearc occurs at middle slope, through mud diapirs and volcanoes and venting at faults and landslides, whereas at the volcanic arc it occurs through magmatic devolatilization. Inside the subduction zone the incoming material is transformed, mobilized or fractionated into different volatile reservoirs and phases. These phases are either ejected into the exosphere through the upper plate, accreted to the leading edge of the upper plate, or are transported into the lower mantle.

In addition to their role on the planet's current configuration, subduction zones profoundly impact civilization. The largest earthquakes, volcanic eruptions and slumps, and most of the tsunamis occur in subduction zones, where they endanger about 70 per cent of the world population. But it is in these regions as well, where most of the mineral resources of the planet are found. Research on subduction zones, hence, not only enhances our scientific knowledge about our planet, but this understanding could be used to improve the life of millions of persons.

The convergent margin and subduction zone of Central America has been the target of several large-scale international research projects in the last decades and specially

since the 1990s. This relatively small area presents a variable character, suitable to investigate the impact of the subduction of oceanic crust of different origin, structure, age and morphology on the configuration of the subduction zone, the upper plate and the formation of different volatiles and material output ways.

The present study has been carried out within the project SFB 574 “Volatile and fluids in subduction zones: climate feedback and trigger mechanisms for natural disasters”, funded by the German Research Society (DFG) and led by the University of Kiel. The objective of the SFB574 is to explore the effects of the subduction processes on the long- and short-term development of the Earth’s climate, the geochemical evolution of the hydrosphere and atmosphere, and the causes of natural disasters. While the current phase investigates the accretionary margin of central Chile, the first and second phases of the project concentrated in studying the subduction zone of Central America, with focus in Costa Rica and Nicaragua, as an example of an erosive margin. Additionally, since 1998 the Central American margin has been selected by the U.S. Margins Program for investigating a typical seismogenic zone, thereby providing opportunities of international sharing of ideas and resources.

The SFB574 consists of three main themes, each comprising subprojects which interact with each other: (A) Material input and tectonic behaviour during plate subduction, (B) Transformation and partitioning of volatiles into different reservoirs, and (C) Devolatilization by magmas and metamorphic processes in the fore-arc. Group A, within which this study was conceived and carried out, uses geophysical imaging techniques to study major parts of the subduction system, including the incoming plate, forearc, mantle wedge and magmatic arc. Major research topics are the structure and hydrogeology of the offshore forearc, the study of earthquake processes and seismicity, slab dehydration, serpentinization of the incoming plate and mantle wedge, regions of melt formation and lithospheric structure.

The tectonic style of subduction, the structure of the margin wedge, and the properties and configuration of the down-going plate all exert a first-order control on volatile budget, its transformation, and return pathway. Investigation of the seismicity and the velocity structure of the margin provide valuable insights and constitute a platform to obtain a better understanding of subduction processes. With this motivation, and among other surveys, two temporal “amphibian” seismological networks, consisting of land and ocean-bottom stations, have been installed within the first phase of the SFB574 along the margin in Central Costa Rica; their location is shown in Figure 1.1. This work concentrates on the results obtained by the Jacó network, installed during approximately six months on the Central Pacific area of Costa Rica.

In the following, a description of the tectonic setting of the experiment is given, together with an overview of previous work on the area, including the concepts of subduction erosion and seismogenic zone, of prime relevance for the interpretation and discussion presented in this study.

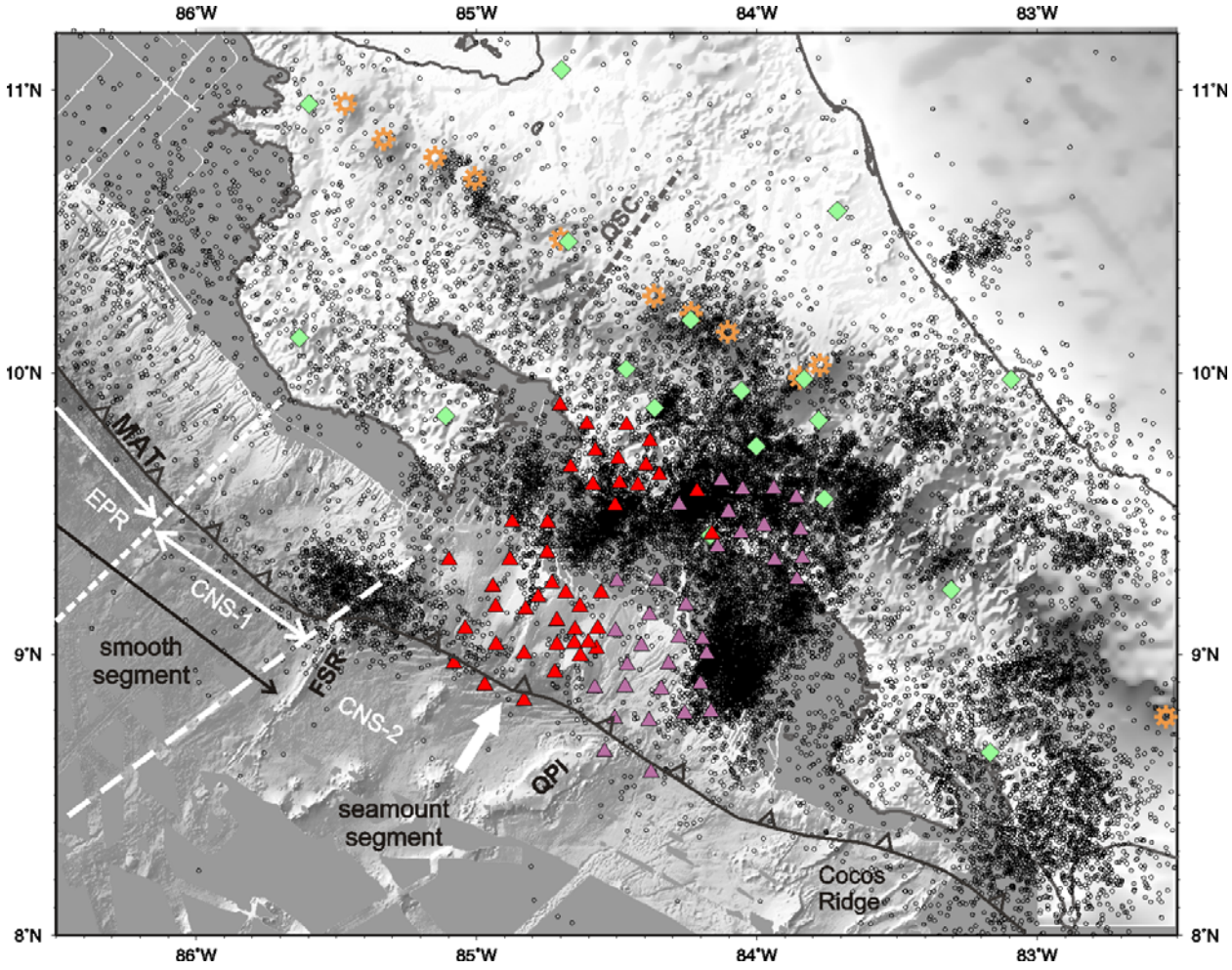

Figure 1.1. Location of the Jacó seismological network (red triangles), which recorded the data for this study. Seismicity in Costa Rica from the catalogue of the local observatory Red Sismológica Nacional (RSN) for the period 1992-2007 (open circles) is included. Events from the RSN catalogue recorded by at least six stations and a rms < 1 are shown. Rhombuses represent permanent seismological stations from RSN. Purple triangles are stations from the Quepos network, operating from October 2002 to the beginning of April 2003. Radiating circles mark the position of Holocene volcanoes. Bathymetry (exaggerated) and main tectonic segments after von Huene *et al.* (2000) and Barckhausen *et al.* (2001), respectively. MAT: Middle America Trench axis, QSC: Quesada Sharp Contortion proposed by Protti *et al.* (1994), FSR: Fisher Seamount and Ridge, QPl: Quepos Plateau, EPR and CNS: segments of the Cocos Plate oceanic crust generated at the East Pacific Rise and the Cocos-Nazca Spreading Center, respectively.

1.1 Tectonic setting

Costa Rica is located on the western margin of the Caribbean Plate, where subduction of the Cocos Plate takes place along the Middle America Trench (MAT) (Figure 1.2) with a convergence direction of 32° and subduction rates varying from 8.3 cm yr^{-1} in northwestern Costa Rica to 9.0 cm yr^{-1} in the southeast (DeMets *et al.* 1994). The high seismic activity in the area is generated by the subduction process, crustal deformation and magmatic activity along the volcanic front (Figure 1.1). Another

source of seismicity seems to be the proposed Central Costa Rica Deformed Belt (CCRDB, Marshall *et al.* 2000, Montero 2001), a diffuse zone of active faulting resulting from the arcward propagation of a deformation front due to subduction of thickened oceanic crust, i.e. the Cocos Ridge and the flanking seamount segment. This faulting zone links the North Panama Deformed Belt with the MAT, defining the western boundary of the Panama Block microplate (Adamek *et al.* 1988).

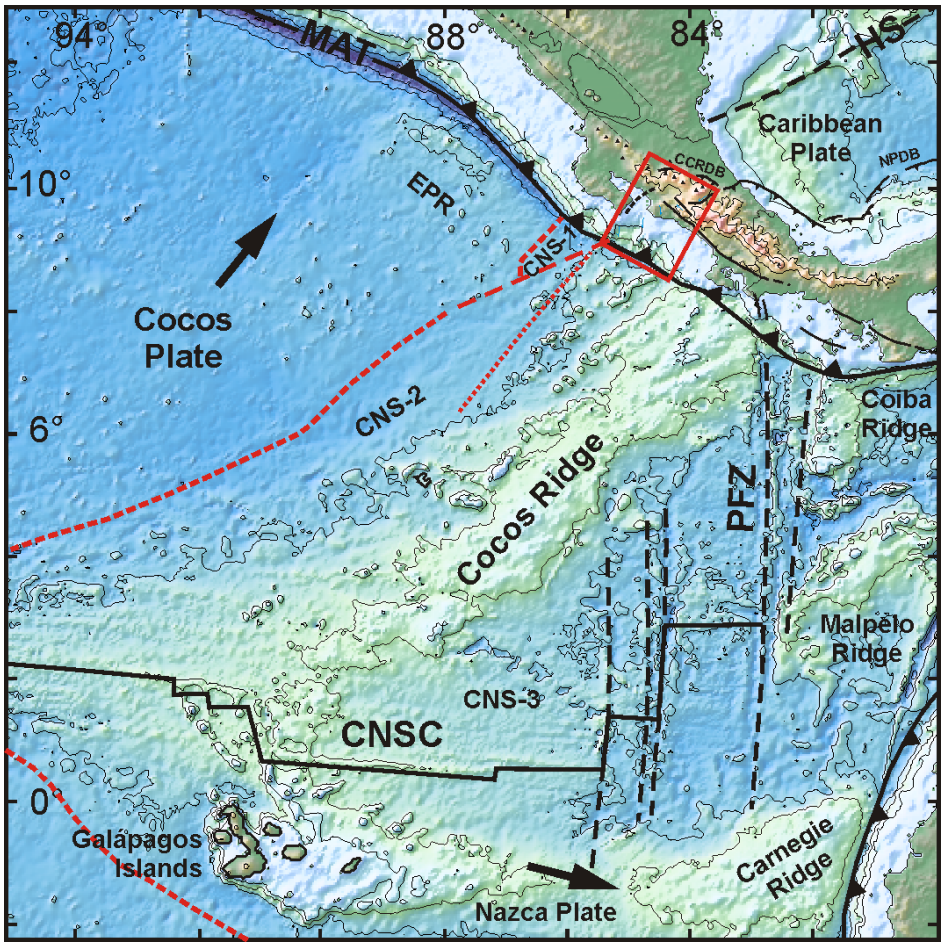

Figure 1.2. Tectonic setting of Costa Rica, showing the interaction between Cocos, Caribbean and Nazca plates. Bathymetry from Smith & Sandwell (1997), with contours every 1000 m. Main tectonic segments after Barckhausen *et al.* (2001) and the works referenced by them. CNSC: Cocos-Nazca Spreading Center, PFZ: Panama Fracture Zone, EPR and CNS: oceanic crust created at the East Pacific Rise and the Cocos-Nazca Spreading Center (the numbers indicate ridge jumps), respectively, MAT: axis of the Middle America Trench, CCRDB: Central Costa Rica Deformed Belt, NPDB: North Panama Deformed Belt, HS: Hess Escarpment.

As mentioned above, input variations in the subducting oceanic lithosphere occur along the Costa Rican margin. The Cocos Plate lithosphere subducting at the MAT today (Figure 1.1) has been created at the fast-spreading East Pacific Rise (EPR) and at the present slow-spreading Cocos-Nazca Spreading Center (CNS) and its precursors, the latter partially modified by Galapagos hotspot magmatism. The crust formed at the EPR is 24 Myr old at the MAT, while the crust offshore central and

southeastern Costa Rica has ages ranging from 19 to 15 Ma (Werner *et al.* 1999, Barckhausen *et al.* 2001), respectively. The thickness of the Cocos Plate crust varies from 5-7 km offshore Nicoya (Sallarès *et al.* 2001, Walther & Flueh 2002), to 6-8 km in the seamount domain (Ye *et al.* 1996, Walther 2003), and reaches up to 19-21 km beneath the Cocos Ridge (Walther 2003, Sallarès *et al.* 2003). Several hundred meters of pelagic and hemipelagic sediments are carried by the plate to the trench (Kimura *et al.* 1997).

The different composition and origin of the subducting plate is also evidenced by the highly variable morphotectonics displayed by the Cocos Plate offshore Costa Rica (Figure 1.1). Von Huene *et al.* (1995, 2000) recognized and analyzed three different morphological segments off Costa Rica, each causing their own imprint on the shape and configuration of the continental slope. Facing the Nicoya Peninsula, the subducting seafloor has a smooth relief, whereas to the southeast the Cocos Ridge stands 2 km high over the surrounding ocean floor. The segment in between, the area of this study, stretches from the Fisher Seamount and Ridge until the Quepos Plateau, and it is 40 per cent covered by seamounts displaying Galapagos geochemistry and ages of 13-14.5 Myr adjacent to the margin (Werner *et al.* 1999). Substantial deformation of the continental slope in the form of deep furrows and domes indicates seamount subduction and there is evidence that they remain attached to the subducting plate to depths of ~25 km, eventually causing coastal uplift (Fisher *et al.* 1998, Gardner *et al.* 2001) and large earthquakes (Husen *et al.* 2002, Bilek *et al.* 2003).

High-quality seismic lines, high-resolution bathymetry and ocean drilling allow the conclusion that the Middle American convergent margin has been tectonically erosive since the Middle Miocene (Ranero & von Huene 2000, von Huene *et al.* 2000, Vannucchi *et al.* 2001). Basal tectonic erosion offshore Costa Rica causes mass removal, and subsequent crustal thinning and margin subsidence. Offshore Nicoya Peninsula, high non-steady rates ranging from long-term ~45 km^3 Myr^{-1} km^{-1} to 107-123 km^3 Myr^{-1} km^{-1} during the last 6.5 Ma have been estimated (Vannucchi *et al.* 2003). Besides, subduction erosion by seamount tunnelling and removal of large rock lenses from the upper plate have been identified as two special mechanisms along the Middle American margin (Ranero & von Huene 2000).

The along-strike segmentation of the Cocos Plate appears to have a strong tectonic effect on the upper plate. Significant variations in the subduction angle, the nature of the incoming plate, and magmatic composition along the volcanic arc occur along this margin (Carr & Stoiber 1990, Protti *et al.* 1995a, von Huene *et al.* 2000, Husen *et al.* 2003). On southeastern Costa Rica, cessation of volcanic activity and accelerated uplift of the Talamanca Cordillera since 3.5 Ma have been attributed to the northwest-to-southeast shallowing of the slab as a response to the subduction of the Cocos Ridge solely or, more recently, first to the subduction of the Coiba Ridge and the passage of the Cocos-Nazca-Caribbean triple junction and subsequent subduction of Cocos Ridge (MacMillan *et al.* 2004). This slab shallowing, together with trench retreat by forearc erosion, have been invoked to explain the northeastward migration of the

volcanic front in central Costa Rica from its position during the Miocene-Pliocene to its current location (Marshall *et al.* 2003) (Figure 1.3).

The basic structural configuration of the margin offshore Costa Rica and Nicaragua (Hinz *et al.* 1996, Kimura *et al.* 1997, Ranero *et al.* 2000) consists of a margin wedge composed of the same ocean igneous and associated sedimentary rocks that outcrops at several spots along the coast in Costa Rica (von Huene & Flueh 1994), covered by slope sediments, underthrust by trench sediments and gouge made of upper-plate material, and faced by a small frontal prism. This basic structure is altered in places where seamounts are in the first stages of subduction, but it is a short-term damage: after ~0.5 Myr the morphology and structure of the margin become nearly undistinguishable from places were no seamount subducts (von Huene *et al.* 2000).

Coinciding with the seamount segment, the Central Pacific region of Costa Rica shows a high seismicity rate along the southern sector of the MAT (Figure 1.1). The absence of very large earthquakes (Mw > 7.5) and the high rate of small earthquakes define this part of the subduction zone as seismically decoupled (Protti *et al.* 1994), while coupling increases to the northwest and to the southeast. Several studies have found evidence for a relationship between the subduction of bathymetric highs and the generation of large subduction earthquakes, like the Mw-7.0 Cóbano earthquake in 1990 (Protti *et al.* 1995b, Husen *et al.* 2002) and the Mw-6.9 Quepos earthquake in 1999 (Bilek *et al.* 2003).

1.1.1 Geology of Central Costa Rica

The oceanic assemblages exposed along the coast (unit b1, Figure 1.3) include a pre-Campanian oceanic plateau association in the Nicoya Peninsula and in the outer Herradura Promontory; an accreted oceanic island of Maastrichtian to lower Eocene age which forms the main edifice of the Herradura Promontory; and the Quepos Promontory, formed by the accretion of a Upper Cretaceous-Paleocene seamount (Hauff *et al.* 2000, Denyer *et al.* 2006). Upper Cretaceous and Paleogene deep marine and slope sediments flank these oceanic assemblages (s1, Figure 1.3). The coastal piedmont on the inner forearc is composed by Neogene shallow marine to deltaic sediments, as well as Pleistocene debris avalanches and pyroclastic flows deposits and Quaternary fluvial and coastal deposits (s3, s4, v2 respectively in Figure 1.3).

The volcanic arc in central Costa Rica displays a complex configuration, involving an active Central Cordillera and two extinct volcanic fronts, the Aguacate Range and the Talamanca Cordillera. The Central Cordillera (v3, Figure 1.3) features broad Quaternary basaltic-andesitic stratovolcanoes, some of them active (Poás, Irazú, Turrialba) or dormant (Barva, Hule). Seaward from the active volcanic front, the remnants of the Aguacate Range (v2, Figure 1.3) are constituted by Neogene basaltic-andesite lavas and pyroclastic flows. The Central Valley, located between the Aguacate Range and the Central Cordillera, is a basin topped by thick sequences of Quaternary basaltic to andesitic lavas, pyroclastic flows and lahars.

The Talamanca Cordillera, east from the Central Valley, represents a 175-km gap in the active volcanic arc, stretching between Irazú -Turrialba massif to Barú volcano in Panama. The cordillera displays Neogene intrusive (i1, Figure 1.3) and extrusive rocks (v1), similar in age to the Aguacate Group. The intra-arc Candelaria basin, at the southern flank of the Aguacate Range, is formed by Paleogene deep marine and Neogene deposits (s2, Figure 1.3). The Fila Costeña or Coastal Range (s2, hatched pattern), an inverted forearc basin located at the toe of the Talamanca Cordillera, is composed by a series of Upper Paleogene-Neogene marine slope and subcoastal sediments, cut by northwest-trending inverse faults. The uplift of the range began probably in the Quaternary (Fisher *et al.* 2004).

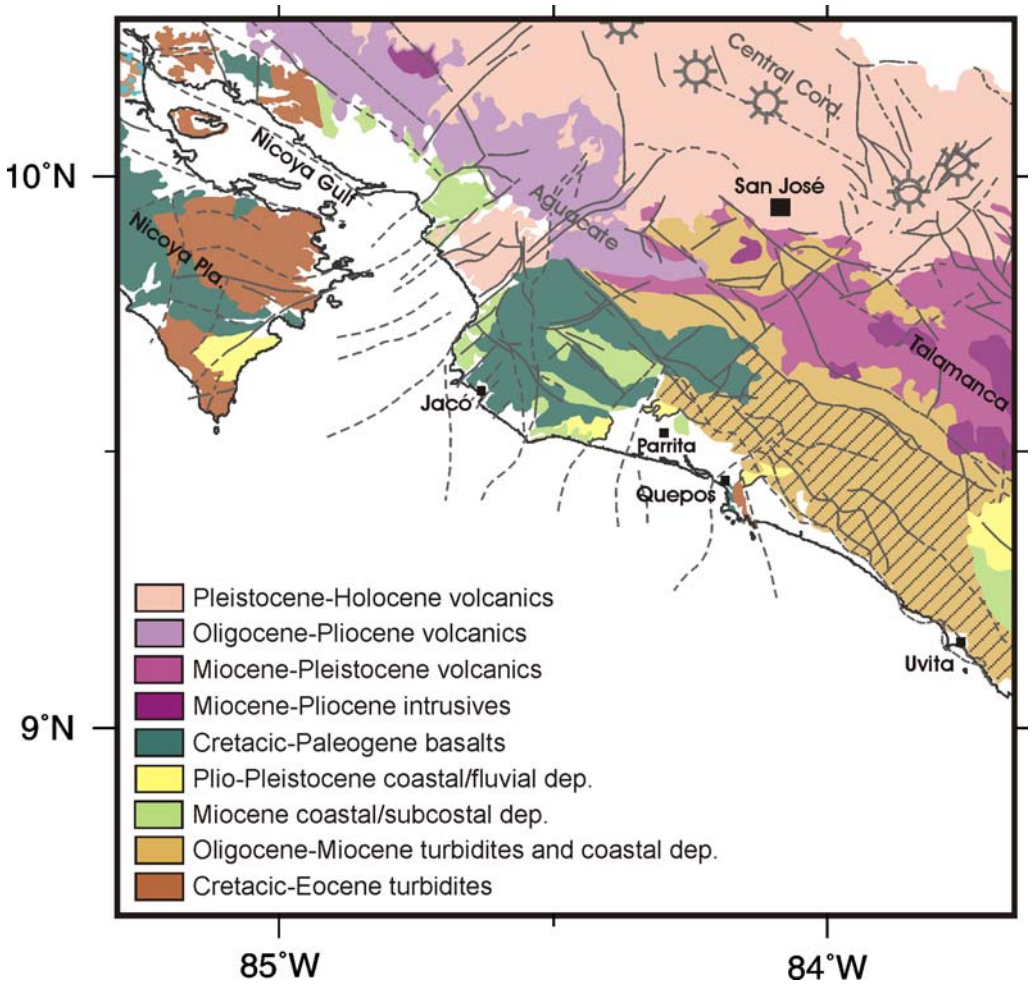

Figure 1.3. Geologic map and faulting (grey lines) of Central Costa Rica, simplified from Denyer & Alvarado (2007). Geologic units as indicated. Areas in white are Quaternary continental and coastal sediments. Radiating circles denote Holocene volcanoes in central Costa Rica.

1.2 Seismogenic zone

Earthquakes are the result of stick-slip frictional instability (Brace & Byerlee 1966), generated by sudden slippage along a pre-existing fault or plate interface. Scholz (1998), further building on the constitutive law for rock friction, points out that seismogenesis and seismic coupling, pre- and post-seismic phenomena, and the insensitivity of earthquakes to stress transients, appear as manifestation of friction.

The stick-slip behaviour on a fault depends on the velocity along the plane and the physical properties of the material implicated. Temperature and normal stress influence the material properties. Materials prone to rupture under increasing velocity slip are called velocity-weakening, while those that resist rupture are known as velocity-strengthening. In a stable frictional regime, the material along the fault plane exhibits a velocity-strengthening behaviour and is unable to generate earthquakes. Earthquakes are nucleated in the unstable regime. In a third, transitional regime, known as conditionally stable, the system is stable under quasistatic loading but may become unstable under strong enough dynamic loading. Earthquakes may propagate into this conditionally stable field (Scholz 1998). In subduction zones, the depths at which transition between stable and unstable regimes occur are greater than observed at crustal faults. Since the plane available for rupture is wider as well, and because it tends to be more continuous along strike, subduction zones produce the largest earthquakes in the world (Scholz 1998).

Within this frame, hence, models of temperature and pressure with depth along the subduction megathrust, together with knowledge about the properties of the materials involved and their response to varying stress, are necessary to understand earthquake generation.

Determination of the location and mechanism controlling the upper and lower limits of the seismogenic zone of the subduction megathrust is of extreme importance to asses the earthquake generation potential and, hence, the seismic risk. Several mechanisms have been proposed to explain the transition from aseismic, stable sliding to seismic, stick-slip behaviour on the shallowest part of the plate interface in subduction zones (Figure 1.4). Since most of the research, until recently, has been carried out on accretionary margins, the models reflect this circumstance.

Byrne *et al.* (1988) observed that the rupture of megathrust earthquakes do not normally propagate all the way to the trench, the shallower part of the interface moving rather through aseismic slip. Those authors pointed out that the sediments composing the accretionary prism are weak and overpressured, lacking the necessary consolidation for seismogenesis, and suggested the location of the backstop as the beginning of the interplate seismicity. A variety of diagenetic, chemical and mechanical processes happening at temperatures between 60° and 150°C have been since then invoked to account for the updip initiation of seismicity. Vrolijk (1990) suggested that the transition from smectite to illite at 100°-150°C on the décollement

may play a decisive role on the sediment consolidation processes and consequently on the onset of interplate seismicity. Nevertheless, laboratory tests (Saffer & Marone 2003) recently concluded that under increasing temperature and pressure, illite is a velocity-strengthening material, which does not favour the unstable sliding.

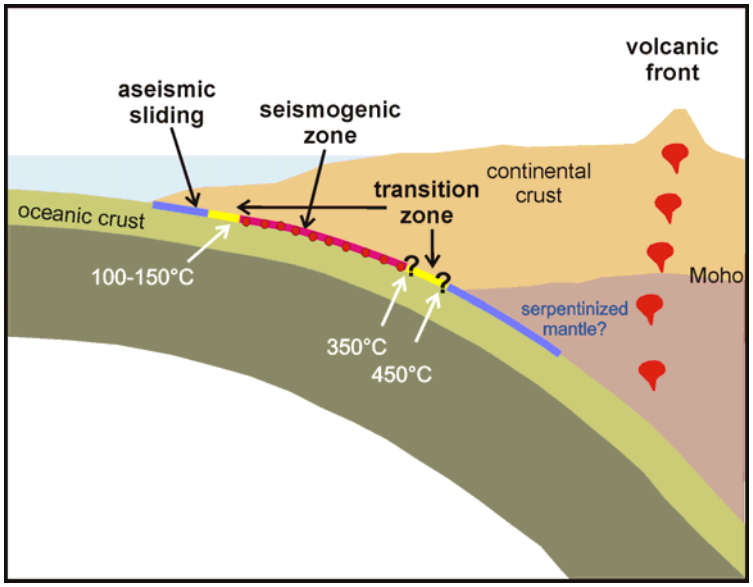

Figure 1.4. Schematic diagram illustrating the seismogenic and aseismic portions of the plate interface, modified from Hyndman *et al.* (1997). See text for discussion.

Hyndman *et al.* (1997) and Oleskevich *et al.* (1999) found a good correlation of the 150°C isotherm along the subduction zone predicted by thermal models and the seismicity at Nankai, Cascadia, South Alaska and Chile, and suggested that the transition to seismic behaviour is determined by temperature-controlled reactions on the subducted sediments. Moore & Saffer (2001) and Moore *et al.* (2007), for their part, explain the changeover to stick-slip behaviour in accretionary margins as a combination of pressure- and temperature-dependent processes that take place between 100°- 150°C and cause progressive changes on subducted and accreting sediments, such as porosity reduction, fault zone cementation, dewatering, and consolidation of accreted sediments. The combined effect of this changes augment the effective stress and coupling at the plate boundary, allowing the storage of elastic energy released during earthquakes.

The lithology at the plate boundary varies between accretionary and erosional margins, namely from sediments to igneous or metamorphic rocks, respectively. Nevertheless, the isotherm of 150°C still seems to play the same control on the updip limit of the seismogenic zone on both type of zones (Figure 1.5). From this observation, Ranero *et al.* (2008) deduce that a common first-order process must control the updip limit on both types of convergent margins. Decrease on fluids abundance at the plate boundary close to the transition to seismic behaviour have been documented on both environments, suggesting the abundance of fluids rather than changes related to lithology at the plate boundary as the main common factor.

Ranero *et al.* (2008) point our that along the Middle American margin, while the 150°C isotherm varies from ~70 km landward from the trench off Nicaragua, to ~60 km off Nicoya Peninsula, to only ~30 km NW Osa Peninsula, the seaward limit of the interplate seismicity varies accordingly. Even in areas where subduction earthquakes have been associated to seamount subduction the onset of seismicity is enveloped by the 150°C isotherm, despite the local increase in stress caused by the seamounts. In the shallower parts of the subduction zone, seamounts cause strong but primarily aseismic deformation of the margin slope. With depth, the release of fluids diminishes and the water is drained, favouring grain-to-grain contact that causes an increase on effective stress and seismic coupling at the fault zone (Ranero *et al.*, 2008). The conceptual model for fluid distribution in erosional margin from Ranero *et al.* (2008) is summarized in section 1.3 (Figure 1.5).

The downdip limit of the seismogenic zone (Figure 1.4) has also been subject of speculation. Tichelaar & Ruff (1993) observed that in most of Circum-Pacific subduction zones, the maximal depth of interplate coupling extends to ~40 km depth. Based on findings from other tectonic environments, they called on the critical-temperature concept to explain the deep transition from unstable to stable slip. Assuming a constant coefficient friction, they determined two critical temperatures at ~400°C and 550°C along the plate interface, speculating that the lower temperatures could be characteristic of regions with relatively thick continental crust and vice versa.

Based on analysis of rupture zones of recent great interplate earthquakes in southwest Japan, Alaska and Chile, and thermal modelling, Hyndman *et al.* (1997) and Oleskevich *et al.* (1999) proposed that their downdip limit is determined by the depth at which the plate boundary temperature is ~350-450°C, or at ~40 km depth if the 350°C is reached at greater depths. The latter depth approximately corresponds with the intersection of the upper-plate Moho with the diving slab. Those temperatures would correspond to the transition from brittle to ductile behaviour in mechanical or frictional properties of the plate interface, i.e. the return from unstable to stable sliding. Optionally, the intersection with the continental Moho may imply stable sliding against a forearc mantle wedge with high amounts of serpentinite, talc, and other hydrated mantle rocks. The 350° C thermal limit is applicable to young oceanic plate such as at Cascadia and Nankai margins, while the forearc limit applies for older plates, like Alaska and Chile (Oleskevich *et al.*, 1999).

1.3 Subduction erosion

Convergent margins dominated by subduction erosion are systems in which upper-plate material is removed at the margin front and along the underside of the upper plate, and introduced into the subduction channel. At least 50 per cent of the active margins of the Earth are erosional (von Huene & Scholl 1991, Clift & Vannucchi 2004), but until recently, research on subduction processes have been concentrated on

accretionary margins. Von Huene *et al.* (2004a) integrated earlier ideas with recent observations and proposed a generic subduction-erosion model. In this model, the relatively small, frontal sediment prism seen in erosional margins is a dynamic mass that elevates pore-fluid pressure, reducing friction along the plate interface and allowing trench-sediment subduction with minimal disruption. Once the incoming plate subducts and is increasingly loaded by the upper plate, overpressured fluid invades fractures in the upper plate and separates fragments that are dragged into a subduction channel along the plate interface. This processes thin the upper plate, causing a long-term subsidence and steepening of the continental slope, landward migration of the trench axis and the volcanic front (Sallarès & Ranero 2005).

Previously, Ranero & von Huene (2000) identified two specific mechanisms of subduction erosion along the Middle America margin: erosion by seamount tunnelling and removal of large rock lenses of a distending upper plate. The segment of the margin opposite to the seamount segment recognized by von Huene *et al.* (2000), and subject of this study, presents a thin margin wedge and a strongly indented continental slope (Ranero & von Huene 2000). Several grooves in the slope, parallel to the convergence vector, signal the paths of subducted seamounts. They erode the base of the continental slope, causing re-entrants; in the next 30-40 km further landward, the margin wedge remains semi coherent over the seamounts, although they uplift, fracture and thin the upper plate, generating a rough relief. Seismic images from subducted seamounts indicate that only the upper part of the slope sediment slides above the subducting seamounts. Yet deeper, the seamounts do not disrupt the slope, but tunnel beneath exerting active basal erosion; the pervasive fracturing observed above seamounts provides fluid conduits for venting, which may release pressure. Where the upper plate is thicker than 6-8 km, the surface over the seamounts is smooth, disrupted only by landward dipping normal faults (Ranero & von Huene 2000).

Several seismic lines show, at depths greater than 6 km, plate-boundary reflections bifurcating and surrounding rock masses in the form of megalenses (10-15 km long, 1.5-2 km high), which do not generate strong deformation on the margin wedge as seamounts do. They occur at depths were the temperature-controlled mineral transitions have taken place, and may be formed along pre-existing planes of weakness, when fluids expelled from subducting sediment reach the structure and reduce friction, detaching a lens of margin wedge rock (Ranero & von Huene 2000).

Ranero *et al.* (2008) further discuss the role of fluids distribution in convergent margins. They propose a model of hydrogeological system (Figure 1.5) emphasizing the effect of fluids on the tectonics of erosional margins, based on geophysical, geochemical and geological data collected along the MAT offshore Nicaragua and Costa Rica in the last years, and observations from another erosional margins, like northern Chile. According to their model, other than in accretionary margins, where the fluids contained in the sediments and liberated by early dehydration reactions migrate toward the deformation front along the décollement, in erosional margins

fluids migrate from the plate boundary through a fractured upper plate to seep at the continental slope.

The slope of the upper plate is crossed by faults mostly normal that have been imaged by seismic methods and high-resolution bathymetry in Costa Rica (Ranero & von Huene 2000) and other margins: Chile (von Huene & Ranero 2003), Ecuador (Sage *et al.* 2006) and northeast Japan (von Huene *et al.* 1994). Multibeam bathymetry, deep-towed side-scan sonar, video observations, and sediment and fluid sampling revealed oozing of fluids out from the margin-wedge fault system, mud mounds and at the trail scars left by subducted seamounts have been detected on the middle and upper slope of the margin offshore Nicaragua and Costa Rica (Hensen *et al.* 2004, Ranero *et al.* 2008). Their chemical composition (Hensen *et al.* 2004) indicates that they are originated by clay dehydration at temperatures up to 150°C, superior than those found at the slope sediments. Hence, they likely ascend through the weakened upper plate, were the faults and fractures provide escape channels. Comparison of the estimations of fluid flow budgets from mineral dehydration and from the seeps indicate that almost all water released from sediments and possibly the uppermost oceanic crust at the plate boundary could be potentially evacuated through the fault and fracture system (Ranero *et al.* 2008).

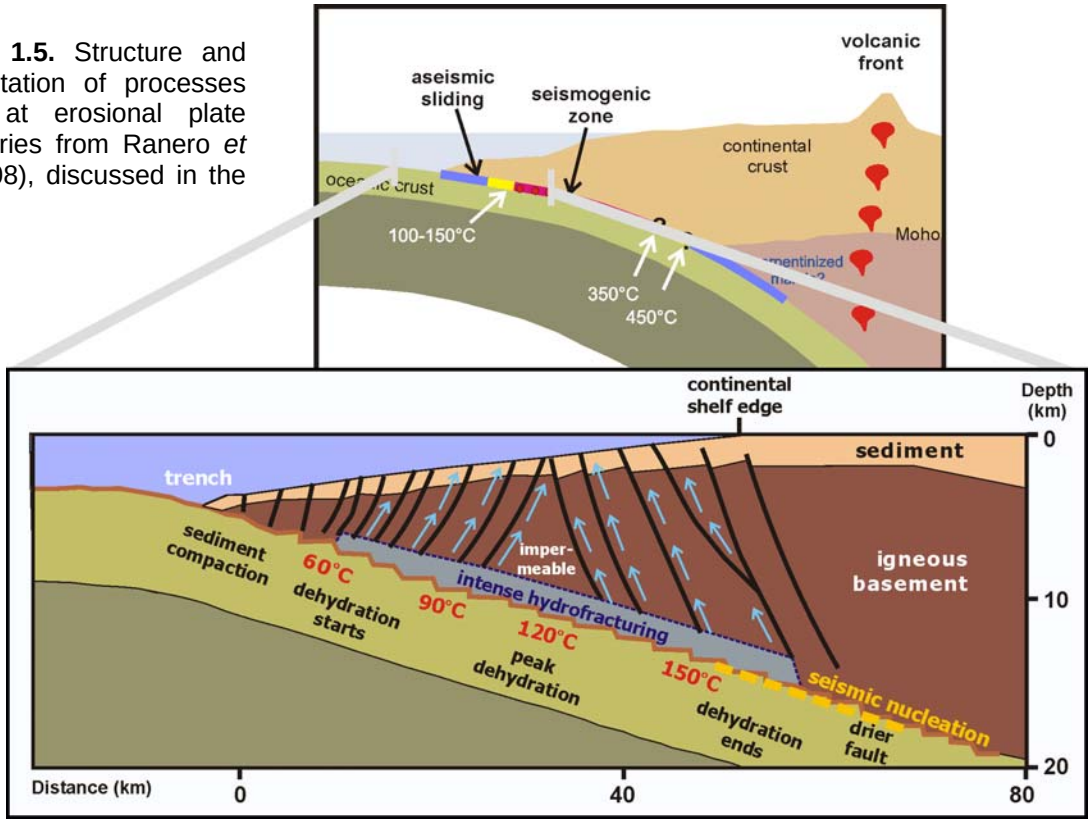

Figure 1.5. Structure and interpretation of processes active at erosional plate boundaries from Ranero *et al.* (2008), discussed in the text.

A close match has been found by Ranero *et al.* (2008) between the mineralogical compositions of sediments entering the subduction in Costa Rica (Spinelli & Underwood 2004), the dehydration temperatures of those minerals, such as smectite transforming to illite (~50-100°C) and biogenic opal to quartz (~60-160°C), the distribution of seeps (>60°C to ~140°C) on the margin slope and the temperature at the plate interface estimated from heat-flow and the depth of the BSR. Furthermore, those authors emphasize that on multichannel seismic reflections lines, only the sector of the plate boundary over which fluid percolation has been detected displays reflectivity patterns that strongly indicate the presence of fluids: relative high-amplitude, negative polarity reflections. This pattern fades away beneath the transition from the upper slope to the shelf.

Tectonic erosion processes weaken and cause the thinning of the margin wedge. Von Huene *et al.* (2004a) suggest that the fracturing along the base of the upper plate may begin within the seismogenic zone and increase updip as the plate interface shallows. Seismogenesis then occurs where the upper plate is coherent and sufficiently thick to store the elastic strain released in large earthquakes.

In this concept, further developed by Ranero *et al.* (2008), it is the fluid distribution, abundance and discharging through a focused flow at the faults and fractures the main parameter controlling the onset of interplate seismicity, contrary to models described for accretionary margins. There, the flow is assumed to be controlled by décollement permeability with dispersed flow across the upper plate. Where fluids are more abundant, tectonic erosion thins the overriding plate, which fractures and subsides. Fluids escape to the seafloor through this fracturing, favouring the building up of friction downdip.

Tectonic erosion seems to stop abruptly under the outer region of the continental shelf. Yet, over the time, the erosion causes migration of the trench landward and this would create a plate interface geometry unrealistically steep on the first 30-40 km, a situation not imaged with seismic data. Ranero *et al.* (2008) point out that some erosion and little subsidence must take place beneath the continental shelf. This could be explained by a reduced amount of overpressured fluids.

1.4 Objectives of the study and agenda

The Jacó experiment was designed with the main goal of obtaining reliable and precise hypocenter locations for the first time offshore the Central Pacific area of Costa Rica. The emphasis are the seismogenic zone and the effect of seamounts at different stages of subduction. Seismic catalogues from the two country-wide permanent networks lack coverage offshore, which limits the location quality.

Local Earthquake Tomography (LET) is a robust technique which allows to obtain high-quality earthquake locations and simultaneously, a good knowledge of the three-dimensional velocity structure of a region. The method has proven valuable and efficient in studying subduction zones, further illuminating the processes taking place there and their link with seismicity. It comprises the inversion of traveltimes to solve for Vp and Vs velocities or Vp/Vs and hypocenter locations. The model parameters are perturbed in order to minimize the difference between observed and calculated traveltimes in a least-square sense. Recently, several tomographic studies have been successfully conducted along the Middle American margin (Protti *et al.* 1996, Husen *et al.* 2003, DeShon *et al.* 2006).

Chapter 2 describes the layout and operation details of the Jacó seismological network, including an evaluation of the station parameters, such as location and timing, and their uncertainty. Careful review of these parameters is important, since wrong estimations could greatly reduce the quality of the model.

Chapter 3 offers an account of the processing and gathering of the local earthquake data, including event detection, merging of available data, magnitude distribution and phase picking.

In chapter 4, the method used in this work to obtain precise earthquake locations and a 3-D velocity model of the studied segment of the margin is described. This includes the derivation of the minimum 1-D model with station corrections for the dataset, previous to the LET. Information provided by controlled source seismology profiling from previous studies is incorporated into the modelling. An assessment of the resolution quality of the final LET model is performed by using standard resolution tools and synthetic tests. A detailed interpretation of the results, focused on the velocity structure and anomalies detected in the margin, is then presented. Most of Chapter 4 has been submitted for publication, which explains its structure.

Chapter 5 concentrates on the seismic activity recorded during the approximately six months of operation of the Jacó network. The seismicity is analyzed on the light of the model interpretation from the previous chapter, earthquakes being related to the source areas of convergent margins. Special attention is given to the seismogenic zone, one of the main targets of the experiment.

Finally, general conclusions are summarized and an outlook for future work is given in chapter 6.

Chapter 2

The “amphibian” Jacó network

2.1 Experiment layout

The central Pacific region of Costa Rica exhibits a very high seismicity rate (Figure 1.1), coinciding with the subduction of ocean floor characterized by rough-relief, which includes seamounts, plateaus and ridges. The area has generated earthquakes with magnitude up to seven in the past, most recently a Mw-6.9 event in 1999 and a Mw-6.4 in 2002.

This activity has been recorded since the 70s by temporal networks installed in different areas of the land, and since the 80s by two permanent country-wide networks, operated by the Universidad de Costa Rica and the Instituto Costarricense de Electricidad, working together as the Red Sismológica Nacional (RSN), and by the Universidad Nacional through its Observatorio Vulcanológico y Sismológico de Costa Rica (Ovsicori). Since these networks are land based, their catalogues lack the coverage necessary for high-quality hypocenter determination offshore. Precise local earthquake locations and detailed knowledge of the three-dimensional velocity structure can provide valuable insights into the dynamics and structure of subduction zones, including the limits and geometry of the seismogenic zone. These reasons motivated the SFB574 to deploy temporal seismological networks to survey the shallow, until now uncovered part of the subduction zone off central Costa Rica.

Due to the structure of the margin in Central Costa Rica, a good coverage of the target area called for an “amphibian” network configuration, consisting of both, land and ocean-bottom subnetworks (Figure 2.1 and Table 2.1). Two networks were installed for six months each, the Jacó and the Quepos networks, named after the coastal towns were the operation centers were located (Figure 1.1). Jacó network, base of this work, was active during from April to October 2002. The network extended from the incoming Cocos Plate to the forearc, covering the Herradura Promontory and

surroundings. In order to improve the station coverage on land, thus increasing the number of well-constrained events toward the downdip end of the seismogenic zone and the volcanic arc, in a later stage, readings from 14 short-period permanent stations of the RSN were incorporated into the dataset. Due to geometrical considerations while taking into account the target area of this experiment, further modelling included readings from only ten RSN stations (Figure 2.1 and Table 2.1). An area of ~19 500 km^2 was covered with the final combined array. In the following, the Jacó subnetworks, the RSN network and their operation are described.

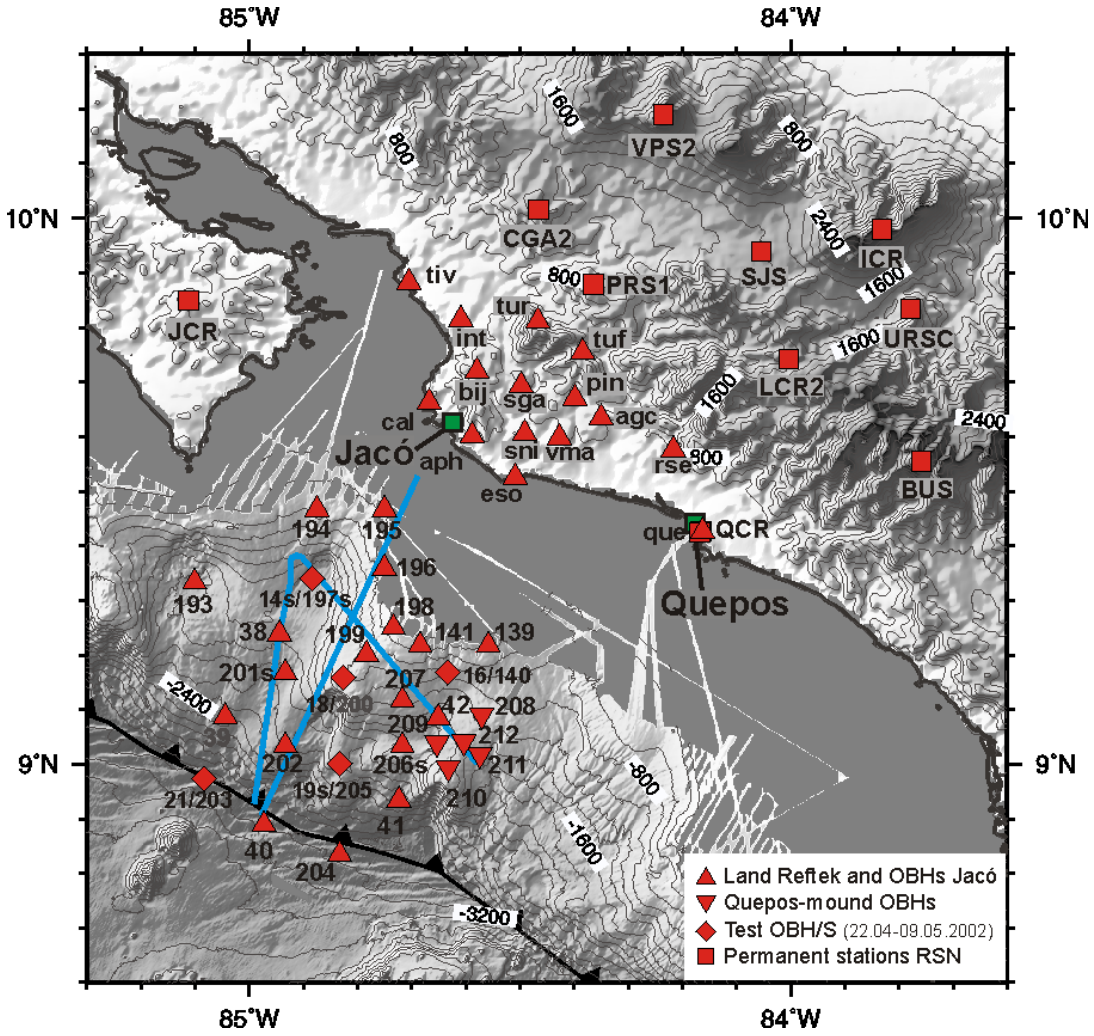

Figure 2.1. Network layout of the Jacó experiment. Symbols represent different equipment and subnetworks, as indicated on the insert. Station labelled in grey failed. Topography and bathymetry from Smith & Sandwell (1997) and von Huene *et al.* (2000), respectively, with superimposed contours every 200 m. Three shooting lines for OBH relocation shown in blue. Dented line represents the axis of the Middle America Trench.

2.1.1 Jacó – Ocean-bottom network

The basic configuration of the subnetwork consisted of 23 ocean-bottom hydrophones (OBH) installed from April until October 2002, distributed from the trench to the upper slope of the margin. Their depths ranged from 0.3 to 3.6 km under the sea level and they covered an area of ~70 x 70 km^2 (Figure 2.1). From May to middle July 2002, five additional OBH were deployed on Quepos mound, at the eastern border of the subnetwork, and their signals added to the dataset. The average station spacing was ~12 km. No stations were deployed at the marine shelf with depths shallower than 200 m.

The deployment was conducted by IfM-GEOMAR using the German research vessel "Sonne" as platform, during the cruise SO163 (Weinrebe & Flueh 2002) in April-May 2002. Previous to the final deployment, seven instruments were installed during two weeks at the beginning of the leg to test the equipment and for data quality. Five of them operated and recorded adequately, the other two being affected by sensor and recorder failures. The readings were included in the dataset. At the end of the leg, the test stations that worked properly were deployed again, at the same positions, together with the rest of array (Figure 2.1). The stations recorded continuously at a sampling rate of 100 Hz, with the data being stored onto flashcards.

Once deployed, active seismic shooting was carried out following the baselines of the subnetwork. The shooting was performed using two G-Gun arrays and an additional single Bolt gun of 32 litres volume. Unfortunately, the quality of the recordings is medium to bad, which can be attributed to the configuration of the seismological array with respect to the shooting lines (Figure 2.1).

The OBH stations were equipped with a hydrophone or with a broadband differential pressure gauge sensor (DPG). The subnetwork was designed to include three combined OBH/OBS stations, i.e. stations including hydrophones as well as seismometers. It was foreseen to use PMD broadband seismometers for the OBS, but the aforementioned testing period revealed that the available instruments were drawing more power than specified and stopped recording prematurely. The OBS were finally deployed using 4.5-Hz Owen seismometers, which were adapted on board to the available MLS recorders. Unfortunately, in spite of these efforts, the seismometers rendered no data.

The recovery of the stations was achieved with the research vessel "Meteor" during the leg M54-3B (Soeding *et al.* 2003), in early October 2002. Most of the stations operated without problems (Figure 2.2). Only two of the OBHs, *39* and *200*, rendered no data at all being affected by sensor problems. At OBHs *205* and *206* the strong signal drift caused the zero level of the signal to go off scale, inhibiting the recording of seismic signals after around one month of operation. Quepos-mound stations *211* and *212* were only operational for about one month.

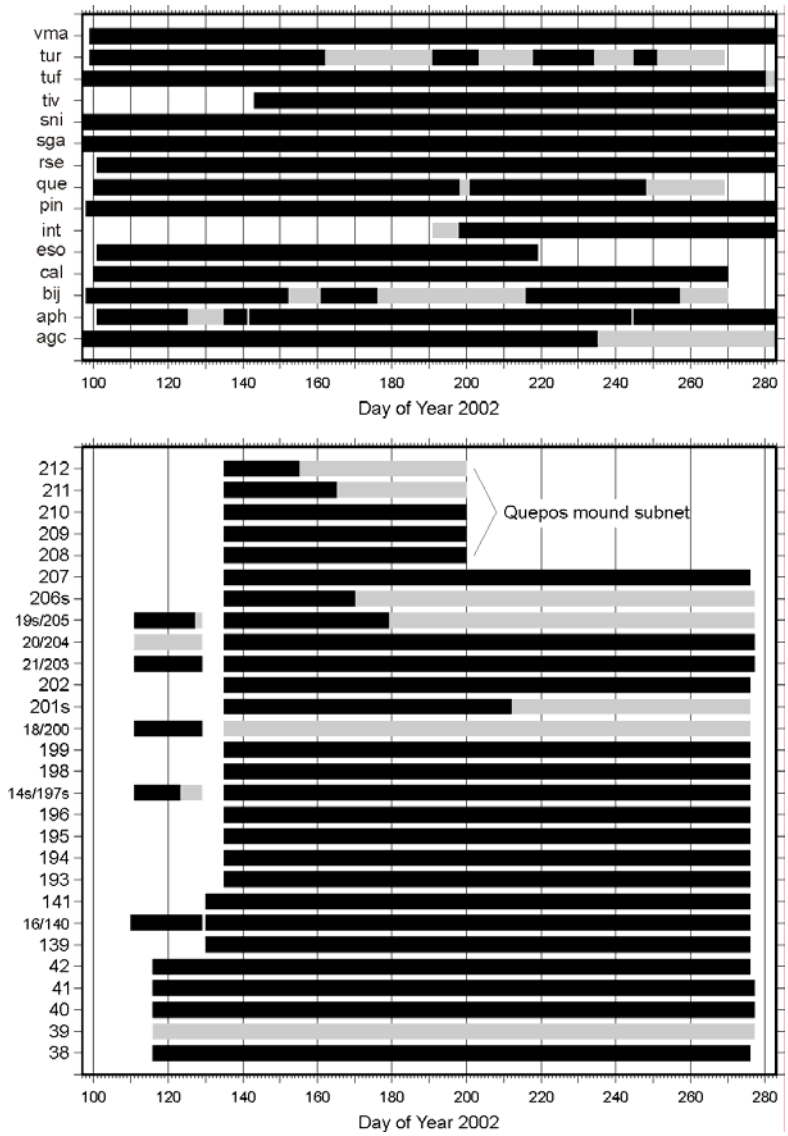

Figure 2.2. The effective recording periods of the stations of Jacó network. Black bars denote days of effective recording, while grey marks periods without data. Time is given in Julian days.

2.1.2 Jacó – Land network

Two weeks before the deployment of the ocean-bottom subnetwork, and through the combined efforts of the Universität zu Kiel, the Instituto Costarricense de Electricidad (ICE) and IfM-GEOMAR, the land network was installed in the surroundings of Jacó town. It consisted of 15 three-component short-period stations, equipped with Mark L-4C-3D seismometers and RefTek dataloggers sampling at 100 Hz and recording in a continuous mode. The elevation of the stations ranged from 0.3 to 0.9 km above the sea level and the network extended ~75 km along the coast and ~30 km inward (Figure 2.1). The average spacing between stations was ~12 km.

Maintenance of the station took place approximately every three to four weeks, including inspection of the power supply and GPS proper function, and changing of the 3-GB portable hard disks. The raw data from the latter was downloaded to an industry-type PC provided with SCSI interfaces, which was permanently located in

Jacó town. Then two identical DAT tapes were recorded after each change, one for ICE and one to be sent to Germany, where a backup was made on a tape robot.

Most of the land stations operated correctly during the six months. The effective recording periods of each station is shown in Figure 2.2. Stations *bij* and *tur* had frequent power problems, resulting in data loss. Stations *agc* and *que* stopped working before the last service interval. At *que,* located at the same site as the permanent one-component station from RSN *QCR*, the power supplies and batteries of both were stolen. The installation of stations *int* and *tiv* was delayed because of initial recorder failures. Station *eso* was closed earlier to replace equipment on station *bij*, which was hit by lightning. The proximity of *eso* to a secondary road originated more noise than at the other sites. The vertical component of station *rse* failed relatively often due to a problem with the recorder channel.

2.1.3 RSN permanent land network

Preliminary hypocenter locations of the events recorded by Jacó network revealed that an important percentage of the seismicity in the area originated close to the borders of the land network. In order to improve the station coverage, thus increasing the number of well-constrained events (GAP ≤ 180°), signals from 14 of the permanent land stations of the RSN were incorporated into the dataset. Due to the limited extension of the target area of this experiment, for further modelling readings from only ten of the RSN stations were used (Figures 2.1 and 2.13, Table 2.1).

The RSN covers the whole country but there is a clustering of stations on the central part, where most of the population lives. The RSN stations used in this work are all equipped with short-period one-component sensors (see Table 2.1). Their elevations vary from 0.7 to 3.5 km above sea level. The signals are transmitted via telephone to the recording centre in San José, where they are digitized at a sampling rate of 50 Hz, synchronized with a Garmin GPS and stored in a ringbuffer disk. The events are triggered with a short-term-average versus long-term-average (STA/LTA) algorithm. The data acquisition is accomplished using the SEISLOG system (Utheim & Havskov 2002).

Table 2.1. Final station positions for all stations used during the experiment and their estimated uncertainties.

station	location	type	latitude [° N]	longitude [° W]	elev. [m]	horizontal [m]	vert. [m]	time
Jacó land network								
agc	Fila Aguacate	RefTek	9.6344	84.3499	363	± 50	± 20	< 2 ms
aph	Altos Playa Hermosa	RefTek	9.6012	84.5880	205	± 50	± 20	< 8 ms
bij	Bijagual	RefTek	9.7193	84.5795	595	± 50	± 20	< 6ms
cal	Caletas	RefTek	9.6610	84.6707	89	± 50	± 20	< 2 ms
eso	Esterillos Oeste	RefTek	9.5264	84.5083	46	± 50	± 20	< 1 ms
int	Intermedios	RefTek	9.8146	84.6088	125	± 50	± 20	< 1 ms
pin	San Vicente	RefTek	9.6706	84.3978	363	± 50	± 20	< 5 ms
que	Quepos	RefTek	9.4263	84.1622	74	± 50	± 20	< 5 ms
rse	Río Seco	RefTek	9.5773	84.2171	158	± 50	± 20	< 8 ms
sga	San Gabriel	RefTek	9.6936	84.4979	375	± 50	± 20	< 8 ms
sni	San Isidro Tulín	RefTek	9.6063	84.4915	160	± 50	± 20	< 2 ms
tiv	Tivives	RefTek	9.8822	84.7050	70	± 50	± 20	< 3 ms
tuf	Túfares	RefTek	9.7542	84.3841	904	± 50	± 20	< 8 ms
tur	Turrubares	RefTek	9.8115	84.4668	911	± 50	± 20	< 1 ms
vma	Vista de Mar	RefTek	9.5982	84.4273	234	± 50	± 20	< 8 ms
Jacó ocean bottom network								
14s	upper slope	OAS	9.3331	84.8833	-1741	± 250	± 10	< 5 ms
16	upper slope	HTI	9.1662	84.6336	-944	± 250	± 10	< 5 ms
18	middle slope	OAS	9.1566	84.8265	-827	± 250	± 10	< 5 ms
19s[1]	lower slope	OAS	8.9999	84.8342	-2206	± 250	± 10	< 5 ms
21	outer rise	HTI	8.9672	85.0841	-3602	± 250	± 10	< 5 ms
38	middle slope	DPG	9.2395	84.9437	-1752	± 250	± 10	< 5 ms
40	outer rise	DPG	8.8888	84.9738	-3420	± 250	± 10	< 5 ms
41	lower slope	DPG	8.9340	84.7238	-2615	± 250	± 10	< 5 ms
42	middle slope	DPG	9.0845	84.6501	-1481	± 250	± 10	< 5 ms
139[1]	upper slope	OAS	9.2170	84.5585	-379	± 250	± 10	< 5 ms
140	upper slope	OAS	9.1670	84.6332	-939	± 250	± 10	< 5 ms
141	upper slope	OAS	9.2163	84.6832	-351	± 250	± 10	< 5 ms
193	middle slope	HTI	9.3332	85.1010	-1880	± 250	± 10	< 5 ms
194	upper slope	OAS	9.4670	84.8750	-560	± 250	± 10	< 5 ms
195[1]	upper slope	OAS	9.4667	84.7500	-324	± 250	± 10	< 5 ms

Table 2.1 (continuation)

196	upper slope	HTI	9.3579	84.7510	-413	± 250	± 10	< 5 ms
197s	upper slope	HTI	9.3333	84.8831	-1745	± 250	± 10	< 5 ms
198[1]	upper slope	OAS	9.2497	84.7333	-291	± 250	± 10	< 5 ms
199[1]	upper slope	HTI	9.1989	84.7828	-734	± 250	± 10	< 5 ms
201s[1]	middle slope	OAS	9.1655	84.9343	-2080	± 250	± 10	< 5 ms
202[1]	lower slope	HTI	9.0320	84.9340	-2237	± 250	± 10	< 5 ms
203[1]	outer rise	OAS	8.9662	85.0833	-3561	± 250	± 10	< 5 ms
204[1]	outer rise	OAS	8.8333	84.8333	-3474	± 250	± 10	< 5 ms
205	lower slope	HTI	9.0000	84.8333	-2210	± 250	± 10	< 5 ms
206s[1]	middle slope	OAS	9.0333	84.7168	-1726	± 250	± 10	< 0.2 s
207	middle slope	OAS	9.1153	84.7155	-1159	± 250	± 10	< 5 ms
208	middle slope	HTI	9.0884	84.5698	-1155	± 250	± 10	< 5 ms
209[1]	middle slope	OAS	9.0371	84.6523	-1615	± 250	± 10	< 5 ms
210	middle slope	HTI	8.9930	84.6318	-1202	± 250	± 10	< 5 ms
211[1]	middle slope	OAS	9.0167	84.5743	-1411	± 250	± 10	< 5 ms
212[1]	middle slope	OAS	9.0383	84.6021	-1326	± 250	± 10	< 5 ms
RSN network								
ACR[2]	Golfito	L4C	8.6538	83.1680	471	± 1	± 1	< 10 ms
BARC[2]	Buenos Aires	L4C	9.1660	83.3345	378	± 1	± 1	< 10 ms
BUS	Buena Vista	L4C	9.5553	83.7583	3487	± 1	± 1	< 10 ms
CGA2	Cerro Gallo	Kin. SS-1	10.0162	84.4655	1200	± 300	± 50	< 10 ms
FORC[2]	Fortuna	L4C	10.4668	84.6718	392	± 10	± 10	< 10 ms
ICR	Irazú	L4C	9.9800	83.8312	3302	± 10	± 10	< 10 ms
JCR	Jicaral	L4C	9.8498	85.1118	575	± 10	± 10	< 10 ms
LCR2	La Lucha	Kinemet. SS-1	9.7422	84.0030	1730	± 10	± 10	< 10 ms
PRS1	Puriscal	Electrotech EV17	9.8795	84.3640	1120	± 300	± 50	< 10 ms
QCR	Quepos	L4C	9.4265	84.1623	66	± 300	± 20	< 10 ms
SJS	San José	Teledyne S13	9.9392	84.0542	1196	± 10	± 10	< 10 ms
TRTC[2]	Tortuguero	Kinemet. SS-1	10.5753	83.7135	105	± 300	± 20	< 10 ms
URSC	Urasca	Kinemet. SS-1	9.8350	83.7782	1500	± 300	± 50	< 10 ms
VPS2	Poás	L4C	10.1902	84.2353	2570	± 10	± 50	< 10 ms

[1] reversed polarity
[2] not used for further modelling

2.2 Station parameters

During the inversion process, hypocenter locations and velocities are adjusted to fit the observed traveltimes, which together with the station positions are the known variables. Hence, the estimation of uncertainty in arrival times and station locations is an important step in the analysis of the quality of the data being inverted. The accuracy of the observed arrival times depends on the accuracy of the station position and the recorder timing system, as well as on the sampling rate and the picking accuracy. In this section the station parameters, i.e. the error in the timing system and the quality of the geographic coordinates estimation for the recorders, are discussed. Table 2.1 summarizes the parameters of the stations used in this work and their estimated uncertainty. The picking accuracy is described in Chapter 3.

2.2.1 Jacó – Ocean-bottom network

OBH/S tend to drift from the deployment position due to marine currents and winds. The accuracy of the vessel position is another factor to consider, as well as the delay between the emersion of the station and actual recovering. Therefore, using the deployment or recovering positions of the ship, or an average, is uncertain. To accomplish a better estimation of the real location of the stations, airgun shooting along profiles over the OBHs was carried out. The drift along the profile direction is then determined by fitting the hyperbola of the direct wave of airguns shots in a least-square sense. As mentioned above, three profiles were shot following the baselines of the ocean bottom network during cruise SO163-2 (Figure 2.1). Unfortunately, the records from most of the stations display very poor quality. Even more, the configuration of the profiles also hinders the relocation of the stations. Only five stations located directly under the shooting lines could be relocated. To relocate stations positioned off the shooting lines, good-quality records from two profiles are needed. This condition was met only by one station (*199*). Finally, it was possible to relocate seven off-line stations along just one profile. The estimated drifts vary from 30 to 190 m in latitude, and from 28 to 160 m in longitude. OBHs *42* and *212* drifted as much as 243 and 217 m respectively from the deploy position, being the biggest estimated drifts. Based on these estimates, a general position accuracy of ±250 m is assumed for the ocean bottoms recorders. The stations depth during deployment is taken from the Simrad EM120 multibeam echosounder system available on board. The depths are calibrated by conductivity-temperature-depth (CTD) profiling, which estimates the change in sound speed of the water with depth. An accuracy of ±10 m on the vertical is appraised for the OBHs.

OBH *141* stopped recording before recovering. This made clock synchronization after recovering impossible. Nevertheless, comparison of arrival times with OBHs located less than 8 km away from OBH *141* rules out significant timing errors. The skew times for the rest of OBH ranged between 69 and 614 milliseconds in ~145 days of operation, except for OBH *206s* with an unusual value of 7.34 seconds in 32 days.

The uncertainty of the internal clock is therefore estimated in less than 5 ms per day, except for OBH *206s* (± 0.2 s).

2.2.2 Jacó – Land network

The Reftek instruments are equipped with GPS receivers, which provide clock synchronization and position determination every hour. Since this information is stored on a log file, between 2000 and 4500 measurements of those parameters are available for the whole period of the experiment for each station. Following Haslinger (1998), the station positions were taken as the center of the ellipses resulting from plotting all the positions estimated by GPS during the experiment. Examples of the plots are given in Figure 2.3. Comparisons between GPS single-point location estimations and exact geodetic measurements in Greece have resulted in accuracies of ±100 m and ±50 m in the horizontal and vertical directions, respectively (Haslinger 1998). For the Jacó experiment, a geodetic measurement of the position of station *que* is available. The difference between this measurement and the estimation obtained from the ellipse yields 25 m in the horizontal direction and 8 m in the vertical sense. Moreover, since the Selective Availability was deactivated on 2000, a better accuracy than that reported by Haslinger (1998) is to be expected in the GPS single-point locations. For the Jacó network land stations, hence, a conservative position accuracy of ±50 m is estimated in the horizontal direction, and ±20 m in the vertical (Table 2.1).

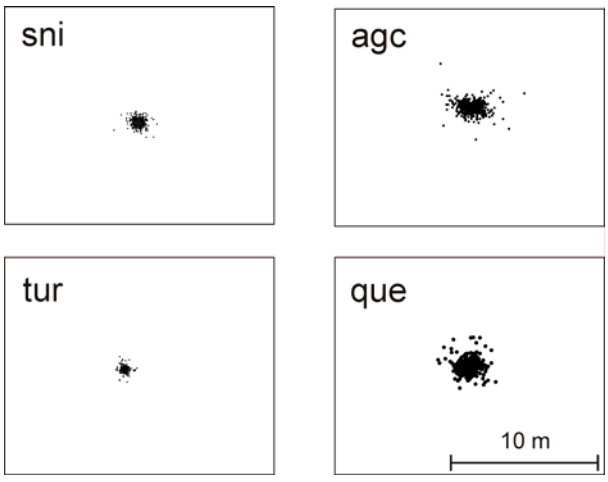

Figure 2.3. Examples of ellipses resulting from plotting all the positions estimated by the GPS of the Reftek land stations during the experiment. Land station positions were taken as the center of the ellipses. Scale for all plots as indicated.

GPS receiver operation problems detected during the Jacó experiment were scarce. Only station *aph* did suffer from the complete loss of the GPS signal from the end of August until the end of the experiment. The readings from this period have been deleted from the database used for inversion, but remain in the catalogue to take advantage of the S-P times in the single-event locations when the quality of the signal is good. Synchronization of the internal clock of Reftek stations also uses the GPS

signal and is performed every hour, which kept the drift below 8 ms per hour (Table 2.1).

Seeking for other possible undetected timing errors, histograms of traveltime residuals were plotted after locating the earthquakes with the same initial velocity model (Quintero & Kissling 2001) as suggested by Husen (1999). Only well locatable events have been examined. Station corrections were not applied in order to avoid the time problems to be "absorbed" by them. A Gaussian distribution is expected if the time synchronization was correct. Examples are shown in Figure 2.4, where the effect of the GPS failure suffered at station *aph* is clear.

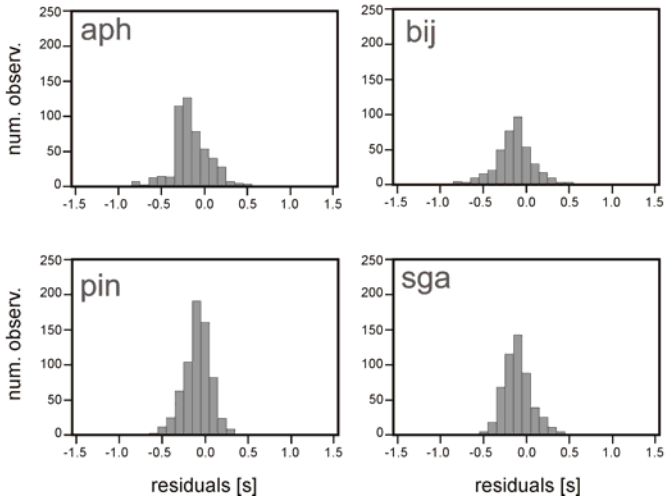

Figure 2.4. Examples of traveltime residuals of Jacó land stations. Deviation of the Gaussian distribution for *aph* reflects the loss of the GPS signal.

2.2.3 RSN permanent land network

Position and elevation accuracy for the RSN stations varies, as some locations have been measured by topography surveys which render uncertainties smaller than ±1 m, while the rest were determined by single-point GPS measurements and the use of topographic charts scaled 1:50,000. Comparison between some station locations based first on maps and a following geodetic survey, allows to determine that uncertainties do not surpass ±300 m and ±50 m in the horizontal and vertical directions, respectively (see Table 2.1).

As mentioned above, the signals from the RSN stations are transmitted by telephone line to a center where the GPS signal is added. A considerable timing difference between RSN and Jacó network signals was detected during this experiment. This subject is addressed in detail below.

Time inconsistency of RSN data

During merging of the readings from the Jacó and RSN catalogues, differences in the timing of both networks were detected. Not only there were considerable traveltime residuals from the RSN stations frequently, but also the station corrections resulting

from the first P-wave 1-D inversions for stations *que* (Jacó) and *QCR* (RSN), which were located at the same place, were quite different (-0.35 s and +0.10 s, respectively). Station *que* operated from the middle of April until the beginning of September 2002, when hard disk problems turned the last month of recording useless. No other problems with the station were detected.

A set of 125 events with P-wave arrival times from both stations, *que* and *QCR*, were selected and the P-arrivals differences plotted. Figure 2.5 shows two clearly defined populations, with peaks around 0 to 100 milliseconds and 1 to 1.1 seconds. The first set may be associated to picking uncertainties, considering differences in the sampling rate (50 Hz for *QCR*, 100 Hz for *que*). But the second set displays values far too high for this explanation.

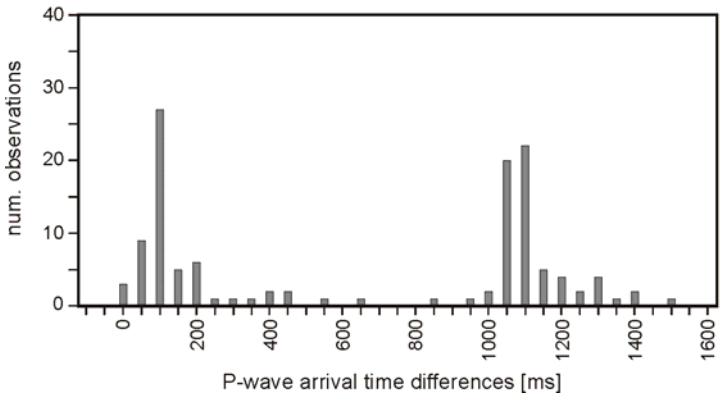

Figure 2.5. Differences on P-wave arrival times between stations *QCR* (RSN network) and *que* (Jacó network), installed at the same site, for 125 earthquakes from April to August 2002. Two populations are observed. The group of data with the highest (positive) differences suggests that there is a timing inconsistency between both networks.

In order to further explore whether there was actually a timing difference rather than local problems with station *QCR*, a new dataset of 201 events was chosen, following the criteria of a GAP ≤ 180° with at least 18 P-wave observations alone from the Jacó network (Figure 2.6). This dataset was used to adjust the minimum 1-D P-wave velocity model for Costa Rica from Quintero & Kissling (2001), hereafter referred to as CM model, to the data by inverting with VELEST (Kissling *et al.* 1995) to obtain station corrections for the Jacó network. The earthquakes were relocated using the CM model and the station corrections with VELEST in single-event mode. The resulting hypocenter locations were kept fixed, while readings with only the lowest picking uncertainty category (±0.05 s, see chapter 3) from RSN stations were added for each event and the program run again to compute traveltime residuals. Examples of residuals from four RSN stations are shown in Figure 2.7. Again, a double-population distribution is observed.

Direct conversations with staff from RSN revealed that at the time there was actually a problem with the timing of their network. Since it did not happen all the time, it was difficult to detect during the merging with Jacó data. The causes of the flaw are not clear yet. Because all the stations share the same time signal, this does not represent a problem for the local usage of the signals. Nevertheless, readings for earthquakes with

magnitudes M_L 4 and higher are routinely merged with data from the other local networks in Central America. For this reason, a channel with the UTC signal from the atomic clocks of the United States' National Institute of Standards and Technology (NIST) located near Fort Collins (Colorado), is added regularly to the waveforms. The laboratory has a radio-controlled clock (RCC) which receives the signal broadcasted by Colorado. Comparisons between the GPS time and the atomic clock make the corrections possible. This is performed using the WAVFIX routine from the SEISAN package (Havskov & Otemoeller 2005), which shift the starting time of the waveforms.

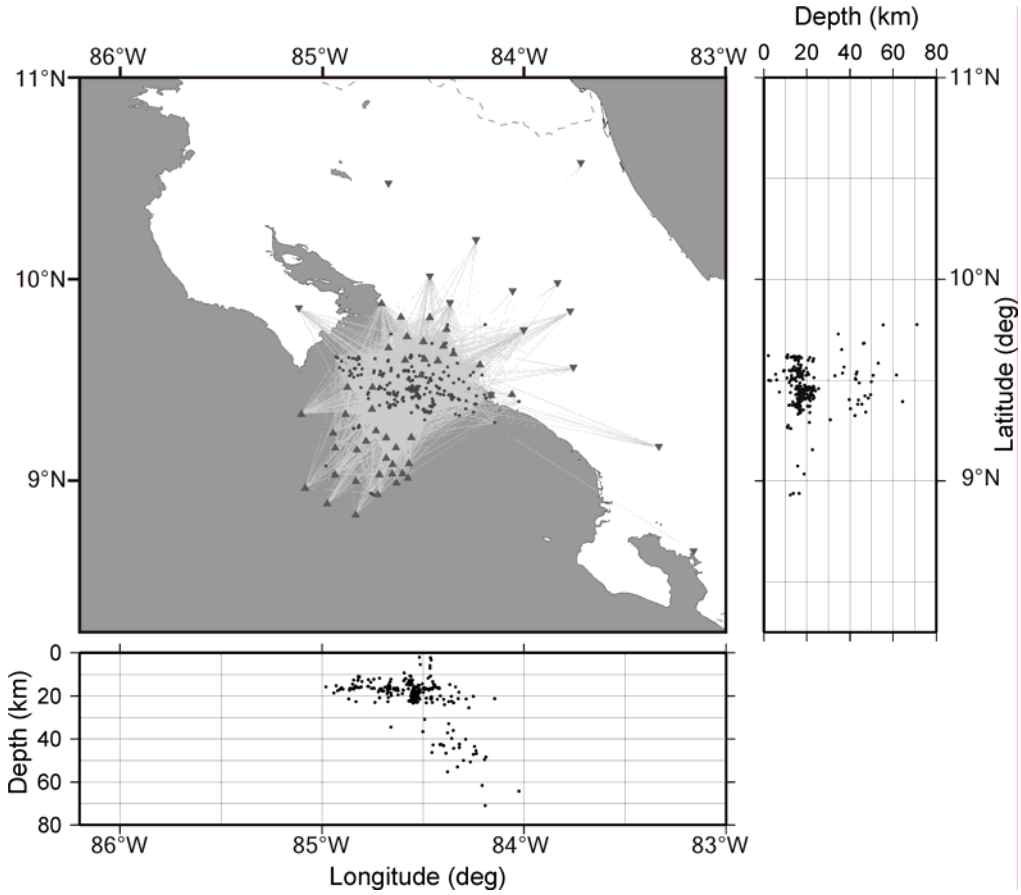

Figure 2.6. Earthquake dataset used to investigate the timing problem of RSN stations. Events included have a GAP ≤ 180° and at least 18 P-wave observations from Jacó network stations (triangles). RSN stations are represented by inverted triangles.

Consequently, all the readings from RSN network had to be checked over again. From a total of 500 events in the target area that included RSN readings, 324 showed the timing problem. The rest needed no correction since both timing agreed. Figure 2.8 presents the time corrections per hour per day. In the great majority of the cases the timing from RSN showed a positive delay when compared to the atomic clock, ranging from few tenths of a second up to two seconds. Note for example, the higher correction average starting on September 5 (Julian day 248). Besides, every single waveform from that date in ahead had to be shifted, which was not the case for the

previous months. In the following, the RSN data used for the tests have the lowest reading uncertainty (±0.05 s).

Once the corrections were made, the procedure of relocating the same dataset was repeated. Examples from new traveltime residuals from the RSN stations are shown in Figure 2.9a. Although the distribution approaches the expected Gaussian behaviour, two populations can still be recognised. As mentioned before, for September the corrections were in general much higher than for the rest of the months. Whatever the reason for this discrepancy, the effect of including readings from RSN stations from September was also tested. The relocation was made again including the readings from RSN stations but excluding September and October. Figure 2.9b displays distributions more in accordance to the expected results.

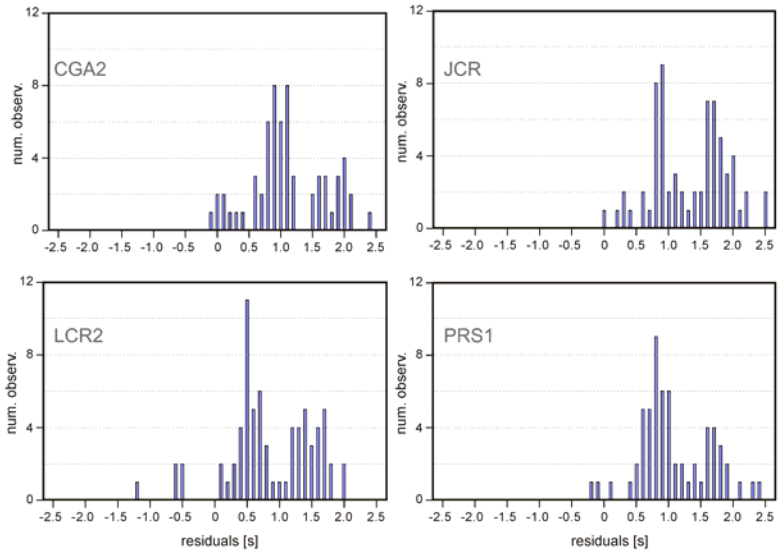

Figure 2.7. P-wave travel time residuals of original readings from four RSN stations, after single-mode relocation. The original hypocenter locations from the inversion of Jacó data were kept fixed (see text). Only arrivals with the lowest reading uncertainty level (±0.05 s) are used. The distribution suggests again two populations within the dataset.

To test if this last discrepancy on the data from September/October when compared to the other months was rather caused by the velocity model itself, the same dataset was again inverted but including the corrected readings from RSN this time, with and without September/October data. The dataset was then relocated in single-event mode using the same CM model and stations corrections for both networks. The results using September/October and excluding them are presented in Figure 2.10. In addition to the general decrease in the traveltime residuals, the distribution suggests that the readings from September might not be correct, even after the time shifting. The reason is in the moment unknown. Finally, the data from RSN from April to August was used for further modelling, excluding definitely those from September and October.

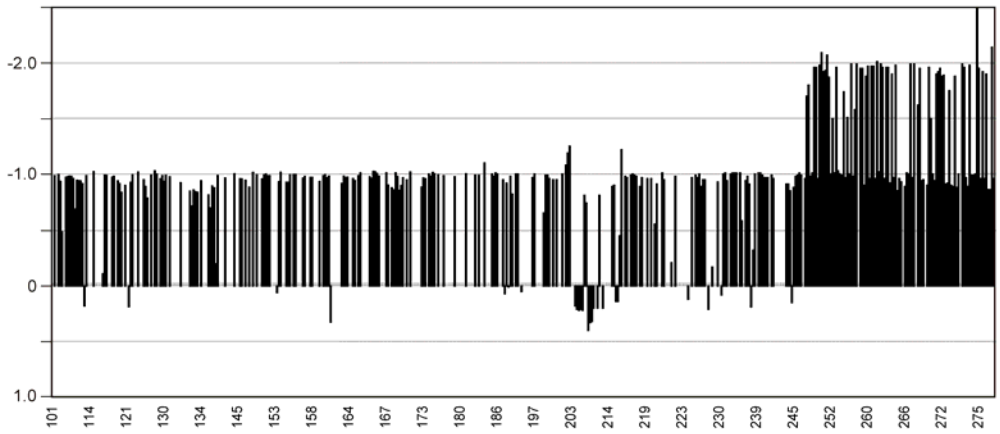

Figure 2.8. Time corrections per hour per (Julian) day for RSN readings, from April 11 to October 10, 2002. In the great majority of the cases the timing from RSN showed a positive delay when compared to the UTC time (hence the negative shifts). It is notorious the higher delay average starting on September 5 (Julian day 248).

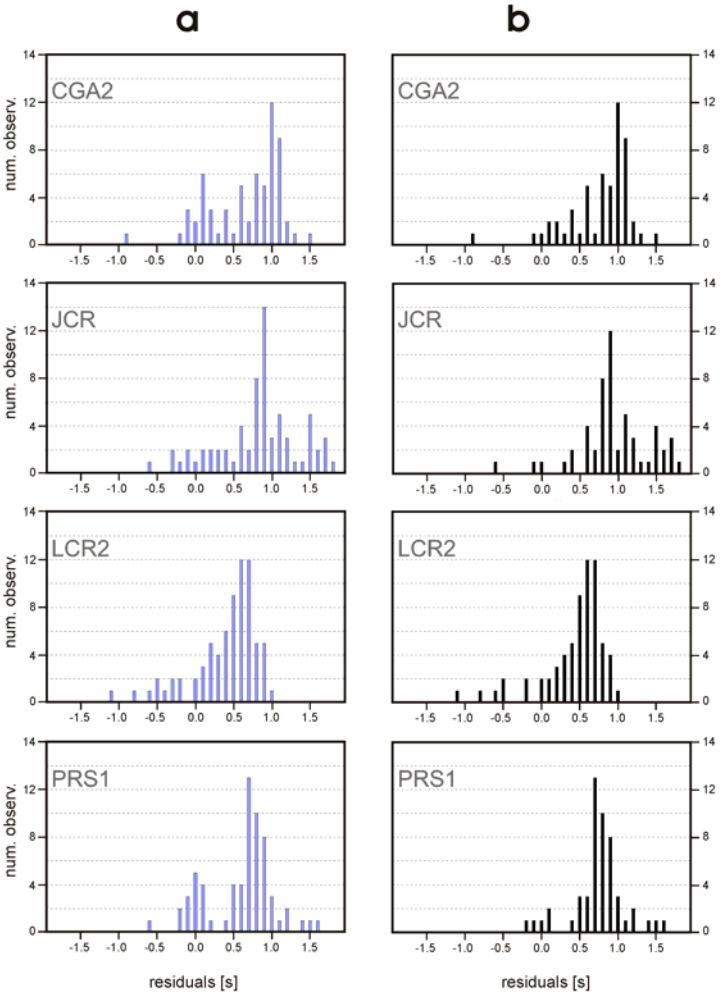

Figure 2.9. P-wave traveltime residuals of corrected readings from four RSN stations, after single-mode relocation. The original hypocenter locations from the inversion of Jacó data were kept fixed (see text). Only readings with the lowest uncertainty level (± 0.05 s) are used: a) including readings from September and October, and b) without those readings.

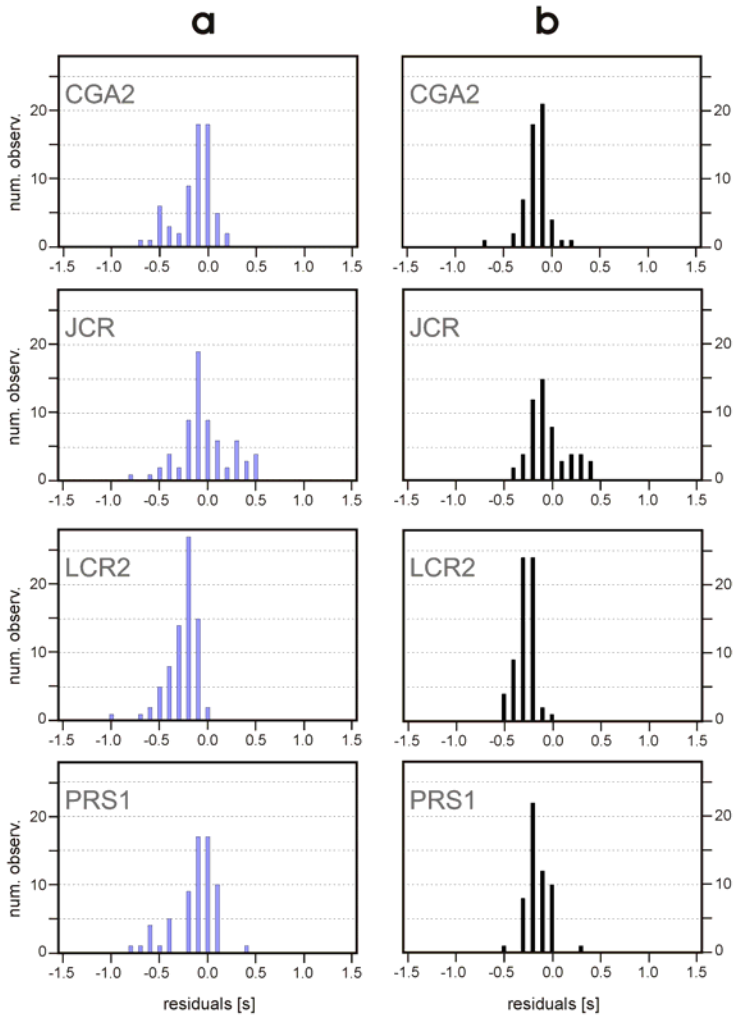

Figure 2.10. P-wave traveltime residuals of corrected readings from four RSN stations, after single-mode relocation. Only readings with the lowest uncertainty level (± 0.05 s) are used: a) including readings from September and October, and b) without those readings.

Chapter 3

Local earthquake dataset

In chapter 2, the layout of the Jacó experiment was sketched, and the estimation of the station parameters and the associated uncertainty discussed. In this chapter, the process of gathering and reading the data is detailed.

While data from the RSN were obtained as files containing all available waveforms per event already, a laborious, time-consuming process was required to extract the events detected by the Jacó subnetworks during six months of continuous recording. More than 6000 events were retrieved from the continuous data stream and readings from multiple stations for more than 3000 of them were collected. Figure 3.1 shows an example of an earthquake that occurred in the middle of the combined network and was acquired by the three arrays, from which selected records are displayed.

3.1 Pre-processing

Jacó – Ocean-bottom network

During the deployment on the seafloor, the continuous recordings of the OBH/S stations were stored onto 1-GB flashcards. After recovery, the contents of the flashcards were downloaded on SUN workstations on board. They were converted into RefTek files first and then into pseudo-PASSCAL SEGY format. Previously to conversion into pseudo-SEGY format and to simplify the handling of the large amount of data, the RefTek files were cut into records 30-days long for the OBH and 10 days for the OBS stations. The single pseudo-SEGY traces were cut into records of 25-hour length with one hour overlap between adjacent records. This splitting allowed time corrections to be applied on a daily basis. Two types of timing errors had to be taken into account:

a) Time slips (extra or missing samples) due to a mismatch of the desired and actual sample rates while using dataloggers of type MLS (Marine Longterm Seismocorder). This mismatch arises because the clock rate of the crystal oscillator in the MLS recorder is temperature dependent (Klaus Schleisiek, SEND GmbH, private communication). The dependence is known and corrected in the determination of the system time, but for performance reasons the sampling pulses are directly generated from the oscillator signal without any time correction. The time slips are detected by the routine send2pas and are reported when the accumulated sample-rate inaccuracies cause an effective timing error of one sample. On average, the resulting total timing error for wide-angle profiling of a few days is of 200 to 400 ms, and it could be of tens of seconds for a seismology deployment lasting several months. While this problem is currently corrected during conversion to pseudo-PASSCAL SEGY format, at the time of the Jacó experiment it had to be corrected manually. All time slips were read from the log files for each station. The time slips before the beginning of the records were added up and applied as static shift to the start time of the record. For time slips during the record, a sample is added (positive time slips) or removed (negative time slips) at the appropriate time. Although this procedure is only approximate (a correct treatment would require resampling of the whole record), in general the apparent time of a sample can be off by up to half a sample length.

b) The slow drift of the internal clock relative to GPS time. The timing is synchronized with GPS time at the beginning and at the end of the deployment, and a drift rate is inferred from the observed difference, known as “skew”. The skew is typically ~1-2 msec per day. The time of each 25-hour record was corrected by applying the shift appropriate for the time 12.5 hours after the beginning of the record. This is based on the assumption that the system clock drifts linearly, and that the drift over a 24-hour period is negligible, i.e. much less than one sample length, which was the case in this experiment.

A STA/LTA trigger algorithm was applied to the data to search for seismic events. Previously, a 5-20 Hz band-pass filter was temporally applied in order to suppress the typical marine long-period noise at ~0.2-0.5 Hz. The STA/LTA trigger parameters are the length of the short term (s) and long term (l) time windows, the mean removal window length (m), the trigger (t) and detrigger ratio (d), the minimum number of stations (S), and the network trigger time window length (M). The trigger parameters used on the offshore network are shown in Table 3.1. The selected trigger values yielded good results, since less than 5 % of the obtained triggers did not correspond to seismic activity. After detection of events, they were cut from the PASSCAL SEGY files and stored in individual subdirectories. The SEGY traces in the event directories were converted into SEISAN waveform format and registered into a SEISAN database (Havskov & Ottemöller 2005).

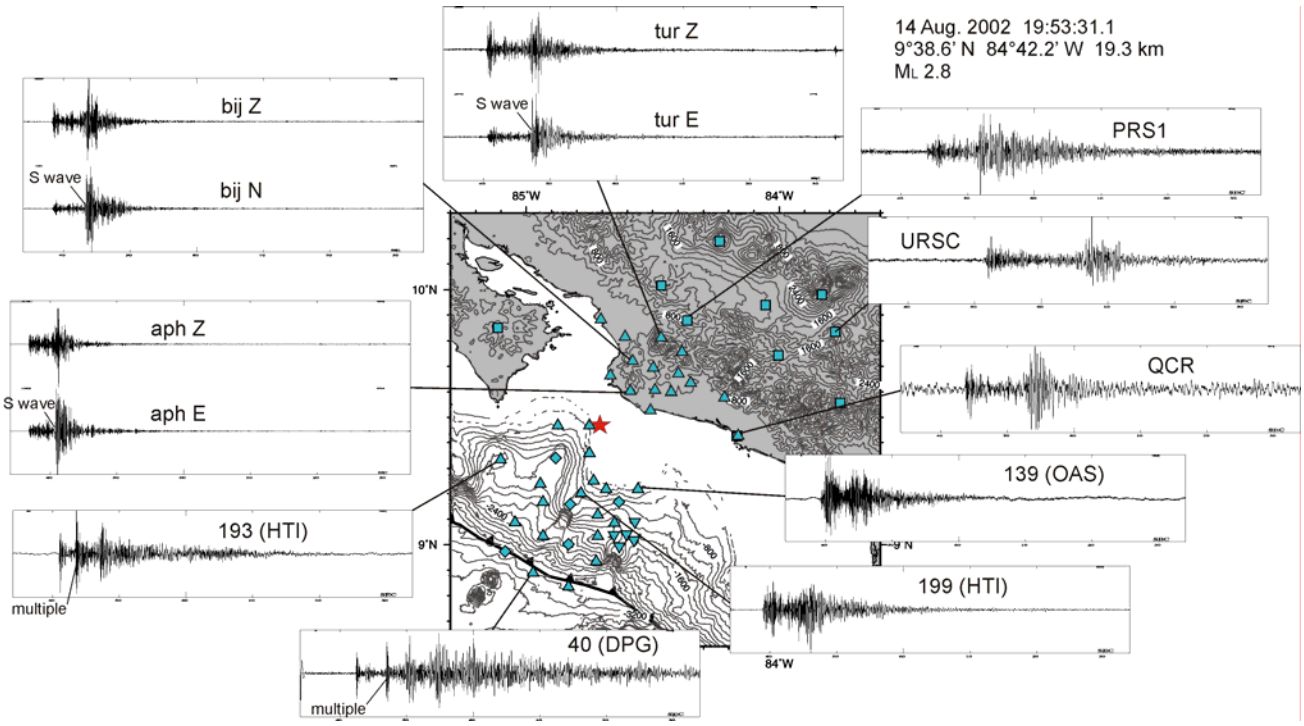

Figure 3.1. Examples of earthquake recordings from Jacó and RSN networks. The red star represents the event epicenter. Station legend as in Figure 2.1. Stations *aph*, *bij* and *tur* are RefTek recording at 100 Hz; *PRS1*, *QCR* and *URSC* are permanent stations equipped as indicated on Table 2.1 and recording at 50 Hz; the rest are OBHs equipped as indicated and recording at 100 Hz. For RefTek stations, one of the horizontal channels is also shown (lower trace). The traces are 60 s long. Only records from OBHs *40* and *199* have been band-pass filtered between 2 and 20 Hz to reduce marine long-period noise.

Table 3.1. STA/LTA trigger parameters (defined in the text) to scan the continuous offshore recordings for seismic events.

Parameter	s	l	m	t	d	S	M
Value	0.5 s	60 s	500 s	2.8	0.8	5	30 s

Jacó – Land network

The pre-processing procedure applied to the continuous records of the land stations is very similar to that described for the offshore network. The RefTek stations synchronize their GPS signal every hour, which in theory yields a more accurate timing; nevertheless, timing errors were checked and corrected carefully. Afterward, the data were stored on one-hour PASSCAL SEGY files.

Triggering was executed without using a prefilter since the seismometers are short period and the long-period oceanic noise is dramatically reduced on land sites. The

parameters (Table 3.2) applied to the land data differ from that used for the offshore data: the long term interval (l) is bigger in order to reduce the sensibility to single-impulse events caused frequently by cultural noise. Since the land data are not contaminated by high-amplitude, low-frequency noise, as the offshore data often are, the mean removal time length (m) was reduced.

Table 3.2: STA/LTA trigger parameters (defined in the text) to scan the continuous land recordings for seismic events.

Parameter	s	l	m	t	d	S	M
Value	0.5 s	200 s	100 s	3.0	0.5	5	30 s

For equipment safety reasons and power supply, most of the onshore stations were located within populated areas, close to or within villages. This led to an increased noise level, with characteristics similar to earthquakes, i.e. sharp onsets, high amplitudes. Triggering of the continuous data returned up to 60 % of false triggers.

3.2 Phase identification and picking

Phase picking and initial locations were accomplished using the SEISAN software package (Havskov & Otemoeller 2005), which includes the program HYPO71 (Lee & Lahr 1975), and HYP, a modified version of HYPOCENTER (Lienert & Havskov 1995). The software was chosen because it provides a complete set of programs and a simple database structure for analyzing earthquakes, allowing phase picking with a cursor, event location, determination of spectral parameters, seismic moment, focal mechanisms, etc. It also enables easy search and extraction of subsets from the database. The files with the readings are easily converted to CNV format, required later by the program VELEST (Kissling *et al.* 1995). Besides, the waveforms and reading files from RSN are stored in the formats used by SEISAN, simplifying its incorporation into the Jacó dataset.

As described above, earthquakes on the offshore and land data were triggered separately. Phase picking was then conducted in two databases as well. Pre-locations were performed with an initial 1-D P-wave velocity model based on the wide-angle model of Ye *et al.* (1996). The SEISAN routine ASSOCI was used to merge the readings from both subnetworks corresponding to the same event. The merged files were inspected manually one by one. All readings from RSN waveforms were examined and added to the merged Jacó database. Band-pass filtering to suppress marine noise was often required to read arrivals from OBHs (Figure 3.1).

Observation weights are used during hypocenter determination and traveltime inversion. They account for different quality on the determination of first arrivals, which depends on the signal-to-noise ratio. For Jacó experiment, a weighting scheme for quality of the P- and S-arrivals was applied. It is based on the picking uncertainty caused by noise, as exemplified in Figure 3.2 and summarized in Table 3.3. The weights were assigned following the HYPO71 definition.

Table 3.3. Observation weights and respective time uncertainties of wave first arrivals.

weight number	weight	P-wave uncertainty [s]	S-wave uncertainty [s]
0	1.0	< 0.10	< 0.1
1	0.75	0.10	0.1
2	0.50	0.15	0.2
3	0.25	0.20	0.3
4	0	> 0.30	> 0.35

The RSN stations used in this study are all equipped with seismometers of vertical component solely. As described before, unfortunately the seismometers deployed at the offshore network failed, and hydrophones record only converted S-waves, which are very difficult to identify. As a result, S-arrivals were picked only on the horizontal components of the Jacó land stations. Once a first location of the earthquakes was determined, a second check of the S-wave arrivals was carried out rotating the horizontal components for a better identification. Additionally, Wadati diagrams were plot for each event, to further constrain the S-wave picking.

Apart from P- and S-wave onset identification, the records from onshore stations were filtered to simulate a Wood-Anderson seismometer to obtain maximum peak-to-peak amplitudes for M_L determination. The amplitudes were read and M_L calculated from the horizontal components of the Reftek stations and the magnitude averaged from all available observations per event. Coda magnitudes (Mc) were calculated for offshore stations. Since a percentage of the events were recorded solely by the offshore network, in order to standardize the catalogue, a relationship between Mc and M_L was derived using measurements from 541 events for which both magnitudes could be calculated. Figure 3.3a displays the discrete and cumulative distribution of M_L for 1612 earthquakes recorded by the Jacó network in the whole Central Pacific region of Costa Rica. Magnitudes range from 0.8 to 5.6, with an average of 2.3. Since all the events with magnitudes greater than 4.5 took place to the SE, most of them associated to the Osa earthquake of June 16, 2002 (Figure 3.4), Figure 3.3b shows the distribution of M_L for 1184 earthquakes recorded only in the area covered by Jacó network. In this area, magnitudes vary from 0.8 to 4.3 and the average is 2.1; completeness of the catalogue is appraised at about 2.0. An estimation of the b-value for this second dataset using the magnitude distribution from 2.0 to 4.2 yields 0.98.

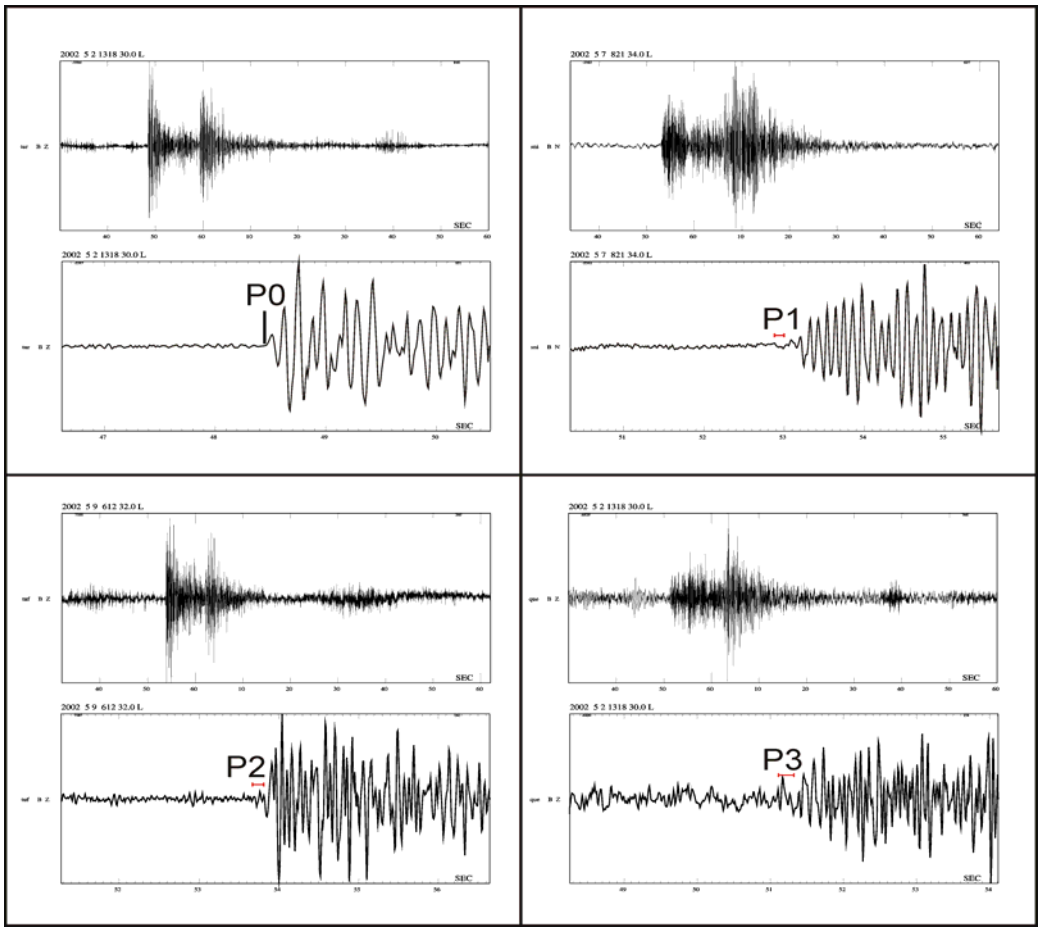

Figure 3.2. Examples of P-wave arrivals showing the weighting scheme used to asses the reading uncertainty (marked with horizontal bars). The weighting scheme is summarized in Table 3.3. Upper plots are 90-s long.

With the use of teleseismic arrivals, shooting records, and a land explosion planned and carried out by ICE in the surroundings of the village San Isidro, close to station *sni* (Figure 2.1 and, later, Figure 5.2), the polarities of the hydrophones and DPGs deployed with the offshore network were identified and controlled, for subsequent focal mechanisms determination (see chapter 5).

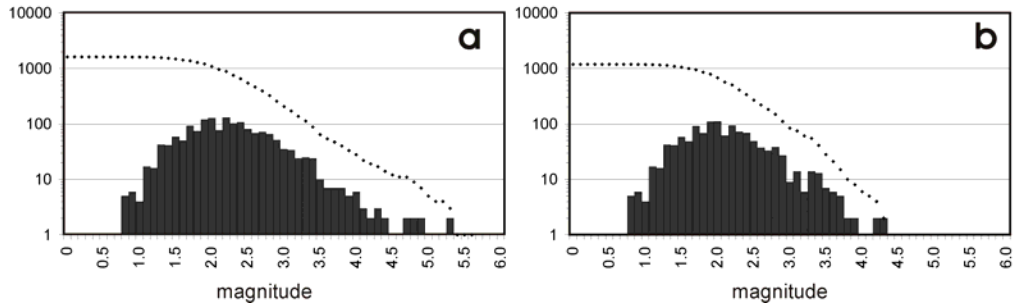

Figure 3.3. Discrete (bars) and cumulative (diamonds) frequency-magnitude distribution of: a) 1612 events recorded in the whole Central Pacific area, and b) 1184 events originated only in the area directly covered by Jacó network, excluding the southeast Pacific area and the activity associated to the Osa earthquake (June 16, 2002).

More than 3000 events were recorded by at least four stations of the Jacó array from April until the first days of October 2002. They originated all over the country, in the Pacific off Nicaragua and along the Panama Fracture Zone. Around 1900 events were recorded in the Central Pacific region from Costa Rica, between Nicoya and Osa peninsulas, which was the broad target area. The stations recorded the 6.4-Mw main shock from June 16 and its aftershocks in the Osa area, further to the southeast and outside the Jacó network. Figure 3.4 displays the hypocenter locations calculated with HYPO and at least six readings of the extended, Jacó-RSN array. These preliminary locations were obtained using the P-wave 1-D minimum velocity model for Costa Rica from Quintero & Kissling (2001) and a Vp/Vs ratio of 1.68, determined as the best value to fit the Wadati diagram for the dataset selected for tomography (see chapter 4). The trench-perpendicular depth section of the hypocenter locations yields a first impression of the downgoing plate and shows the highest seismicity rate associated to the interplate section, between 15 and 35 km depth (Figure 3.4).

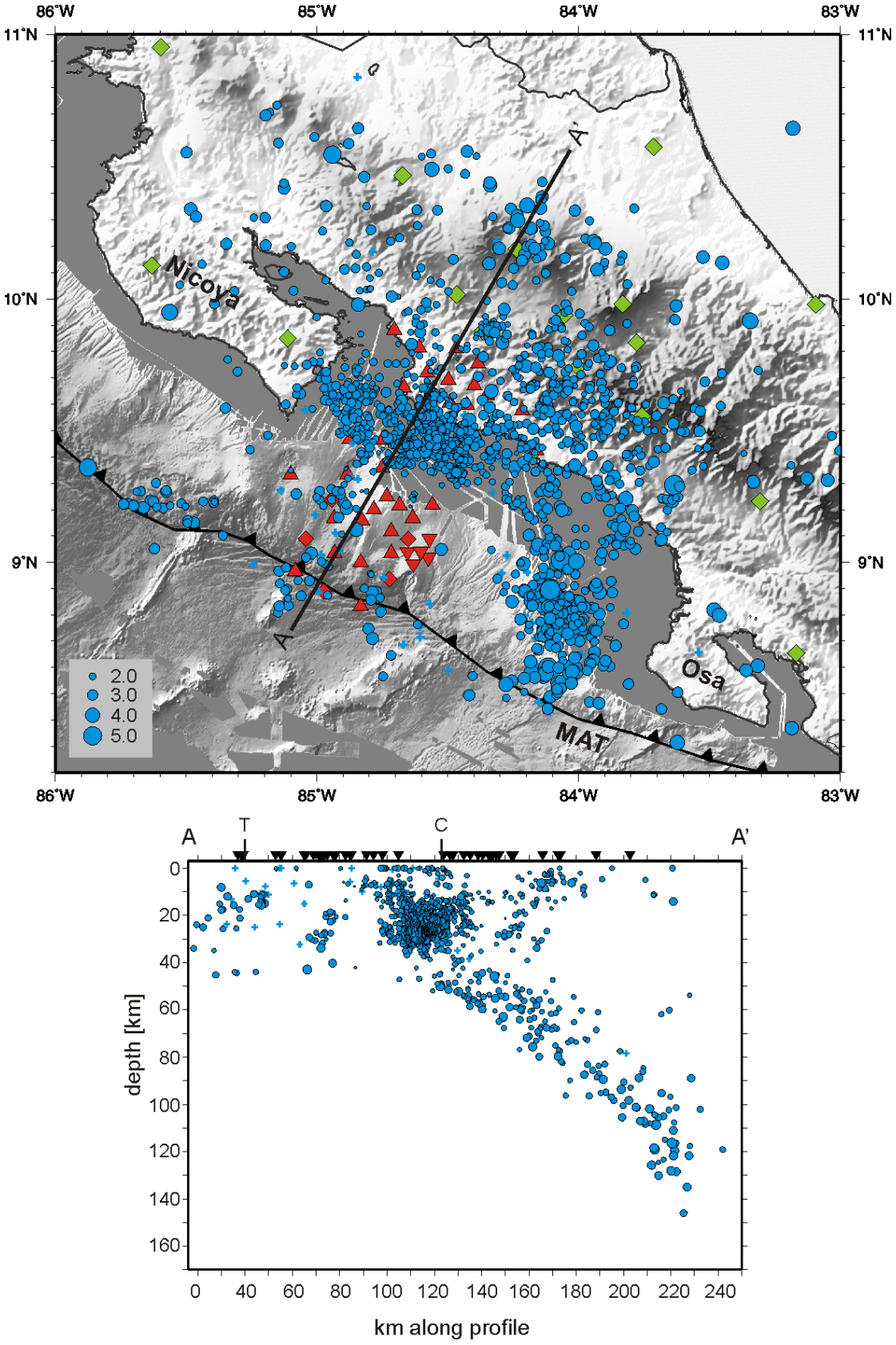

Figure 3.4. Preliminary hypocenter locations calculated with the program HYPO, using at least six arrivals from the Jacó-RSN network and the P-wave 1-D minimum velocity model from Quintero & Kissling (2001). Station legend as in Figure 2.1. ML scaled as shown in the insert. Seismicity projected from up to 50 km to both sides of the cross-section line. Inverted triangles on cross-section represent stations.

Chapter 4

Velocity structure

Tomographic inversion of traveltime data is a powerful technique to illuminate the velocity structure of a volume. For the derivation of a 3-D model, sufficient ray coverage is needed and an 1-D model acts as a reference. Traveltime residuals are computed for each datum by subtracting the predicted time from the observed time. The 3-D model is obtained by inverting the traveltime residuals for velocity perturbations relative to the reference model. If the perturbations are fairly small, the problem can be linearized. The main goal of the technique is to resolve the lateral velocity perturbations which are not accounted for in a 1-D model. In seismology, the problem is further complicated because ray paths are a function of the velocity model, the distribution of sources and receivers is nonuniform, the location of the sources is not well known and trade off with the velocity model, and picking and timing errors in the data could be present (Shearer, 1999).

The use of earthquake data for seismotectonic interpretation depends strongly on their location accuracy. Hypocentral location of earthquakes is an inverse problem where the unknown variables, i.e. model parameters, location and origin time of the earthquake, are estimated from a set of observed traveltimes.

In routine earthquake location, the velocity model is treated as known *a priori*, and the problem is simplified. But since measurement errors are intrinsic to the dataset and therefore prevent a model to match exactly the observed data, a meaningful estimate of the model parameters should be based on a larger number of observations. Furthermore, the traveltime is a non-linear function of the four hypocentral parameters (origin time, longitude, latitude and depth) and the seismic velocities found along the ray path. This dependency is known as “the coupled hypocenter-velocity problem”. Since direct solutions of the problem are generally not possible, it can be linearized and solved iteratively, provided that an initial guess of the model parameters close to the true solution is available.

The concept of "minimum 1-D model" was introduced by Kissling (1988) referring to the 1-D model with corresponding station corrections that lead to the smallest possible uniform location error for a large set of well-locatable events. The model results from the iterative simultaneous inversion of hypocentral parameters, station corrections and layer velocities, incorporating all possible *a priori* information into the definition of the layering and initial velocities. The resulting model is the optimum for location of earthquakes from the dataset used to derive it. The main purpose of a minimum 1-D model is to provide an adequate reference model for 3-D tomography, ensuring that the linearization represents a solution close to the true model (Kissling *et al*. 1994).

The tomographic method applied in this study, SIMULPS, is based on the code developed by Thurber (1983), who introduced an iterative simultaneous inversion for 3D velocity structure and hypocenter parameters using parameters separation and an approximate ray tracer. The code has been further developed through the years (Eberhart-Phillips 1990, Evans *et al*. 1994, Haslinger 1998) and is one of the most widely applied.

The inversion process is terminated when a number of specified iterations is reached, or when model perturbations become insignificant as determined by a F-test. The adjustments of the model are obtained by minimizing the traveltime residuals in a least-squares sense. For an array of earthquakes and receivers, the traveltime residuals equation can be written in matrix notation as:

$$\Delta d \cong G\, \Delta m$$

where the vector Δd contains the residuals for all observations, the matrix G the partial derivatives for hypocentral and velocity parameters, and the vector m the model adjustments in hypocenters and velocity. The equation is a linearized approximation of the original non-linear problem, which implies that no perfect solution could be achieved, even with perfect data, and that the final solution resides in the vicinity of the initial values of the model parameters. To solve the equation for Δm, the inverse of the matrix product G^TG is computed. As mentioned before, irregular distribution of source and receivers in seismology is common. This causes an irregular ray distribution, rendering overdetermined and underdetermined model parameters in the same problem. A damping parameter (λ) is then introduced to avoid very small or zero eigenvalues for the underdetermined parameters, which can destabilize the solution. The damped least-square solution is expressed:

$$\Delta m \cong (G^TG + \lambda^2 I)^{-1}\, G^T \Delta d$$

In order to facilitate computation of the inversion, $G\Delta m$ is split into a part containing only the velocity parameters and one containing only hypocentral parameters, but retaining the formal coupling between both (Pavlis & Booker 1980). After separation, the part of the equation containing the model parameters can be written as:

$$\Delta v = (V^TV + \lambda^2 I)^{-1}\, V^T \Delta d'$$

where Δd' contains the traveltime residuals after separation. Thus, using parameter separation, the earthquakes are relocated separately with the updated velocity model after the inversion for model parameters. The modelling is thus an iterative process due to the linearization and the damping.

SIMULPS is able to solve for Vp and Vp/Vs using P and S-P traveltimes, respectively. In most earthquake datasets the quantity and quality of S-wave arrival times are significantly decreased with respect to the P-wave data, this causes great variations in possible artefacts and modelling errors which are minimized by inverting for Vp/Vs instead of Vs (Evans *et al*. 1994).

The amplitude of the velocity heterogeneities and their spatial distribution resolvable with ray tomography depend on the accuracy of the forward calculations, i.e. the determination of the propagation path and traveltime through the velocity model (Haslinger & Kissling 2001). The version 14 of the code, used in this study, includes two ray tracing methods. The original, pseudo bending ray tracer (ART_PB, Um & Thurber 1987), in which the initial traveltimes are computed for a set of arcs with different radii and laying in different planes, connecting the source and the receiver; the arc that corresponds to the smallest traveltime is then chosen and perturbed by pseudo-bending, i.e. the segment endpoints are moved in the direction of the largest velocity gradient. The second ray tracer (RKP) is a full 3-D shooting and perturbation algorithm, in which they ray connecting station and source is determined by varying initial azimuth and take-off angles at the source; the variation of the initial angles is performed using first-order perturbation theory (Virieux & Farra 1991, Haslinger 1998). Initial shooting angles for the RKP ray tracing are obtained by ART_PB ray tracing on the first iteration; subsequent ray tracing iterations use the previously determined shooting angles as initial values (Haslinger & Kissling 2001). Usually, the endpoint of a ray calculated by shooting methods does not coincide with the station location; the accuracy to which the ray path coincides with the receiver is specified by the user, considering, for example, the station location uncertainty. Using synthetic model testing, Haslinger & Kissling (2001) determined that both ray tracing schemes are precise within ±10 ms in traveltime for ray lengths inferior to ~60 km, but for longer rays, the RKP technique yields significantly smaller errors.

The assessment of the solution quality is a very important step in tomographic modelling, and interpretation should be based on it. Different tools have been conceived to estimate solution quality *a posteriori*: while analysis of the resolution and covariance matrices provide mathematical resolution estimates, weighed ray lengths or ray density tensors examine the illumination properties by the dataset (Kissling *et al.* 2001). Nevertheless, those tools provide correct assessment assuming appropriate model parameterization, which they do not evaluate. The latter could be done by applying synthetic tests using synthetic 3-D velocity models that mimics expected or *a priori* known real structures (Kissling *et al.* 2001).

In this chapter, the quality of the Jacó dataset is revised, a minimum 1-D model for the experiment is derived and tested, and used to relocate all available earthquakes. From this relocated database, the earthquakes with the best quality, i.e. well constrained, are selected to perform a Local Earthquake Tomography. Information provided by controlled-source seismology profiles that have surveyed the area in the last years is taken into account during the modelling. The preferred solution is then examined through resolution assessment tools and synthetic tests. Furthermore, a detailed interpretation of the resolved velocity structure is discussed. Although the resolution capacity for Vp/Vs inversion of the Jacó experiment has been reduced by the failure of the seismometers installed offshore (chapter 2), the results of the model are included here. Most of the contents of this chapter have been submitted for publication, and the structure largely maintained.

Three-dimensional P-wave velocity structure on the shallow part of the Central Costa Rican Pacific margin from Local Earthquake Tomography using off- and onshore networks

I.G. Arroyo[1], S. Husen[2], E.R. Flueh[1], J. Gossler[1], E. Kissling[2], G.E. Alvarado[3]

[1]Leibniz-Institute for Marine Science (IFM-GEOMAR) and SFB574, Kiel, Germany.
[2]Swiss Federal Institute of Technology Zurich, ETH Hoenggerberg, Zurich, Switzerland.
[3]Instituto Costarricense de Electricidad (ICE) and Universidad de Costa Rica, San José, Costa Rica (Red Sismológica Nacional-RSN).

SUMMARY

The Central Costa Rican Pacific margin is characterized by a high seismicity rate, coincident with the subduction of rough-relief ocean floor, and has generated earthquakes with magnitude up to seven in the past. We invert selected P-wave traveltimes from earthquakes recorded by a combined on- and offshore seismological array deployed during six months in the area, simultaneously determining hypocenters and the 3-D tomographic velocity structure on the shallow part of the subduction zone (< 70 km). The results reflect the complexity associated to subduction of ocean-floor morphology and the transition from normal to thickened subducting oceanic crust. The subducting slab is imaged as a high-velocity perturbation with a band of low velocities (LVB) on top encompassing the intraslab seismicity deeper than ~30 km. The LVB is locally thickened by the presence of at least two subducted seamounts beneath the margin wedge. There is a general eastward widening of the LVB over a relatively short distance, closely coinciding with the onset of an inverted forearc basin onshore and the appearance of an aseismic low-velocity anomaly beneath the inner forearc. The latter coincides spatially with a sector of the subaerial forearc where differential uplift of blocks has been described, suggesting tectonic underplating of eroded material against the base of the upper plate crust. Alternatively, the low velocities could be induced by an accumulation of upward migrating fluids. Other observed velocity perturbations are attributed to several processes taking place at different depths, such as slab hydration through bend faulting at the trench and outer rise, tectonic erosion and slab dehydration.

4.1. Introduction

The convergent margin along the Middle America Trench (MAT) off Costa Rica and Nicaragua has been the focus during the first stage of the project SFB574 “Volatiles and Fluids in Subduction Zones”, which aims to better understand the processes involved in the exchange of fluids on erosional convergent margins. The diversity on structure and morphology of the incoming Cocos Plate and its associated effects on the structure of the margin, such as variations on the subduction angle, depth of the Wadati-Benioff seismicity, deformation style, plate coupling, and magmatic composition along the volcanic front, confer special interest to the area.

Being a direct response to the dynamics and structure of subduction zones, their seismicity and velocity structure provide valuable insights into the processes taking

place in these regions, where more than 80 per cent of the seismic energy of the Earth is released. Local earthquake tomography (LET) is one of the most powerful methods to obtain precise local earthquake locations and detailed knowledge of the three-dimensional velocity field, as proved in this (Protti *et al.* 1996, Husen *et al.* 2003, DeShon *et al.* 2006) and other subduction zones.

The Central Pacific region of Costa Rica displays a very high seismicity rate, coinciding with the subduction of rough-relief ocean floor, which includes seamounts and plateaus. The area has generated earthquakes with magnitude up to seven in the past, most recently a Mw-6.9 event in 1999 and a Mw-6.4 in 2002. As part of the SFB574, an "amphibious" network, consisting of land and ocean-bottom stations, was installed in the area for a period of six months. Since commonly the trench and forearc regions of subduction zones are located offshore, the availability of ocean-bottom hydrophones offers an excellent opportunity to study the shallower part of the margin. This makes the determination of high-quality hypocenter locations possible for the first time in this area, where the quality and completeness of the seismic catalogues from the two permanent country-wide networks is impaired by the lack of coverage offshore.

The main goals of the experiment include the characterization of the seismicity in this portion of the margin and its correlation with the tectonic and velocity structure, with emphasis on the seismogenic zone, i.e. the zone were the overriding and subducting plates are coupled. Foregoing studies lacked the coverage necessary to define the limits of the interplate seismicity, which are essential for the definition of the seismogenic zone and the process controlling its extent. The Costa Rican Central Pacific margin provides also the possibility of studying the effects on seismicity, velocity structure and the seismogenic zone of seamounts at different stages of subduction. Moreover, with most of the research on the seismogenic zone carried out to date on accretionary margins, the results of this and similar experiments in the area could augment our understanding of the processes taking place on tectonically erosive margins as well as the characteristics common to both types.

Furthermore, the Costa Rican margin has been the target of several controlled-source seismology (CSS) campaigns for more than 30 years. In addition to swath bathymetry, gravimetric and magnetic surveys, heat flow measurements and drilling projects, an extensive assemblage of modern near-vertical and wide-angle reflection lines has been collected in the area, largely offshore, specially since the 1990s. In this study, we collect information from CSS lines available on the area resolvable with LET and incorporate it indirectly into the inversion process, aiming to preserve the strength of each method. Instead of including shots into the inversion, we rather adjust the reference model with information from CSS, which also facilitates greatly the interpretation of observed tomographic anomalies.

We present here the results of the simultaneous inversion of Vp and hypocentral parameters, with focus on the 3-D velocity structure of the Central Pacific margin of Costa Rica. The LET images the subducting slab as a high-velocity feature topped by

a continuous band of low velocities from the trench down to ~70 km, where the resolution of our model ends. This low-velocity band broadens downdip and, more conspicuously, towards the east. We interpret these and other results as the outcome of slab dehydration, subduction erosion, tectonic underplating or fluid accumulation at the base of the overlying plate, and the subduction of thickened oceanic crust and accompanying bathymetric highs.

4.2. Tectonic framework

Costa Rica is located on the western margin of the Caribbean Plate, where subduction of the Cocos Plate takes place along the Middle America Trench (MAT) with a convergence direction of 32° and subduction rates varying from 8.3 cm yr^{-1} in northwestern Costa Rica to 9.0 cm yr^{-1} in the southeast (DeMets *et al*. 1994). The high seismic activity in the area is generated by the subduction process, crustal deformation and magmatic activity along the volcanic front.

The Cocos Plate lithosphere subducting at the MAT today has been created at the fast-spreading East Pacific Rise (EPR) and at the present slow-spreading Cocos-Nazca Spreading Center (CNS) and its precursors. The CNS segment has been partially modified by Galapagos hotspot magmatism. The boundary between the oceanic crusts formed at both centers is located offshore the Nicoya Peninsula (Figure 4.1). The crust formed at the EPR is 24 Myr old at the MAT, while the crust offshore central and southeastern Costa Rica has ages ranging from 19 to 15 Ma (Werner *et al*. 1999, Barckhausen *et al.* 2001), respectively. The thickness of the Cocos Plate crust varies from 5-7 km offshore Nicoya (Sallarès *et al.* 2001, Walther & Flueh 2002), to 6-8 km in the seamount domain (Ye *et al.* 1996, Walther 2003), and reaches up to 19-21 km beneath the Cocos Ridge (Walther 2003, Sallarès *et al.* 2003). Three domains have been identified by von Huene *et al*. (1995, 2000) on the highly variable morphotectonics displayed by the Cocos Plate offshore Costa Rica (Figure 4.1). Facing the Nicoya Peninsula, the subducting seafloor has a smooth relief, whereas to the southeast the Cocos Ridge stands 2 km high over the surrounding ocean floor. The segment in between, the area of this study, stretches from the Fisher Seamount and Ridge until the Quepos Plateau, and it is 40 per cent covered by seamounts. Substantial deformation of the continental slope in the form of deep furrows and domes indicates seamount subduction and there is evidence that they remain attached to the subducting plate to depths of ~25 km, eventually causing coastal uplift (Fisher *et al*. 1998; Gardner *et al.* 2001) and large earthquakes (Husen *et al.* 2002). The seamounts have a Galapagos geochemistry, being 13-14.5 Myr old adjacent to the margin (Werner *et al.* 1999).

High-quality seismic lines, high-resolution bathymetry and ocean drilling allow the conclusion that the Middle American convergent margin has been tectonically erosive since the Middle Miocene (Ranero & von Huene 2000, von Huene *et al.* 2000, Vannucchi *et al.* 2001). Basal tectonic erosion offshore Costa Rica causes mass removal, and subsequent crustal thinning and margin subsidence, at high non-steady

rates ranging from long-term ~45 km^3 Myr^{-1} km^{-1} to 107-123 km^3 Myr^{-1} km^{-1} during the last 6.5 Ma (Vannucchi *et al.* 2003). Ranero & von Huene (2000) identified two specific mechanisms of subduction erosion along the Middle America margin: erosion by seamount tunnelling and removal of large rock lenses of a distending upper plate.

The along-strike segmentation of the Cocos Plate appears to have a strong tectonic effect on the upper plate. Significant variations in the subduction angle, the nature of the incoming plate, and magmatic composition along the volcanic arc occur along this margin (Carr & Stoiber 1990, Protti *et al.* 1995a, von Huene *et al.* 2000, Husen *et al.* 2003). On southeastern Costa Rica, cessation of volcanic activity and accelerated uplift of the Talamanca Cordillera since 3.5 Ma have been attributed to the northwest-to-southeast shallowing of the slab as a response to the subduction of the Cocos Ridge solely or, more recently, first to the subduction of the Coiba Ridge and the passage of the Cocos-Nazca-Caribbean triple junction and subsequent subduction of Cocos Ridge (MacMillan *et al*. 2004). This slab shallowing, together with trench retreat by forearc erosion, have been invoked to explain the northeastward migration of the volcanic front in central Costa Rica from its position during the Miocene-Pliocene to its current location (Marshall *et al.* 2003) (Figure 1.3).

The basic structural configuration of the margin offshore Costa Rica and Nicaragua (Hinz *et al.* 1996, Kimura *et al.* 1997, Ranero *et al.* 2000) consists of a margin wedge composed of the same ocean igneous and associated sedimentary rocks that outcrops at several spots along the coast in Costa Rica, covered by slope sediments, underthrust by trench sediments and gouge made of upper-plate material, and faced by a small frontal prism. This basic structure is altered in places where seamounts are in the first stages of subduction, but it is a short-term damage: after ~0.5 Myr the morphology and structure of the margin become nearly undistinguishable from places were no seamount subducts (von Huene *et al.* 2000). The oceanic assemblages cropping out at the Pacific coastal areas (Figure 1.3) include a pre-Campanian oceanic plateau association in the Nicoya Peninsula and in the outer Herradura Promontory; an accreted oceanic island of Maastrichtian to lower Eocene age which forms the main edifice of the Herradura Promontory; and the Quepos Promontory, formed by the accretion of a Upper Cretaceous-Paleocene seamount (Hauff *et al*. 2000, Denyer *et al.* 2006).

Coinciding with the seamount segment, the Central Pacific region of Costa Rica shows the highest seismicity rate along the southern sector of the MAT. The absence of very large earthquakes (Mw > 7.5) and the high rate of small earthquakes define this part of the subduction zone as seismically decoupled (Protti *et al.* 1994), while coupling increases to the northwest and to the southeast. Several studies have found evidence of the relationship between the subduction of bathymetric highs and the generation of large subduction earthquakes, like the Mw-7.0 Cóbano earthquake in 1990 (Protti *et al.* 1995b, Husen *et al.* 2002) and the Mw-6.9 Quepos earthquake in 1999 (Bilek *et al.* 2003) (Figure 4.1).

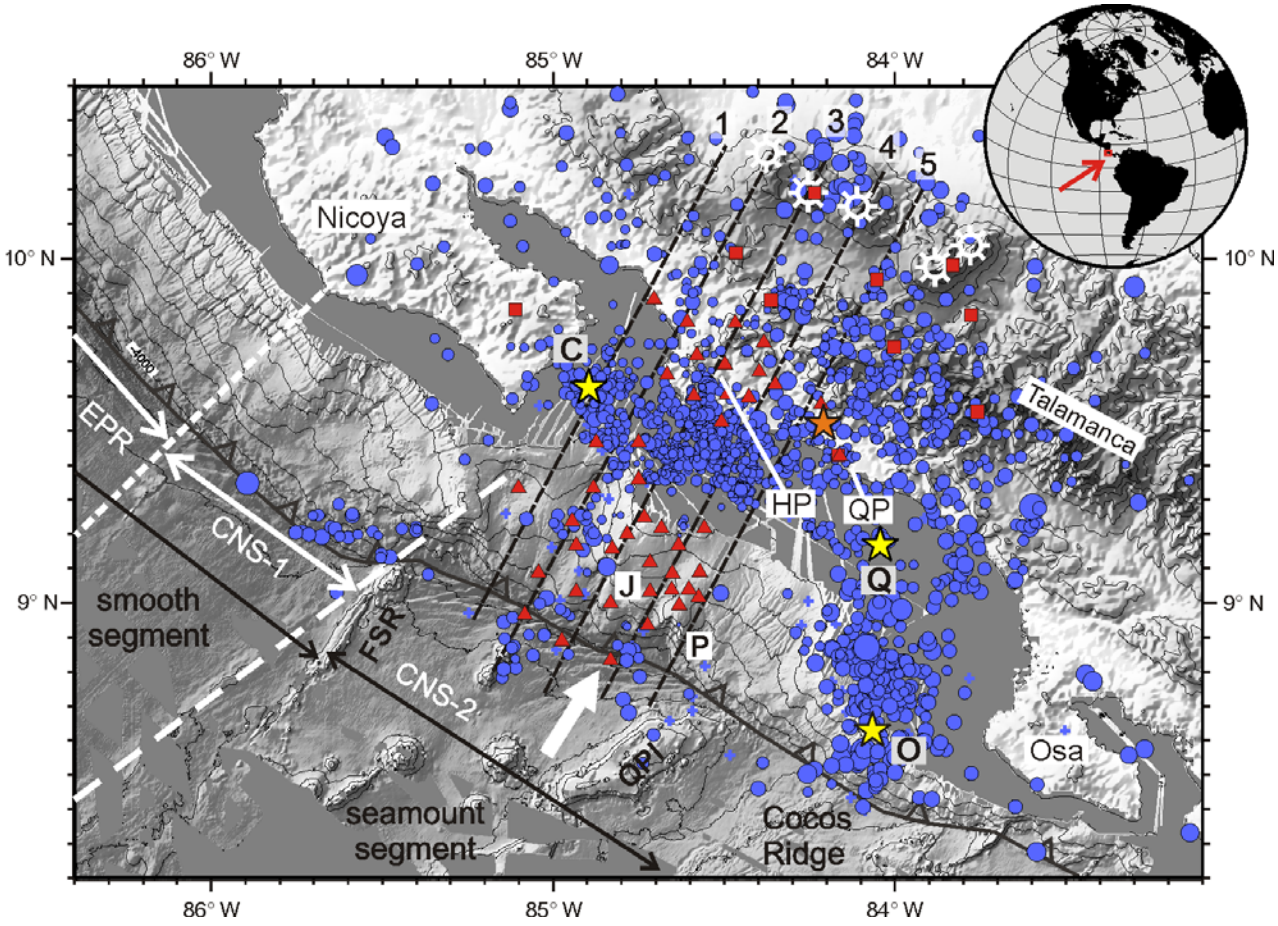

Figure 4.1. Setting of the Jacó seismological experiment in the Central Pacific margin of Costa Rica. The network (red triangles) consisted of land and ocean-bottom stations that operated from April to October 2002; additional readings from land stations of the permanent network RSN (red squares) improved the coverage. Total recorded seismicity during the experiment is shown (blue circles). Dashed lines denote the location of vertical cross-sections shown in Figure 4.17. Bathymetry (exaggerated), including contours every 500 m, and main tectonic segments after von Huene *et al*. (2000) and Barckhausen *et al*. (2001), respectively. Cocos Plate oceanic crust was formed at the East Pacific Rise (EPR) and at the Cocos-Nazca Spreading Center (CNS). Cocos Plate motion azimuth (thick white arrow) from DeMets *et al*. (1994). Radiating circles denote Holocene volcanoes in central Costa Rica. Yellow stars represent the epicenters of recent large earthquakes associated to subduction of bathymetric highs: C: 1990 Mw-7.0 Cóbano (Husen *et al*. 2002), Q: 1999 Mw-6.9 Quepos (location from Universidad Nacional de Costa Rica), and O: 2002 Mw-6.4 Osa (preliminary location from Jacó and RSN networks combined). Orange star: upper-plate, 2004 Mw-6.4 Damas earthquake (Pacheco *et al*. 2006). HP: Herradura Promontory, QP: Quepos Promontory, FSR: Fisher Seamount and Ridge, QPl: Quepos Plateau, J: Jacó Scar, P: Parrita Scar.

4.3. Data

4.3.1. The Jacó experiment and data quality

The Jacó network, named after the coastal town were the base of operations was located, recorded more than 3000 events from April until the first days of October

2002 (Figure 4.1). Around 2000 events were originated in the Central Pacific region from Costa Rica, the target area. The network recorded also the 6.4-Mw Osa earthquake from June 16 and its aftershocks, which occurred ~30 km eastward from the Osa Peninsula (Figure 4.1).

The network extended from the incoming Cocos Plate to the forearc, covering the Herradura Promontory and surroundings (Figure 4.1). It consisted of 15 short-period three-component stations, supplied by the German National Research Center for Geosciences, equipped with Mark L4-3D seismometers and Reftek data loggers, and 23 ocean-bottom stations (OBH), with hydrophones or broadband differential-pressure gauge sensors (Flueh & Bialas 1996, Bialas & Flueh 1999). The land stations were operated and maintained by the local Instituto Costarricense de Electricidad. Additional readings from 16 of the permanent short-period vertical-component stations of the Red Sismológica Nacional (RSN) were included in the database improving the coverage toward the volcanic front (Figure 4.1). An area of 19 500 km^2 was covered with the combined array. The average station spacing for the Jacó network was 13 km, except for the area of the marine shelf where depths shallower than 200 m prevented the deployment of OBH. The station spacing in the area covered only by RSN stations is 25 km on average.

The land stations and OBH from Jacó network recorded at a sample frequency of 100 Hz. Since all stations operated for six months in continuous mode, the pre-processing of the raw data was laborious. A short-term-average versus a long-term-average (STA/LTA) trigger algorithm was applied to search for seismic events, with the OBH data previously treated with a 5-20 Hz band-pass filter to suppress the typical marine long-period noise.

The accuracy of the observed traveltimes depends on the accuracy of the receiver position, the precision of the internal clock of the receiver, the sampling rate and the picking accuracy (Haslinger 1998, Husen *et al.* 2000). The Reftek instruments were equipped with GPS receivers, which provide clock synchronization and position determination every hour. By comparison between the position of one of the land stations determined by a geodetic survey and the positions reported by the GPS, the accuracy of the land stations locations is estimated to be ±50 m and ±20 m in the horizontal and vertical directions, respectively. The GPS time signal kept the clock drift below 8 ms. The accuracy of the OBH positions depends on the accuracy of the ship's position and on the drift during the descent of the station. By relocation of the OBH using the direct water wave from airgun shooting, their accuracy is estimated at ±250 m in the horizontal direction, while ±10 m in depth are appraised from the depth measurements conducted on board with the Simrad multibeam echosounder system and calibrated by conductivity-temperature-depth (CTD) profiling. The internal clock drift of the OBH, evaluated by its synchronization with a GPS time signal before and after recovering, is estimated to be less than 5 ms per day. Positions of most of the RSN stations have been determined by combined use of maps with scale 1:50,000 and single-point GPS measurements; comparison between available geodetic measurements for some RSN stations outside of the study area, the conservatively

estimated position accuracy is ±300 m in longitude and latitude, and ±50 m in elevation.

Analyst-reviewed P- and S-wave arrival readings and initial locations of the events were accomplished using the program HYP (Lienert & Havskov 1995) included in the software package SEISAN (Havskov & Otemoeller 2005). We applied a weighting scheme for phase reading, with quality factors ranging from 0 corresponding to the lowest reading uncertainty (±0.05 s), to factor 4 (>0.2 s) for uncertain readings which were not used for further modelling. Average P-wave reading uncertainty is estimated on ±0.07 s. The minimum 1-D model for Costa Rica, calculated by Quintero & Kissling (2001), was chosen for the initial locations since it represents an average model and deals with the fact that the data set includes earthquakes originated in different tectonic environments.

4.3.2 Controlled-source seismology profiles in the area

Of particular interest for the area surveyed by the Jacó experiment is the CSS profiling carried out by the PACOMAR project. During the cruises SO-76 and SO-81 of the German research vessel Sonne in 1991 and 1992, respectively, the PACOMAR working group collected six wide-angle profiles (Ye *et al.* 1996) and numerous multichannel reflection lines (Hinz *et al.* 1996) along ~250 km of the margin, among other geophysical measurements. The wide-angle lines included some explosions on land but mainly recorded marine airgun shooting. The aim of these studies was to explore the margin wedge and the oceanic plate structure. As part of TICOSECT, in 1995 a marine profile was acquired crossing the area of this study, starting at the trench and running along the Nicoya Gulf entrance. The profile included recording by several land stations located up to 40 km from the coast (Stavenhagen 1998, McIntosh *et al.* 2000).

We extracted information from four CSS profiles, whose location is shown in Figure 4.2, to combine it with the LET: depth-migrated reflection lines SO81-06 (Ranero & von Huene 2000) and 13 (Ranero, private communication), and wide-angle profiles SO81-200 and 100 (Ye *et al.* 1996). Profiles SO81-13 and SO81-200 are coincident. Profile SO81-100 runs parallel to the trench across the continental slope, and traverses line SO81-200. Unfortunately, the central profile from TICOSECT possesses low quality due to high-amplitude coherent noise which caused an apparent lack of reflections from the plate boundary zone (Stavenhagen 1998, McIntosh *et al.* 2000).

Profile SO81-200, with an average shot spacing of 150 m, presents relatively good coverage and reversed observations from six OBH and two land stations distributed along 125 km. It illuminated the margin structure down to 25 km depth and was analyzed by Ye *et al*. (1996) using two-dimensional forward modelling. For a starting model, they used the outline of the crustal and sedimentary structure provided by near-vertical reflection data. Wide-angle line SO81-100 was originally modelled by Stavenhagen (1994) and modified by Ye *et al*. (1996). Five OBH recorded the

shooting, but only the sedimentary layer and the top of the margin wedge were well resolved. Deeper velocities were constrained with those from line SO81-200. Prestack depth migration has been applied to the reflection lines. The iterative migration procedure uses velocities constrained with focusing analyses and common reflection point gathers, and wide-angle data guided velocity picking at depths greater than ~5 km. Resolution at ~10 km is ~0.5 km (Ranero & von Huene 2000).

Recently, Husen *et al*. (2003b) performed a LET for Switzerland using the 3-D Moho topography and associated P-wave crustal velocity structure modelled by Waldhauser *et al*. (1998) from CSS profiles from all over the country. Unfortunately, although several CSS lines traverse the area of the present study, they are not distributed in a network dense enough to allow for off-line migration using the interpolation scheme from Waldhauser *et al*. (1998). Nevertheless, a priori information, such as velocities and thickness of sedimentary basins, can be used to "tune" the reference model, in this case the minimum 1-D model for the data set, adjusting the modelling in zones that can not be resolved by LET. Moreover, the interpretation of observed tomographic anomalies is greatly facilitated by correlation with structures well resolved by near-vertical reflection techniques.

Before using the information from CSS models, the reliability of the structural information needs to be assessed in terms of its uncertainty. We inspected the available CSS profiles crossing the area of this study and extracted the reflectors, i.e. the continuously ray-covered parts of interfaces provided by 2-D seismic modelling or, for reflection profiles, the reflectivity patterns identified as interfaces (Waldhauser 1996). Reflectors belonging to the slope sediments basement, known as "rough surface" (Shipley *et al.* 1992) or "base of slope sediments" (BOSS, Kimura *et al.* 1997), and to the top and the Moho of the subducting plate were identified.

Quality factors were then assigned to the reflectors following the weighting scheme developed by Baumann (1994) and Waldhauser *et al*. (1998). The reflector elements from wide-angle models are weighted according to the data confidence (phase correlation, interpretation method), profile orientation in respect to the 3-D tectonic setting, and profile type (reversed, unreversed profiles). Reflector elements from near-vertical reflection profiles are ranked after the quality of their reflectivity signature, migration type (i.e. source of velocity used for migration) and projection distance (Waldhauser 1996). Total weighting factors (w_{tot}) are obtained by multiplying the individual factors.

Figure 4.2 shows the location of the wide-angle and reflection profiles in the studied area, with the identified 2-D migrated reflectors superimposed and colour-coded according to their quality. A reflector element from a wide-angle profile exhibits maximum quality (w_{tot} =1.0) when the phase picking is very confident, the line is oriented along strike, and the ray coverage is reversed. For example, the reflector element from the oceanic Moho of wide-angle line SO81-200 located under the trench axis and stretching ~10 km southwestward received a w_{tot} of 0.64 (Figure 4.2c). This value resulted from confident phase recognition (phase confidence: 0.8), the profile

orientation perpendicular to the strike (profile orientation: 0.8), and a good reversed ray coverage (profile type and ray coverage: 1.0).

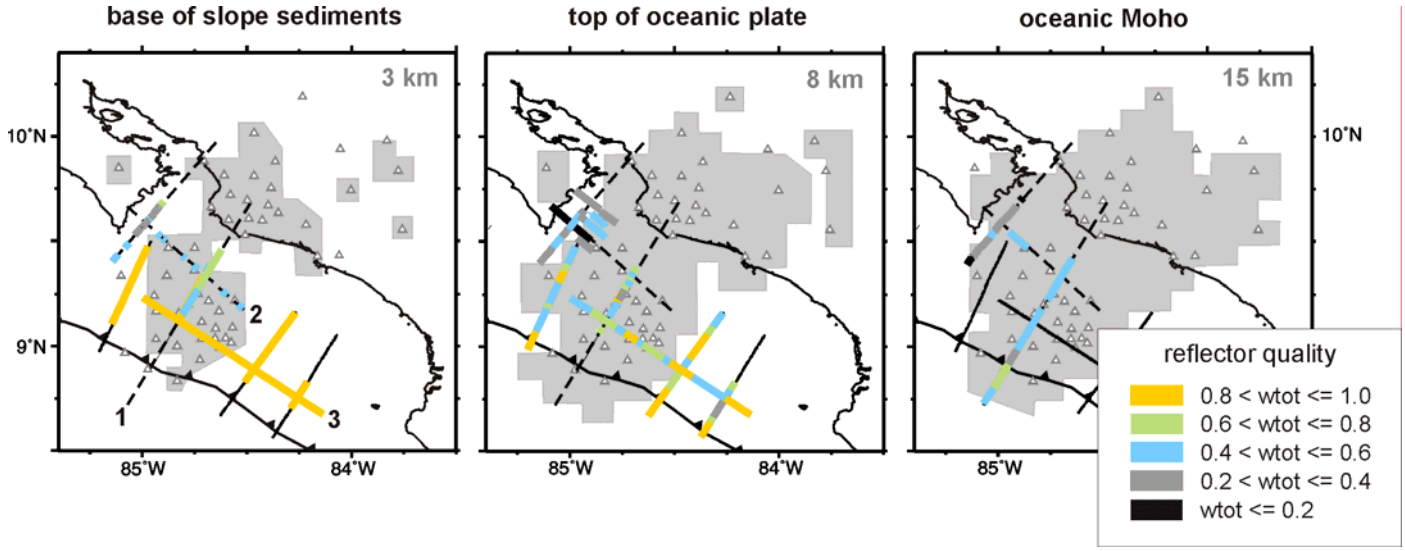

Figure 4.2. Controlled-source seismology profiles in the study area. Dashed lines represent wide-angle profiles; continuous lines, depth-migrated near-vertical reflection profiles. Superimposed are locations of 2-D migrated reflector elements from: a) "rough surface", b) top of the oceanic plate, and c) oceanic Moho. The inset shows the colour scale for total quality weighting factor. The grey shapes indicate areas of good resolution with local earthquake tomography at 3, 8 and 15 km depth from a) to c), respectively. White triangles denote seismic stations of Jacó experiment; the position of the Middle America Trench is indicated by a dented line. 1: profiles SO81-200 and SO81-13; 2: profile SO81-100; 3: profile SO81-06.

As displayed in Figure 4.2, the rough-surface reflectors from the reflection lines present high w_{tot} values, while those from wide-angle are middle to good. Most of the reflectors from the top of the subducting plate from wide-angle profiles have weighting factors from low to middle, the values being somewhat higher from reflection lines. The latter do not provide information from the Moho; middle w_{tot} values are associated to the available Moho reflectors from wide-angle lines. The grey shaded areas in Figure 4.2 mark the regions well resolved with LET, according to criteria discussed later, at 3, 8 and 15 km depth, approximately the depths at which the "rough surface" of the upper plate, and the top and Moho of the oceanic plate are expected, respectively. These are the areas were we can incorporate the CSS information into the LET, because they are resolved by both methods.

4.4. Method

4.4.1. Minimum 1-D velocity model

Linearization of the non-linear, coupled hypocenter-velocity problem demands initial velocities and hypocenter locations to be close to their true values. Moreover, results

of LET and their reliability estimates strongly depend on the initial reference model (Kissling *et al.* 1994). We used the VELEST software (Kissling *et al.* 1995) to determine hypocenters and the minimum 1-D P-velocity model (Kissling 1988, Kissling *et al.* 1994) for the data set, i.e. the velocity model and station corrections that most closely reflect the a priori information obtained by other studies, but at the same time lead to a minimum average of root mean square (rms) of traveltime residuals for all earthquakes. VELEST deals with the coupled hypocenter-velocity problem by performing several simultaneous inversions of hypocentral parameters, 1-D velocity models and station corrections.

A very high-quality subset of 261 earthquakes was selected for the derivation of the minimum 1-D P-velocity model. These events present a maximum azimuthal gap in station coverage (GAP) of 180° or less, show at least 12 P-wave arrival observations with the lowest reading uncertainty (±0.05 s, corresponding to weight 0) and at least one observation within a distance of 1.5 times their focal depth. Figure 4.3 shows the spatial arrangement of the subset, together with the ray coverage and the hypocenter distribution in depth. A total of 4986 P-wave observations from 57 stations integrate the subset. As a result of geometrical considerations and the limits of the target area for the LET we included readings from only 10 of the total RSN stations in the subset. The data set represents a fair sampling of the general distribution of the seismicity recorded over the period of the deployment (Figures 4.1 and 4.3): most of the events originated offshore, beneath the continental shelf, while fewer were generated within the subducting slab and the continental crust.

The ray tracer implemented in VELEST assumes that all the stations are located within the first layer of the velocity model. For the Jacó array, this implies a thickness of ~7 km for the first layer, because the highest land station and the deepest OBH were located at 3487 m and 3561 m over and below the sea level, respectively. Near-surface velocities usually exhibit a strong gradient, therefore such an unrealistic first layer with constant velocity introduces instabilities in the inversion procedure, preventing convergence. Station elevations were therefore neglected during the 1-D inversions. This exclusion however, implies that the resulting station corrections encompass not only the effect of the subsurface geology and large-scale velocity heterogeneities such a dipping slab, but also of the station elevations.

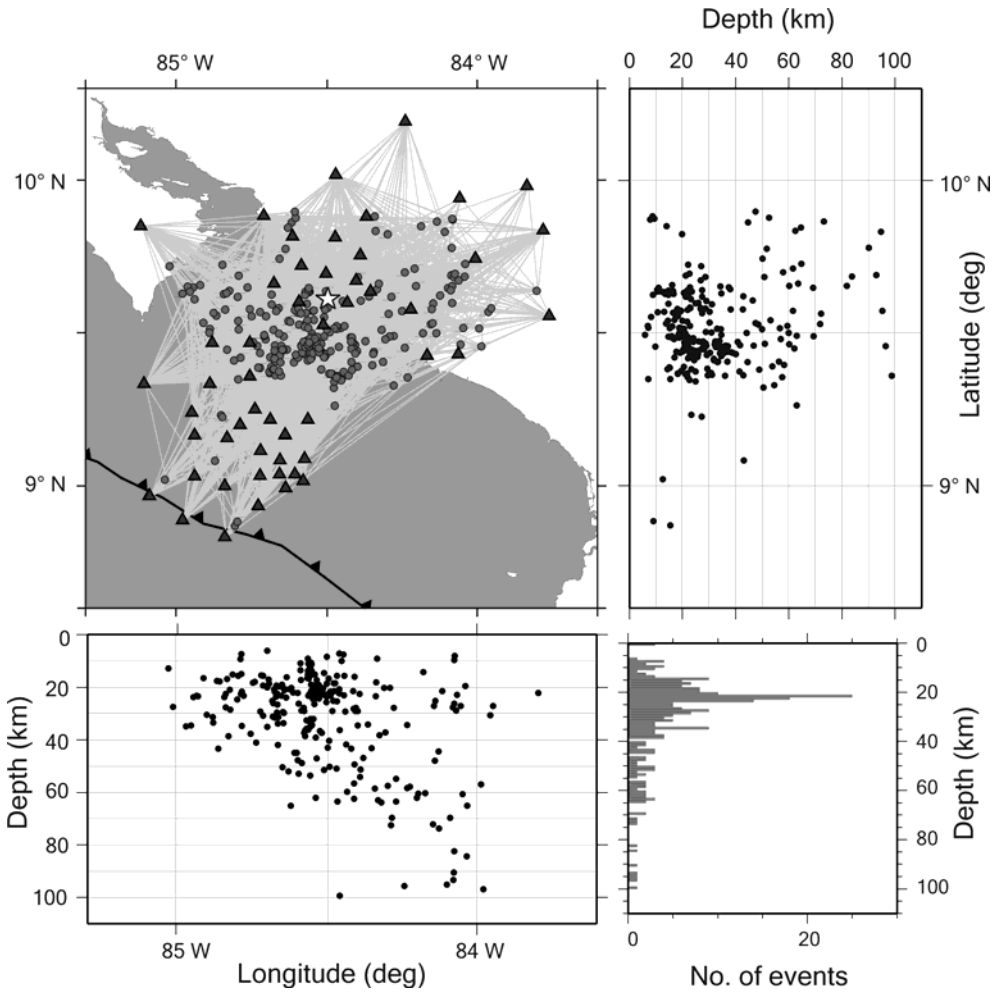

Figure 4.3. Distribution of 261 hypocenters selected for determination of the P-wave minimum 1-D model, in map view and vertical cross sections in E-W and N-S directions. Locations using the 1-D model for Costa Rica from Quintero & Kissling (2001). Only events with at least 12 P-wave observations and a GAP of 180° or less were used. At the lower right corner, a histogram of hypocenter-depth distribution is included. Black triangles represent stations. Gray lines show ray paths between epicenters and stations. Reference station is represented with a white star. The axis of the Middle America Trench is indicated by a dented line.

Determination of the minimum 1-D model is a trial-and-error process, in which a wide range of starting velocity models are tested in order to thoroughly explore the solution space. From initial inversions with several starting velocity models with different layering (e.g. Matumoto *et al.* 1977, Ye *et al.* 1996, Quintero & Kissling 2001) we observed low velocities (less than 3 km s^{-1}) in the first kilometers, strong variation at depths from 10-15 km and under 40 km. A relative good convergence was found between 15 and 40 km depth. After adjusting the layering to the depth distribution of the events in the selected subset, further trials of velocity models were conducted, including high- and low-velocity tests to investigate the dependence of the solution on the initial model. These tests confirmed that the number and distribution of hypocenters shallower than 15 km and deeper than 40 km was not favourable to resolve those layers. Since most of the events recorded by the Jacó network are located on the area where the wide-angle seismic lines SO81-100 and 200 were shot

(Figures 4.1 and 4.2), the velocities for the first 15 km from the model of Ye *et al*. (1996) were adapted into the initial models and were overdamped during the inversion process. Figure 4.4 shows the velocity space sampled and the final velocity model, given in Table 4.1.

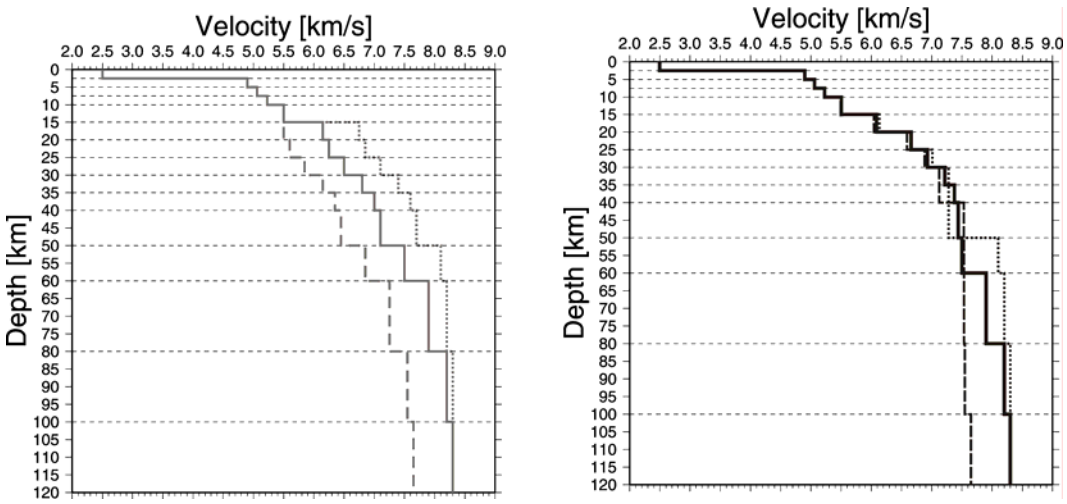

Figure 4.4. Initial (a) and final (b) 1-D velocity models for the last high- and low initial velocity test. Velocities for layers shallower than 15 km and deeper than 40 km have been overdamped (see text for discussion).

Table 4.1. Minimum 1-D P-wave velocity model Jacó experiment.

Depth (km)	Vp (km s^{-1})
0	2.50
2.5	4.90
5	5.06
7.5	5.23
10	5.50
15	6.05 ±0.05
20	6.63 ±0.03
25	6.95 ±0.06
30	7.23 ±0.08
35	7.35 ±0.11
40	7.35 ±0.12
50	7.50
60	7.90
80	8.20
100	8.30

The station corrections, shown in Figure 4.5a, display a meaningful pattern concerning the geometry of the network, distribution of earthquakes and geological setting, as well as the effect of the station elevations (Figure 4.5b). The reference station was located at 160 m.a.s.l. in the Herradura Promontory. The high negative delays for the OBH on the southwestern end of the network compensate for the depths close to the trench and the high velocities expected from the subducting oceanic crust. A consistent positive-correction behaviour is seen for most of the OBH located over the continental slope, where low velocities (2.1-2.9 km s^{-1}) from the 2-3 km-thick slope sediments were modelled by Ye *et al*. (1996). Two OBH placed inside of a broad embayment (Figure 4.5) display positive corrections lower than the rest of the stations on the continental slope. This could be attributed to the effect of their deeper locations (~2 km). No corrections or relatively low negative corrections (< -0.4 s) resulted for onshore stations from the Jacó

network, as expected from elevations and subsurface geology similar to those of the reference station. The positive delays for RSN stations located toward the volcanic front exhibit the influence of their altitude, if somewhat weaker than expected probably because of higher near-surface velocities.

The final average rms and variance for the data set are 0.129 s and 0.021 s^2 respectively, in contrast with the initial values of 0.325 s and 0.036 s^2 from the single-event mode location using the 1-D model from Quintero & Kissling (2001).

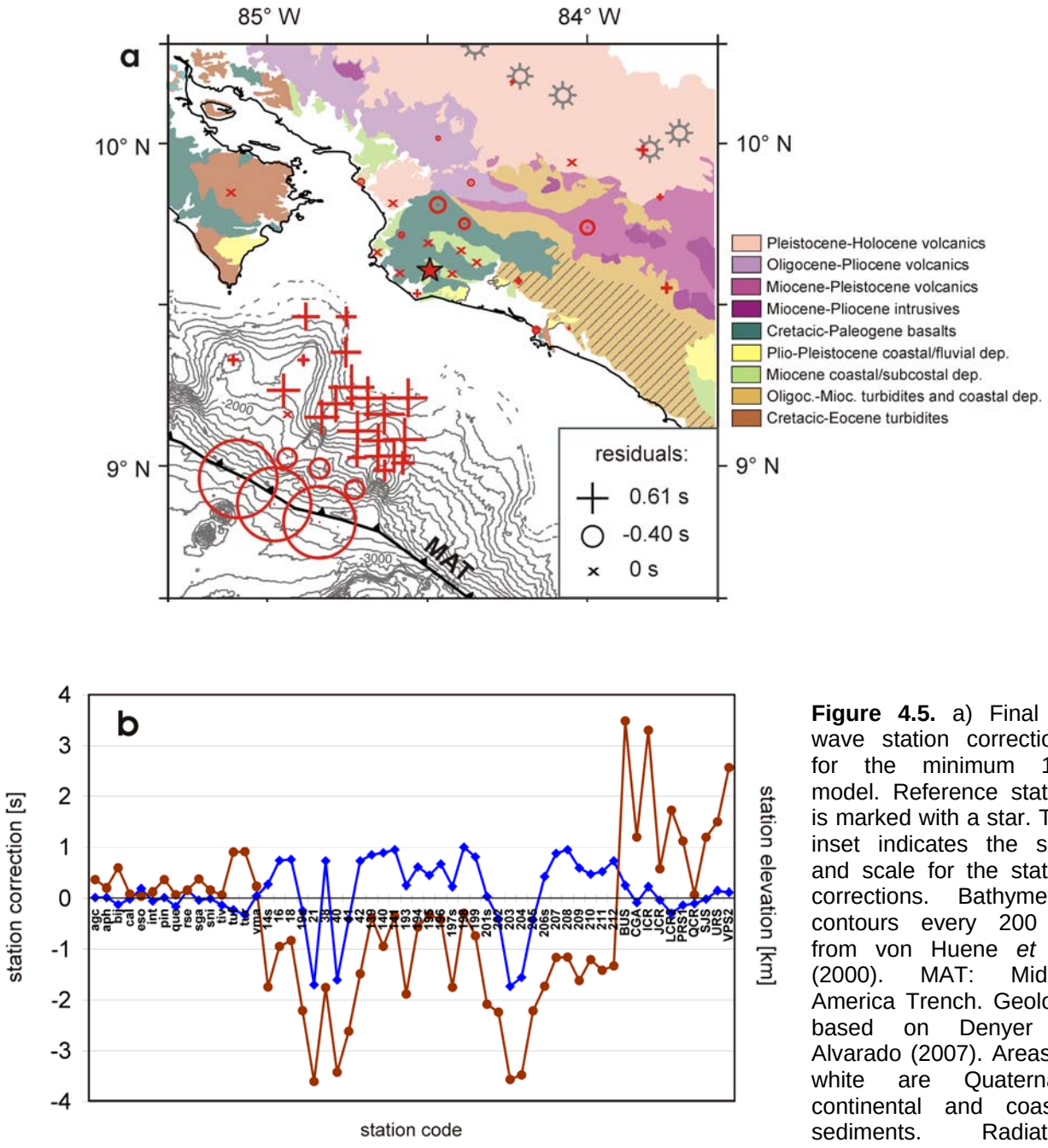

Figure 4.5. a) Final P-wave station corrections for the minimum 1-D model. Reference station is marked with a star. The inset indicates the sign and scale for the station corrections. Bathymetric contours every 200 m from von Huene *et al.* (2000). MAT: Middle America Trench. Geology based on Denyer & Alvarado (2007). Areas in white are Quaternary continental and coastal sediments. Radiating circles denote Holocene volcanoes in central Costa Rica. b) Station elevations (brown line) and delays (blue line): the corrections follow the topographic trend.

While stability tests are required for testing the robustness of the minimum 1-D model, they also yield insights into the coupled hypocenter-velocity problem for the specific data set, and allow the detection of eventual outliers. Following Haslinger *et al*. (1999) and Husen *et al*. (1999), we conducted several tests with randomly (Figure 4.6a) and systematically (Figure 4.6b) shifted hypocenter locations. For the first series of tests, hypocenters resulting from the inversion procedure were shifted randomly up to a maximum of 10 km in any direction, and the inversions were performed both, keeping the model fixed and with a floating model. Both cases show a very good retrieval of the original hypocenter locations, indicating that they are not systematically biased, and in the latter case, variations in velocities and station corrections are very close to the originals. The robustness of the minimum 1-D model was tested by systematically shifting all the hypocenters10 km deeper, and inverting again both, with fixed and floating model. While recovery of the original hypocenter locations in the first case is excellent, they remain close to their shifted positions in the second case. These results indicate a good degree of independence of the epicentres from the velocity structure, and a substantial coupling between the velocity and the depths/origin times.

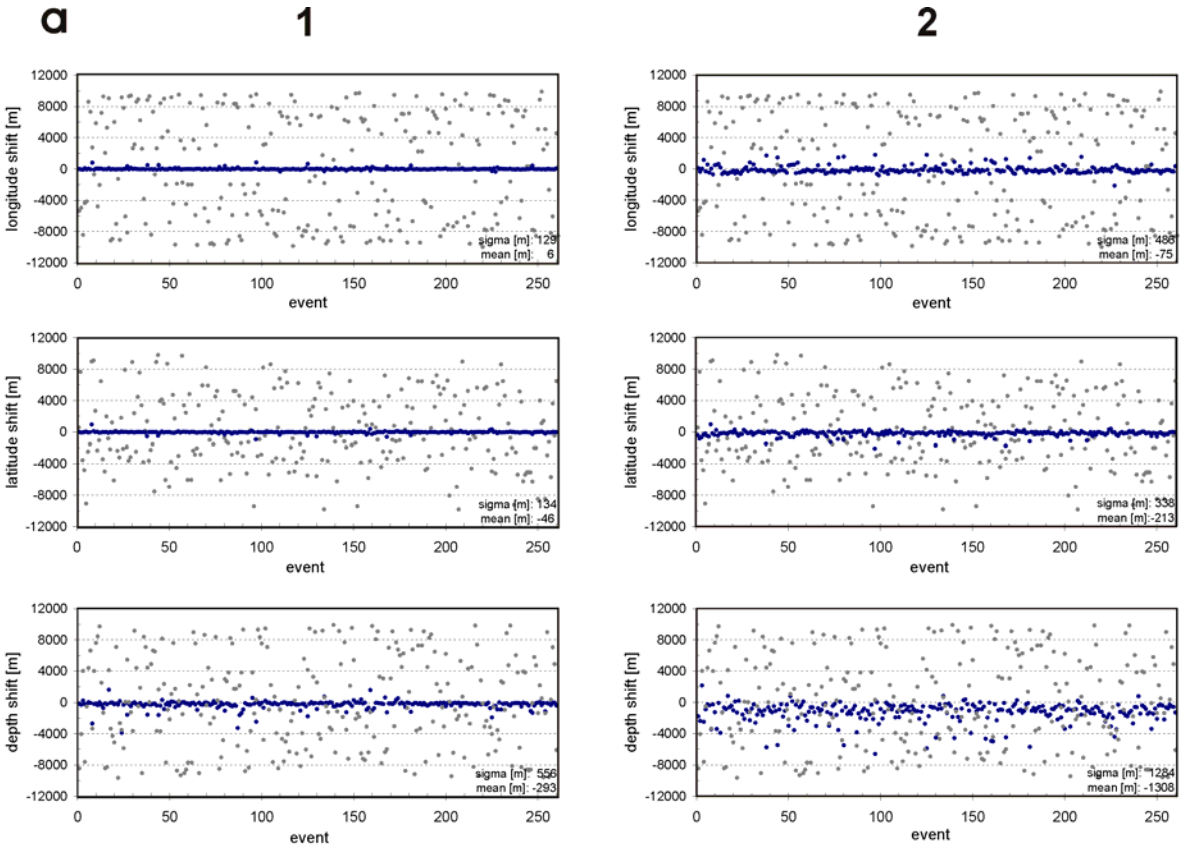

Figure 4.6. Stability tests for the minimum 1-D model. a) Hypocenters have been shifted randomly (grey circles) from their original positions and then used to repeat the inversion keeping the model fixed (column a) and letting the model float (column b); output hypocenters are shown in dark blue. b) Hypocenters shifted systematically 10 km deeper (grey circles) and

retrieved (dark circles) after repeating the inversion keeping the velocities fixed (column 1) and floating (column 2).

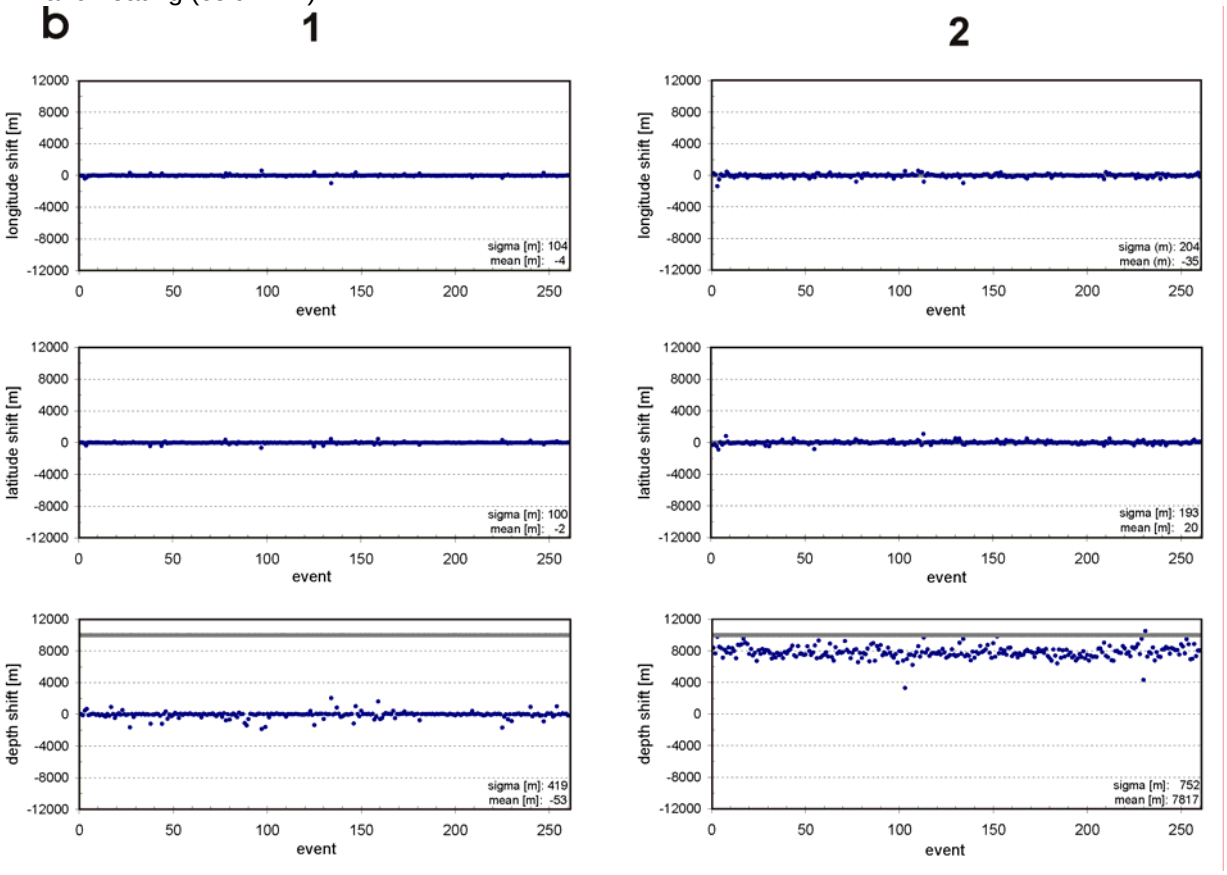

Figure 4.6 (continuation)

4.4.2 Local Earthquake Tomography

We used a damped, least-squared iterative solution, the computer code SIMULPS, to solve the non-linear tomography problem (Thurber 1983, Eberhart-Phillips 1990, Evans *at al*. 1994). Hypocenter locations are treated as unknowns in the inversion as a result of the coupling of hypocenter locations and velocities. Each iteration consists of an inversion for velocities and for hypocenter locations. After each iteration, new ray paths and traveltime residuals are computed using the updated velocity model.

We chose the special version SIMULPS14, which has been modified by Haslinger (1998) to include, besides the standard approximative pseudo-bending ray tracer (ART), the full 3-D shooting raytracer algorithm (RKP) from Virieux & Farra (1991) for the forward solution. It has been demonstrated that for ray paths longer than 60 km the RKP method yields significantly smaller errors than the ART (Haslinger & Kissling 2001).

Previous to 3-D modelling, the entire Jacó database was relocated using the minimum 1-D model with station corrections derived before. Since the coupling between

hypocenter locations and seismic velocities demands a careful choosing of events used in the 3-D inversion, we selected a high-quality data set, including only events with a GAP of 180° or less and at least 8 P-wave arrivals. This data set encompasses 595 earthquakes with 11 310 P-wave observations (Figure 4.7), with an average of 19 observations per event. Most of the events are located between 10 and 30 km depth, beneath the continental shelf, while the rest were generated at the Wadati-Benioff zone to depths of around 100 km, at the continental crust, and several at the oceanic crust close to the trench.

The first inversions revealed that neglecting station elevations during the calculation of the minimum 1-D model, as described before, caused strong coupling between hypocenters and the station corrections for the data set. For this reason, and since the locations resulting from the 1-D inversion are already close to their true values, the hypocenter parameters were kept fixed during the first iteration of the 3-D inversion, while adjustments were allowed only on the velocities. Subsequent iterations permitted updating of both, hypocenter locations and velocities.

The results and the resolution estimates, such as the diagonal element of the resolution matrix (RDE), are strongly affected by the damping parameter. The damping depends mainly on model parameterization and on the average observational error (Kissling *et al.* 2001). In this study we selected a value of 100, following the approach of Eberhart-Phillips (1986). We analyzed trade-off curves between model variance and data variance (Figure 4.8), constructed after two iterations applying damping parameters ranging from 1 to 10 000. The chosen damping value ensures the largest decrease in data variance without causing a strong increase in model variance, leading to the smoothest solution to fit the data. Figure 4.8 also displays the trade-off curve for converged solutions using the different damping values. Values lower than 100 result in a nearly constant data variance while model variance considerably increases, rendering rough models. The chosen damping value also produces the data variance value which more closely approaches the average weighed error of observed P-wave arrival picks and at the same time generates the minimum increase in model variance. It also indicates that noise is not being fit during modelling.

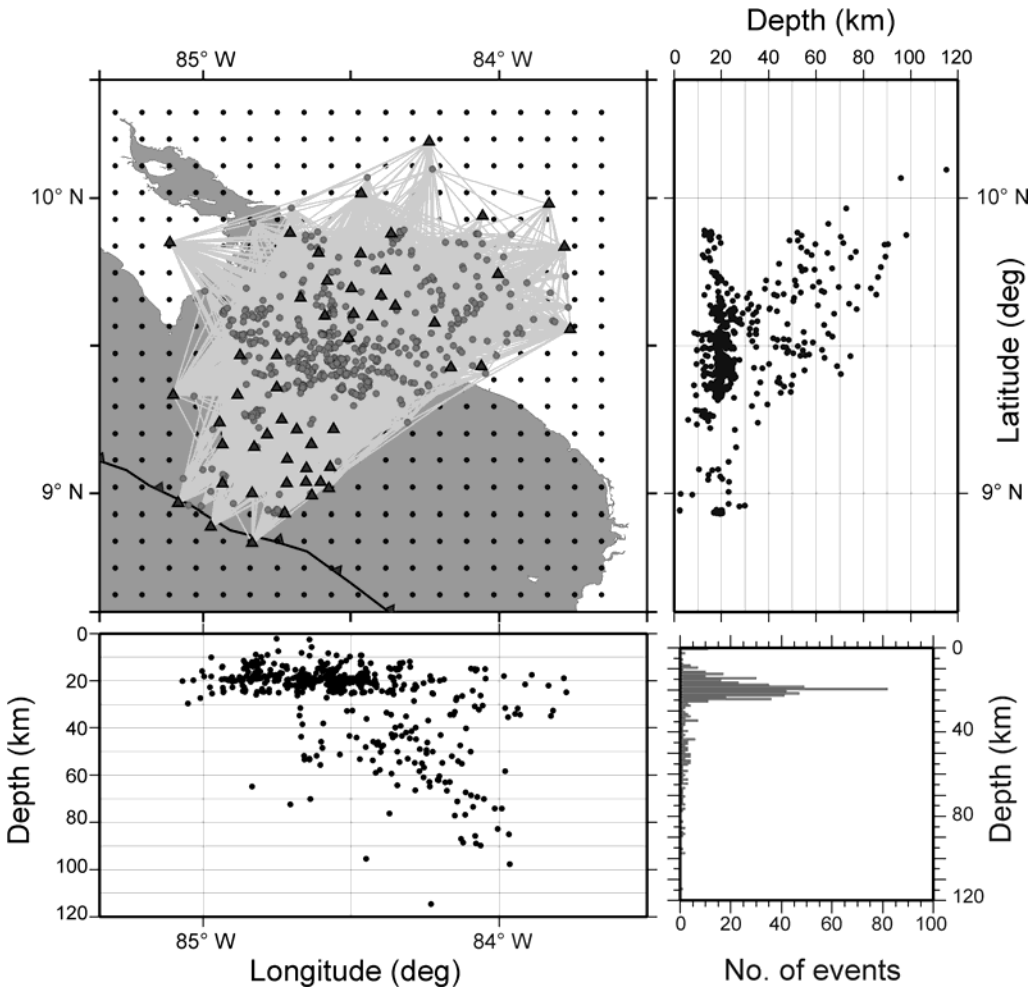

Figure 4.7. Hypocenter locations of 595 events selected for tomographic inversion, shown in map view and vertical cross sections in E-W and N-S directions. At the lower right corner, a histogram of hypocenter-depth distribution is included. Black triangles represent stations. Approximate ray coverage is shown by grey lines connecting epicenters and stations. Small circles denote final, 10 x 10 km^2 horizontal grid-node spacing. The axis of the Middle America Trench is indicated by a dented line.

In SIMULPS14, the velocity model is defined at grid nodes resulting from intersecting lines in x-, y- and z-directions. Velocities are linear-interpolated between the grid nodes. Initial velocities for the LET were taken from the minimum 1-D model and interpolated at depth to match the gradient required by SIMULPS14 (Figure 4.9). The grid spacing was selected to account for the distribution of stations and seismicity, aiming to obtain the highest possible uniformity in ray coverage and crossfiring without appealing to the use of uneven grid spacing, which complicates interpretation of results and resolution assessment (Kissling *et al.* 2001). Velocities were kept fixed at grid nodes that were not hit by any ray and, additionally, for those with a derivative weighted sum (DWS) value of less than 8.

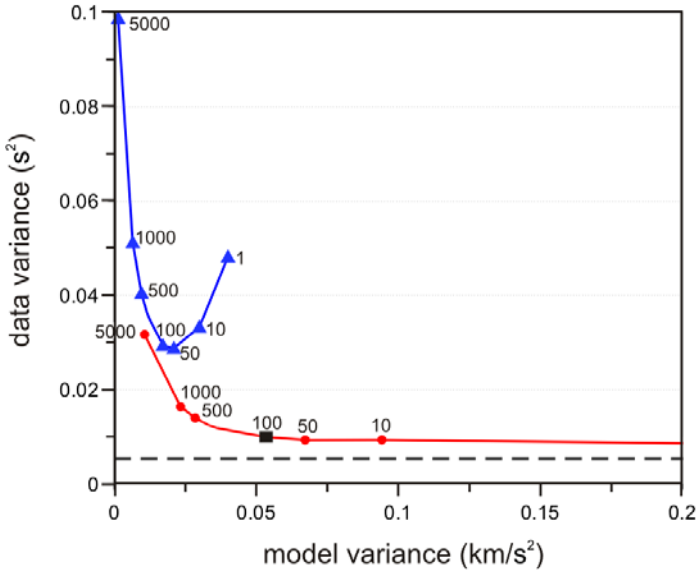

Figure 4.8. Trade-off curves of data versus model variance, constructed with results from single-iteration (triangles) and converged solution (circles) inversions. Damping parameter values as indicated. For reasons of space and clarity, extreme values of the test are omitted. The square marks the chosen damping parameter. The dashed line represents the average weighed error of observed P-wave arrival picks.

We inverted first for a conservative horizontal grid of 15 x 15 km^2 and a vertical node spacing of 7.5 to 10 km for shallow depth (<30 km) and 20 km at greater depth. Subsequent analysis of resolution and tests with synthetic data indicated that we could use a finer horizontal grid spacing of 10 x 10 km^2 without decreasing the resolution quality. The distribution of the DWS, a measure of the ray density, is as homogeneous for the 15 x 15 km^2 as for 10 x 10 km^2 grid spacing, although absolute values are decreased (Figure 4.10).

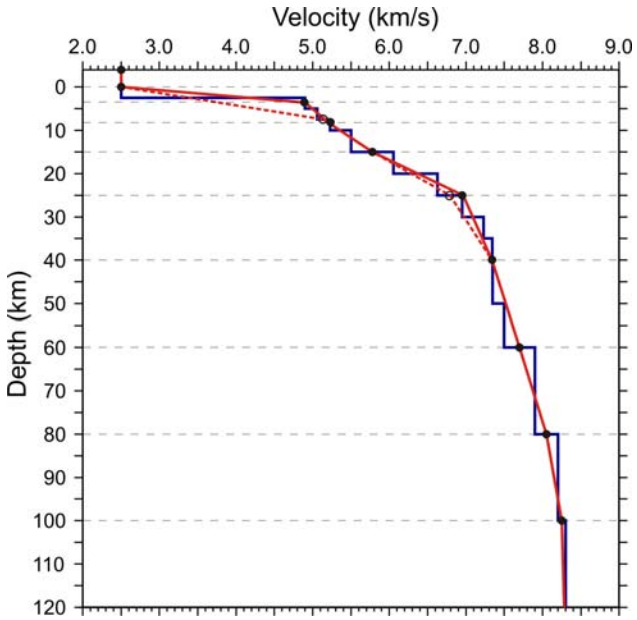

Figure 4.9. Velocity gradient and vertical grid nodes distribution for the 3-D inversion. The dashed line represents the original parameterization; the continuous line, the final starting model after "tuning" with information from controlled source seismology.

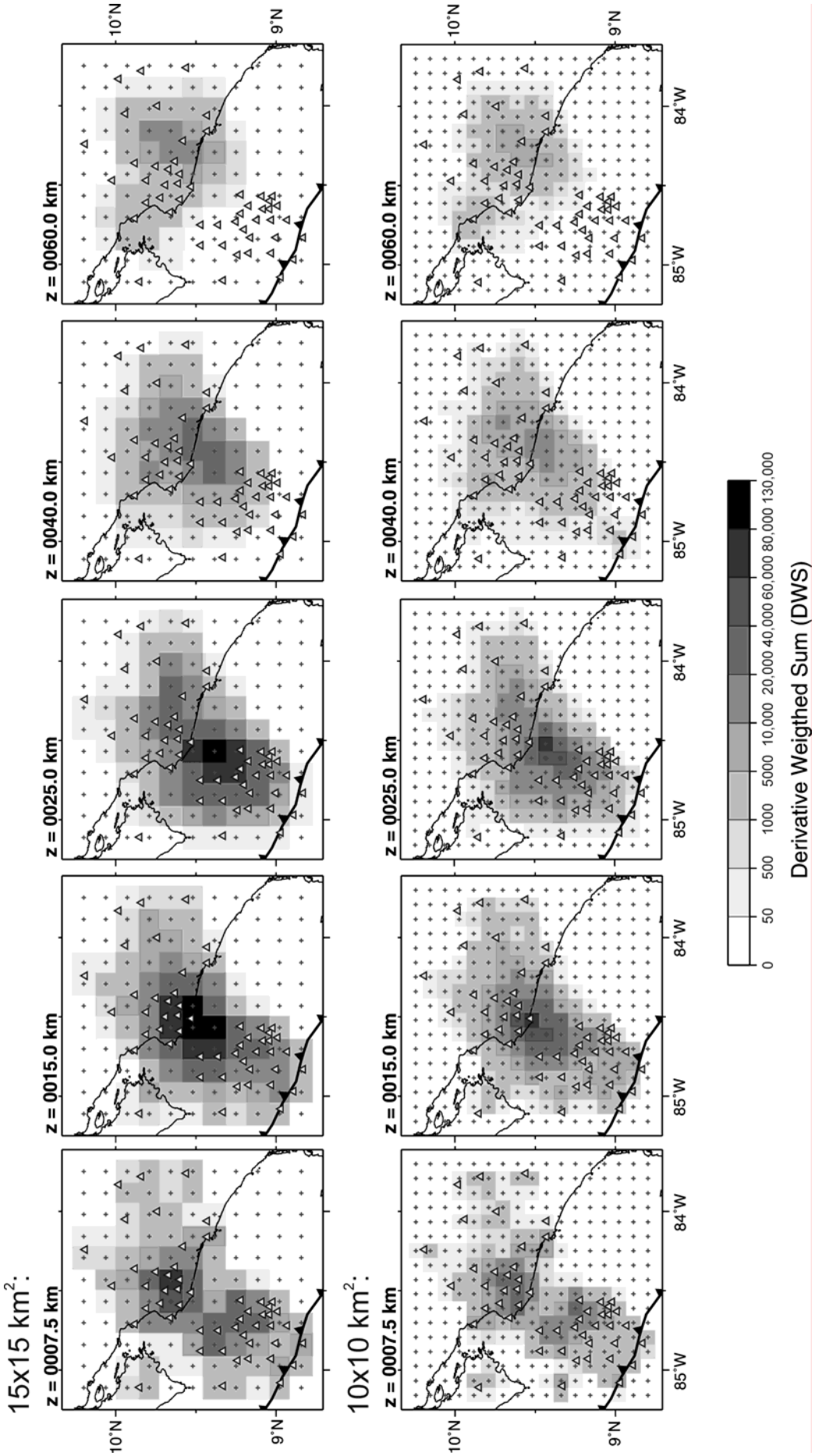

Figure 4.10. Derivative weighted sum (DWS) distribution in some horizontal depth sections for two different model parameterizations, as indicated. Triangles represent stations and small crosses denote grid nodes. The axis of the Middle America Trench is indicated by a dented line.

At this stage of the modelling we inspected the tomographic results in the light of the information provided by the CSS profiles. A first comparison of the absolute velocity distribution from the LET with profile SO81-200 (Figure 4.11a) in areas well resolved by both methods revealed a fairly good agreement (Figure 4.11b), considering the differences in type of data and techniques. Nevertheless, absolute velocities obtained with the LET are lower and the velocity contrasts are located deeper than in the CSS model.

Seeking to include as much information as available for the area in the 3-D inversion, and given that near-surface velocities are more reliably estimated by CSS data, we modified the original upper vertical grid spacing in order to mimic the ~3-km thick sedimentary coverage of the margin wedge with its corresponding velocity gradient, as shown in Figure 4.9. The 3-D inversion resulted in a better match between the tomographic image and the velocity gradient given by the CSS model (Figure 4.11c). Absolute velocities display a good concordance between both models in the upper oceanic crust, the continental crust, and specially in the margin wedge. Tomographic velocities on the lower oceanic crust and on the oceanic mantle, though, are very similar on both coarse and finer, "tuned" tomographic images, and remain lower than the ones from wide-angle modelling at the same depths. The latter, however, are determined from unreversed observations and are thus coupled to the Moho depth uncertainty.

The subducted seamount associated with the Jacó Scar, located ~20 km inward from the trench axis (Figure 4.1), is another feature which provides linking between the tomographic results and the CSS models. The seamount was clearly depicted as a low-velocity anomaly on the tomogram of the inversion using the coarse horizontal grid (Figure 4.12a). This seamount has been displayed by reflection lines SO81-06 and 13 (von Huene *et al.* 2000), which cross each other, and by gravimetric modelling (Barckhausen *et al.* 1998), on an area were its presence was previously suspected from images of high-resolution bathymetry: a portion of the margin slope is disrupted, showing a doming in the middle continental slope and a scar left by failure of the slope sediments (von Huene *et al.* 1995, 2000). Nevertheless, reducing the horizontal grid spacing to 10 x 10 km and introducing a closer vertical spacing in the upper 10 km had a negative effect on the definition of the seamount image, as shown in Figure 4.12b. This loss indicates a decrease on the resolution capability in this area due to limited ray coverage. Moreover, introducing grid nodes at 3 km depth with higher velocities than in the original inversion modifies ray paths and reduces the velocity gradient between 5 and 10 km depth, resulting in a weaker contrast of the low-velocity anomaly at those depths. In a good example of the significance of parameterization in tomography, particularly when studying velocity structure details, we were able to improve the seamount image in the finer grid by slightly shifting (~6 km to the southwest) the location of the fine grid nodes so that a grid node coincides with the seamount position as estimated by CSS lines and the coarse LET (Figure 4.12c).

The final tomographic model achieved a data variance reduction of 66 per cent compared to the 1-D reference model. The final weighted rms over all traveltime residuals is 0.083 s. This value is close to the a priori observational error, indicating convergence of the inversion.

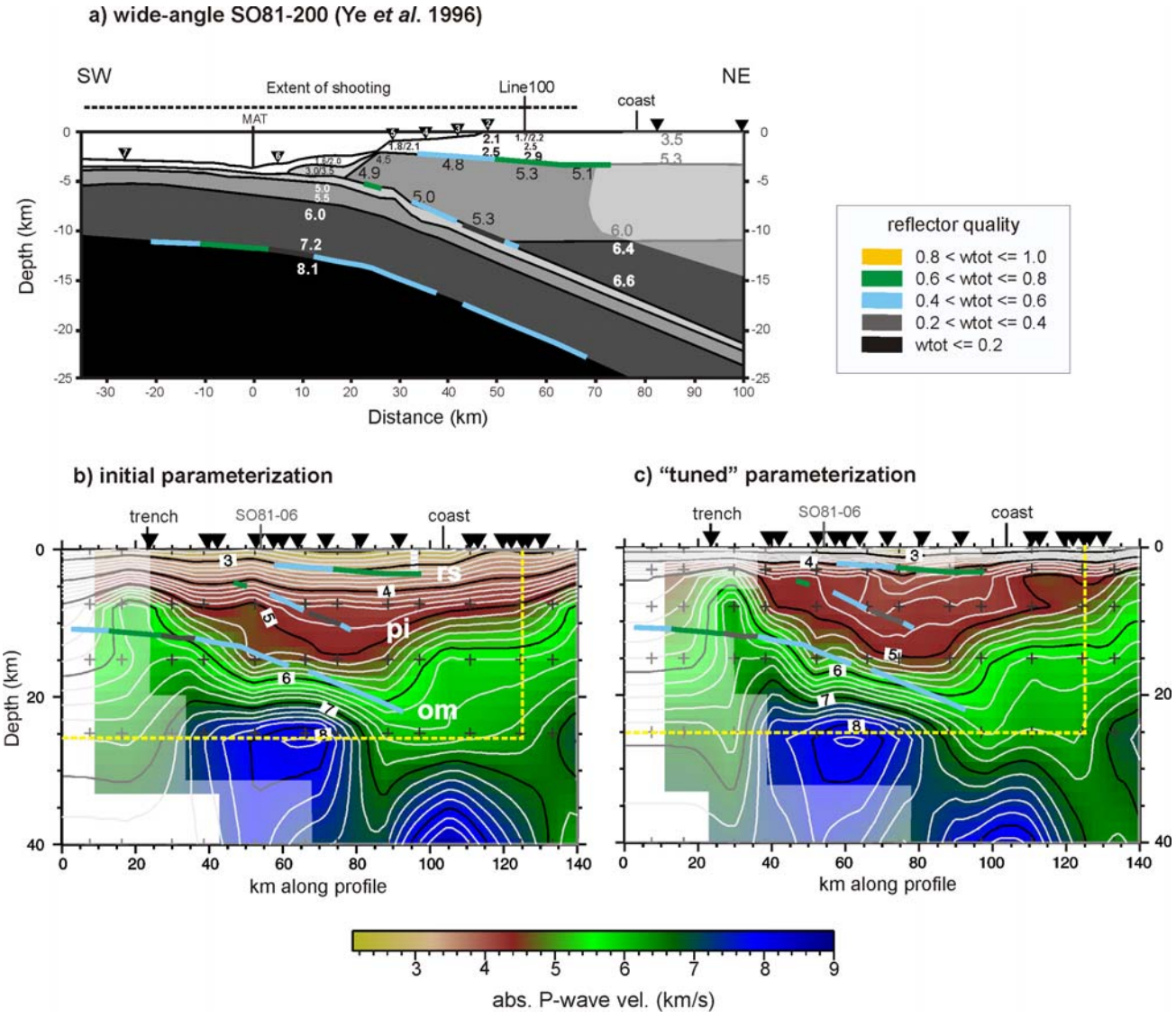

Figure 4.11. Comparison between wide-angle profile SO81-200 model (Ye *et al.* 1996), shown in a), and local earthquake tomography results. b) and c) display absolute velocity tomograms coincident with profile SO81-200, using initial and "tuned" parameterization (see text for description), respectively, and including reflectors from the "rough surface" (rs), the top of the slab (pi) and the oceanic Moho (om) from that profile, as indicated. Areas of lesser resolution are masked. Colour code for reflector quality as indicated. Profile location is given in Figure 4.2. Dashed line on b) and c) marks the area modelled by profile SO81-200. Inverted triangles represent stations.

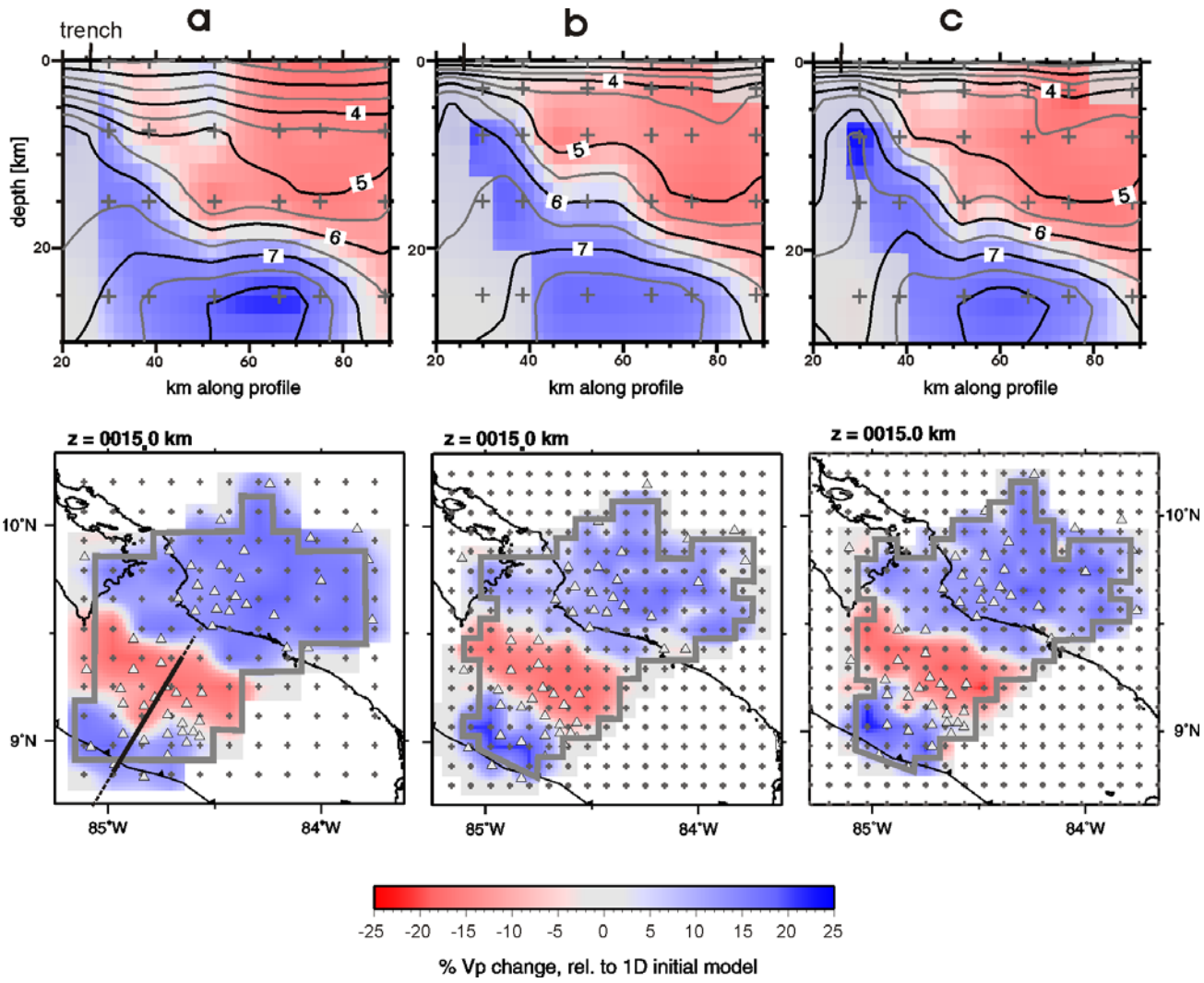

Figure 4.12. Effects of different model parameterizations on the tomographic image of Jacó seamount. Cross section (as indicated) and depth slice from: a) coarse horizontal grid of 15 x 15 km^2; b) horizontal grid 10 x 10 km^2, tuned vertical grid; c) horizontal grid 10 x 10 km^2, tuned vertical grid and slight shifting of the coordinates origin of the horizontal grid. Grey lines encompass well-resolved areas. Triangles represent stations, the dented line the Middle America Trench. See text for discussion.

4.4.3 Solution quality

The heterogeneous arrangement of sources and receivers on a LET limits the area of good resolution and may lead to the introduction of artefacts. In general, the solution quality of a certain volume depends mainly on the geometrical distribution and density of rays. Classical tools to asses ray coverage include the display of resolution estimates such as hit count, derivative weighted sum (Figure 4.10), diagonal elements of the resolution matrix (RDE), and the spread function (see e.g. Reyners *et al.* 1999, Husen *et al.* 2000). Tests with synthetic data are a powerful tool not only to gain

useful information about model parameterization and damping, but to define areas of good and low resolution (Kissling *et al.* 2001). These tests consist of the construction of synthetic input velocity models and the computation of synthetic traveltimes using the same source-receiver distribution of the real data set, and of inversion applying identical model parameterization, damping and number of iterations as with the real data.

We undertook at first two types of synthetic tests, checkerboard and characteristic models (Haslinger & Kissling 2001), and, considering the results of the inversion of real data, we further designed a synthetic model to test for slab structure. The synthetic traveltimes through the models for the tests were calculated using the finite-difference technique of Podvin & Lecomte (1991). Gaussian-distributed noise proportional to the original observational uncertainty was added to the traveltimes.

We performed synthetic checkerboard tests in order to explore the regions of the model where it is possible to resolve small-scale structures. Following Husen *et al*. (2004), two checkerboard models were designed, each consisting of alternating high- and low-velocity anomalies (±10 per cent) with one grid node left open in between to test for horizontal smearing; at the same time, to test for vertical smearing, every other layer is free of anomalies. One model has anomalies placed at 0, 8, 25 and 60 km depth, and the other at 3, 15, 40 and 80 km depth. The tests were conducted for anomalies spanning over two grid nodes in x- and y- direction, and repeated for anomalies encompassing just one grid node. Figure 4.13 presents the results from the different checkerboard tests. In summary, the resolution is very good both off and onshore, even at depths greater than 40 km and with one-grid anomalies. As expected from the earthquake distribution (Figure 4.7), at 60 km depth resolution is still good onshore, also for the model with one-grid anomalies. Vertical smearing is low at all depths, but it is slightly stronger in the first 8 km. Starting at 25 km depth, some minor horizontal smearing in the sense northeast-southwest is detected offshore. Amplitude recovering is also good, reducing to a more moderate ability between 40 and 60 km depth.

Since checkerboard tests can not ensure that the data set is able to resolve larger scale structures (Leveque *et al.* 1993), following Haslinger *et al*. (1999) and Husen *et al*. (2000) we designed an input characteristic model, based on the inversion results obtained with the real data set. This synthetic model retains the sizes and amplitudes of anomalies seen in the tomographic images but with rotated shapes and different signs (Figure 4.14). Areas of good resolution are those which show a good recovery of the synthetic model. In agreement with the checkerboard tests, we observe that the central part of the modelled area is well resolved down to depths of 60 km, with resolution decreasing with depth. Horizontally, the well resolved area extends from the trench, until 25 km depth, to the volcanic front. The area resolved at 40 and 60 km depth is broader to the southeast because the deeper earthquakes used for the tomography occur closer to the trench there. A very good recovery of boundaries between high- and low-velocity anomalies is observed (Figure 4.14). Amplitude restitution is excellent from 3 to 25 km depth, although at levels shallower than 10 km

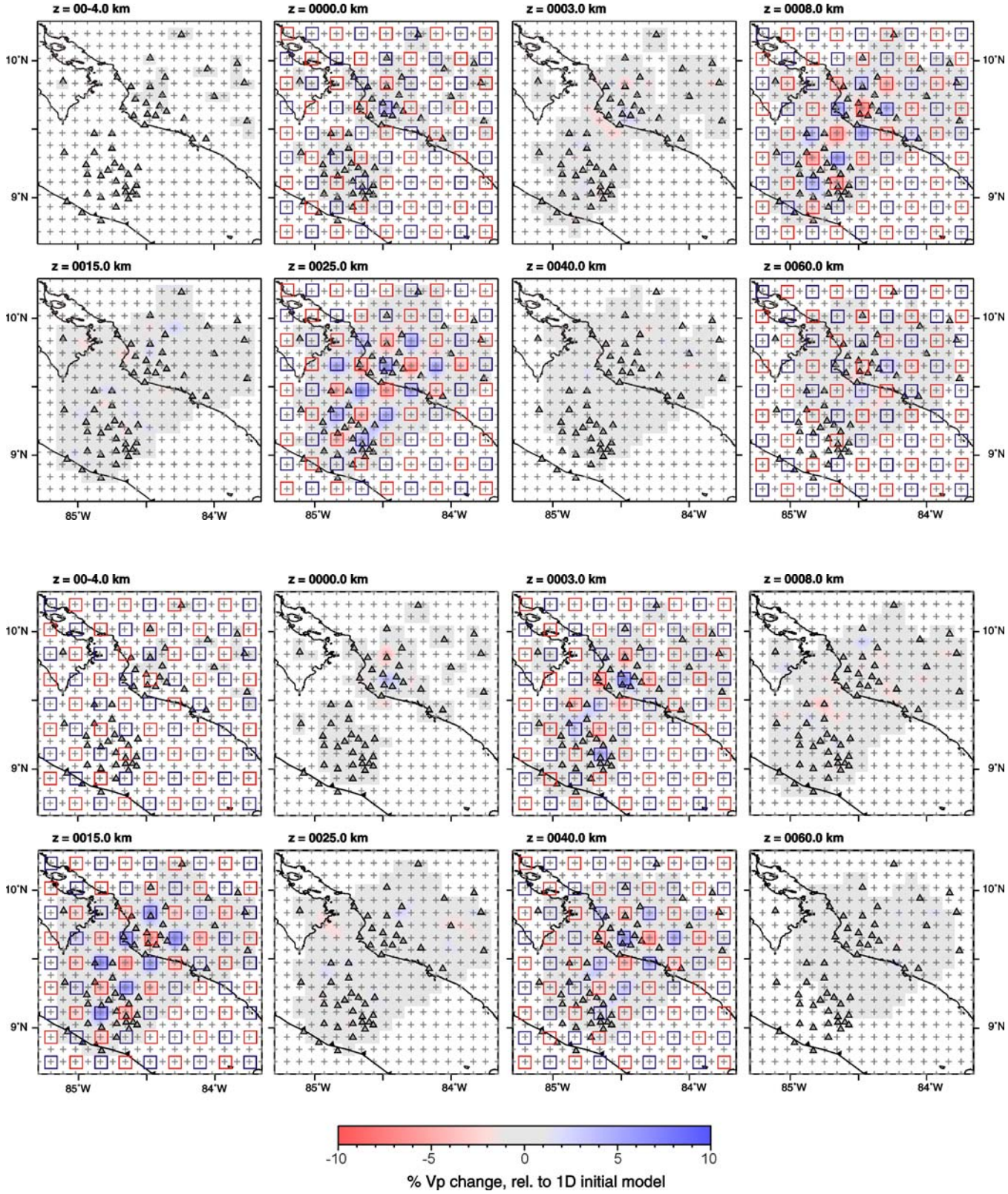

Figure 4.13. Horizontal depth sections with assessment of solution quality using synthetic checkerboard models. Recovered model is shown in plane views at different depths (see text for explanation). Locations of high (+10 per cent) and low (-10 per cent) velocity input anomalies are shown by blue and red squares respectively. Small crosses represent grid nodes of the model parameterization, grey triangles denote seismic stations. The axis of the Middle America Trench is indicated by a dented line.

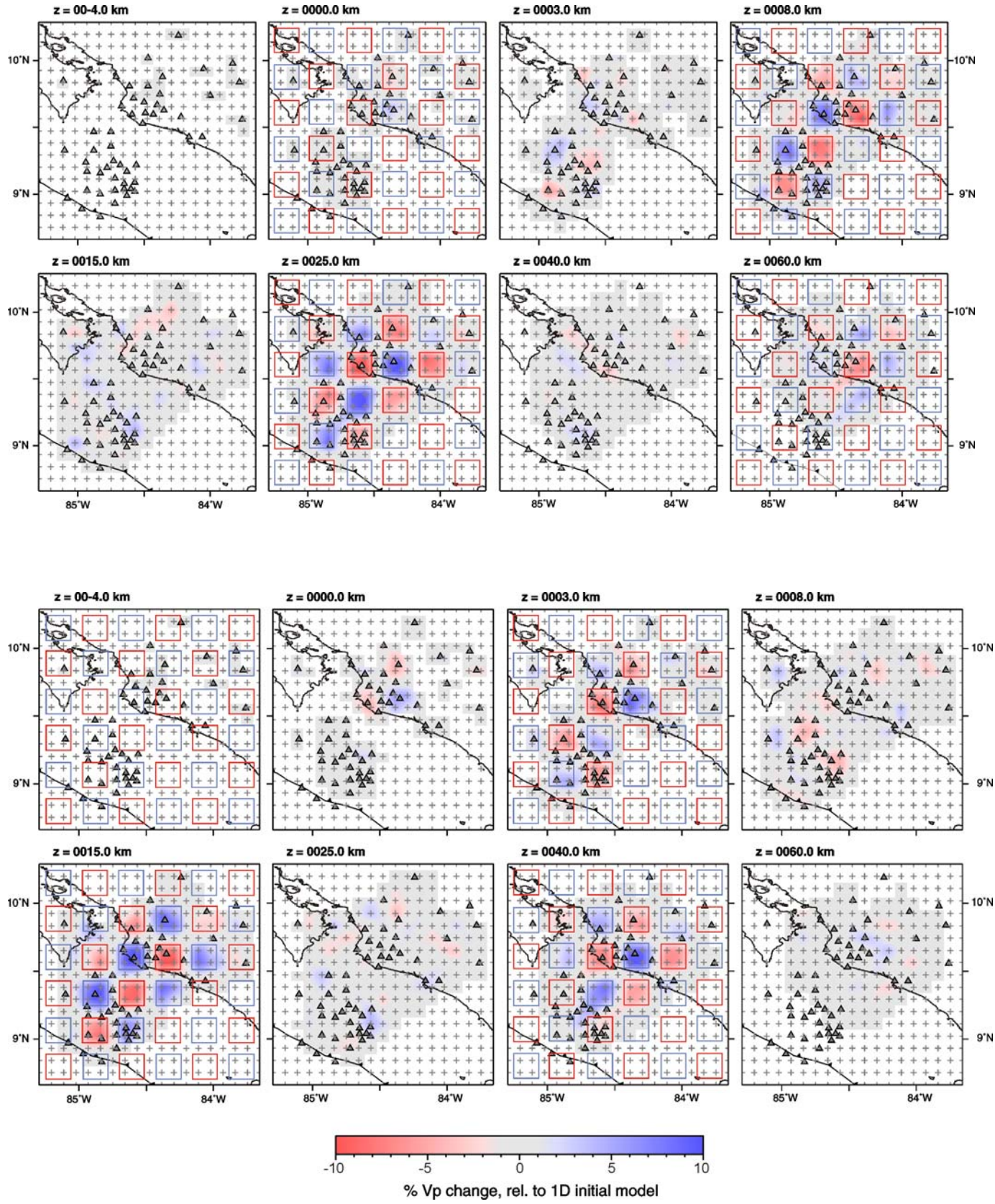

Figure 4.13 (continuation)

the recovery is patchy. At 40 km depth the amplitudes are more reduced, ranging from ~60 to 80 per cent, and at 60 km and deeper, recovery is ~60 per cent. Some horizontal smearing is observed offshore again at 40 km depth, probably caused by the fact that earthquake hypocenters deeper than 30 km are found toward the volcanic front, generating ray paths to the OBH oriented mostly northeast-southwest.

We examined also values and pattern of the RDE and the resolution contours, which help to visualize the orientation and spatial bias of possible velocity smearing in 2-D, i.e. the dependency of the solution of one model parameter on its neighbours (Reyners *et al.* 1999). An excellent correspondence is observed in Figure 4.14 between areas considered as well resolved according to the characteristic model test and the RDE values and resolution contours outlining the regions where the off-diagonal elements of the resolution matrix are still 70 per cent of the corresponding diagonal element. The RDE values of the model range from 0.01 to 0.73; most are between 0.05 and 0.40. These values are the result of the model parameterization and the damping, both conservatively chosen. Additionally, comparison with areas qualified as well resolved by the characteristic-model test yields a cut RDE value of 0.04 for good resolution. Significant smearing, as indicated by the resolution contours, for depths greater than 3 km occurs only at model parameters located at the edges of the model (Figure 4.14).

As seen partially in Figure 4.12 and described later on the section of results, from the trench down to 60-70 km depth the tomographic images illuminate the general configuration of the margin as a high-velocity subducting slab with a band of low velocities on top. In order to test the ability of the data to resolve this structure, we calculated synthetic traveltimes through a model consisting of a high-velocity slab (+15 per cent) overlain by a relatively thin band of low velocities (-10 per cent), displayed in Figure 4.15a. Between 15 and 65 km depth, the vertical grid spacing of this synthetic model is 10 km, which is closer than the parameterization of the real model, making it more realistic. A thickening of the band of low velocities toward the east mimics the results obtained using the real data. Modelling using the same inversion parameters determined for the real data set gave the results presented in Figure 4.15b. Column c in Figure 4.15, showing the results with real data along the same profiles, has been added to ease comparison and discussion.

Figure 4.15b shows that, although decreased toward the borders, the amplitude recovery of the model is very good along the studied portion of the margin. In the center of the model (profiles 2-4) high velocities of the slab are well recovered from the trench down to 40 km depth. Amplitudes are slightly decreased below that depth but the continuity of the slab is still clearly displayed. At the edges of the model volume (profiles 1 and 5) amplitudes are significantly reduced, although the slab still appears as a continuous feature. Comparison of amplitude restitution from profiles 1 to 5 indicates a lateral change in resolution from northwest to southeast, where mainly the upper or the lower part of the volume are well resolved, respectively. The band of

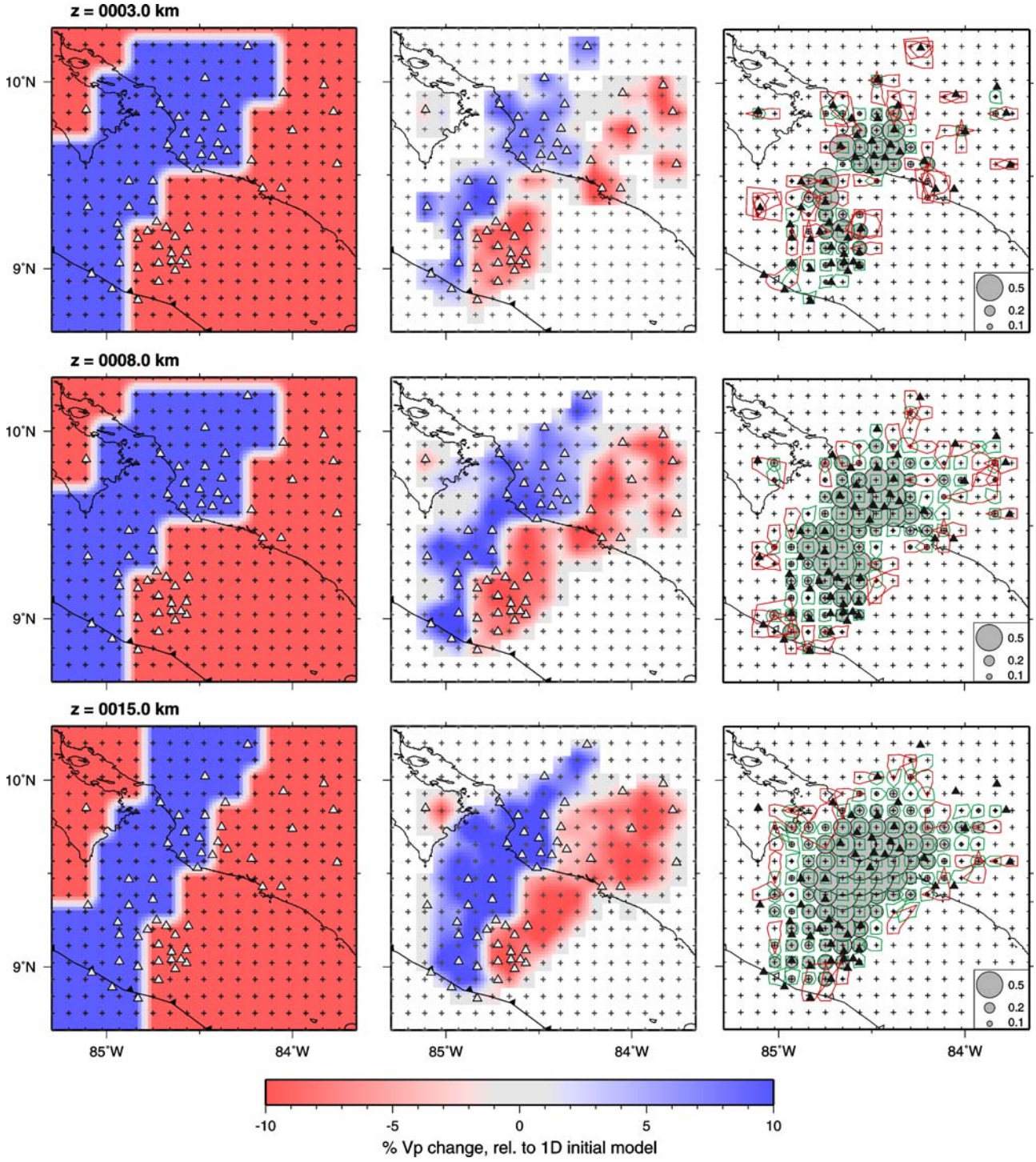

Figure 4.14. Assessment of solution quality at different depths. Left two columns show results of the test with the characteristic model. Right column shows the diagonal element of the resolution matrix (RDE) and resolution contours (Reyners *et al*. 1999). RDE are shown as scaled grey circles. Contour lines denote the area in which the values of the resolution matrix decay to 70% of the value of the RDE; green and red contour lines denote grid nodes with no and significantly velocity smearing, respectively. Triangles represent stations and small crosses denote grid nodes. The axis of the Middle America Trench is indicated by a dented line.

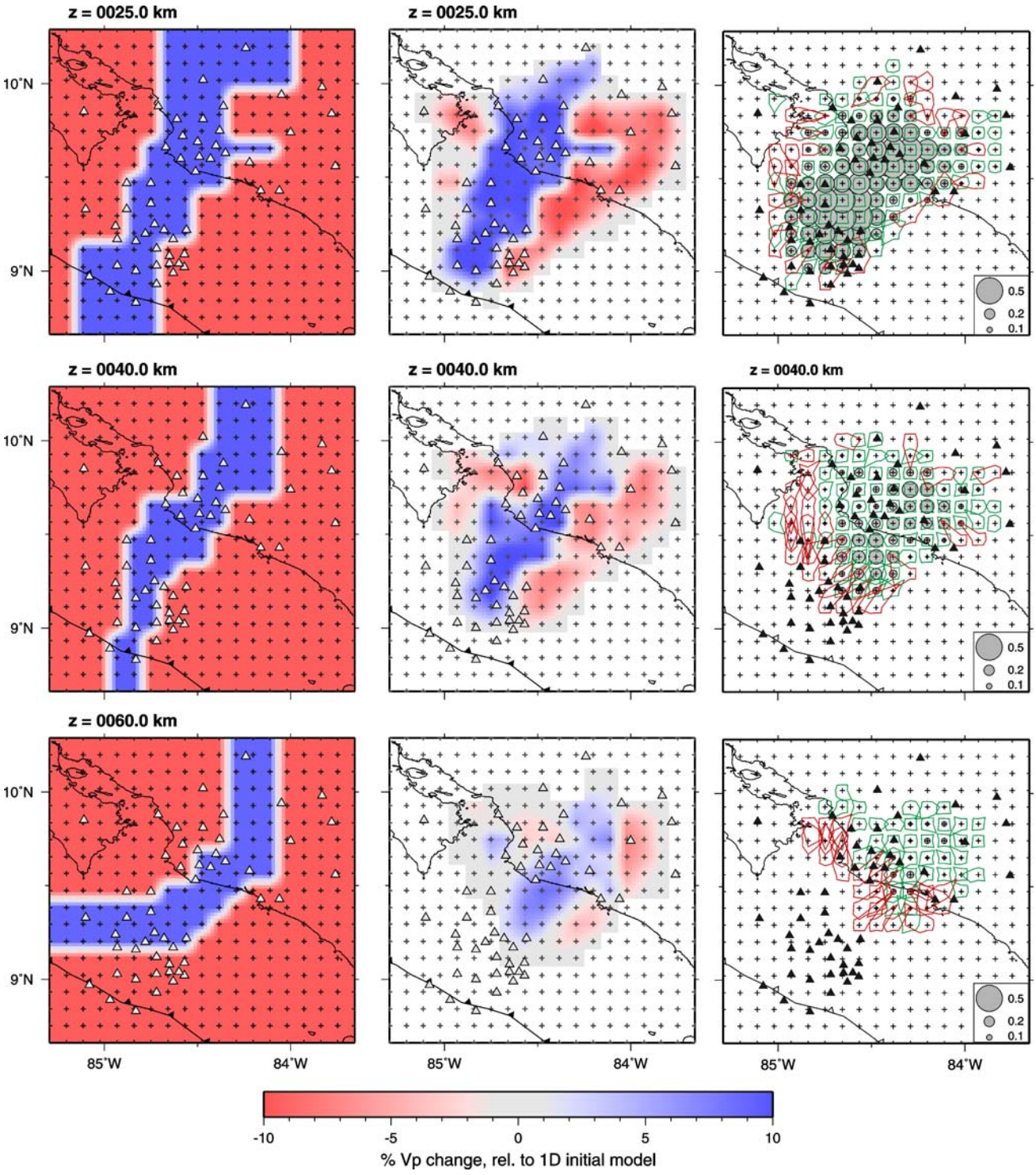

Figure 14 (continuation)

low velocities on top of the subducting slab is well recovered between 15 km and 25 km depth along all profiles. At 40 km depth low velocities are well recovered along profiles 3 to 5, where it appears as a continuous band. Between kilometers 130 and 150 along profile 4 there is a leakage of low velocities from the slab into the overlying forearc mantle, caused by rays travelling through the slab and upward toward the stations located onshore. In summary, the tests revealed that we can reliably image a

low-velocity zone and its eastward thickening on top of a high-velocity slab throughout our model. An additional test using a synthetic model with a thin, uniform low-velocity band showed equally good recovery, increasing our confidence on the capability of the data to reproduce a real feature.

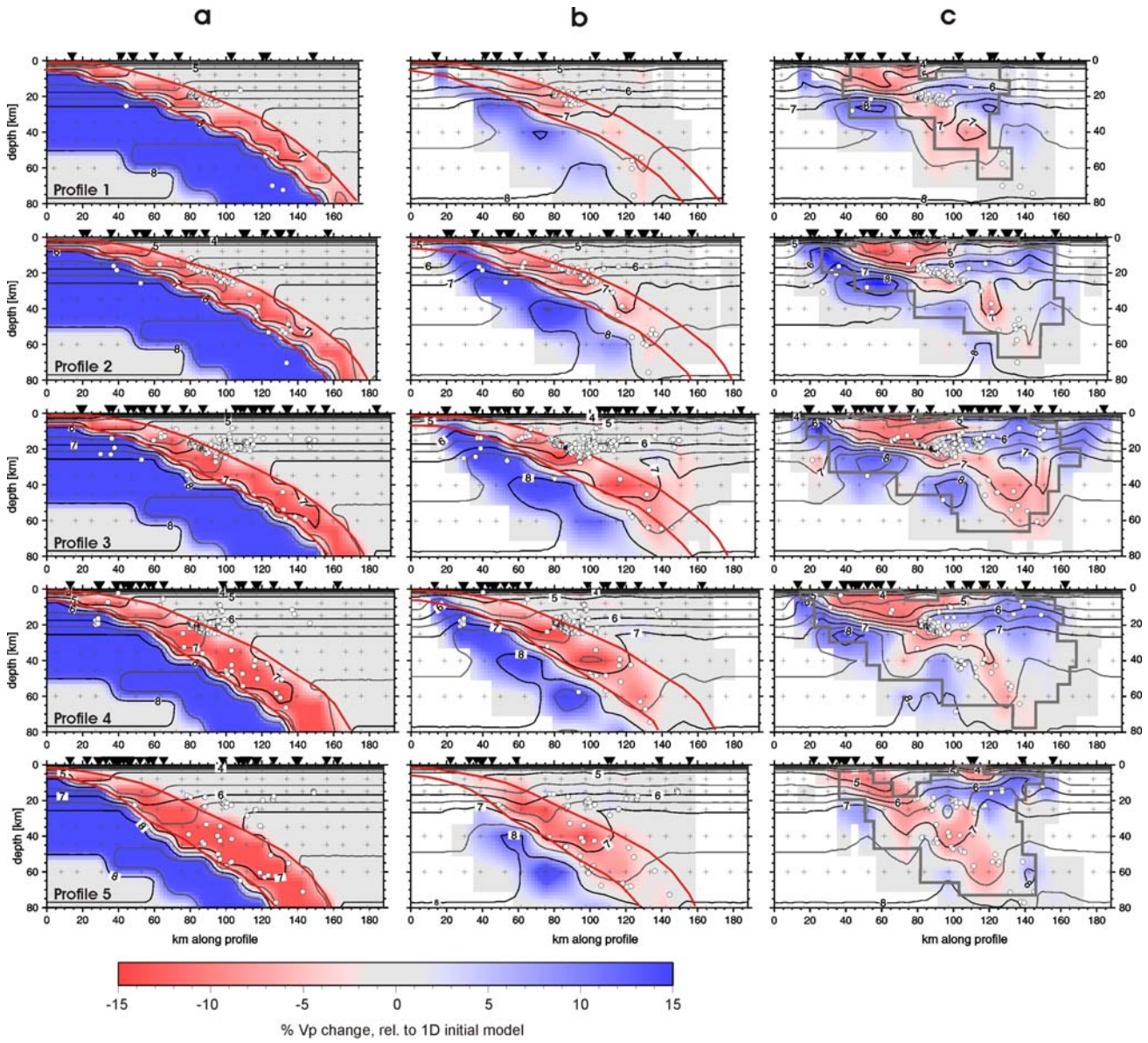

Figure 4.15. Synthetic test to examine the ability of the data to solve the observed slab structure. Column a) shows the model used to derive synthetic traveltimes, while column b) displays the results of their inversion. For comparison, column c) presents the tomograms using the real data (colour scale as in Figure 4.12). Cross-sections show velocity structure as percentage change relative to the minimum 1-D model derived in this study (first two columns); contours correspond with absolute velocities. Location of the cross sections is given in Figure 4.1. Earthquakes located within 8 km of either side are projected onto the profiles (white circles). Inverted triangles represent stations and small crosses denote grid nodes. Red lines delineating the band of low velocities are added to ease comparison.

4.5. Results

The tomographic results are presented in several depth slices (Figure 4.16) and vertical depth sections perpendicular to the trench (Figure 4.17), whose locations are shown in Figure 4.1. Depth sections show Vp in relative and absolute values. Areas of good resolution are indicated, having been defined following the previous discussion on the solution quality. In general, the tomographic model has a good resolution from the trench to the southwestern flank of the volcanic front, varying in the vertical direction down to depths of 60-70 km in the northwest and central parts of the area, and of 80 km in the southeast. We describe the results by zones, referring to the east, central and west sectors of the studied area, which along the coast correspond to the entrance of the Nicoya Gulf, the Herradura Promontory and the Parrita lowland, respectively (Figures 4.1 and 4.16).

In an attempt to define the top of the subducting plate, as shown in Figure 4.17, we consider the position and depth of the trench axis (3.3-3.7 km), the absolute velocities and the velocity perturbations, as well as the distribution of the intraslab and interplate seismicity, which forms a clear dipping planar feature (Figure 4.17). The model of Ye *et al*. (1996) for profile SO81-200 predicts velocities in the upper oceanic crust between 5.0 and 5.5 km s^{-1} (Figure 4.11a). Applying those values as guide in our model renders coherent results with the interplate seismicity for the first 15 km. At greater depths we use the clear contrasts between high- and low-velocity anomalies, and the distribution of the intraslab seismicity.

4.5.1 Near-surface geology

Although the resolution at sea level is restricted to relative small areas and some velocity smearing has been detected, there and at 3 km depth several clear anomalies reflect very well the near-surface geology (Figures 4.5a and 4.16). The oceanic-assemblage formations cropping out along the coast appear as high-velocity anomalies at Nicoya Peninsula and the Herradura and Quepos promontories, with absolute values between 3.0 and 5.4 km s^{-1}. The Pleistocene debris-flows (alluvial) deposits that outcrop northwestward from Herradura and the underlying Miocene coastal sedimentary rocks (Figure 4.5a) are congruously imaged as a low-velocity anomaly. The Pleistocene volcanic front and the volcanic formations from a previous, Miocene-Pliocene magmatic front located closer to the coast represent high-velocity perturbations. The extensive negative anomaly expanding from the trench toward the coast with velocities from 3.8-4.6 km s^{-1} could be related to both, the ~3-km maximum thick sediment coverage revealed by reflection profile SO81-13 (von Huene *et al.* 2000) and to the upper part of the margin wedge. The subducting plate appears at 3 km depth at the trench as a high-velocity anomaly, with absolute velocities up to 5.6 km s^{-1}.

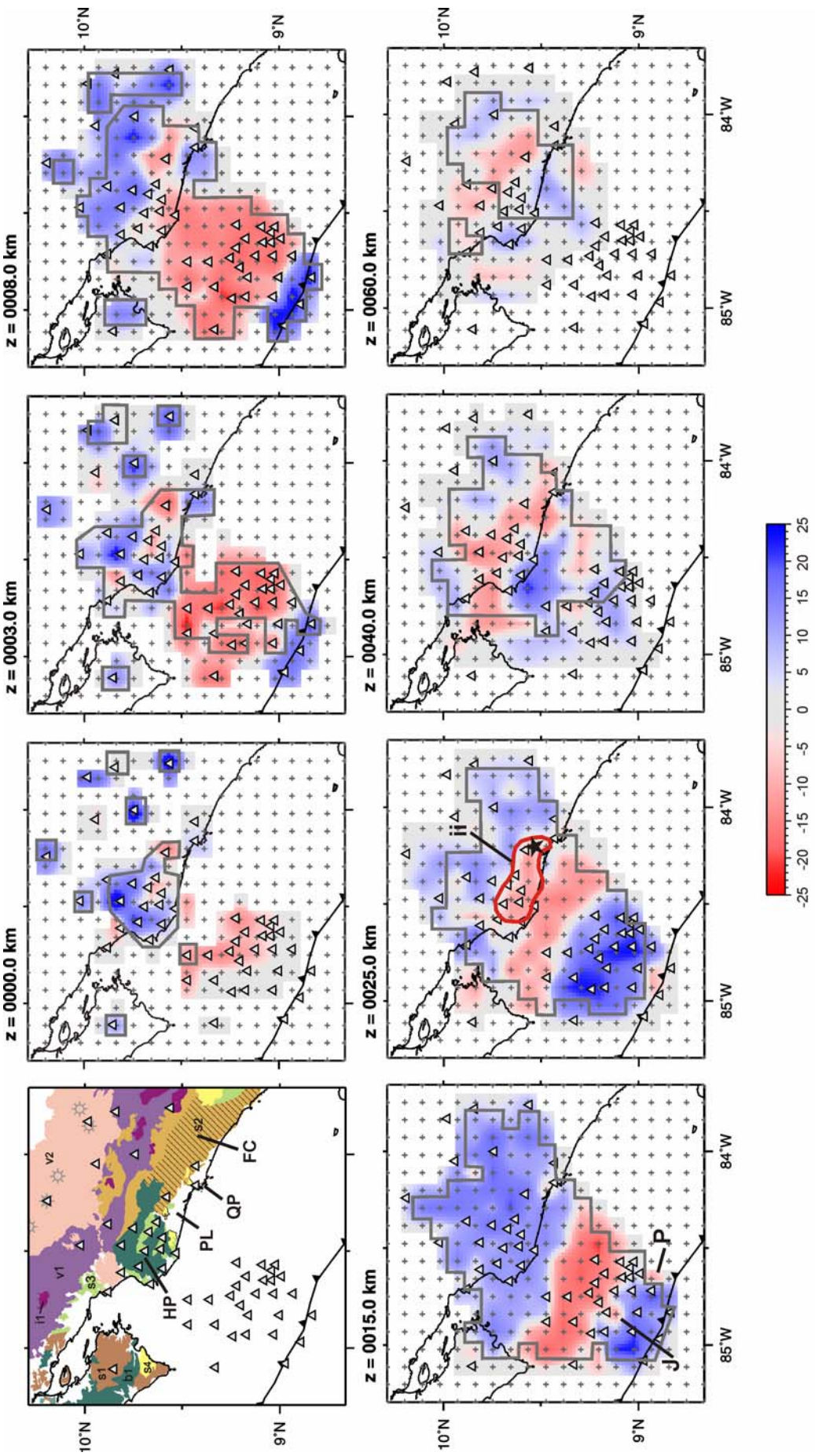

Figure 4.16. Tomographic results of 3-D P-wave velocity model shown at different depths. Velocity perturbations relative to the minimum 1-D model are shown with red to blue colours, for velocities lower and higher than predicted by the minimum 1-D model derived in this study, respectively. Areas with no ray coverage are masked. Dark grey lines contour areas of RDE > 0.04 (see text for discussion). At 25 km depth, red lines contour the low-velocity anomaly ii, observed below the inner forearc (see text for discussion) and the star, the epicenter of the 2004 Mw-6.4 earthquake (Pacheco *et al.* 2006). Triangles represent stations and small crosses denote grid nodes. The axis of the Middle America Trench is indicated by a dented line. HP: Herradura Promontory, QP: Quepos Promontory, PL: Parrita lowland, FC: Fila Costeña (hatched pattern), J: Jacó seamount, P: Parrita seamount. Geology as indicated in Figure 4.5a.

From the surface down to 8 km depth a low-velocity anomaly has been imaged between Herradura and Quepos localities, beneath the Parrita lowland, with absolute velocities of 4-5 km s^{-1} (Figure 4.16; Figure 4.17, profile 5). It likely extends further to the southeast, outside of the model. Its projection on the surface coincides very well with the north easternmost outcrops of the dense sequences of Oligocene turbidites from Térraba Formation (Figures 4.5a and 4.16). They constitute the main part of the Fila Costeña (Coastal Range), an inverted forearc basin thought to have been exhumed as a response to the subduction of the Cocos Ridge (Corrigan *et al.* 1990). To the northwest and north, the perturbation ends sharply against a high-velocity body, possibly related to the Miocene volcanic front. The northwest end follows the strike of the Parrita fault (Marshall *et al.* 2000, Denyer & Alvarado 2007), which limits the Herradura Block (Figure 1.3). This fault is part of an active system oriented at high angles to the margin that segment the forearc and separates blocks with different uplift rates, interpreted as a response to subduction of seafloor roughness (Fisher *et al.* 1998; Marshall *et al.* 2000). Seaward, the low-velocity perturbation is limited by the positive anomaly under Quepos Promontory (Figure 4.16). Stavenhagen *et al*. (1998) report the Térraba Basin to consist of intermediate velocity sediments (3.0 km s^{-1}) and to have a thickness of 2 km; Rivier (1985) estimates 3.5 km thickness on the basis of gravimetry models. The low-velocity zone of our model extends down to 8 km depth, where a down bending of the 5 km s^{-1} contour is found, but some amount of vertical smearing could slightly enlarge the image.

4.5.2 Subducting slab

The portion of the slab resolved by this study shows dipping angles of 10-12° from the trench down to 15 km depth. They increase to 16-25° at the seismogenic zone, from 15 to 25 km depth, steepening toward the east (Figure 4.17, profiles 4 and 5). Deeper than 40 km the slab dips at 40-45°.

Figure 4.17 (next pages). Vertical depth sections along the Central Pacific margin off Costa Rica. Location of profiles is indicated with dashed lines on Figure 4.1. Column a) shows velocity structure as percentage change relative to the minimum 1-D model; grey lines contour areas of RDE > 0.04 (see text for discussion). Column b) presents absolute velocities; areas of good resolution are shown in full colours, areas of lesser resolution in faded tones. Earthquakes located within 8 km of either side are projected onto the profiles (open circles). Inverted triangles represent stations and small crosses denote grid nodes. Bold lines indicate the position of the plate interface and the continental Moho (dotted) as interpreted in this study (see text). The bottom of the low-velocity band (LVB) on top of the slab (see text for explanation) is delineated by red (column a) and white (column b) lines, dashed over artefacts interpreted from test for slab structure (Figure 4.15). Stars represent 1990 Mw-7.0 (profile 1) and 2004 Mw-6.4 (profile 5) earthquakes, from Husen *et al.* (2002) and Pacheco *et al.* (2006) respectively. HP: Herradura Promontory, FC: Fila Costeña (Coastal Range), Ms: Miocene coastal deposits, MPv: Miocene-Pliocene magmatic front, Pv: Pleistocene volcanism, PHv: Holocene volcanic front, Co: Cóbano seamount, J: Jacó seamount, FLV: low-velocity anomaly beneath the inner forearc (see text for discussion).

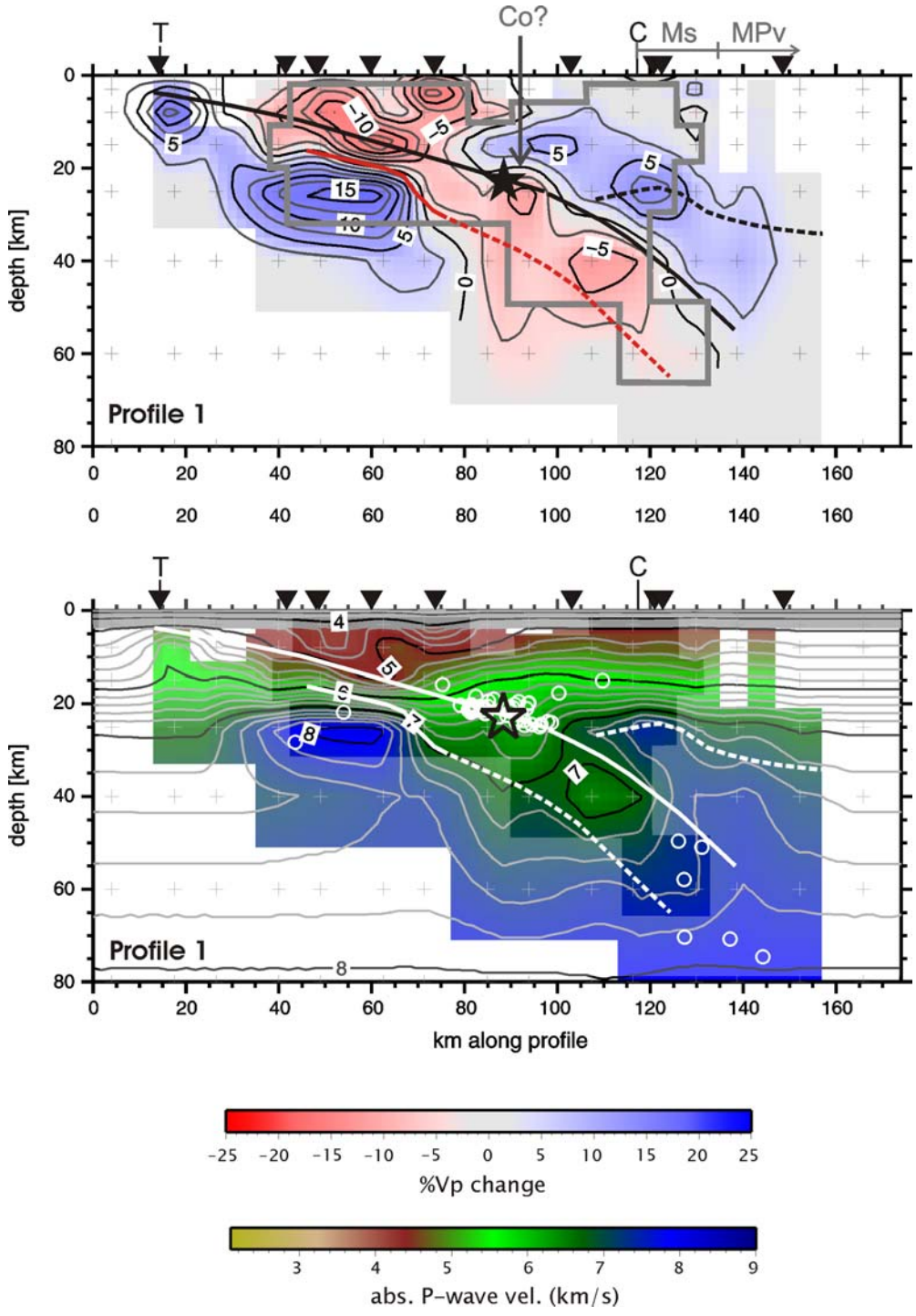

Figure 4.17 (continuation)

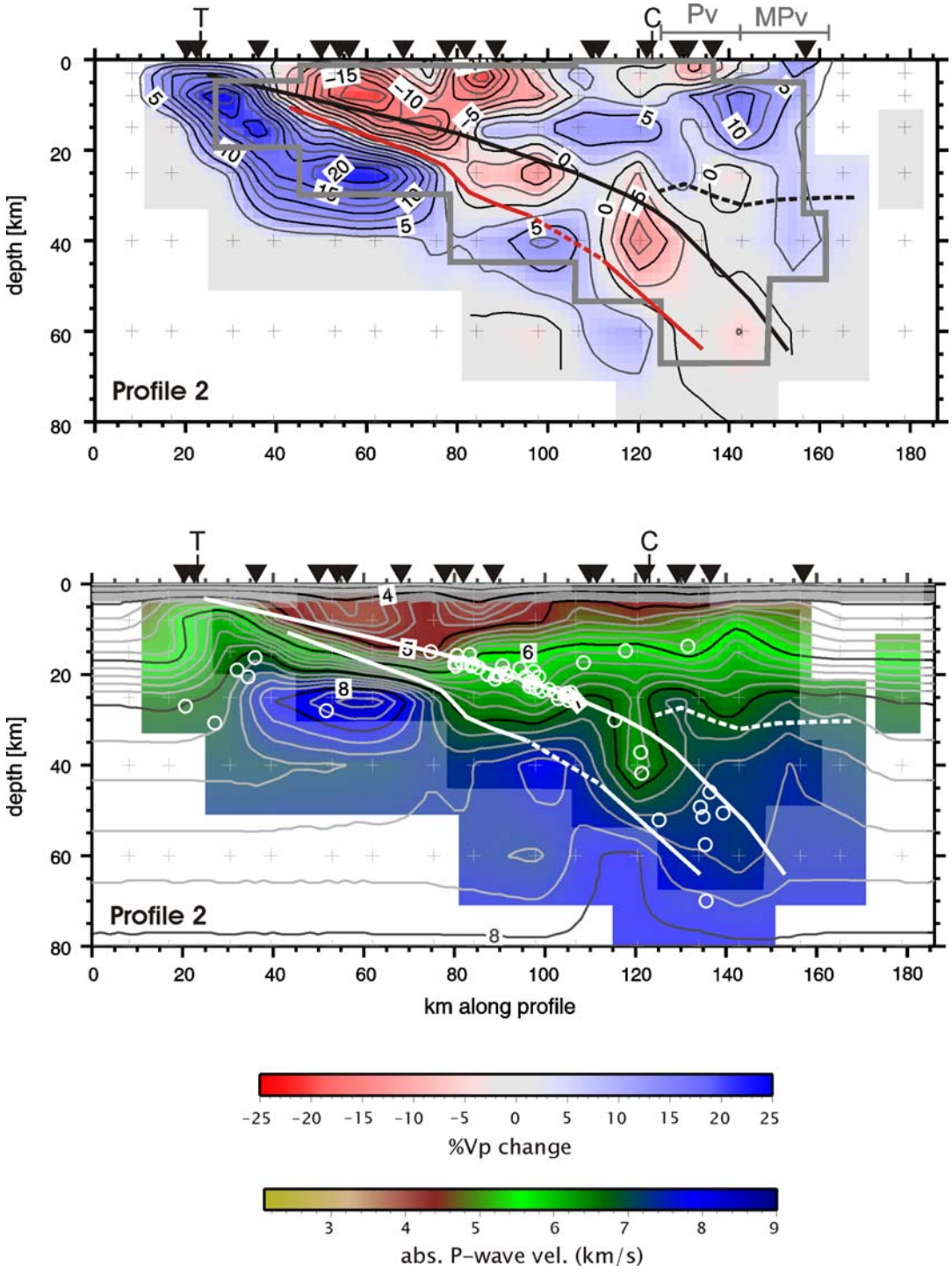

Figure 4.17 (continuation)

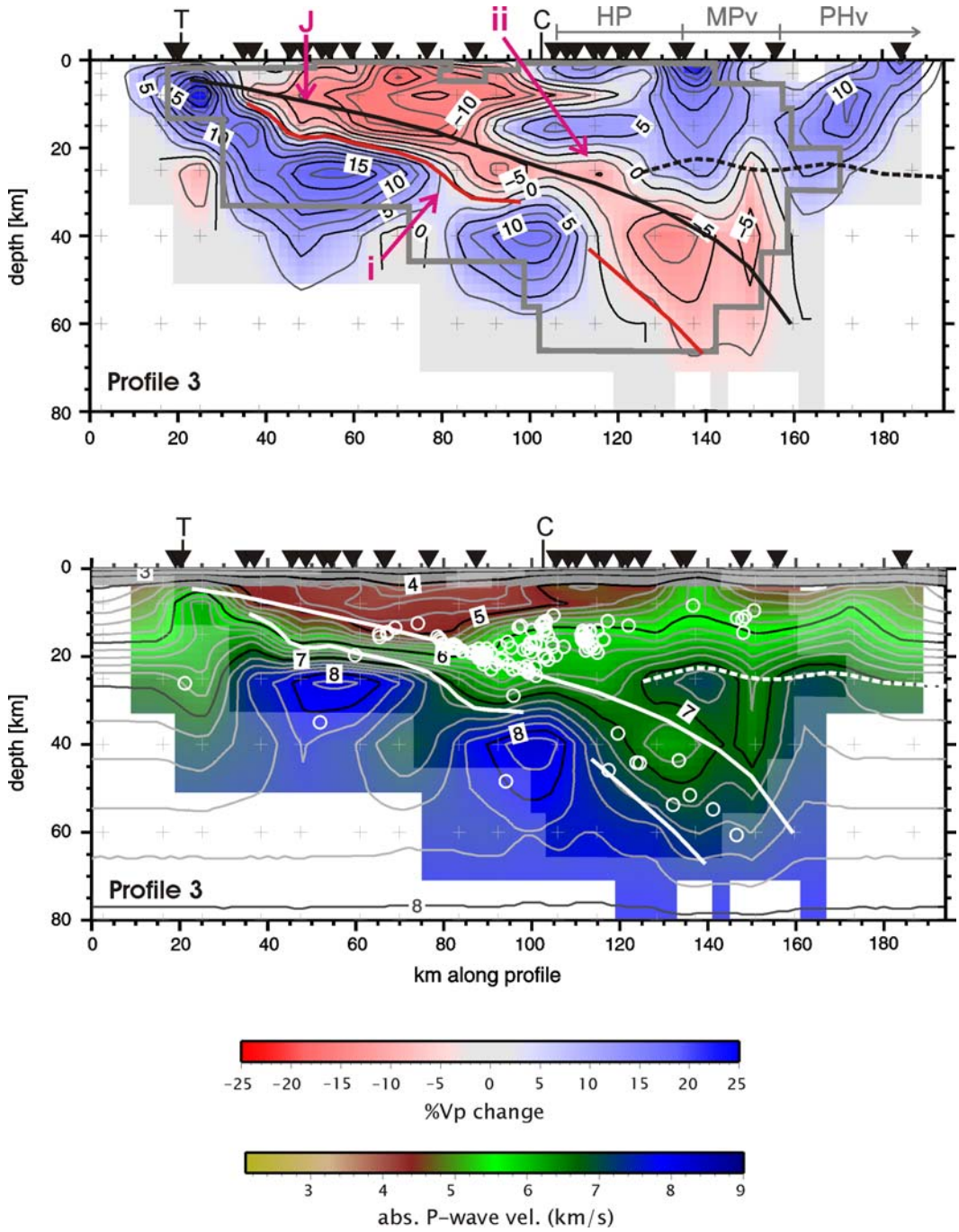

Figure 4.17 (continuation)

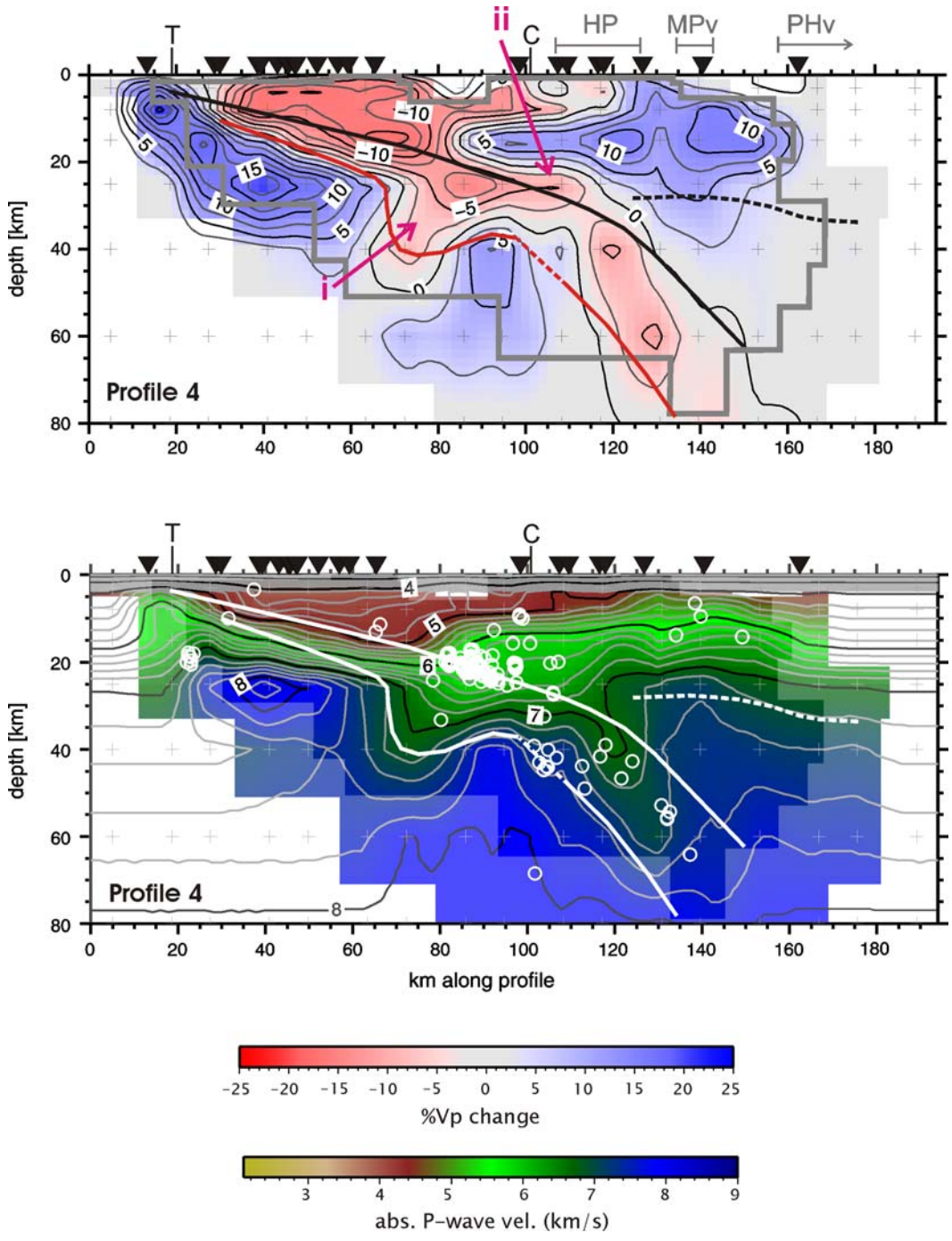

Figure 4.17 (continuation)

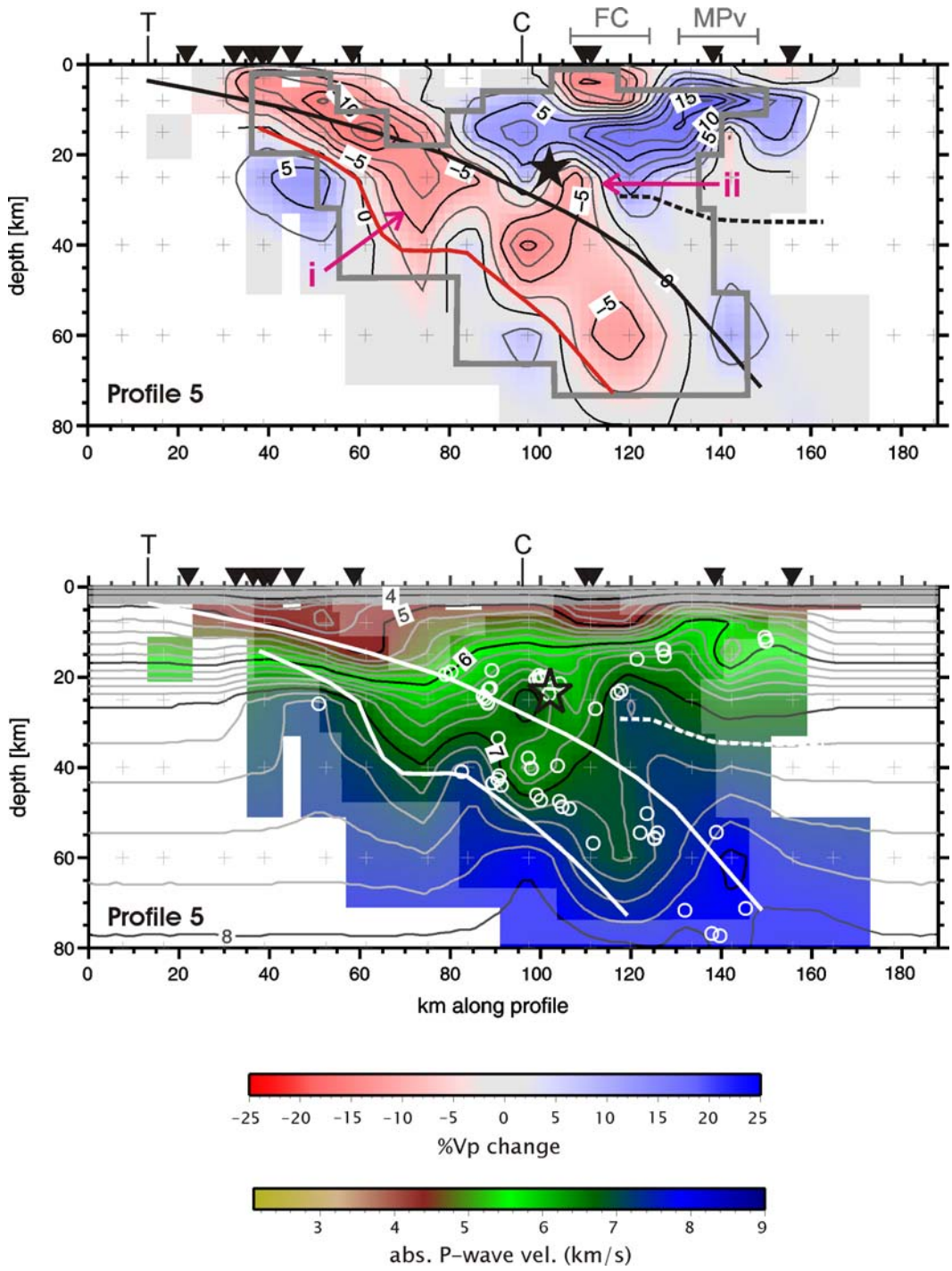

Figure 4.17 (continuation)

The west and central sectors of the studied portion of the margin display basically a similar velocity structure (Figure 4.17, profiles 1-3), although we observe some medium-scale variations. From the Nicoya Gulf entrance to the eastern flank of the Herradura Promontory, and from the trench downward to depths greater than 60 km, the Cocos Plate is imaged as a high-velocity body with a low-velocity band (LVB) on top. The intraslab seismicity deeper than ~30 km takes place on this band. The LVB has been delineated on the profiles in Figure 4.17. Down to 20 km depth, velocity

changes up to -12 per cent on the upper part of the slab; at greater profundity, maximal observed changes are of -5 per cent. The latter value could actually reach -8 per cent, taking into account that the model capacity to recover amplitudes diminishes at levels deeper than 40 km, as indicated by the synthetic tests (e.g. Figures 4.13 to 4.14). The absolute velocity along the top of the slab is 5 km s^{-1} down to 15 km depth; from 15 to ~25 km depth the velocity gradient increases to reach 7 km s^{-1}, a value that persists almost constant down to 40-45 km depth. Velocities of 7.4 km s^{-1} appear along the top of the slab at ~40 km depth on the west but at 50-55 km depth toward the center.

On cross-sections 2-5 in Figure 4.17 the LVB is interrupted by high velocities at around 35-40 km depth, between kilometers 90-110 along the profiles. The results of the test for slab structure (Figure 4.15) discussed above indicate that this gap in the LVB is an artefact only in profile 2. From the trench down to 25 km depth, the LVB encompasses the first 5-7 km of the slab. At 25 km depth and 50-60 km from the trench, the tomographic images show a down bending of the 0 per cent Vp-anomaly contour, indicating an increase on the thickness of the LVB. On cross-sections 1-2 (Figure 4.17) the thickness of the LVB increases to 10-12 km. Starting at profile 3, a pronounced down bending of the lower part of the LVB, marked as anomaly i on Figure 4.17, is found along 30-40 km and between 25-40 km depth, specially conspicuous on cross-section 4. Absolute velocities on this anomaly range from 6 to 7.2 km s^{-1}. Downdip of this sharp contortion, the LVB widens strongly encompassing more than 15 km. Neither the resolution contours maps (Figure 4.14) nor the results from the test for slab structure (Figure 4.15) show vertical velocity leakage or artefacts along this sector of the cross-sections. Furthermore, inversions of the real data set using a closer vertical grid-node spacing (10 km) from 25 to 45 km depth yielded identical results, ruling out the possibility of the widening being caused by a change on the grid-node spacing.

Thus, on the east sector of the studied area, coinciding with the upraise of the Fila Costeña onshore (Figure 4.16), the margin structure changes considerably over a distance of only ~15 km (Figure 4.17, profile 5). Besides the presence of anomaly i, the top of the slab presents here a more uniform absolute velocity gradient on the first 30 km in depth, and the LVB is notably wider at depths larger than that, comprising up to 20 km. The existence of a wider LVB in this area is confirmed by the results from the test for slab structure, which demonstrates that a high-velocity slab could be resolved (Figure 4.15), even if the amplitude recovery is not optimal. Velocities of 5 km s^{-1} along the top of the slab are found down to 10-15 km depth; the 7 km s^{-1} contour appears between 30 and 35 km depth. Velocities of 7.4 km s^{-1} at 45 km and of 7.8 km s^{-1} at 65 km depth are probably overestimated, since amplitude recovery of the model decreases for depths greater than 40 km and in general toward the east (Figure 4.15).

The reflection line SO81-06 reveals that the Jacó seamount has ~25 km diameter and its summit, according to the depth migration, is located at 5 km depth (Figure 4.11). The tomographic image of the seamount (Figure 4.12; Figure 4.17, profile 3)

coincides in horizontal extend with the reflection data, appearing as a low-velocity anomaly down to 15 km depth and suggesting thickening of the oceanic crust. We observe an up bending of the contours slower than 5 km s^{-1}, although the upper part of the seamount is difficult to define because of the similar velocities found on the overlying margin wedge. Some minor vertical velocity smearing is indicated at 8 km depth by resolution contours. Velocities higher than 5 km s^{-1} show a down bending even at 20 km depth (profile 3, Figure 4.17). To the southeast of Jacó seamount, another seamount of similar size, closer to the trench and related to the Parrita scar on the continental slope, has been imaged outside of the area of fair resolution (Figure 4.16, 15 km depth).

4.5.3 Margin wedge and continental crust

The east and central sectors show a pronounced low-velocity anomaly on the upper plate that starts some kilometers from the trench axis and extends from the surface down to the plate interface, to a depth of ~20 km (Figure 4.17, profiles 1-4). Its lower limit shallows toward the coast and finishes at ~75 km and ~85 km from the trench axis in the west and central parts, respectively. The velocity changes up to -10 per cent, with some spots reaching -15 per cent (Figure 4.17, profiles 2-3). The absolute velocities in this anomaly vary from 3.5 to 6.0 km s^{-1}. We identify this low-velocity zone with the margin wedge, based on results from wide-angle profiles, which present a similar velocity distribution. Low velocities are justified by the normal faulting on the margin wedge across the middle slope revealed by high-resolution seismic records (Hinz *et al.*1996, Ranero & von Huene 2000). Moreover, local fluid venting form the plate interface takes place through these faults (Hensen *et al.* 2004). On the east sector, although the uppermost 10 km do not present the best resolution between the continental slope and the coast, the area of the margin wedge seems to narrow again, extending up to 65 km from the trench axis (Figure 4.17, profile 5).

Landward, the margin wedge is laterally limited by a positive anomaly representing the continental crust. It extends down to 30-35 km depth, where absolute velocities range from 3.0 to 7.0-7.2 km s^{-1}. The velocity gradient decreases at depths greater than 10-15 km, a change roughly marked by the 6 km s^{-1} contour. The most conspicuous high-velocity anomalies, with more than 15 per cent velocity change, are located on the upper crust beneath the southwestward edge of the Miocene volcanic arc (Figure 4.17, profiles 3-5).

The high velocities of the upper plate are interrupted beneath the inner forearc by a low-velocity anomaly, termed anomaly ii on Figures 13 and 14. Anomaly ii coincides spatially with the appearance of anomaly i and the thickened LVB on top of the slab (Figure 4.17). The anomaly is aseismic and roughly emerges at the down-dip end of the interplate seismicity. It extends from 25 km down to 35-40 km depth, where it joins the slab top, following the coastline from beneath the west part of the Herradura Promontory until Quepos, and stretching ~20 km landward. Absolute velocities within the anomaly are 6.5-6.8 km s^{-1}. Underneath the Parrita lowland, anomaly ii increases

in amplitude and shows a more conspicuous shape in cross-section (Figure 4.17, profile 5). Eastward from Quepos Promontory the perturbation seems to disappear, although we reach there the limits of the volume illuminated by our data set (Figure 4.16, 25 km depth). In their LET for Costa Rica, Husen *et al*. (2003a) also imaged this low-velocity anomaly and proposed that it could be caused by the presence of a subducted seamount.

4.5.4 Continental Moho and forearc mantle wedge

Previous works in Costa Rica determined depths between 30 and 43 km for the Moho discontinuity, and reported a small velocity contrast between the mantle and the crust (Matumoto *et al.* 1977, Quintero & Kulhánek 1998, Quintero & Kissling 2001, Sallarès *et al.* 2001, DeShon & Schwartz 2004). Wide-angle profiles on the Central Pacific area (Ye *et al.* 1996; Stavenhagen *et al.* 1998) did not illuminate depths greater than ~20 km. DeShon *et al.* (2006) inferred the continental Moho location under Nicoya Peninsula following a turnover of the contour of 7.0-7.2 km s^{-1} P-wave velocities, which they found to be in good correspondence with lower crust velocities from the refraction model of Sallarès *et al*. (2001). Our tomographic results show an increased velocity gradient together with a clear bending of the 7.0-7.2 km s^{-1} contours, supporting DeShon *et al*. (2006) assumption. We observe a sharper velocity gradient on the western and central parts of the area (Figure 4.17, profiles 1-3), becoming more diffuse toward the east (Figure 4.17, profiles 4-5). Beneath the coast and landward, the Moho appears at 30-35 km depth (Figure 4.17, profile 5). The forearc mantle wedge exhibits velocities of 7.2-7.6 km s^{-1} on the east and the west. On the central part, slower velocities of 6.8-7.2 km s^{-1} are modelled (Figure 4.17, profile 3), but they are most likely caused by upward velocity leakage from the LVZ, as indicated by the test for slab structure (Figure 4.15).

4.6. Discussion

In this study, we collected information from CSS lines available on the area resolvable with LET and incorporate it indirectly into the inversion process. Usually, when CSS data are inverted directly in a LET, shots are treated as earthquakes with known origin time and location, and therefore they are not relocated during the inversion process. However, the location of the sources at the surface can negatively affect the inversion because of the strong nonlinearity resulting from the dependence of the ray turning points on the velocity structure (Laigle & Hirn 1999). Moreover, sources and receivers distributed along a seismic profile is one of the worst possible ways to deploy a seismic station array for earthquake location.

A good agreement is observed between the distribution of absolute velocities of the "tuned" tomography and the 2-D model of Ye *et al*. (1996) for wide-angle profile SO81-200, although the velocity contrasts appear 2 to 5 km deeper in the tomograms (Figure 4.11b). This could be attributed to the differences on the estimation of

velocities of each method, as well as their inherent uncertainties. While LET yields a volume-wise average of velocity, wide-angle 2-D ray tracing modelling averages velocities along the ray path. The distribution of earthquakes in 3-D ensures precise information of seismic velocities per volume, provided that there are enough rays per volume, coming from different directions. Also, the location of sources and receivers both outside the studied area restricts the ability of CSS methods to resolve the precise position and true dip of reflecting structural elements. The strength of wide-angle method lies on its sensibility to large-scale vertical and horizontal velocity gradients and discontinuities. Ray crossfiring is limited in 2-D CSS profiles, and the velocities resulting from ray tracing and in-line migration are averages for the specific layers. On the other hand, LET resolution capability is limited by the grid-node spacing, therefore decreasing with depth.

Ye *et al*. (1996) do not discuss the uncertainties of their model for the wide-angle line SO81-200, but they do mention that the denser station coverage over the continental slope and the recordings from the two land stations allowed them to determine the velocity distribution more reliably there. The authors also state that their data did not suffice to resolve the change on the velocities of the oceanic crust farther landward in the subducting slab. A very rough estimation of the vertical uncertainty could be attempted on the basis of Fresnel volumes and the w_{tot} of reflector elements. A reflector element from profile SO81-200 with the highest quality (w_{tot} =1), belonging to the plate interface beneath the margin wedge, at ~10 km depth, would have an uncertainty of ±1.4 km considering a seismic frequency-content range of 6-14 Hz (Ye *et al.* 1996) and an average velocity of 4.3 km s^{-1} for the overlying crust. As suggested by Baumann (1994), dividing that value by the actual w_{tot} of the reflector, 0.5 in this example (Figures 4.2 and 4.11), yields ±2.8 km as an estimate of the real vertical uncertainty for the element. An example of uncertainties on wide-angle modelling is given by Walther (2003), who analyzed a profile shot on the Cocos Plate, close to the MAT and parallel to it, from Quepos Plateau to the southeastern flank of the Cocos Ridge. He applied conventional 2-D raytracing and an algorithm for seismic traveltime inversion for 2-D velocity structures. The distance between stations and the average shot spacing were ~7.5 km and 150 m, respectively. With several uncertainty tests he estimated an average spatial resolution of ±2.0 km for the Moho, whose position ranges from 12 to 20 km depth. Thus, the observed difference on the depth of the velocity contrast between LET and CSS techniques could lie, to some extend, in the range of uncertainties.

The distribution of the high-quality hypocenters obtained by the tomography also suggests a deeper location of the top of the subducting plate than predicted by Ye *et al.* (1996). A clear, dipping planar clustering of events between 15 and 25 km depth (Figure 4.17), interpreted as interplate seismicity, corresponds to a plate interface ~2.5 km deeper than modelled by those authors. Another factor that could explain the differences in velocity distribution between wide-angle and LET techniques is the presence of the Jacó seamount. Seamounts are highly altered and fractured crustal sectors located on top of locally thickened portions of oceanic crust, which cause

decrease on P-wave velocities. This circumstance is clearly imaged on the tomograms but not on the wide-angle model (Figures 9 and 10).

Several studies using LET have been carried out in Costa Rica. Husen *et al*. (2003a) performed a country-wide LET using earthquake data from the two permanent seismological networks of Costa Rica. On the central part of the country, the model has good resolution down to 70 km depth. Their study revealed a complex lithospheric structure beneath Costa Rica, further documenting the influence of the structure and evolution of the incoming Cocos plate on the margin configuration. In general, the results presented here are in good agreement with the work of those authors. However, our model provides new insights into the first 60-70 km of this sector of the subduction zone provided mainly by the offshore coverage, lacked by Husen *et al*. (2003a). In addition, observed discrepancies are attributable to the use of different reference models and model parameterizations. Absolute velocities resulting from both tomographic models are slightly different but consistent at depths greater than 10-15 km.

As imaged by Husen *et al*. (2003a), DeShon *et al*. (2006) and other previous studies in Costa Rica, the Cocos slab is a high-velocity anomaly to first order, as expected from the fact that subduction rates are more rapid than rates of thermal diffusion, yielding a slab relatively cold compared to the warm mantle. This simple image has been modified in the last years with the detection of negative anomalies along the slab in different zones of the world, such as Taiwan (Lin *et al.* 1999), Alaska (Abers 2000, Abers *et al.* 2006) and Costa Rica (Husen *et al.* 2003). The model of the latter authors depicts the upper part of the slab subducting beneath central Costa Rica as high-velocity feature with areas of low velocities appearing at different depths. In our model, on the contrary, along the whole sector of the margin covered by the Jacó network we observe a continuous band of low velocities on the subducting slab starting at depths as shallow as 5-10 km at ~5-10 km from the trench (Figure 4.17), and stretching down to 60-70 km depth, were the resolution ends.

Low velocities on top of the slab have been detected by CSS methods as well. Ye *et al*. (1996) report clear near-vertical PiP reflections recorded over the continental slope from their modelling of line SO81-200. They point out that their appearance requires a high-velocity contrast along the plate boundary, which they depict as a low-velocity layer with a thickness slightly over one km. Further to the southeast, 40 km beyond the area of this work, Stavenhagen *et al*. (1998) observed an up-to-8 km thick low-velocity layer overlaying the subducting slab, which possesses an increased thickness of 14 km itself. The authors attribute the thick low-velocity layer to eroded material from the margin wedge.

The appearance of low velocities inside the subducting slab can be explained by several processes taking place at different depths, in which water and the structure of the oceanic plate play a key role. Subduction transports large amounts of water into the Earth, including free water contained in sediments and the oceanic crust and mantle, as well as in the form of hydrous minerals. As the slab sinks, dehydration of

the slab is thought to take place, releasing fluids most likely continuously, while the dehydrating lithology changes with depth from sediments, to hydrated oceanic crust, to serpentinized oceanic mantle (Ruepke *et al.* 2002). At depths greater than ~100 km, fluids from sediments, crust and mantle are released beneath the volcanic front into the hot mantle wedge, where they may propitiate partial melting by decreasing the temperature, leading to arc volcanism. In the following we will discuss how the different processes outlined above are expressed in our tomograms. Figure 4.18 provides sketches of cross-sections 2 and 5 (Figure 4.17), delineating the observed low-velocity anomalies and their interpretation.

Hydration through slab faulting

It has been suggested that most of the hydration of the oceanic plate takes place during bending near the trench, where water percolation and mineral alteration occur at extensional faulting on the crust and the upper few kilometers of the mantle (Kirby *et al.* 1996), or even deeper, 15-30 km into the mantle (Peacock 2001, Ranero *et al.* 2003, 2005). Like at most of the subduction zones, faulting along the trench is present offshore Middle America, and it has been imaged by high-resolution seafloor mapping, near-vertical reflection lines and outer-rise seismicity (Hinz *et al.* 1996, von Huene *et al.* 2000, Ranero *et al.* 2005, Grevemeyer *et al.* 2007). Northward from the boundary between lithospheres formed at EPR and CNS, offshore Nicoya Peninsula, the oceanic crust is ~5 km thick, favouring a zone of flexure and faulting wider than that to the south. Offshore the Central Pacific area of Costa Rica, the oceanic crust is thicker, the outer rise much smaller and the faulting on the seaward trench slope of the Cocos Plate is less developed (von Huene *et al.* 2000). Between Fisher Seamount and Quepos Plateau, the flexural stress is relieved on a narrow area by faulting along presumed zones of previous structural weakness of the plate, i.e. the spreading fabric (Figure 4.1). In our tomographic images, specially clear on profiles 2, 3 and 4 (Figures 14 and 15), the low-velocity layer toping the subducting slab to depths of ~25 km appears relatively narrow, encompassing the first 5-7 km into the plate, in good agreement with a shallower bend-faulting. The subduction of a less deeply faulted lithosphere beneath Central Costa Rica has been invoked by Ruepke *et al*. (2002) to explain the variations in lava composition between Costa Rica, where they have been originated from a basalt-amphibolite source, and Nicaragua, where the descending lithosphere is pervasively faulted and serpentinized, favouring a deep fluid source from the slab mantle.

Another factor that could contribute to the low-velocity anomalies observed on the first kilometers of the slab is the subduction channel and the fluids stored on it. Reflection lines offshore Costa Rica (Hinz *et al.* 1996) suggest that more than 95 per cent of the sediment coverage, with a thickness of ~0.5 km off Costa Rican Central Pacific margin, remains on the subducting plate (von Huene *et al.* 2000). The subduction erosion process adds large amounts of material removed from the upper plate to the subduction channel, introducing a layer with an estimated thickness of 400-800 m (von Huene *et al.* 2004).

Slab dehydration

At depths shallower than ~20 km, in a low temperature environment, water is released from compaction and diagenesis of subducted sediments and the subduction channel. These fluids could migrate along the plate interface toward the trench, or most likely in erosional margins, ascend along faults formed within the upper plate by hydrofracturing on the forearc region (Ranero *et al*. 2008). High-resolution seismic records and multibeam bathymetry display pervasive normal faulting on the middle slope off Costa Rica (Ranero & von Huene 2000). The chemistry of the cold vent fluids seeping on top of the faults indicate a source at the plate interface (Hensen *et al.* 2004). The weakening of the upper plate basement and the fluid venting, together with deformation and faulting originated by seamount subduction, justify the low velocities obtained on the margin wedge (Figures 4.17 and 4.18).

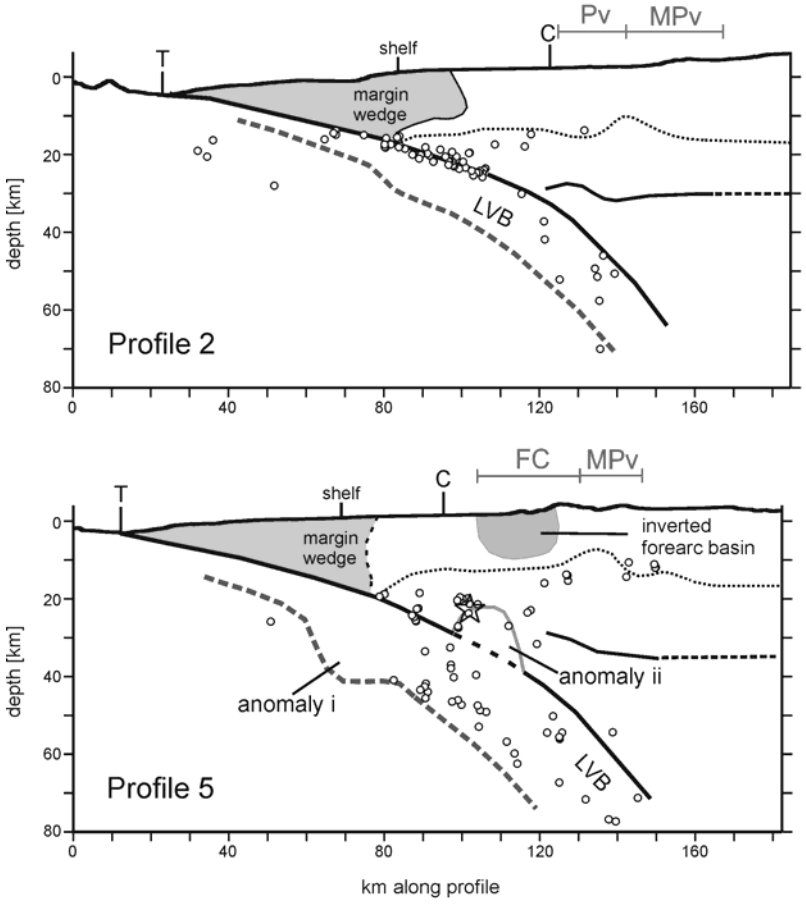

Figure 4.18. Schematic cross-sections through the west (profile 2) and the east (profile 5) sectors of the area resolved by the Jacó array, sketching the configuration of the margin and its variation (see text for explanation). Location is given in Figure 4.1. The dotted line follows the contour line of 6 km s-1, which could represent the limit between upper and lower crust of the overlying plate. Earthquakes located within 8 km of either side are projected onto the profiles (white circles). The topography has been slightly exaggerated, but cross-sections are at scale. The star in profile 5 represents the hypocenter of the 2004 Mw-6.4 earthquake (Pacheco *et al*. 20006). LVB: low velocity band, FC: Fila Costeña (Coastal Range), MPv: Miocene-Pliocene magmatic front, Pv: Pleistocene volcanism.

At deeper levels, from 20 to 100 km depth, progressive metamorphism releases water from sediments and oceanic crust, at pressure and temperature conditions which are too cold to generate arc melting. The 3-D P-wave velocity structure and petrologic

modelling from Husen *et al*. (2003a) indicate the existence of a low-velocity hydrous oceanic crust in the subducting plate beneath central Costa Rica. They found a good correlation between the predicted locations of hydrous minerals in the oceanic crust and the hypocenters of intermediate-depth earthquakes, supporting the hypothesis of the latter being enabled by dehydration (Kirby *et al.* 1996, Hacker *et al.* 2003, Abers *et al.* 2006). For their part, Ranero *et al*. (2005) present evidence from the subduction zones in Middle America and Chile indicating that, even though dehydration embrittlement and eclogitization may contribute to stresses in the slab leading to seismogenesis, much of the intermediate-depth intraslab seismicity occurs by reactivation of old and new faults formed by plate bending near the trench. A hydrated oceanic crust explains the existence of a LVB on top of the slab down to the maximal depths resolved by this study (60-70 km) and probably beyond, at least on the west part (Figure 4.17, profiles 1-2; Figure 4.18). The fact that the LVB encompasses the intraslab seismicity deeper than ~30 km recorded by this experiment (Figure 4.17) agrees with slab dehydration as a seismogenic agent. To distinguish whether the earthquakes are generated by dehydration embrittlement across the slab or they concentrate along pre-existent faults reactivated during subduction, further data analysis is necessary. For example, high-precision relative earthquake locations could eventually depict lineaments associable with faults.

As described above, the tomograms depict widening of the LVB in two senses: a vertical widening that starts at ~25 km depth on the west portion of the margin studied here, and a general eastward widening (Figures 14 and 15). Further growing of the faulting downdip as the slab bends further (von Huene & Ranero 2003, Mikumo *et al.* 2002) and is confronted with the sector, downdip of the disrupted margin wedge, where the upper plate has strengthened, may account for the vertical widening of the LVB.

Thickening of the oceanic crust

At cross-sections 4 and 5 (Figures 14 and 15) the LVB more than doubles its thickness at depths greater than ~30 km. As in the west sector, the intraslab seismicity distributes all over the thickened LVB (Figure 4.17¸ profiles 4-5). Anomaly i protrudes from the bottom of the LVB, noticeable from the area crossed by profile 3 and eastward, and precedes the general downdip widening of the LVB. The shape of anomaly i resembles the structure of the seamounts imaged by this and other studies but with bigger proportions. Its appearance takes place ~10 km closer to trench at profile 5. The onset of intraslab seismicity also draws progressively nearer to the trench, so that at profile 5 it starts ~25 km and ~10 km seaward from the onset at profiles 3 and 4, respectively, at least during the recording period of the Jacó network.

This eastward broadening of the LVB could be caused by the presence there of a portion of the slab displaying a more intensive, and maybe deeper, bend faulting. Nevertheless, the subduction of the Cocos Ridge and its thickened crust suggests another origin for the widening of the LVB. Trench-parallel, wide-angle profiling ~30 km seaward from the MAT reveals that the EPR crust offshore the Nicoya Peninsula

possesses the velocity structure of normal oceanic crust (Walther & Flueh 2002). On the contrary and as expected from the presence of the Cocos Ridge, crustal thickening related to the Galapagos hotspot has been imaged all along a profile stretching from Quepos Plateau to the southeastern flank of the ridge by Walther (2003) and Sallarès *et al.* (2003). The models of those authors show a maximal crustal thickness of 19-20 km below the center of the ridge; the thickening is almost entirely caused by a lower crust with up to three times the thickness of normal oceanic crust. Beneath the northwestern flank of the ridge, in the area of the Quepos Plateau, the CNS crust is ~8-10 km thick (Walther 2003), or even thicker (Sallarès *et al.* 2003), the increase here being attributed to the upper crust and expressed by 3-km thick flow basalts (Walther, 2003). Velocities lower than expected for a crustal layer 2-A constituted mainly by basalts could be caused by high porosity (Walther 2003), as suggested by the slightly to highly vesicular lavas and tuffs dredged from the ridge (Werner *et al.* 1999).

Following the azimuth of the Cocos plate motion as predicted by the model Nuvel-1A (DeMets *et al*. 1994), shown in Figure1, a landward projection of the thickened oceanic crust existent under Quepos Plateau coincides very well with the eastward widening of the LVB (Figure 4.17, profiles 4 and 5). This suggests that the widened LVB imaged by this tomography beneath the Parrita lowland and landward may be caused by the presence of subducted thickened crust with velocities in general lower than the average for normal oceanic crust. In this context, anomaly i could be interpreted as the result from hotspot activity as well, a feature similar in extension to Quepos Plateau. The velocity structure and gradient of the thickened LVB and the anomaly i are very similar to those of the lower crust of Cocos Ridge as modelled by Walther (2003) and Sallarès *et al.* (2003).

Since thickened crust shows an impaired bending ability, hydration of the slab by flexural normal faulting at the trench may be decreased. Bend faulting of the Cocos Plate at the outer rise and the trench decreases southeastward and disappears against Quepos Plateau (von Huene *et al.* 2000) (Figure 4.1). Bathymetry highs and lithologies on the Cocos Plate, such as seamounts, the up-to-900 m thick volcaniclastic aprons extending ~10 km on both sides of Quepos Plateau (Flores-Hernández 1996, Walther 2003) and the thick, high-porosity flow basalts which thicken the upper crust of the plateau, may introduce some amount of water into the subduction zone, but likely stored only on the first few kilometres of the slab. Yet, this and other studies (Protti *et al.* 1995a, Husen *et al.* 2003) observe abundant intraslab seismicity on the area crossed by profiles 4 and 5 (Figure 4.17) and further to the east. Even more, landward from thicker portion of the Cocos Ridge in southern Costa Rica, where there is no evidence of bend faulting, intraslab seismicity as deep as ~65 km distributed on a ~20 km-thick band has been detected by a local network (Arroyo, 2001). If dehydration reactions generate intraslab seismicity, alternative tectonic scenarios for hydration of the oceanic crust, such as spreading centers (Peacock 1990; Kirby *et al.* 1996) and hotspots (Seno & Yamanaka 1996), may play an important role too, at least in the case of subducted thickened crust and low-magnitude (< M_L 5) seismicity.

Serpentinization of the forearc mantle wedge

The fluids released at depths from 20 to 100 km may rise buoyantly along the slab-wedge interface to hydrate the cold upper mantle wedge (Hyndman & Peacock 2003). The subduction of oceanic lithosphere reduces the temperature of the overlying forearc, providing conditions for stability of hydrous serpentine minerals in the forearc mantle. Serpentinized forearc mantle may justify the aseismic nature of that portion of the subduction zone and the downdip limit of the subduction thrust earthquakes (Hyndman *et al.* 1997, Hyndman & Peacock 2003).

The model of Husen *et al*. (2003a) predicts hydrated, serpentine- and/or chlorite-bearing mantle in a narrow zone just above the subducting slab and in a larger area in the "tip" of the mantle wedge beneath central Costa Rica. According to empirical relationships between the degree of serpentinization and seismic P-wave velocities of peridotites (Carlson & Miller 2003), velocities of 7.2-7.6 km s^{-1} obtained in the narrow part of the mantle wedge resolved by this study, in the east and west sectors (profiles 1, 2, 4, 5 in Figure 4.17), indicate a serpentinization of ~5-15 per cent (2 - 4.5 wt% H_2O). This value could be slightly underestimated, given that the characteristic model test suggests an anomaly recovery of 70-80 per cent on the forearc mantle wedge. Using LET, DeShon *et al*. (2006) report a serpentinization of 20-25 per cent on the forearc mantle wedge beneath the Nicoya Peninsula, which could also be higher considering the reduced anomaly recovery of the model. These results correspond well with the work of Hyndman & Peacock (2003), who examined a wide range of geophysical and geological data and concluded that serpentinization of the forearc mantle is a global expected phenomenon, commonly reaching values of 20 per cent and locally up to 50 per cent.

Subduction of ocean-bottom morphology

The configuration of the Central Costa Rican Pacific margin is modified by the subduction of seamounts, ridges and plateaus imprinted on the Cocos Plate by the Galapagos hotspot. Two subducted seamounts upward from the seismogenic zone have been imaged by the tomographic modelling in this study, the Jacó seamount (Figures 1, 10, 13 and 14) and ~20 km to the southeast, already at the edge of the area resolved by the LET, the Parrita seamount (Figure 4.16). The latter is located ~10 km landward from the trench axis, has a diameter of ~18 km and is associated to the Parrita Scar (Figure 4.1) on the middle margin slope. It has also been previously imaged by reflection line SO81-06 (von Huene *et al.* 2000). Both seamounts appear as negative anomalies in the tomograms, their roots clearly signalled by a down bending of the contours of absolute velocities higher than 5 km s^{-1} on the oceanic crust and upper mantle, and an up bending of the contours of slower velocities into the margin wedge. A similar tomographic image has been obtained by Husen *et al*. (2002) for a seamount located at the entrance of the Nicoya Gulf. Discerning the summit of the seamounts in the tomogram is difficult because of the lack of velocity contrast between the top of the slab and the base of the margin wedge.

Profile 1 in Figure 4.17 crosses the area where the Mw-7.0 Cóbano earthquake occurred in 1990, at the entrance of the Nicoya Gulf (Figure 4.1). By analyzing the source-time function of the earthquake, Protti *et al*. (1995b) suggested that it was generated by the rupture of an asperity, likely a seamount, that propagated to a weaker zone. Husen *et al*. (2002) observed a tomographic low-velocity anomaly at ~30 km depth and interpreted it as the signature of the seamount. In our results, the absolute velocity distribution is similar to that described by those authors, but the image of the seamount is not clear. We see a slight thickening of the low velocities on top of the slab in the area, at around 20-30 km depth (Figure 4.17, profile 1), but the decrease on velocity contrasts caused by the presence of the LVB and the proximity to the border of the model at this position may complicate the recognition of a seamount.

Inner forearc

Another remarkable characteristic of the portion of the margin resolved by the LET is the low-velocity anomaly ii, imaged directly over the subducting slab, from 25 to 35-40 km depth below the inner forearc, from Herradura until Quepos promontories (Figures 13 and 15; Figure 4.17, profiles 3-5). The occurrence of this anomaly spatially coincides with the subduction of anomaly i and the thickened oceanic crust. Furthermore, the location of this anomaly closely matches the area of the subaerial forearc where underplating of seamounts has been invoked to explain the differential uplift of forearc blocks (Fisher *et al.* 1998, Marshall *et al.* 2000, 2007; Gardner *et al.* 2001). This uplift is superimposed to the general elevation caused by the subduction of the Cocos Ridge further to the southeast, where the forearc deforms more uniformly by rapid shortening across the Fila Costeña (Kolarsky *et al.* 1995, Fisher *et al.* 2004).

Several hypothesis could explain the low velocities found underneath the inner forearc. Husen *et al*. (2003) suggested that anomaly ii, also imaged in their LET, could be a subducted seamount. Subducting seamounts offshore central Costa Rica cause erosion and subsidence on the offshore forearc (Ranero & von Huene 2000), but several studies evidence that they travel downward unscathed (Barckhausen *et al.* 1998, von Huene *et al.* 2000, Ranero & von Huene 2000), even to depths of 20-25 km (Husen *et al.* 2002).

The concurrence of a subsiding outer forearc (Vannucchi *et al*. 2001, 2003; von Huene *et al*. 2004) and an uplifting inner forearc (Fisher *et al.* 1998, Marshall *et al.* 2000) in an erosive convergent margin could also be justified by tectonic underplating. Accretion of subducted material beneath the base of the coastal forearc since ~2 Ma, synchronous with tectonic erosion under the trenchward part of the forearc is described by Clift & Hartley (2007) in Peru and northern Chile. They propose a style of non-steady state tectonic erosion in which periods of slower erosion and coastal uplift alternate with times of faster erosion and trench retreat. Such underplating has been modelled by frictional wedge analysis (Adam & Reuther 2000) and imaged as low-velocity anomaly by LET (Husen *et al*. 2000) beneath the Mejillones Peninsula in North Chile. In our case, tectonic underplating could be

explain by an increase in the buoyancy of the subducting slab causing an augment on lateral stress which propitiates an accumulation of eroded material against the base of the upper plate, at the downdip limit of the coupled interface. Velocities of 6.5-6.8 km s^{-1} modelled for anomaly ii at 25-35 km depth suggest that it may be composed of mafic igneous rocks (Christensen & Mooney 1995), probably from seamounts and the oceanic assemblages constituting the margin wedge. Removal from upper-plate material during subduction contributes enough material for underplating. Ranero & von Huene (2000) have identified two specific mechanisms of subduction erosion along the Middle America margin, namely erosion by seamount tunnelling and removal of large rock lenses of a distending upper plate. Further evidence of the undermining of the overlying plate, besides the relief disruption associated to recently subducted seamounts, is displayed by the two broad embayments affecting the upper and middle slope of the continental margin offshore the Nicoya Gulf entrance and the Parrita lowlands (Figure 4.1), 45 and 70-km wide respectively (von Huene *et al*. 2000).

Additional information for this sector of the margin is provided by the 2004 Mw-6.4 Damas earthquake (Figure 4.1). According to the work of Pacheco *et al*. (2006), the main shock was located at 24 km depth, at the flank of anomaly ii as imaged by this study (Figure 4.16 and 4.18; Figure 4.17, profile 5), with the aftershocks distributed between 15-25 km depth. The slip distribution resembles that of a simple circular rupture with a radius of 8 km, a dimension consistent with the tomographic image of anomaly ii in this sector (Figure 4.17, profile 5). The authors conclude that deformation takes place throughout the whole thickness of the continental crust, probably caused by "seamount subduction and strong basal friction on the upper plate, due to subduction of a thick, young, and buoyant oceanic plate, rough seafloor, and underplating of large seamounts".

Nevertheless, the apparent aseismic quality of anomaly ii, inferred from Jacó records and the distribution of the 2004 earthquake aftershocks (Pacheco *et al*. 2006), may fit better on yet another scenario. The low velocities underneath the inner forearc could be explained by an accumulation of upward migrating fluids, overpressured and confined at the base of the overlying crust by the presence of the seamount or plateau and the expected increased coupling on the plate boundary. Elevated fluid pressure could increase stress on the adjacent rocks. The presence of the seamount or plateau and the thickened crust alone could justify the coastal uplift and the occurrence of the 2004 earthquake.

The hypothesis described above partially justify the coinciding observations, but if they are in effect linked, further information is needed to better constrain the interpretation. For example, Vp/Vs or S-wave tomography and thermal modelling could render valuable insights on the presence and distribution of fluids, improving the characterization of the different factors interacting on the margin.

4.7. Conclusions

We have used the P-wave traveltimes from 595 earthquakes recorded during six months by an "amphibian" station array, combined with information provided by controlled-source seismology profiles, to obtain a 3-D tomographic model of the shallow part of the subduction zone (< 70 km) in the Central Costa Rican Pacific margin. The use of ocean-bottom stations allowed us to determine reliable hypocenters from the trench to the coast for the first time in this area.

The 3-D velocity structure of this sector of the Costa Rican margin, well resolved from the trench down to 60-70 km depth, presents a certain degree of complexity, evidenced by subducted seamounts, the transition from normal to thickened subducted oceanic crust and, possibly, tectonic underplating, taking place along a relatively short distance. This structure also reflects various processes recognised in subduction zones, invoked here to account for the observed anomalies, such as slab hydration through bend faulting, tectonic erosion and slab dehydration.

The subducting slab is resolved down to ~70 km depth, as a high-velocity perturbation with a conspicuous band of low velocities (LVB) on top, which contains the intraslab seismicity deeper than ~30 km. This LVB is the expression of several processes varying in depth and along the trench. From the trench down to 20-25 km depth, the low velocities encompass the first 5-7 km of the slab, originated mainly by the fault system reactivated by bending at the trench and the outer rise and by hydration (Ranero *et al.* 2005). The LVB is locally thickened by the presence of Jacó and Parrita seamounts. A vertical widening of several kilometers of the bottom of the LVB takes place at around 25 km depth, roughly coinciding with the interplate seismicity above, the increase in the dipping angle and, consequently, with the augment in strength of the upper plate. Further development of the bend-faulting system under those conditions may justify the widening.

The broadening of the LVB is stronger toward the east, where it is preceded by an even sharper widening of the low velocities, interpreted as a big seamount or plateau, both with velocity structure similar to that reported for the Cocos Ridge (Walther 2003, Sallarès *et al.* 2003). The maximal thickness of the LVB imaged in this study concurs with the onset of the Fila Costeña (Coastal Range) onshore, considered as an inverted forearc basin (Kolarsky *et al.* 1995). We believe that this striking change represents the transition from subduction of normal oceanic crust to Galapagos hotspot modified, thickened oceanic crust. The occurrence of intraslab seismicity distributed all over the thickened LVB suggests that slab hydration at tectonic scenarios other than the trench-outer rise may also play an important role.

The presence of the thickened crust and the accompanying big seamount or plateau shows spatial reciprocity with an aseismic low-velocity anomaly revealed beneath the inner forearc, at the base of the crust of the upper plate. This anomaly could constitute the first geophysical evidence for the tectonic underplating of seamounts and material eroded from the upper plate, previously proposed to explain the differential uplift of

blocks of the inner forearc in Central Costa Rica (Fisher *et al.* 1998, Marshall *et al.* 2000). The buoyancy of the underplated material could increase crustal stress above, as indicated by the 2004 Mw-6.4 Damas earthquake (Pacheco *et al*. 2006). Alternatively, its aseismic quality suggests that the anomaly underneath the inner forearc could be caused by accumulation of upward migrating fluids, trapped at the base of the overlying crust by the presence of the seamount or plateau, which increases interplate coupling.

The margin structure presented here is the result of a relatively short recording period. The complex dynamics of subduction zones calls for longer deployment periods in order to more fully understand the processes and their evolution through time. Valuable information from complementing data and techniques, such as Vp/Vs modelling, attenuation, gravimetry, focal mechanism determination and geodesy, could contribute to a better characterization of the rocks physics, stress and deformation, and therefore to constrain interpretation and gain further insights into the subduction processes.

AKNOWLEDGMENTS

We wish to thank the masters, crews and scientists of the RV Sonne and RV Meteor for their accustomed excellent performance during cruises SO163 and M54, respectively. We thank also the superb work of personnel from ICE during installation and maintenance of the land network, as well as the people who graciously allowed us to place equipment on their estates and took care of it. T. Diehl from the Institute of Geophysics at ETH Zurich kindly provided us with some of his scripts. Most of the figures were created with the Generic Mapping Tool (GMT) by Wessel & Smith (1998). This publication is contribution no. 155 of the Sonderforschungsbereich 574 “Volatiles and Fluids in Subduction Zones” at Kiel University, funded by the German Research Society (DFG). I.G. Arroyo wishes to thank the German Academic Exchange Service (DAAD) for financing most of her studies in Germany, and to ETH Zurich for providing further allowance for her stay in Zurich.

4.8. 3-D Vp/Vs model

Information provided by Vp/Vs ratios can provide valuable further criteria to characterize the mechanical properties of the rocks in an area, helping to constrain the interpretation. The S-phases from local earthquakes recorded by the Jacó-RSN array have been picked solely from the records of the 15 Jacó land stations, which are three-component, as described in chapter 3. The failure of the offshore seismometers mentioned in chapter 2 is expected to decrease the resolution of Vp/Vs modelling. In spite of that circumstance, the inversion of S-wave data recorded by the Jacó experiment has been attempted and is described in the following.

Due to the fact that most earthquake datasets include fewer S-wave than P-wave observations, the separate inversion for those parameters can result in low resolution of Vs in areas of good resolution for Vp, complicating the interpretation. Besides, picking of both types of data possesses different quality. For these reasons, inverting for Vp/Vs could yield a better solution, where reliable ratios are expected in areas of good P- and S-wave resolution (Evans *et al*. 1994, Husen 1999).

To invert for Vp/Vs, the 3-D P-wave velocity model and a constant Vp/Vs ratio of 1.68 are used as the initial model. The latter value has been determined as the better fit for the Wadati diagram of the dataset used for P-wave tomography, as shown in Figure 4.19. Since the number of available S-wave observations is around 30% of the total number of P-wave readings, the sampling of the space for Vp/Vs modelling is significantly inferior. The use of the 3-D P-wave velocity model and a constant Vp/Vs value ensures that variations of this initial ratio can be resolved in areas with good S-wave coverage, while in other areas the average ratio is not modified (Haslinger 1998).

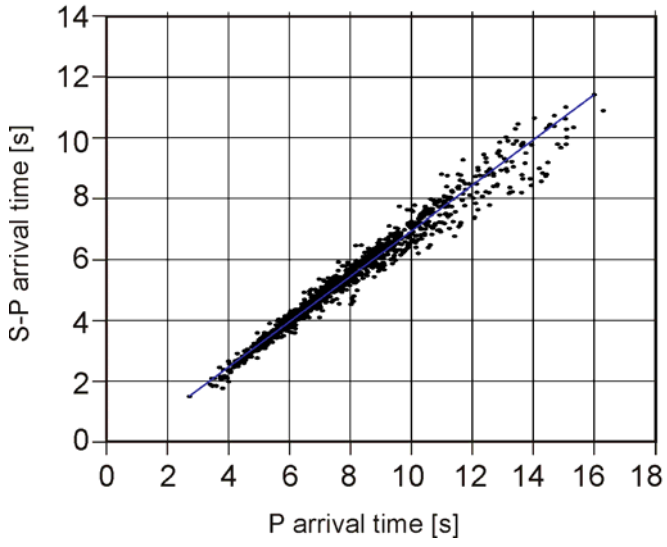

Figure 4.19. Wadati diagram of events selected for P- and S-wave inversion. The estimated Vp/Vs ratio is 1.68.

A sub-dataset of 551 events with at least four S-wave readings was selected from the data used for P-wave tomography. The dataset comprises 3363 S-wave and 10,881 P-wave observations; the coverage with S-wave data is shown in Figure 4.20. Because it is already the result of a tomographic inversion, the P-wave velocity model was kept strongly damped (1000) while a damping parameter of 50 was applied for Vp/Vs, chosen from a trade-off curve as for the Vp previously.

The final weighted rms over all traveltime residuals for the combined dataset is 0.010 s. This value is close to the a priori average observational error. There is no significant shift on earthquake locations or change in the P-wave velocity model. The inversion was also performed with the minimum P-wave 1-D velocity model and the same ratio of 1.68 for Vp/Vs as starting model and solving for both, 3-D P-wave velocity and Vp/Vs ratio. The results are very similar, with the same pattern of anomalies although their amplitude tends to be slightly higher.

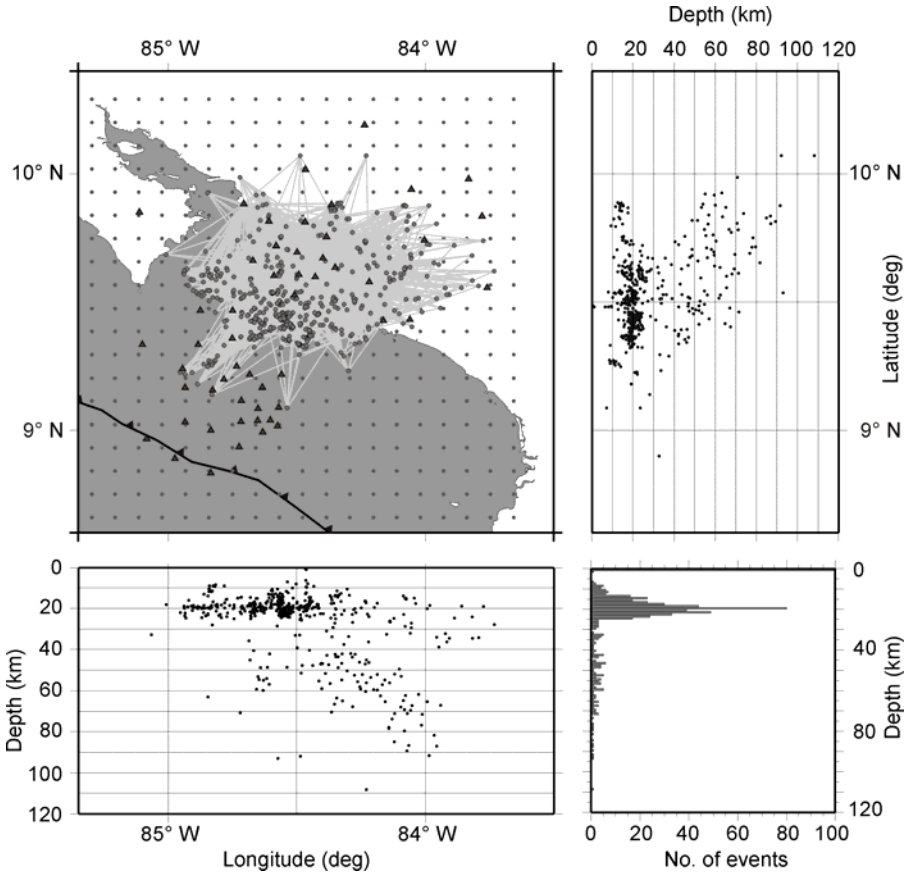

Figure 4.20. Hypocenter locations of 551 events selected for tomographic inversion, shown in map view and vertical cross sections in E-W and N-S directions. At the lower right corner, a histogram of hypocenter-depth distribution is included. Black triangles represent stations. Approximate ray coverage is shown by grey lines connecting epicenters and stations. Small circles denote final, 10 x 10 km^2 horizontal grid-node spacing. The axis of the Middle America Trench is indicated by a dented line.

As described for the Vp inversion, checkerboard synthetic tests for Vp/Vs were performed to explore the resolution ability and the amount of blurring in the dataset. Anomalies with input amplitude of 1.51/1.85 and encompassing two and single grid nodes were designed following again Husen *et al*. (2004). Figure 4.21 displays the results of one of the tests for each anomaly size. As expected from the geometrical distribution of sources and receivers, considering the lack of coverage for S-wave within the ocean-bottom network, anomaly recovery is good onshore, in the sector coincident with the three-component Reftek stations from the temporal land network, and between 8 and 40 km depth. A significant amount of vertical velocity smearing is found within the first 10 km in depth. Horizontal velocity leakage to the southwest is substantial between 15 and 25 km depth, and to the southeast at 40 km depth.

The inversion results are displayed in Figure 4.22. In general, Vp/Vs ratios resulting from the inversion are higher than the starting values for depths shallower than ~40 km and slightly lower at deeper levels. The more conspicuous anomaly, highest ratios (~1.9) appear at 15-25 km depth offshore, close to the border of the resolved area and could be affected by velocity blurring, as shown by the checkerboard test (Figure 4.21).

In the case of the Jacó network, the lower quantity of S-wave data usual in earthquake catalogues has been aggravated by the malfunction of the seismometers installed offshore. The area of good resolution is further diminished in view of the checkerboard tests results. The lack of the continuity of the resolved area at different depths hinders the interpretation of variation across the margin. In conclusion, the information obtained from Vp/Vs seems to be, unfortunately, not reliable enough to contribute in the evaluation of the configuration of the margin.

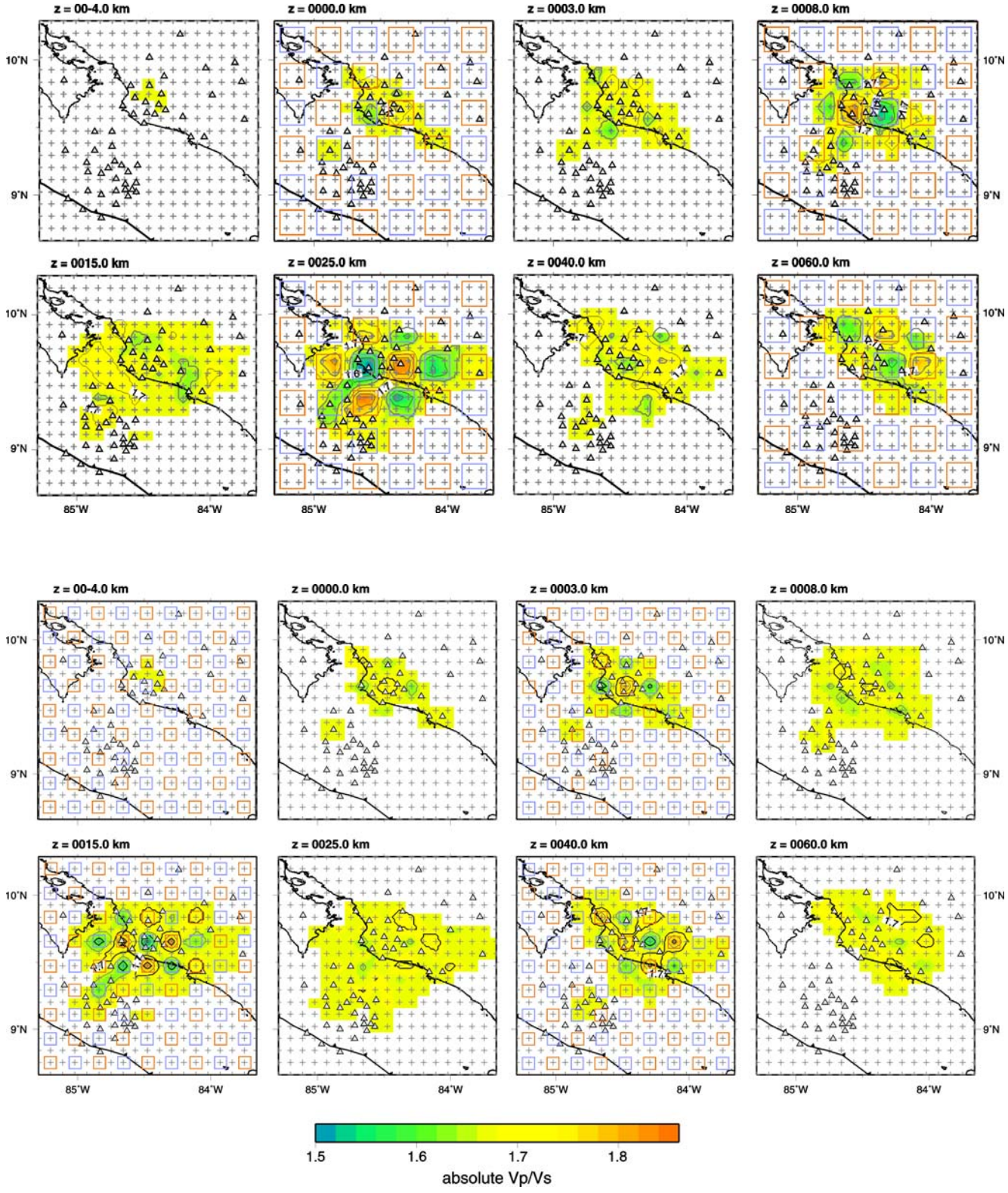

Figure 4.21. Examples of synthetic checkerboard test for assessment of solution quality. Recovered model is shown in plane views at different depths (see text for explanation). Locations of high (1.85) and low (1.51) Vp/Vs input anomalies are shown by red and green squares respectively. Small crosses represent grid nodes of the model parameterization, grey triangles denote seismic stations. The axis of the Middle America Trench is indicated by a dented line.

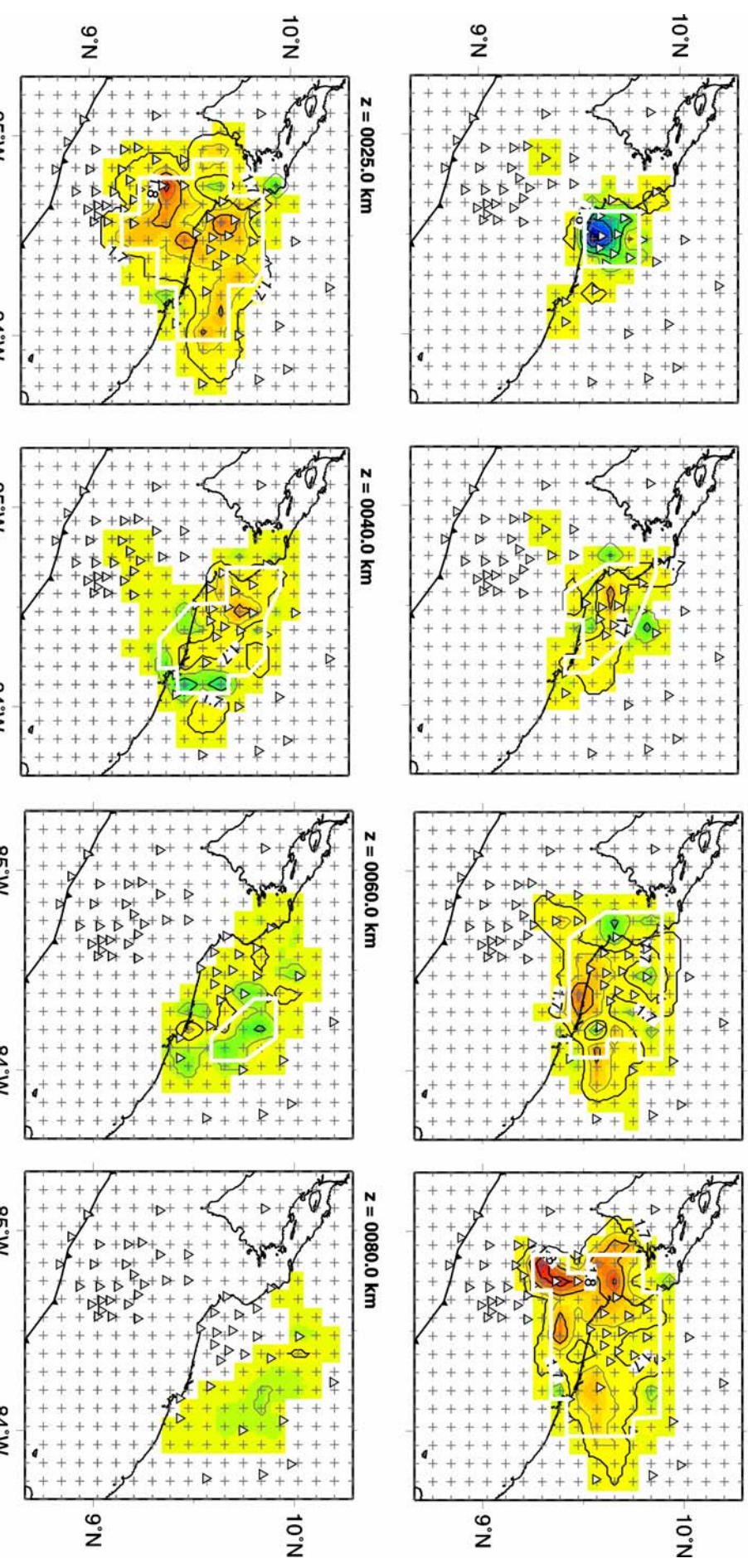

Figure 4.22. Tomographic results of 3-D Vp/Vs inversion shown in plane view at different depths. Areas with no ray coverage are masked. Thick white lines contour areas of fair resolution as indicated by analysis of several criteria. Triangles represent stations and small crosses denote grid nodes. The axis of the Middle America Trench is indicated by a dented line.

Chapter 5

Seismotectonic interpretation

As pointed out by Eberhart-Phillips (1993), "one of the primary benefits of local earthquake tomography in earthquake source regions is the joint interpretation of the 3-D velocity structure, earthquake hypocenters, and fault-plane solutions". The author adds that together, they yield the most through and precise picture of the structure and deformation that can be obtained from arrival time data for a region.

Three categories of seismicity are commonly originated at subduction zones (Lay & Wallace 1995). The diving of an oceanic plate beneath the overriding plate creates a zone of contact between both where frictional sliding takes place, generating interplate seismicity. The largest earthquakes of the planet occur here. The second type of seismicity results from the internal deformation of the overriding plate. The third category is induced by deformation on the subducting slab, as it sinks and interacts with the surrounding mantle. The deeper intraslab seismicity is known as Wadati-Benioff zone (WBZ). Additionally, during the last decade, a set of strain-release processes which manifest as slow and silent earthquakes, continuous and episodic slip and non-volcanic seismic tremors, have been modelled and/or detected, contributing to construct a more complex, but improved, view of subduction zones (Schwartz & Rokosky 2007).

In this chapter, the historic seismicity of the Central Pacific segment of Costa Rica and the seismicity generated at the plate interface and at the oceanic and overriding plates recorded during the Jacó experiment are described, and their origin compared to current hypothesis derived from other studies in convergent margins. Special attention is conceded to the extension of the seismogenic zone, being the area of the margin where the most damaging earthquakes are generated. It also produced the most abundant seismicity during the recording time of the experiment. The Central Pacific segment off Costa Rica generates hazardous events which have severely affected not only the towns in the coastal areas, but also poses a moderate risk due to

site effects (Montero & Climent 1990) for the most populated region of the country, the Central Valley, located less than 100 km away from the epicenters of the last large earthquakes generated in this segment.

The 3-D velocity structure of the margin derived in this study and presented in chapter 4 provides the basis for interpretation of the observed seismicity. As discussed before, the structure of this segment of the margin reflects the complexity associated to subduction of ocean-floor morphology and the transition from normal to thickened subducting oceanic crust. The subducting slab is imaged as a high-velocity perturbation with a band of low velocities (LVB) on top encompassing the intraslab seismicity deeper than ~30 km (Figure 4.17). A relatively abrupt, eastward widening of the LVB is observed and has been attributed to the subduction of hotspot modified, thickened oceanic crust. The thickening is accentuated by the presence of a big seamount or plateau (anomaly i, Figure 4.17). Landward, it coincides with the onset of an inverted forearc basin onshore and the appearance of an aseismic low-velocity anomaly (anomaly ii, Figure 4.17) beneath the inner forearc. The latter concurs spatially with a sector of the subaerial forearc where differential uplift of blocks has been described (Fisher *et al.* 1998, Marshall *et al.* 2000), suggesting tectonic underplating of eroded material against the base of the upper-plate crust. Alternatively, the low velocities could be induced by an accumulation of upward migrating fluids.

5.1 Seismicity in the Costa Rican Central Pacific segment

Tectonic differences along the Nicaraguan - Costa Rican margin have been recognized long ago. From advances on marine research and seismology in the last decades, segmentation along the margin have been further characterized with studies about the variation on the seismogenic and Wadati-Benioff zones (Burbach *et al.* 1984, Morales 1985, Güendel 1986, Protti *et al.* 1994, von Huene *et al.* 1995).

Using the catalogue of one of the permanent seismological networks in Costa Rica, Ovsicori from the Universidad Nacional de Costa Rica, and data from a network in Nicaragua, Protti *et al.* (1994, 1995a) imaged the geometry of the seismically-active subducting slab, from a steep dipping portion reaching up to 220 km beneath Nicaragua to a slab seismicity shallower than 50 km in southeastern Costa Rica. Those authors proposed the existence of a contortion on the slab, the Quesada Sharp Contortion (QSC), a landward projection of the Fisher Ridge, between northern and central Costa Rica (Figures 1.1 and 5.1). The QSC is distinguishable only below 70 km depth and separates a portion of the slab dipping at 80° and seismically active down to 200 km depth in northern Costa Rica, from a portion diving with an angle of 60° and reaching maximal depths of 125 km in the central part of the country. Husen *et al.* (2003a) found only weak tomographic evidence of the existence of the QSC. Those authors do also observe the gradual decrease on maximum depth from northern to southern Costa Rica.

Protti *et al.* (1994) explained the along-strike diversity on the WBZ geometry as the result of abrupt age variations of the Cocos Plate, which reach 5-10 m.y. or more at the tip of the slab across the QSC, with the argument that older lithosphere should show a deeper transition from brittle to ductile deformation. Petrologic and tomographic modelling from Husen *et al.* (2003a), on the other hand, favours enabling of the intermediate-depth seismicity within the Cocos Plate by dehydration, which stops at ~130 km and ~100 km beneath northern and central Costa Rica, respectively, where the age difference is 10 m.y. Underneath southern Costa Rica, where the subducting plate is only 2 m.y. younger than in the central part (Barckhausen *et al.* 2001), it stops at ~50 km. Although earthquake data for southeastern Costa Rica are scarce due to a reduced station coverage (Arroyo, 2001) and a lower seismicity rate (Figure 1.1), situation that prevented good LET resolution there, Husen *et al.* (2003a) rather subscribe to the previously suggested possibility that a slab window may have formed beneath southeastern Costa Rica (Johnston & Thorkelson 1997, Abratis & Woerner, 2001). Such window would heat the slab, reducing the depth of eclogite formation and causing the shallowing of the WBZ. The thermal modelling from Peacock *et al.* (2005) along the Nicaraguan and Costa Rican margin found only minor along-strike variations in the thermal structure. They suggest that these variations are more likely related to regional differences in slab stresses, sediment subduction, crustal structure and the distribution of hydrous minerals in the incoming lithosphere.

The effects of subduction of different ocean-floor morphological domains have also been invoked to account for variations in the margin structure observed along the MAT (Protti *et al.* 1994; von Huene *et al.* 1995, 2000), as discussed before. This influence seems to include the degree of coupling between the plates. Protti *et al.* (1994) delineate three segments with varying coupling in Costa Rica: from Papagayo Gulf to the end of the Nicoya Peninsula, from the entrance to the Nicoya Gulf to the northwest Osa Peninsula, and from Osa Peninsula to the Panama Fracture Zone. Historic, very large (M > 7.5) underthrusting earthquakes have occurred in northwest and southeast Costa Rica, but not on the central segment. In the area of the Nicoya Peninsula, subduction of smooth ocean floor promotes a larger continuous area of contact between plates; in southern Costa Rica, the presence of the shallow Cocos Ridge, causes moderate coupling able to generate events with magnitudes up to Mw 7.4. In contrast, the rough relief of the seamount domain (Figure 5.1) reduces the coupling to patches that break generating moderate earthquakes in Central Costa Rica (Protti *et al.* 1994). A good example of the segmentation in coupling is given by the 1990 Mw 7.0 Cóbano earthquake, an event that took place on the western end of the Central segment (Figure 5.1) and whose aftershocks did not propagate into the Nicoya segment. The 2002 Mw 6.4 Osa sequence, recorded by the Jacó network (Figure 5.1), is another example from the eastern limit of the same segment.

Evidence from the influence of seafloor roughness on the rupture behaviour of megathrust earthquakes is presented by Bilek *et al.* (2003). Those investigators analyzed the rupture histories of the 1983 Mw 7.4 Golfito, 1990 Cóbano and 1999

Mw 6.9 Quepos earthquakes (Figure 5.1). Cóbano and Quepos events took place on the area where the seamount domain is subducting; the correspondence between their rupture history and size and the presence and dimensions of bathymetric highs observed close to the trench, indicates a linkage between both. The 1983 earthquake, nucleated on the seismogenic zone opposite to the Cocos Ridge, shows a more complex rupture history and a longer source duration. Bilek *et al.* (2003) consider that the event was associated to rupture on the crest of the Cocos Ridge, with additional southeastward rupture propagation.

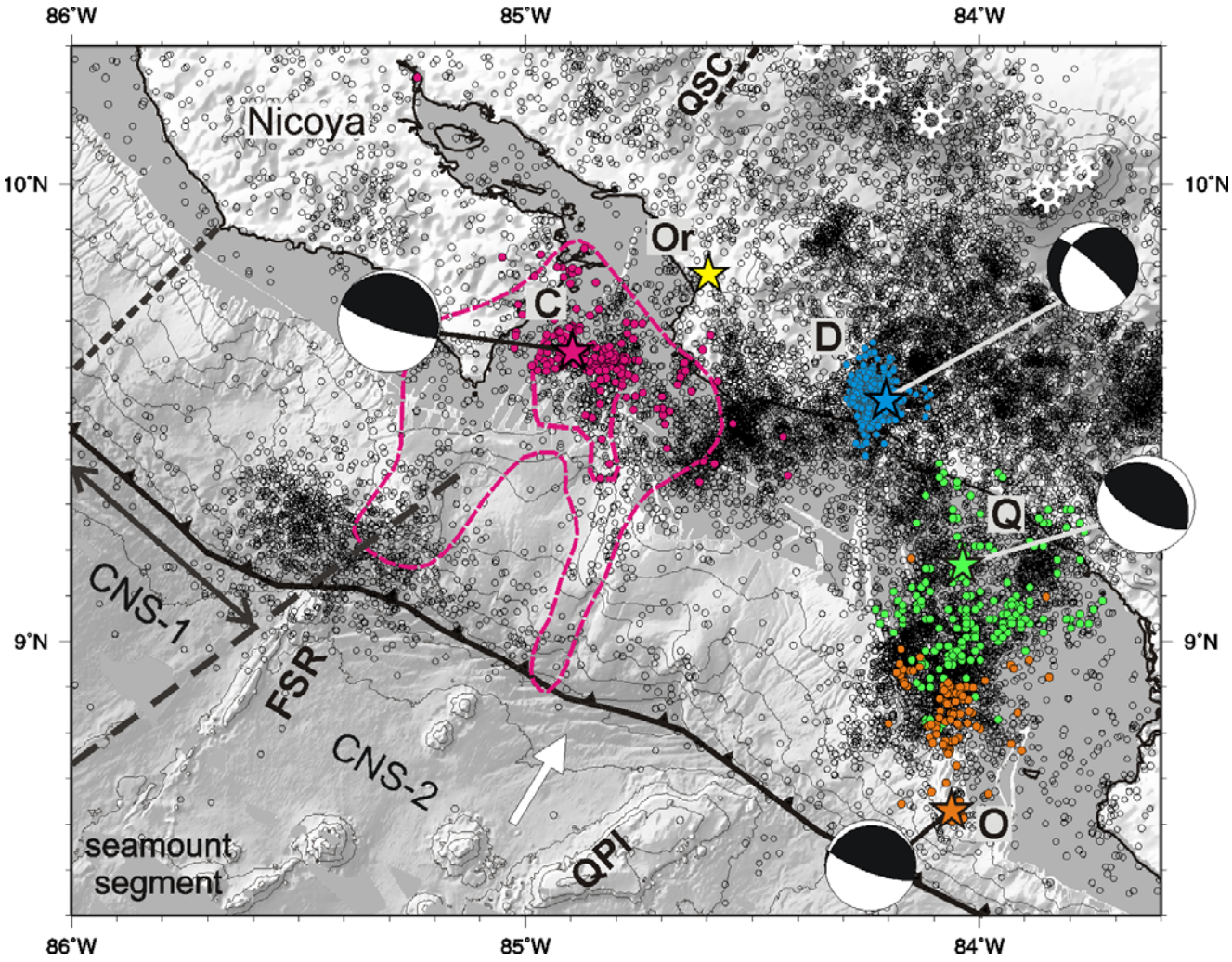

Figure 5.1. Seismicity recorded by the RSN on the period 1992-2007 (open circles), and large earthquakes (Mw > 6.4) nucleated on the seismogenic zone and the inner forearc in the last century. Events from the RSN catalogue recorded by at least six stations and a rms < 1 are shown. Mainshock and one-month aftershocks (in magenta) of 1990 Mw 7.0 Cóbano event (marked C) from Husen *et al.* (2002), and aftershocks area (dashed lines) after ~16 hours and 69 days from Protti *et al.* (1995b). Mainshock from 1999 Mw 6.9 Quepos (Q) from Bilek *et al.* (2003) and aftershocks (in green) from DeShon *et al.* (2003). Sequence of 2002 Mw 6.4 Osa (O; in orange) according to preliminary locations with observations from Jacó and RSN networks. Location of the mainshock for the 1924 Ms 7.0 Orotina sequence (Or) after Montero (1999). Mainshock and aftershocks (in blue) of 2004 Mw 6.4 Damas (D) activity from Pacheco *et al.* (2006). Harvard centroid moment-tensor solutions are shown. Bathymetry (exaggerated), including contours every 500 m, and main tectonic segments after von Huene *et al.* (2000) and Barckhausen *et al.* (2001), respectively. Radiating circles represent Holocene volcanoes. QSC: Quesada Sharp Contortion after Protti *et al.* (1994), FSR: Fisher Seamount and Ridge, QPl: Quepos Plateau, CNS: segments of the Cocos Plate oceanic crust generated at the Cocos-Nazca Spreading Center.

Seismicity recorded by the RSN from 2007 back to 1992, the year where digital recording started, is displayed in Figure 5.1. Although location uncertainties could be high offshore, three separated areas of earthquake concentration on the Central Pacific region can be distinguished: at the entrance of the Nicoya Gulf, offshore the Herradura Promontory, and offshore the coastal segment between the localities of Quepos and Uvita (Figure 1.3 or 5.2 for localities). Large underthrusting earthquakes associated to rupture of bathymetric highs have been generated in recent years coinciding with the first and third areas. In this study, the LET have revealed the existence of a big seamount or plateau offshore Herradura (chapter 4).

5.1.1 Large earthquakes

Eight events with magnitude higher than Mw 6.4 have been originated on the Central Pacific segment of the Costa Rican margin since the end of the XIX century. Six of them (in 1882, 1939, 1952, 1990, 1999, 2002) have been associated directly to the seismogenic zone, while the remaining two (1924, 2004) nucleated at the inner forearc, in the upper plate.

On March 25, 1990, the Mw 7.0 Cóbano earthquake ruptured at the entrance of the Nicoya Gulf (Figure 5.1). The earthquake caused large damage to civil structures, landslides and liquefaction, but fortunately no casualties, reaching intensities of VIII (Modified Mercalli) in a radius of 60 km around the epicenter, VI in San José. As mentioned before, the event took place at the northwest border of the Central Costa Rica seismic region (Protti *et al.* 1994), and a sequence of foreshocks was recorded 16 hours before the mainshock. Analyzing the source-time function of the latter, Protti *et al.* (1995b) determined that it was dominated by two sources: the first was impulsive and the second, emergent, suggesting the rupture of an asperity and propagation to a weaker zone southeastward. Based on this and the rough-relief subducting seafloor in this area, Protti *et al.* (1995) proposed that the earthquake was caused by the rupture of a subducted seamount. Husen *et al.* (2002) performed a LET in the area that revealed a low-velocity anomaly at around 30 km depth, overlain by a high-velocity zone at 20 km depth, which they interpreted as a seamount, possibly belonging to the Fisher Ridge chain (Figure 5.1).

The aftershocks distributed mainly to the southeast, inside an area of less than 600 km^2 in the first day after the main event. Figure 5.1 includes the mainshock and the first month of aftershocks of the Cóbano sequence form Husen *et al.* (2002), relocated in their 3-D P-wave velocity model, and the aftershocks area after ~16 hours and after 69 days according to Protti *et al.* (1995b), who used routine location and an 1-D velocity model. This last distribution of aftershocks is commented on later. The mainshock rupture area defined by the aftershocks relocated by Husen *et al.* (2002) nearly coincides with the imaged subducted seamount.

Given the similarities in reported intensities and damage, Protti *et al.* (1995b) suggest that two more large earthquakes, in 1882 and 1939, could have ruptured the same region as the event in 1990, yielding, in a very rough estimate, a recurrence period of 54 years for the Nicoya Gulf entrance sector.

A Mw 6.9 underthrusting earthquake occurred on 20 August 1999 southwest and offshore the Quepos Promontory (Figure 5.1). It was preceded by a Mw 5.5 foreshock on August 10 (Güendel & Protti 1999, DeShon *et al.* 2003). Bilek *et al.* (2003) determined the rupture history of the earthquake using several techniques. They estimated an optimal depth of 21 ± 4 km and a very simple moment-release history, with most of the moment liberated during the first 10 s. Empirical Green's function deconvolution of surface and body waves suggests a rupture length of ~16-20 km with southeast azimuth from the epicenter. Body-wave inversion provided a very simple rupture-time function, with two main pulses of moment release in the first 10 s. An "amphibian" seismological network was installed on the area 19 days after the mainshock and was recovered at the end of November 1999. Analyzing the aftershocks distribution (Figure 5.1) through relocation techniques, DeShon *et al.* (2003) found that a good coincidence with the width of the mainshock rupture determined from waveform inversion by Bilek *et al.* (2003) and with the along-strike width of the Quepos Plateau.

Locations from the ISS and from Güendel (1986), together with a study of macroseismic observations from Montero and Climent (1990), suggest that a Ms 7.0 earthquake that took place on September 1952 could have been originated offshore Quepos, where it caused maximal intensities of VII-VI (Modified Mercalli). Montero & Climent (1990) propose that also the afore mentioned event from 1882 might have been nucleated on the same area.

At the west side of the Herradura Promontory, in the inner forearc, a Ms 7.0 earthquake took place on March 4, 1924 (Figure 5.1). The event generated maximal intensities between VIII and IX (Modified Mercalli) in the towns of Orotina, San Mateo, San Ramón and Esparza, causing great damage. The aftershocks included several events with Ms magnitudes between 5.0 and 6.4. Through a detailed neotectonic study, combined with the analysis of the intensity distribution and coseismic effects, Montero (1999) attributes the earthquake to rupture along the Tárcoles fault and possibly along the abutting Bijagual fault system. These faults trend northeast and north, and have been ascribed to the Central Costa Rica Deformed Belt (Marshall *et al.* 2000, Montero 2001). The Tárcoles fault delimits the Herradura Promontory to the west (Figure 1.3), and it is part of the trench-perpendicular fault system crossing the inner forearc and accommodating differential uplift (Marshall *et al.* 2000). In 1989 a seismic sequence originated in the same area as the Orotina earthquake, causing extensive damage in Central Costa Rica.

On 20 November 2004, a Mw 6.4 earthquake occurred beneath the forearc as well, close to the towns of Parrita and Quepos (Figure 5.1). Damage in the coastal localities was extensive, associated mainly to liquefaction and ground failure in Parrita and the

nearby Damas Island. Maximal intensities of VII (Modified Mercalli) were observed in the epicentral area. Pacheco *et al.* (2006) located the event and its aftershocks using the double-difference algorithm of Waldhauser & Ellsworth (2000) and reported a depth of 24 km for the main shock, which place its rupture in the lower crust of the overriding plate (Figure 4.17). The study included a regional moment-tensor inversion which shows a strike-slip mechanism with a large normal dip-slip motion for the main event (Figure 5.1), while the largest aftershocks exhibit different mechanisms. Aftershock locations were distributed between 15 and 25 km, with a peak in their distribution at about 18 km, and do not delineate a preferable plane. Using teleseismic P wave and local strong-motion records, the authors inverted for slip distribution, which resulted similar in both nodal planes, resembling a simple circular rupture. The rupture lasted ~6 s and broke a circular asperity with a radius of 8 km.

The size of the event, the limited resolution from teleseismic data and the poor distribution of near-field and regional stations hindered the recognition of the fault plane. Although they do not rule out the conjugated, Pacheco *et al.* (2006) prefer the nodal plane that shows the same orientation as the left-lateral faults predominant on the inner forearc. Based on depth distribution of aftershocks, depth of the top of the slab from previous works, mainshock hypocenter and its slip distribution, and Quaternary faulting at the surface, the authors suggest that deformation takes place through the entire crustal thickness, possibly caused by seamount subduction and strong basal friction on the upper plate, due to subduction of a thick, young, and buoyant oceanic plate, rough seafloor, and underplating of large seamounts.

5.2 Seismicity during the experiment

In order to aid visualization and discussion of results, contours representing the top of the subducting slab at different depths, as interpreted in this study, have been projected onto the profiles crossing the tomographic model, e.g. Figure 4.17 and, later, Figure 5.5. For their construction, several cross-sections along the entire portion of the margin imaged here, separated by 5 km from each other, have been examined. The position and depth of the trench axis (3.3-3.7 km), the absolute velocities and the velocity perturbations, as well as the distribution of the intraslab and interplate seismicity, were considered. The wide-angle profile model of Ye *et al.* (1996) predicts velocities between 5.0 and 5.5 km s^{-1} for the upper crust of the subducting plate offshore the Herradura Promontory. In the tomograms, the distribution of those values matches the plate geometry suggested by the interplate seismicity (Figure 4.17). This definition of the top of the subducting plate serves also to distinguish the seismicity from the three source areas in the margin, described in the next sections.

In the definition of the top of the slab and for interpretation, the earthquake location uncertainties obviously play a relevant role. The algorithm used by SIMULPS provides standard error estimates for the hypocenters. The mean values for the dataset

used for the tomography in this study are 0.09 s in origin time, 0.44 km in east and north directions, and 0.93 km in depth.

The application of non-linear probabilistic earthquake relocation in different tectonic scenarios has shown that, in general, well constrained hypocenter locations are obtained when more than six P-wave observations are available in a good azimuthal distribution (GAP < 180°); furthermore, focal depths are not well constrained without a station located within a distance similar to the focal depth, regardless of the total number of observations (Husen *et al.* 2003b, Husen & Smith 2004). Previous to the inversion, the dataset selected for the LET in this study was chosen following those observations, hence, well-constrained locations are expected.

Relocation of shots and blasts provides a good opportunity to estimate the absolute error in hypocenter locations. Within the frame of the Jacó experiment, a land explosion was planned and successfully carried out. For "Montelimar" explosion, ~600 kg of explosive were used in a river bed in the Herradura Promontory, at around 300 m above sea level and ~3.5 km away from station *sni*. It was recorded with variable quality by 28 stations of the combined array Jacó-RSN, including two stations located at the trench and one station in the volcanic arc. Figure 5.2 shows the location of the explosion, and the maximum ray coverage achieved. Relocation of the event using the 3-D velocity model derived in chapter 4 yielded very good results. Using the total 28 readings, the epicenter was relocated 700 m away from the real value, and the hypocenter at 7 km depth. A relocation including only the 19 readings with weight 0 or 1 (see chapter 3 for an explanation of the readings weighing scheme) yielded the epicenter 500 m away of the measured position and a depth of 6.5 km. A third relocation, including only 9 readings from Jacó land stations positioned the epicenter 400 m away of the real value and the hypocenter at 5 km depth. The errors expected from relocation of shots performed at the surface are much larger than those associated to earthquakes happening at greater depths, because in the first case the waves travel twice through the highly heterogeneous structure of the first kilometers of the ground which are only poorly modelled with LET. Moreover, the nearest station to the explosion is forcibly located much farther than the focal depth, thus increasing the uncertainty. From this test, a very conservative, upper-limit hypocentral error of ~5 km could be estimated for earthquakes resulting from the tomography.

As described in chapter 4, only the 595 best-quality earthquakes were included in the tomography. But since the interest of this chapter is to discuss general seismicity patterns, the rest of the seismic activity recorded by Jacó network has also been examined. This is particularly relevant for the definition of the updip limit of the seismogenic zone and the characterization of seismicity offshore the Parrita lowlands, as discussed on the following. Thus, events recorded by at least six stations and with a GAP of 220° or less have been relocated using the 3-D P-wave velocity model of the margin determined during this work. Some 300 events fulfilled the selection criteria and are included in the figures with different symbols. However, it must be noted that location uncertainties of these events, particularly on hypocentral depths, are higher

than those included in the tomography dataset. Consequently, no interpretation is based on these events.

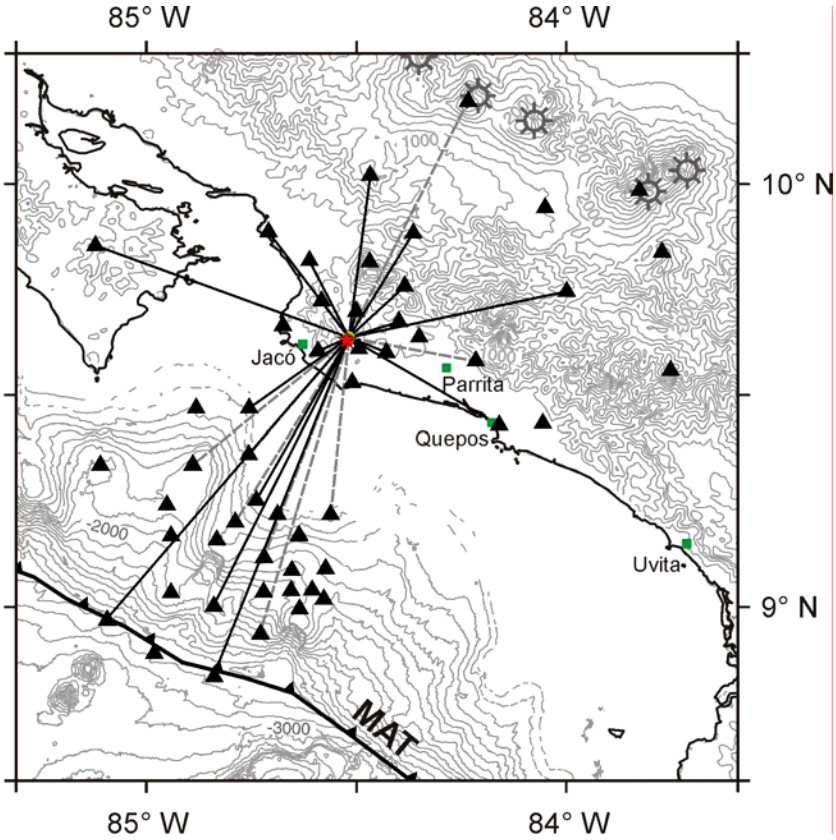

Figure 5.2. Location and ray coverage of "Montelimar" explosion. The event was planned within the Jacó experiment. The red star represents the measured location of the explosion. It was recorded by 28 stations (triangles). Ray paths in grey indicate observations not used for the second relocation (see text for explanation). Bathymetry (von Huene *et al.* 2000) and topography (Smith & Sandwell 1997) contours every 200 m. Radiating circles denote Quaternary volcanoes. MAT: Middle America Trench axis.

5.2.1 Determination of focal mechanisms

First-motion, double-couple focal mechanisms were determined for earthquakes with magnitudes between 1.9 and 4.3 M_L, generated on the three source areas of the margin. They are displayed in Figure 5.3 and listed in Table 5.1. The focal mechanisms were determined using the version of the program FOCMEC (Snoke *et al.* 1984, Snoke 2003) included in the version 8.1 of the SEISAN software package (Havskov & Otemoeller 2005); the program uses P-wave polarities and amplitude ratios (SV/P, SH/P, and SV/SH) as input. Given the good station coverage, the knowledge about the velocity structure gained through the modelling presented here, and by using clear P-wave first arrivals, reliable estimate for the fault-plane solutions were obtained. Solutions are based on P-wave arrival polarities; amplitude ratios from the three-component stations of the Jacó network were used with caution to further constrain the range of equally good solutions for the events. Take-off angles were calculated in a layered medium. On average, there are 25 P-wave polarities per event; polarity distribution and all possible solutions for each earthquake are included in the appendix. S-wave amplitudes were read from the radial (SV) and the transverse (SH) components of the seismographs. The search for solutions is controlled by the following selection parameters: number of allowed polarity errors (no more than 3 in

this study), an acceptable range for deviations between observed and calculated amplitude ratios (0.2 in this case), the number of ratio errors allowed to be outside that range (no errors accepted), and the fineness of the search in degrees (5°). The quality of the focal mechanisms has been classified according to the number of available polarities, their azimuthal distribution, the number of polarity errors and number of the possible solutions (Table 5.1, appendix). The focal mechanisms are discussed in the next sections, together with the seismicity of each source area.

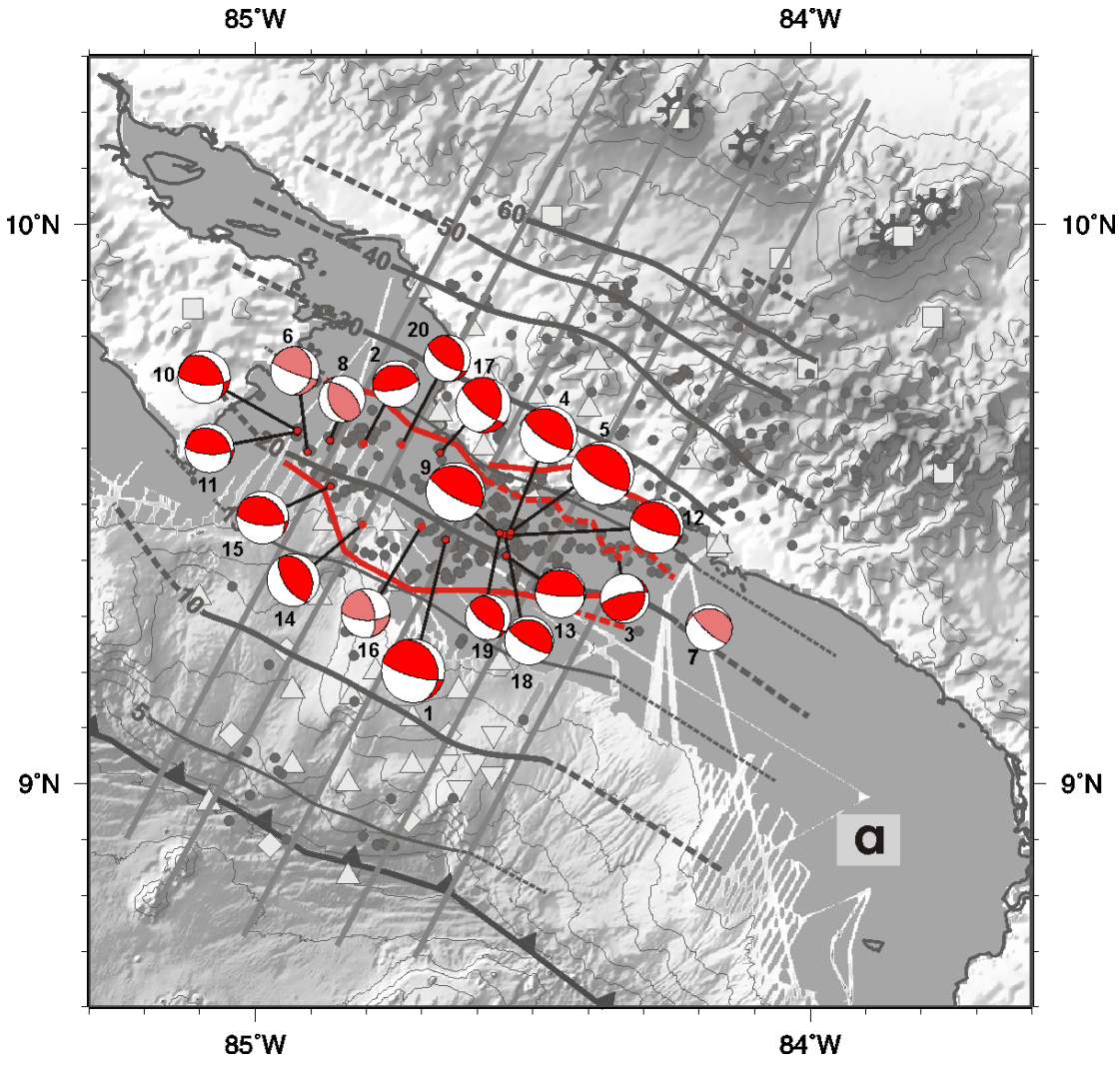

Figure 5.3. First-motion, double-couple focal mechanism solutions determined in this work for events nucleated at a) the plate interface, b) the oceanic slab, and c) the upper plate. Lower hemisphere stereographic projection, solid quadrants are compressional. Numbers follow numeration in Table 5.1. Shading indicates solution quality, from bright colours for best to faded tones for lesser quality (Table 5.1). Contours of top of the slab as determined in this study are shown. Red lines on a) denote the limits of the seismogenic zone (see text); brown lines on c) denote faulting after compilation from Denyer & Alvarado (2007). Lines perpendicular to the trench axis represent cross-sections 1 to 5 (from west to east) displayed in Figures 4.17 and 5.5.

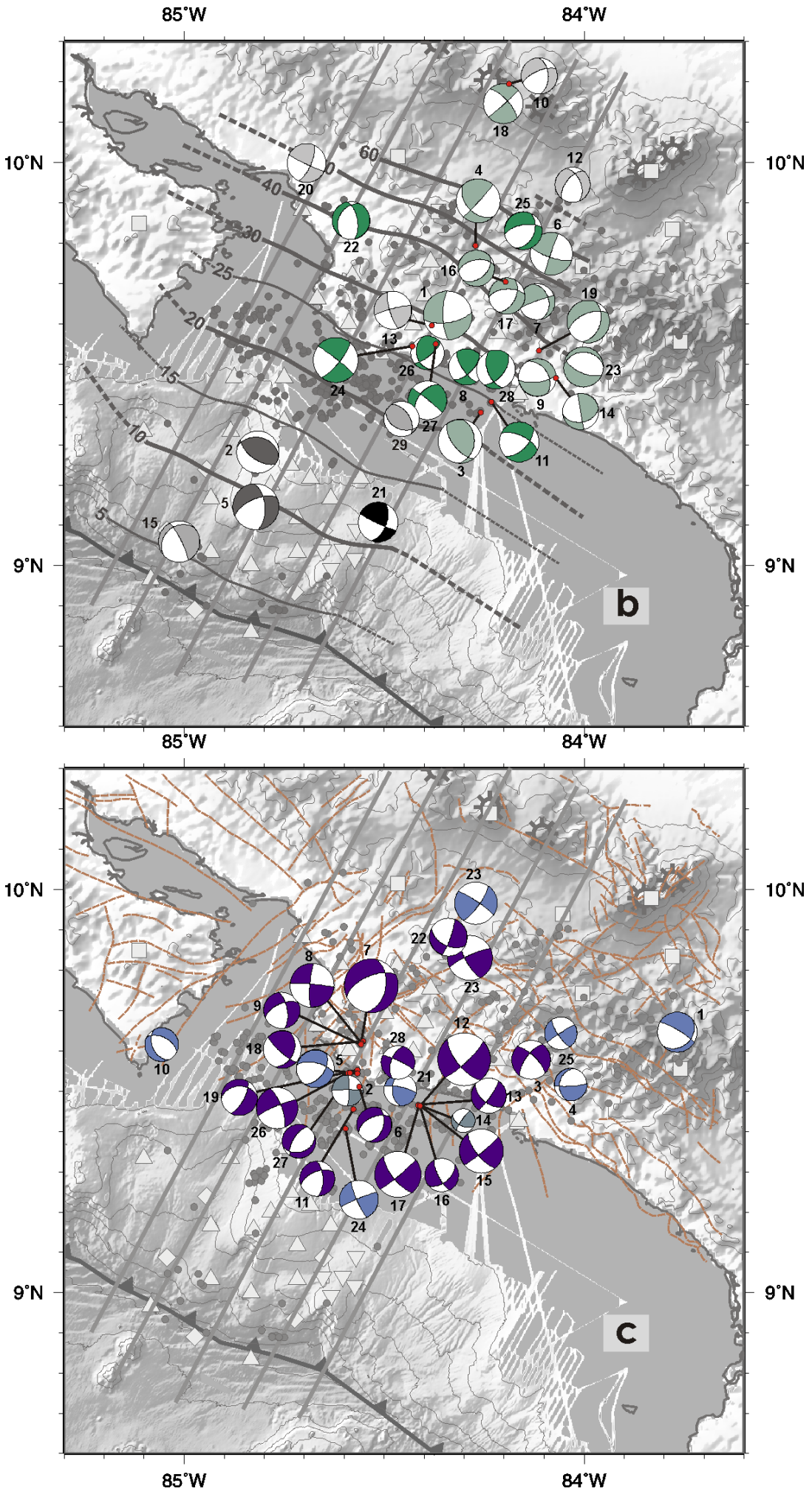

Figure 5.3
(continuation)

Table 5.1. First-motion, double-couple focal mechanisms determined in this study (Figure 5.3). Solutions for events belonging to a swarm are indicated in bold letters.

No.	Date yymmdd	Time hhmm	Longitude [° W]	Latitude [° N]	Depth [km]	M_L	Strike [°]	Dip [°]	Rake [°]	Class
Plate interface:										
1	020510	0906	84.659	9.439	21.2	3.7	343	25	145	A
2	020519	1432	84.806	9.610	23.7	2.7	274	21	104	A
3	020520	1223	84.348	9.408	25.7	2.8	28	21	44	A
4	020523	0930	84.542	9.452	22.9	3.3	318	21	104	A
5	020523	2122	84.542	9.452	22.8	3.7	318	21	104	A
6	020606	2033	84.908	9.595	19.7	2.8	7	32	163	B
7	**020611**	**2344**	84.185	9.280	26.3	2.7	264	21	44	B
8	020623	1950	84.867	9.616	21.8	2.7	161	42	113	B
9	020703	2207	84.562	9.451	22.3	3.4	300	15	90	A
10	**020706**	**1800**	84.925	9.633	22.7	3.0	327	35	138	A
11	**020706**	**2009**	84.926	9.631	22.9	2.8	313	25	128	A
12	020802	0516	84.543	9.446	22.1	3.1	324	18	124	A
13	020802	0728	84.549	9.410	21.3	2.9	301	11	117	A
14	020807	0008	84.808	9.466	18.1	3.0	339	30	100	A
15	020814	0534	84.866	9.534	20.7	3.0	312	29	122	A
16	020814	1953	84.703	9.463	19.3	2.8	348	61	152	B
17	020818	1838	84.668	9.594	25.0	3.2	13	36	149	A
18	020831	1304	84.552	9.447	22.0	2.8	282	16	71	A
19	020831	1728	84.562	9.449	21.9	2.6	343	29	122	A
20	020908	0812	84.738	9.608	24.9	2.7	349	32	131	A
Intraslab:										
1	020413	0259	84.343	9.620	42.0	3.9	81	66	-18	B
2	020426	2227	84.817	9.282	14.2	3.4	282	32	71	B
3	020428	1355	84.260	9.379	45.5	3.5	142	62	67	B
4	020505	0742	84.274	9.793	64.2	3.5	136	45	5	B
5	020514	2219	84.822	9.146	33.6	3.7	246	63	-37	B
6	020524	0425	84.084	9.773	77.9	3.4	108	75	-3	B
7	020526	0038	84.120	9.654	67.2	2.9	250	86	-55	B
8	020529	0819	84.296	9.492	46.5	2.9	146	71	30	A
9	020531	1146	84.119	9.466	49.5	3.0	328	42	-31	B
10	020606	0947	84.190	10.194	104.2	2.9	246	67	-46	C
11	020607	0400	84.234	9.406	46.4	3.2	295	63	-37	A
12	020614	0549	84.031	9.944	103.5	2.8	218	58	-48	C
13	020616	1804	84.383	9.595	42.1	3.0	255	83	13	C
14	020701	1432	84.073	9.465	64.6	2.9	170	90	50	B
15	020704	0246	85.014	9.059	20.5	3.3	225	27	-20	C
16	020705	0734	84.199	9.703	56.1	2.9	259	52	-71	B
17	020711	1930	84.195	9.668	55.2	2.9	267	58	-48	B
18	020712	1244	84.204	10.145	103.8	3.2	317	70	-4	B
19	020729	1511	84.115	9.533	56.2	3.4	246	59	-60	B
20	020806	0034	84.696	9.998	68.2	3.1	115	85	19	C
21	020810	0432	84.516	9.108	25.0	3.2	115	84	35	A
22	020810	0914	84.585	9.856	52.6	3.0	211	36	-54	A
23	020815	1609	84.004	9.492	70.3	3.2	114	65	-79	B
24	020823	1657	84.431	9.544	44.1	3.6	308	86	-14	A
25	020906	0734	84.154	9.830	68.3	3.0	260	64	-56	A
26	020917	1346	84.394	9.527	43.9	2.7	167	36	31	A
27	020924	1141	84.373	9.549	44.4	3.1	216	50	-4	A
28	020930	0034	84.223	9.486	49.9	3.1	159	55	45	A
29	021001	1356	84.458	9.364	30.3	2.8	117	42	67	C
Upper plate:										
1	020420	2342	83.769	9.645	17.6	3.2	301	81	-65	B
2	020423	0231	84.593	9.500	17.6	2.5	270	84	-8	C
3	020425	0701	84.134	9.576	26.1	3.1	216	67	-20	A
4	020626	0721	84.035	9.515	15.7	2.6	86	81	-60	B
5	020626	2355	84.568	9.542	19.9	3.0	283	64	-44	B
6	020702	0650	84.564	9.510	16.6	2.8	244	54	-59	A
7	**020715**	**1413**	84.559	9.615	15.1	4.3	246	60	-55	A
8	**020715**	**1732**	84.558	9.618	15.0	3.5	275	85	9	A
9	**020715**	**2108**	84.560	9.615	14.4	2.9	246	61	-28	A
10	020718	0337	85.058	9.614	13.9	2.7	154	44	-60	B
11	**020719**	**1415**	84.578	9.454	16.0	2.8	248	57	-33	A

Table 5.1 (continuation)

12	**020721**	**2131**	84.412	9.460	19.6	4.2	47	80	-23	A
13	**020721**	**2256**	84.417	9.462	19.5	2.8	34	82	-34	A
14	**020722**	**0624**	84.416	9.464	19.0	1.9	215	80	39	C
15	**020722**	**0625**	84.411	9.463	20.0	3.5	50	85	-19	A
16	**020722**	**0628**	84.411	9.461	20.3	2.7	51	54	-20	A
17	**020722**	**1910**	84.415	9.461	19.9	3.7	50	85	-19	A
18	**020731**	**2153**	84.554	9.622	15.9	3.0	132	78	54	A
19	020816	0648	84.568	9.551	16.2	2.9	268	38	-36	A
20	020828	1133	84.287	9.829	9.9	3.6	245	80	18	A
21	**020829**	**0503**	84.461	9.502	9.3	2.6	282	76	43	B
22	020902	1507	84.341	9.881	11.4	3.0	19	80	-39	A
23	020908	1518	84.272	9.965	16.3	3.4	36	77	8	B
24	020914	1920	84.598	9.406	19.3	3.1	247	85	9	B
25	020917	0437	84.060	9.642	26.7	2.6	237	87	15	B
26	**020925**	**0922**	84.591	9.544	12.9	3.3	247	82	-18	A
27	**020925**	**2158**	84.587	9.544	13.7	2.7	73	36	-54	A
28	020926	0957	84.467	9.570	19.2	2.7	199	56	-10	A

5.2.2 Interplate seismicity

5.2.2.1 Characterization

In general, the interplate seismicity occurs beneath the continental shelf (Figure 5.4), between 15 and 25 km depth and 55 to 80-85 km from the trench axis, in a well defined plane dipping 16-25°, steepening toward the east (Figure 5.5). It takes place within slab-top velocities of 5.0 to 7.0 km s^{-1}. Nevertheless, revealing medium-scale variations along the margin and a clear change toward the east are observed. The area generating interplate seismicity is wider offshore the Herradura Promontory, narrowing toward the west and decreasing and retreating landward to the east. This distribution closely resembles the variable morphology of the continental slope (Figure 5.4), which displays two big embayments, offshore the entrance to the Nicoya Gulf and Parrita-Quepos area, separated by a headland offshore Herradura (von Huene *et al.* 2000).

The onset of the interplate seismicity closely coincides with a rapid increase on the gradient of the absolute velocities along the plate boundary. This augment takes place toward the downdip end of the margin wedge, at velocities of ~5 km s^{-1} (Figure 5.5). This increase in absolute velocities has been mapped in Figure 5.4. Next, the bulk of the seismicity occurs along a decrease in the velocity gradient, ending toward the onset of the contour of 6.8-7.0 km s^{-1}. This velocity then continues further down in depth for around 20 km along the top of the slab, before the velocities start to increase again at ~40 km depth.

In the west and central sectors, the interplate seismicity is easy to distinguish visually, as a tightly packed clustering of hypocenters following a dipping alignment. It is located on top of the LVB at the upper part of the downgoing plate. This low-velocity anomaly broadens notably where the interplate seismicity occurs (profiles 2 and 3, for

example), as discussed in chapter 4. In the west sector (profiles 1 and 2), the rise of the interface seismicity coincides with the end of the low-velocity zone interpreted as the margin wedge and the start of the high velocities on the upper plate. This correspondence is less clear toward the center (profile 3), where the onset of the seismicity happens beneath the margin wedge. The downdip end of the interplate seismicity on the west sector is marked by an up-bending of the velocity contour of 7 km s^{-1} within the slab, while on the central sector the termination of the seismicity is less sharp, concurring with the appearance of low-velocity anomaly ii.

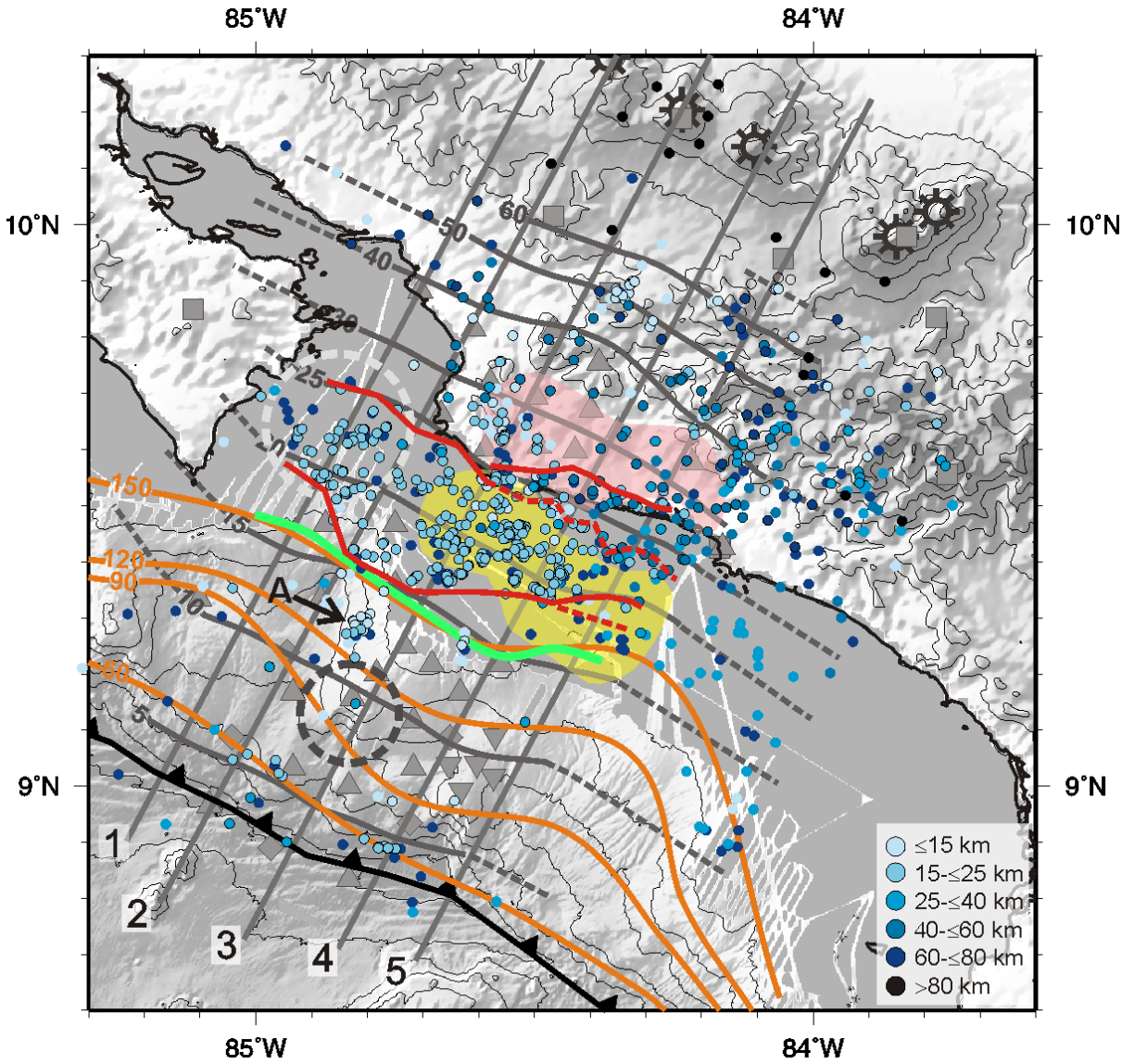

Figure 5.4. Seismicity recorded by Jacó network from April to October 2002. Focal depths are colour coded as noted. Epicenters from the dataset used for tomography have a black border. Grey bold lines are contours of the top pf the slab. Bold lines in orange represent the isotherms 60°, 90°, 120° and 150°C of temperatures at the plate boundary (Ranero *et al.* 2008). Red and green lines denote the limits of the seismogenic zone and the increase in velocity along the plate boundary, respectively (see text). Shapes in yellow and pink denote the extension of anomalies i (big seamount or plateau) and ii (beneath the inner forearc), respectively. Dashed circles mark the position of Cóbano (Husen *et al.* 2002) and Jacó seamounts. "A" indicates the seismic sequence of April 2002 (see text). Lines perpendicular to the trench axis represent cross-sections displayed in Figures 4.17 and 5.5.

On the east sector (profiles 4 and 5) the image is notoriously different. With a rapid change, along ~20 km offshore the Parrita lowland, the interplate seismicity begins almost 5 km deeper and ~10 km farther from the trench when compared to the central sector. These values are reduced to 3 km deeper and 5 km farther from the trench when taking into account the hypocenters of earthquakes not included in the tomography. Nevertheless, the seismic activity is significantly decreased, consisting of few scattered events, in contrast to the clear planar distribution of the abundant activity observed at the west and central parts of the area (Figures 5.4 and 5.5). The interplate seismicity starts at ~18 km depth with a cluster of few events, followed by two other clusters at around 26 and 30 km depth, ~7 and ~18 km further down along the plate interface, respectively (cross-section 5). The position of the second clustering is marked by a red dashed line in Figure 5.4, it concurs closely with the landward edge of anomaly i. The last cluster ends against the rising of the low-velocity anomaly ii. Interplate and upper plate seismicity distributes surrounding this anomaly, but no earthquakes were located inside.

There is a ~10-km wide transition zone between the central and the east margin configurations (profile 4). In this region, the interplate seismicity shows a more diffuse pattern around the plate boundary.

Several focal mechanisms (Figures 5.3a and 5.5) were determined for events whose origin is presumed at the plate interface. The quality is in general good, and all of them correspond with thrust-type events, reinforcing the interpretation of the position of the interplate seismicity.

Figure 5.5 (next pages). Cross-sections along the Central Pacific margin. Location of the profiles is indicated in Figure 5.4. Velocity structure is shown as percentage change relative to the minimum 1-D model (upper plot), interval of absolute Vp-velocity contours is 0.5 km s^{-1}, grey lines encompass areas of good resolution (see chapter 4); hypocenter locations (grey circles) projected onto the depth sections from within four km to each side, open circles denote events not included in the dataset for the tomography. In the lower plots interpretation of the model is displayed; note that the sketches include earthquakes projected from seven km to both sides of the section. Isotherms along the plate boundary after Ranero *et al.* (2008), burst-type swarms (magenta and blue circles) and focal mechanisms (equal-area projection onto the western hemisphere, solid quadrants are compressional). In profile 1, the star is the hypocenter from 1990 Mw 7.0 Cóbano earthquake after Husen *et al.* (2002). In profile 5, star and solid green circles are mainshock and aftershocks from the 2004 Mw 6.4 Damas sequence (Pacheco *et al.* 2006); aftershocks have been projected from four km to each side of the section. Geologic units (text in grey over the plots) as indicated in Figure 1.3.

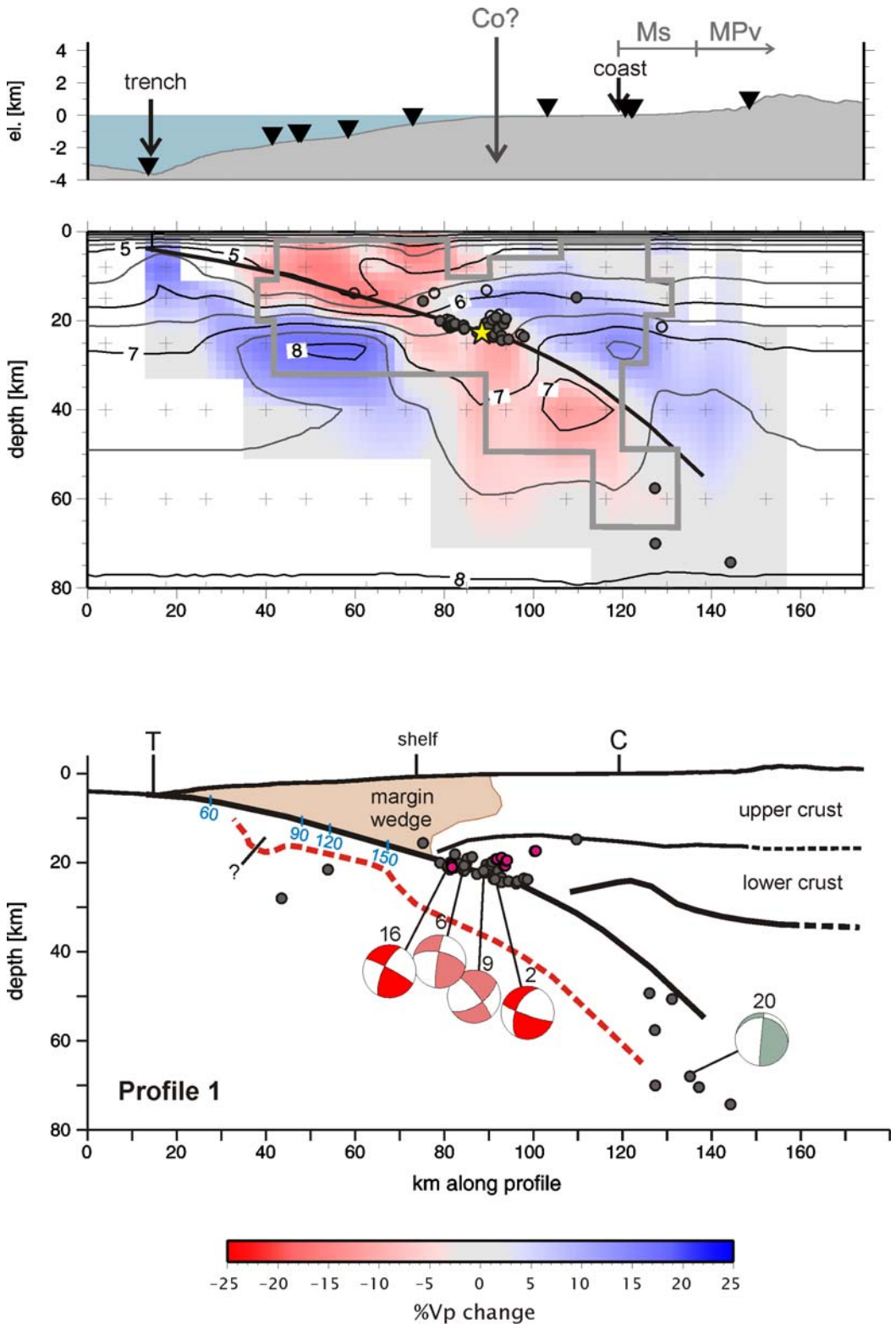

Figure 5.5 (continuation)

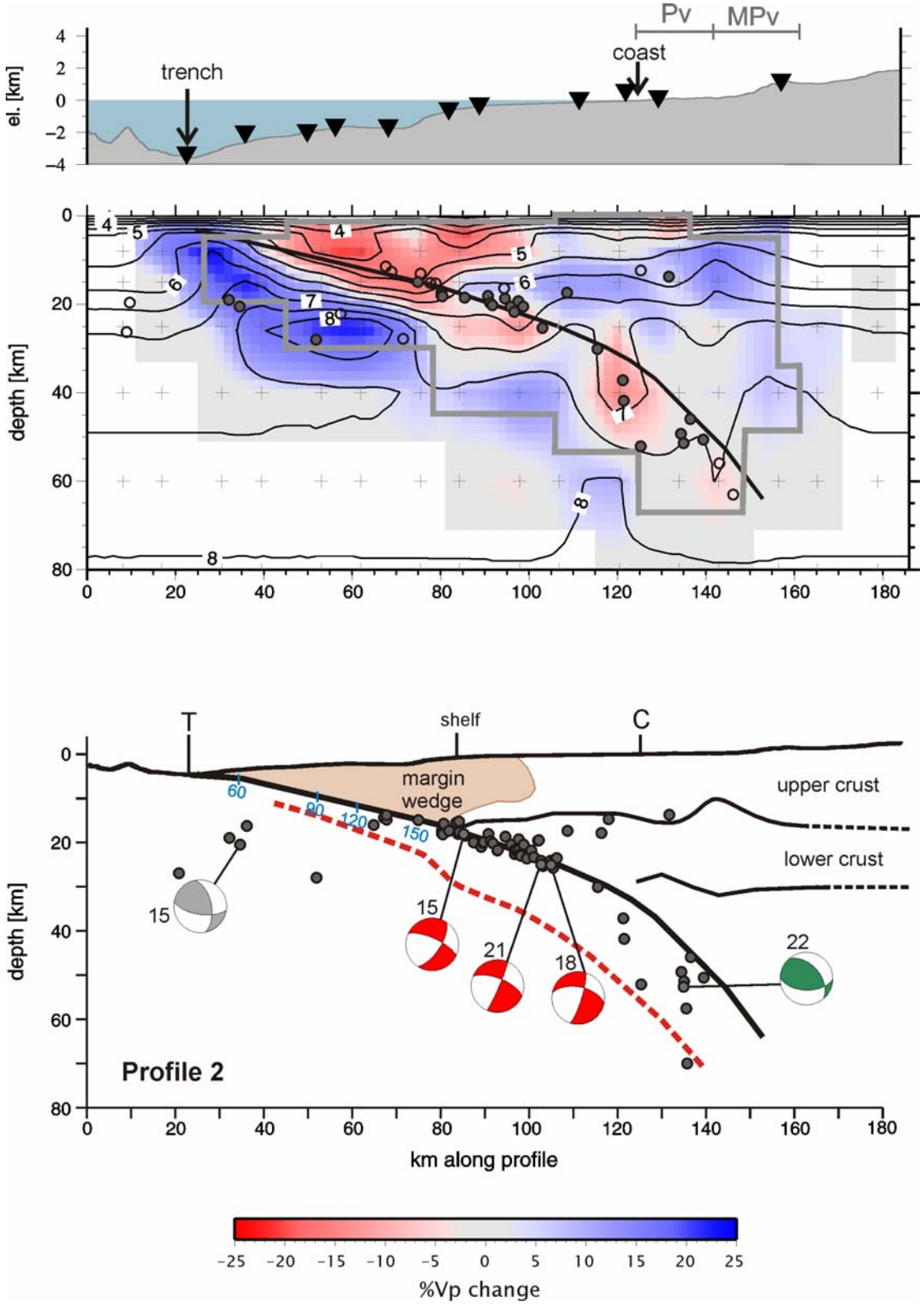

Figure 5.5 (continuation)

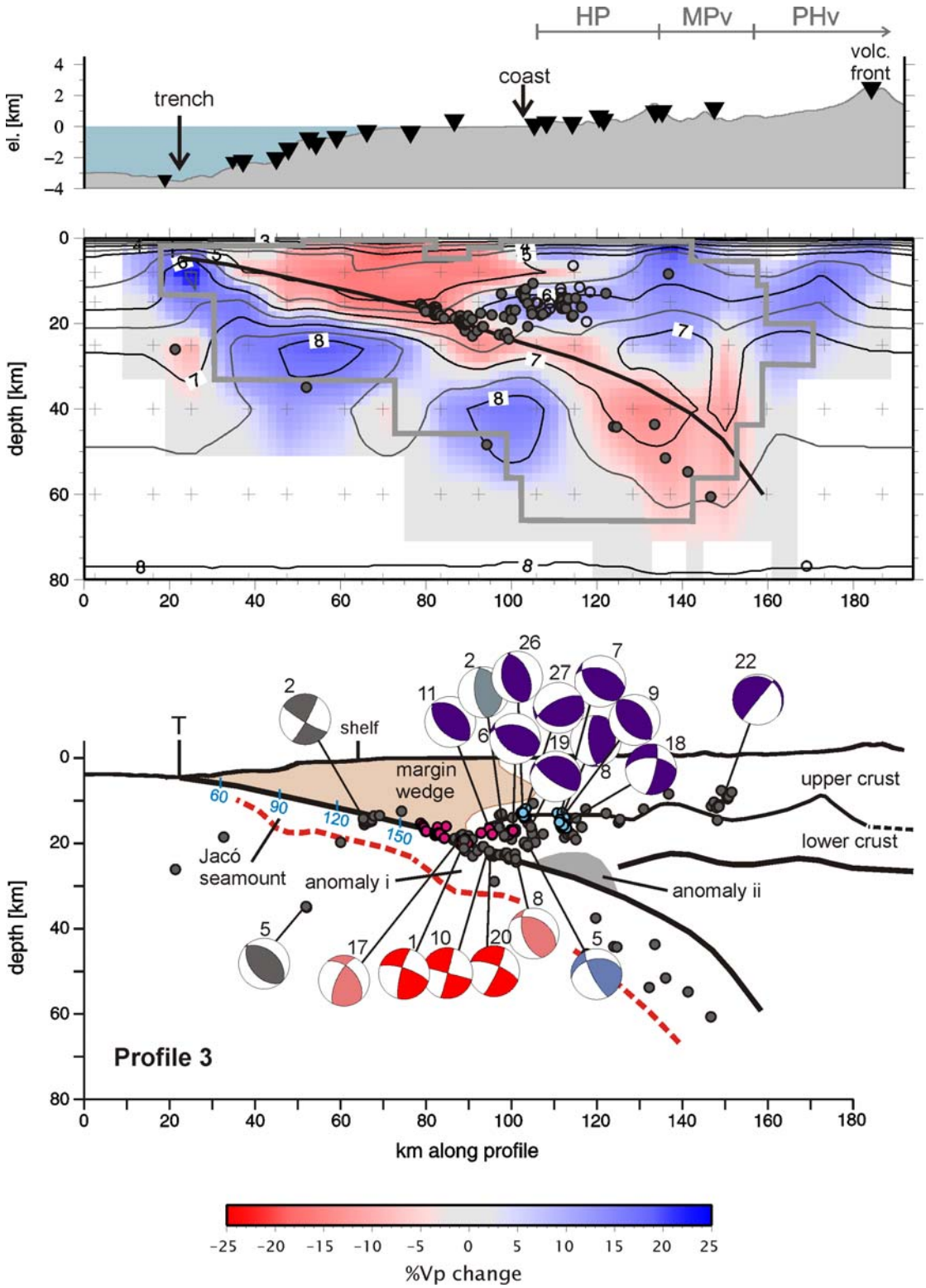

Figure 5.5 (continuation)

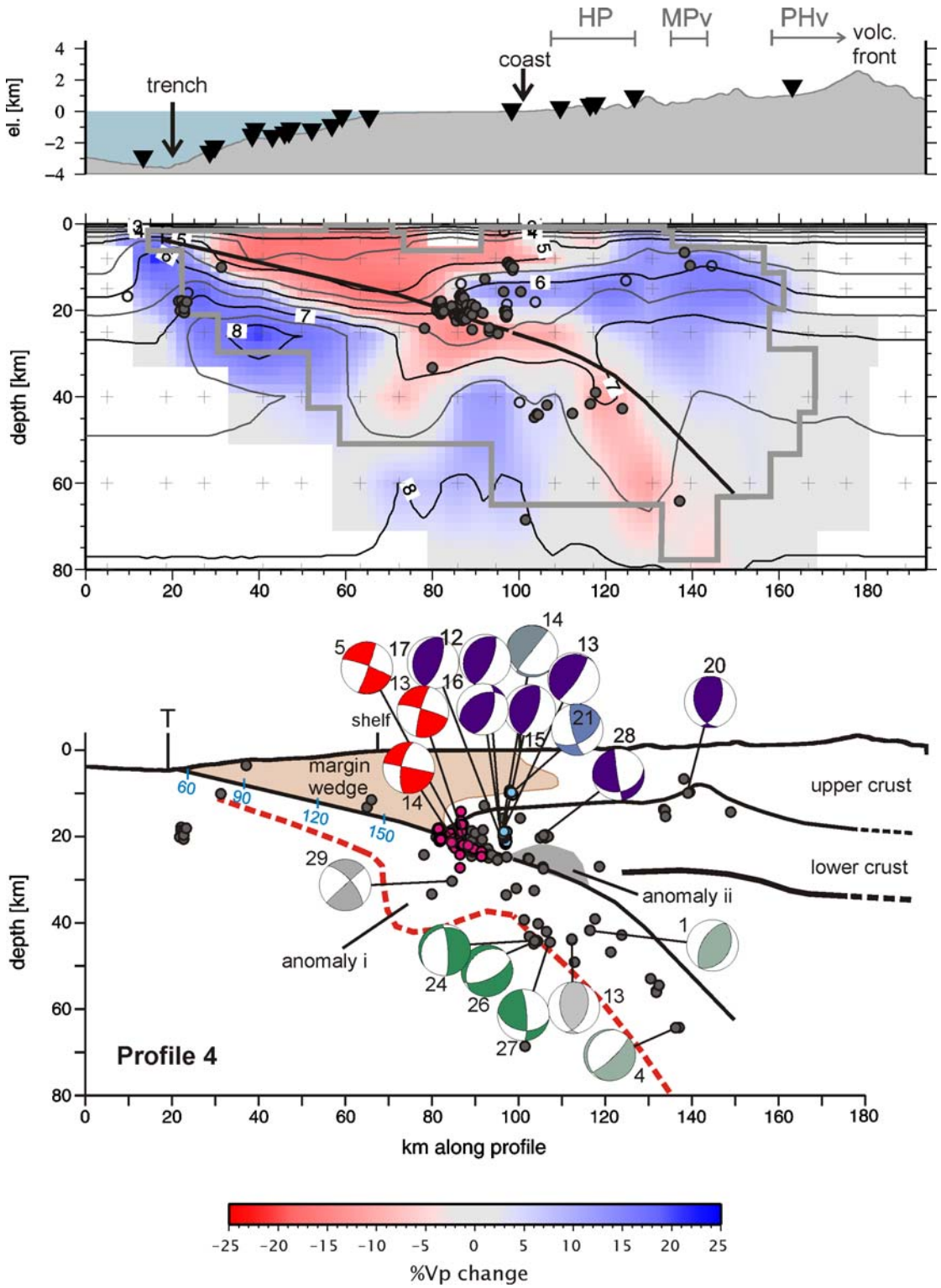

Figure 5.5 (continuation)

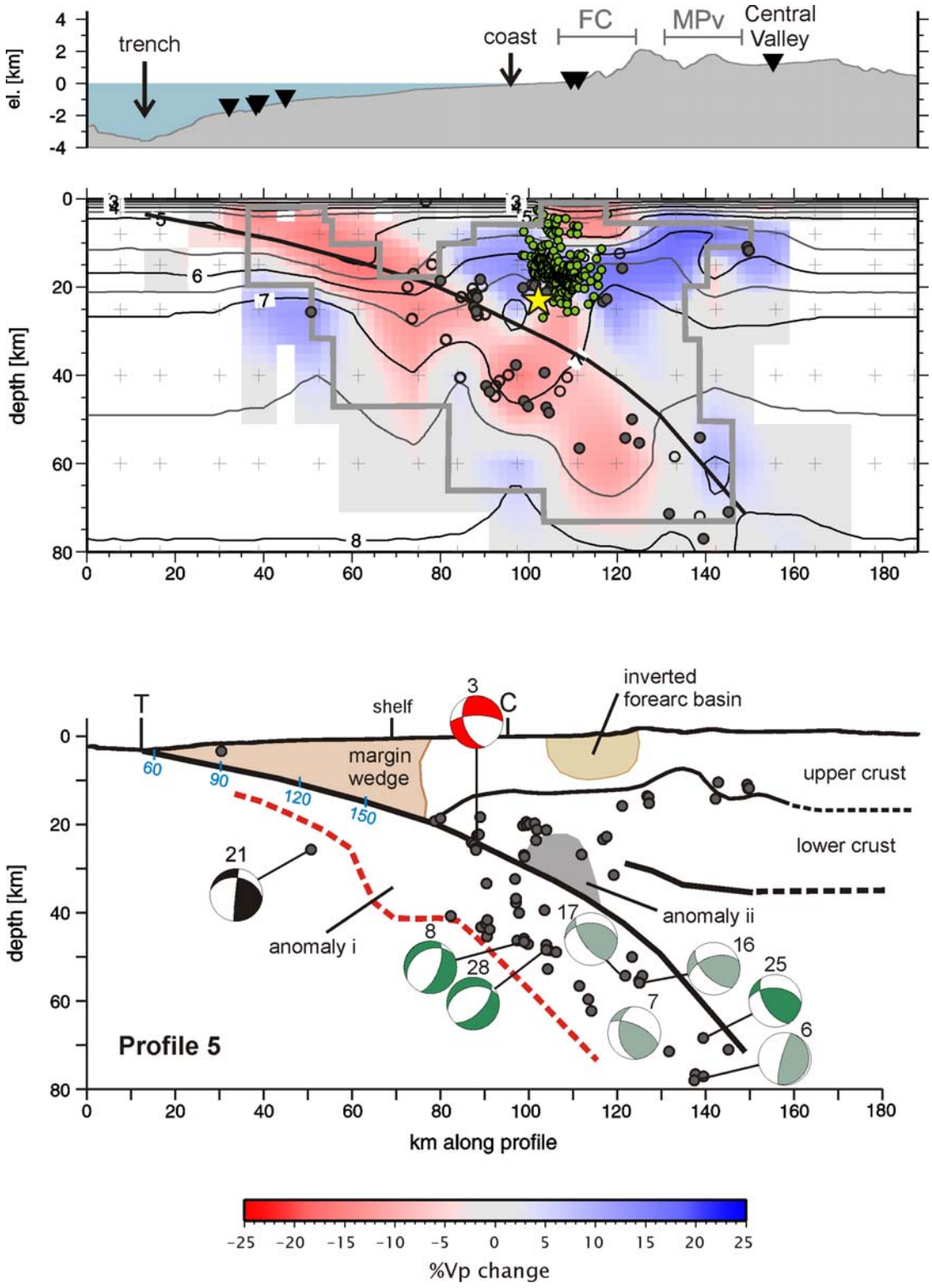

Figure 5.5 (continuation)

The earthquake activity along the plate boundary is characterized by frequent clusters of repeating earthquakes taking place over a very short period, as seismic swarms, referred to as "burst" type (Igarashi *et al.* 2003, Templeton *et al.* 2008). During the Jacó experiment, 24 swarms of three and up to nine events were detected on the plate interface, with magnitudes between 1.0 and 3.1 M_L. Magnitude variation in each swarm does not surpass 1.0. The swarms are spatial and temporal clustering of events, lasting periods of two minutes (three events) to one day, which display similar waveforms. A rough estimation indicates that around 20 per cent of the interplate seismicity occurs in small swarms. They are distributed all along the plate interface, from west to east, but are more frequent offshore the Herradura Promontory. No swarms were detected seaward from the Parrita lowlands. Epicenters of the swarms are shown in Figure 5.6 and in the profiles (Figure 5.5). Figure 5.7 shows waveform examples from the swarms. Three focal mechanisms of events belonging to swarms have been determined (Table 5.1, Figures 5.3a and 5.5), all of them inverse, supporting the premise that they originate at the plate interface.

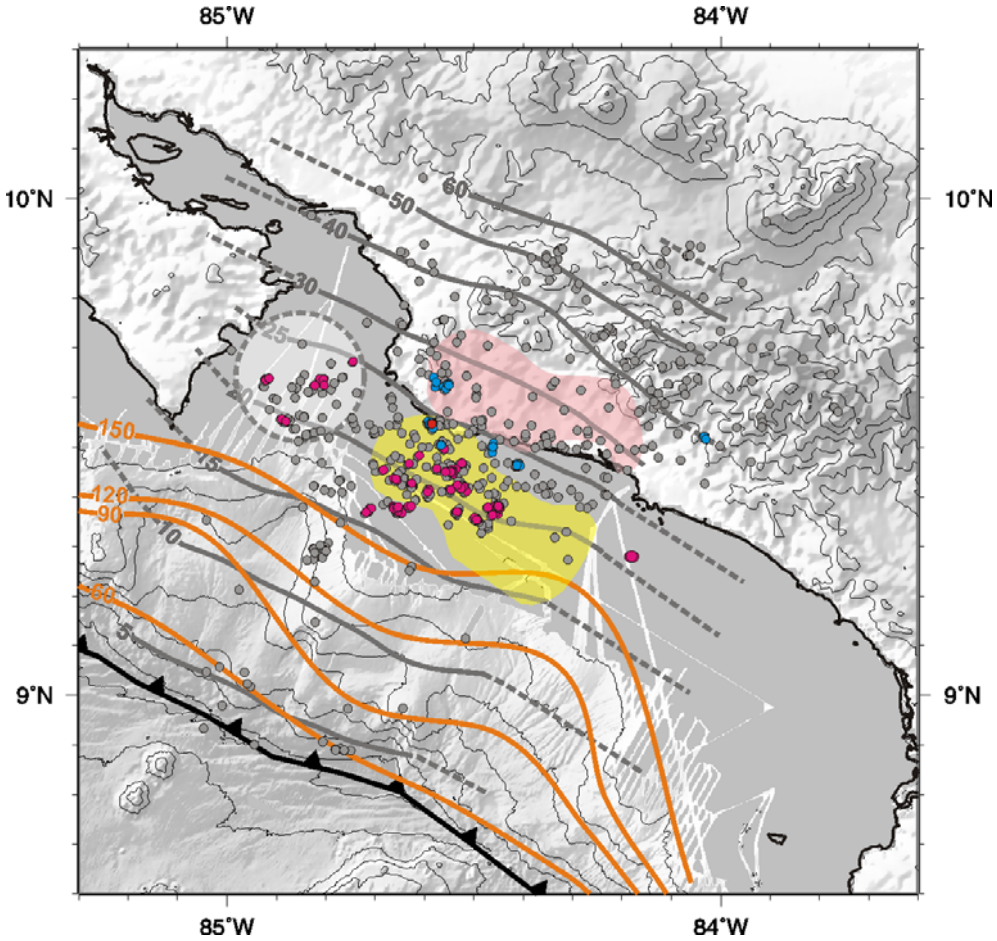

Figure 5.6. Distribution of burst-type swarms detected during this experiment, generated at the plate interface (magenta) and the upper plate (blue). Dashed circle represents the Cóbano seamount (Husen *et al.* 2002).

5.2.2.2 Discussion

Updip limit

The results obtained with the Jacó network appear congruent with the processes involved in subduction erosion and associated distribution of fluids, described in more detail in chapter 1. The model for the hydrogeological system in erosional margins recently assembled by Ranero *et al.* (2008) proposes that the onset of interplate seismicity is controlled by fluid migration taking place immediately updip. Most of the fluids contained in the pores of subducted sediments are liberated by early dehydration reactions and escape upward from the plate interface through fractures in the upper plate. The sector of the plate boundary where fluids are profuse, coincident with temperatures between 60°C and 150°C, corresponds to the area where tectonic erosion is evidenced by subsidence and formation of the continental slope. The decreasing in the amount of fluids with depth enables the transition from stable to unstable, seismic behaviour along the plate interface (Figure 1.5).

The isotherms of 60°C, 90°C, 120°C and 150°C along the plate boundary from Nicaragua to the Osa Peninsula have been estimated from heat flow measurements and the depth of bottom-simulating reflectors (BSR) (I.Grevemeyer private communication, Ranero *et al.* 2008), considering thermal conductivity of sediments and basement. Their values are within uncertainties of temperatures calculated by 2-D modelling off Nicoya Peninsula (Harris & Wang 2002, Spinelli & Saffer 2004, Ranero *et al.* 2008). Figures 5.4 and 5.8 display these isotherms; Figure 5.8 also includes the seismicity recorded along the Costa Rican margin by this study and the work of DeShon *et al.* (2003) to the southeast and DeShon *et al.* (2006) to the northwest.

As predicted by the model of Ranero *et al.* (2008), the updip onset of the interplate seismicity recorded by Jacó network offshore the Herradura Promontory starts beneath the continental shelf and closely follows the 150°C isotherm, as well as the upper end of the margin slope. Landward from the two big embayments affecting the continental slope in this segment of the margin, though, the updip limit of the seismicity occurs ~12-15 km further deeper along the plate interface than the isotherm. Even considering the earthquakes not included in the tomography (Figures 5.4 and profiles 1 and 5, Figure 5.5). However, the increase in the velocity gradient at the plate boundary mentioned before does coincide very well with the 150°C isotherm (Figure 5.4). This increase in the velocities could be associated to the predicted decrease in fluids abundance; the delayed start of the seismicity, if not an effect of the limited duration of the experiment, could be attributed to a local reduction in the thickness of the upper plate. In effect, along most of the sector of the margin, the interplate seismicity begins when the margin wedge reaches a thickness of ~18-19 km, equivalent to ~0.6 GPa (Figure 5.5).

In the area crossed by profiles 2 and 3 (Figure 5.5) the thickness of the upper plate above the onset of interplate seismicity is reduced to 13-15 km. Interestingly, also in

this area a small seismic sequence occurred between April 26 and 27, ~10 km updip of the clustered interplate seismicity and at the northern flank of the Jacó seamount (Figure 5.4; profile 3, Figure 5.5). The main event happened at 14 km depth and had a M_L 3.4; 18 events more were detected, at depths from 13 to 16 km, with magnitudes varying between 1.7 and 2.9. The sequence took place between the 120° and 150°C plate-boundary isotherms. The depth of the events indicate their source in the upper oceanic crust or the plate boundary. The focal mechanism of the main event, although not from the best quality, is of inverse type (Figure 5.3b, number 2), in agreement with the compressive regime expected so close to the plate interface.

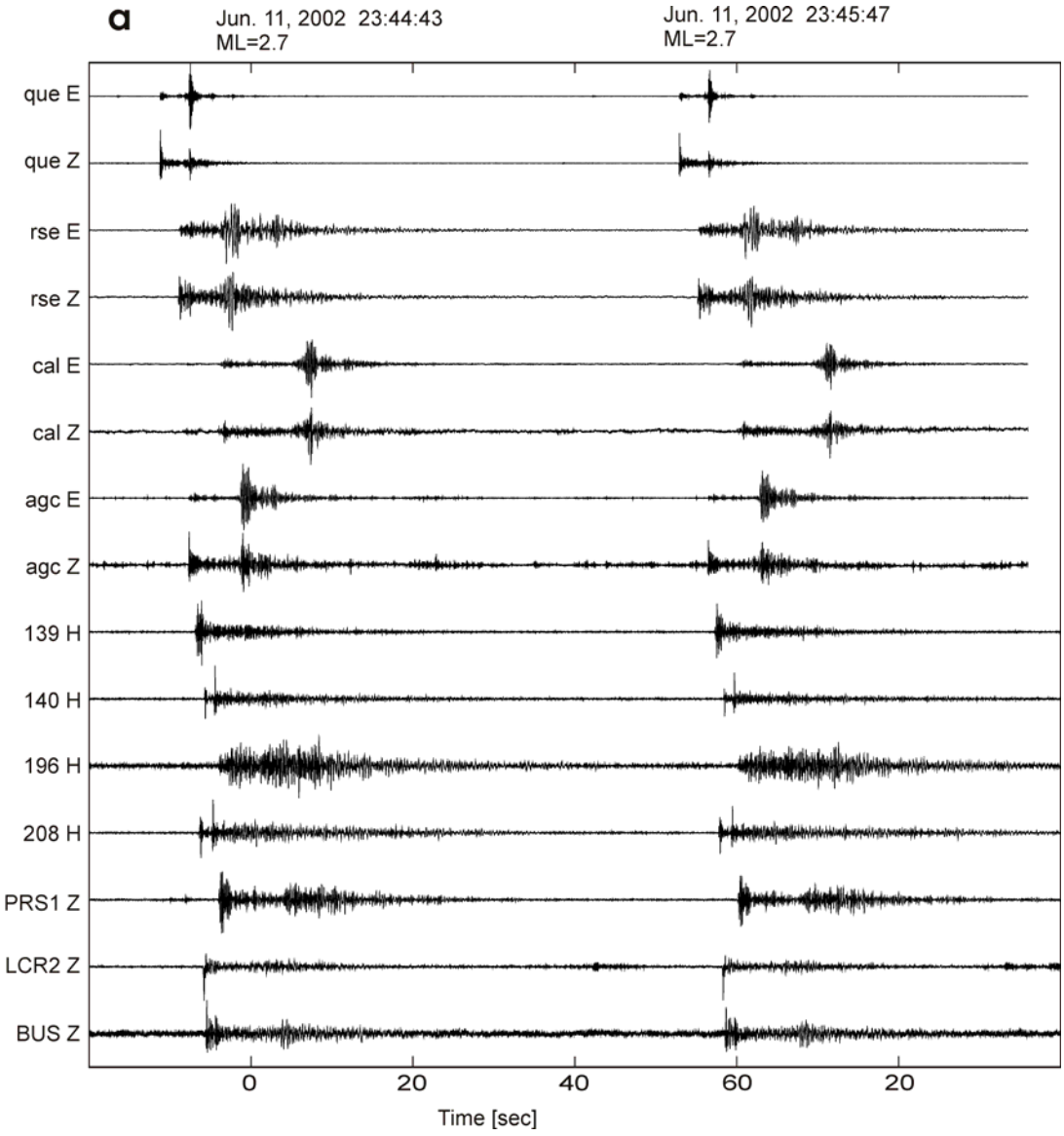

Figure 5.7. Examples of waveforms from events belonging to burst-type swarms along the plate boundary: a) records at several stations; stations labelled in low cases are from Jacó land network (Z: vertical and E: east components), with numbers are from OBHs (2-20 Hz band-pass filtered), and with upper-case from RSN. b) events from another swarm recorded at land station *sni* with origin times and magnitudes as indicated; traces are vertical component seismograms.

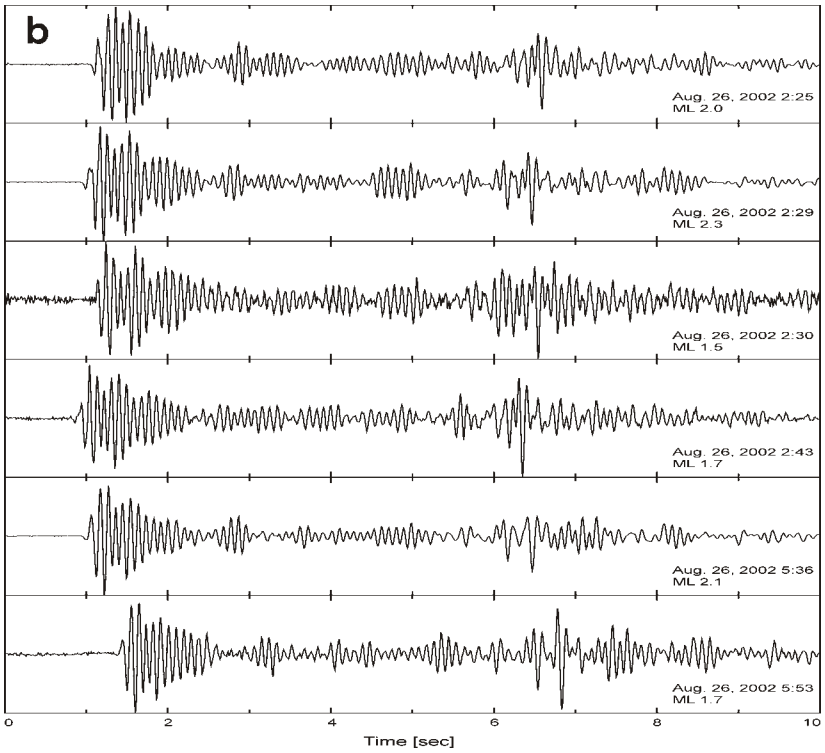

Figure 5.7 (continuation)

It could be speculated that the sequence is triggered by an increase of stress generated by the presence of Jacó seamount, that probably reactivates one of the plate-bending related faults, and may favour migration of fluids from the oceanic plate. Moreover, the deformation and disruption on the margin wedge (Dominguez *et al.* 1998, von Huene *et al.* 2000) generated by the passing of Jacó seamount may also provide more intense and concentrated fluid paths for water escape, propitiating the shallower updip limit of the interplate seismicity observed between profiles 2 and 3 (Figures 5.4 and 5.5).

Interesting as well, is the patchiness and the decrease in the rate of the interplate seismicity and the landward shift of its downdip limit offshore Parrita lowlands (Figures 5.1, 5.4 and 5.8). This reduction in the seismic activity takes place where the thickened oceanic crust and the associated anomaly i are already subducting. It seems to coincide spatially with the augment in size and amplitude of anomaly ii beneath the Parrita lowlands, while offshore the Herradura Promontory, where low velocities beneath the forearc have also been imaged, the interplate seismicity is still abundant (Figure 5.4). This decreasing of seismicity offshore Parrita lowlands doest not seem to be an effect of the relative short recording period of the Jacó network: the catalogue from the RSN, spanning over more than 25 years of recording, also shows a clear reduction on the seismic activity in this sector (Figure 5.1). The interplate seismicity becomes profuse again offshore Quepos and further to the east, an area that most recently generated the 1999 Mw 6.9 Quepos earthquake and its aftershocks (DeShon *et al.* 2003) (Figures 5.1 and 5.8).

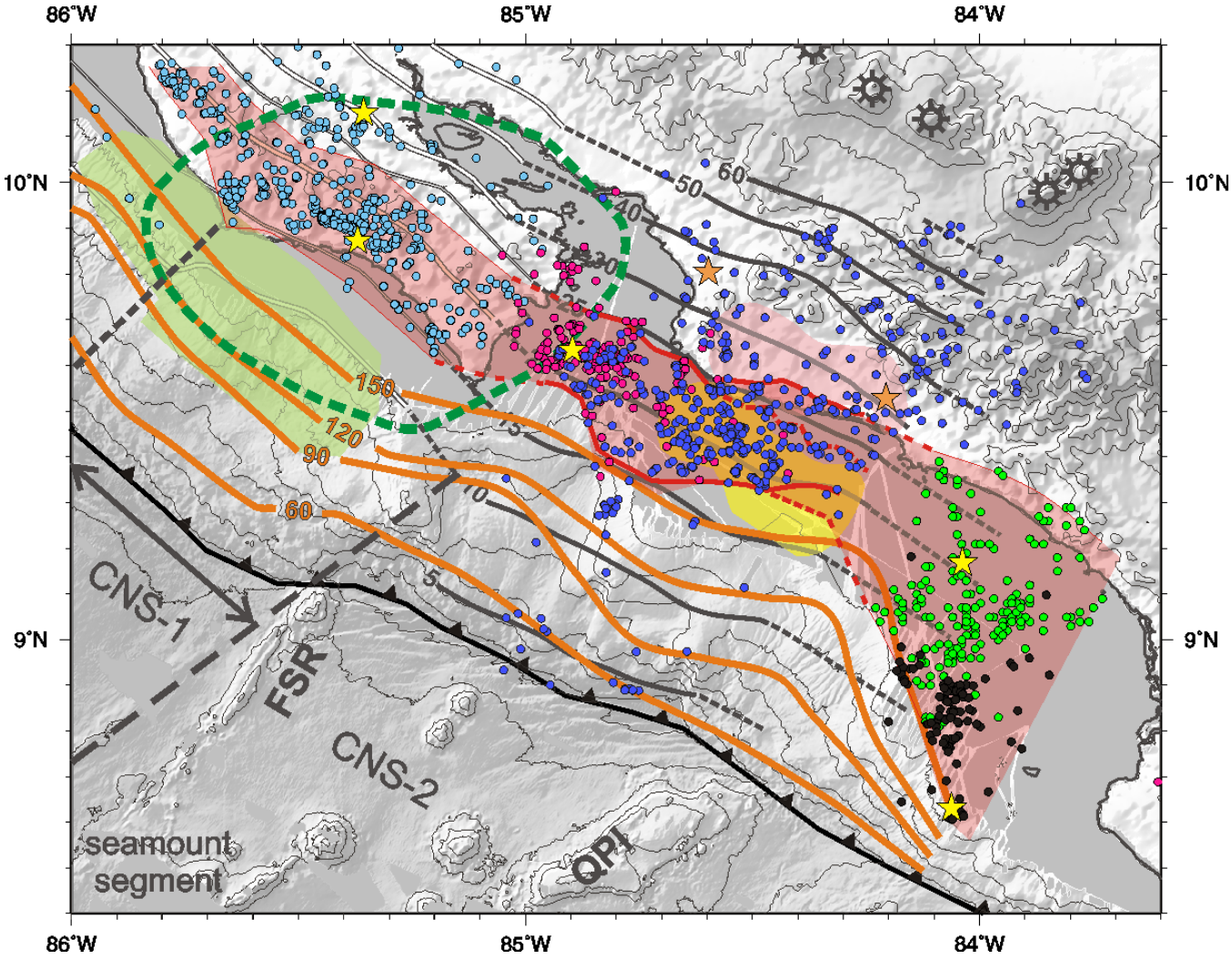

Figure 5.8. Synopsis map of the interplate seismicity (red shadow) recorded in Costa Rica by "amphibian" seismological networks, and recent large earthquakes. Contours of the top of the slab from this study and from DeShon *et al.* (2006) in Nicoya. Blue epicenters recorded by the Jacó network. Epicenters in Nicoya area (light blue) from DeShon *et al.* (2006) and in Quepos-Uvita segment (green) from DeShon *et al.* (2003). Large earthquakes in the Central Pacific sector as in Figure 5.1. Epicenters in magenta from the 1990 Cóbano earthquake after Husen *et al.* (2002). Epicenters in black are preliminary locations of the 2002 Osa sequence, as determined with records from Jacó and RSN networks. Epicenters of 1950 Mw 7.7 (northernmost) and 1978 Mw 6.9 earthquakes and aftershocks area of 1950 (green line) in Nicoya Peninsula from Avants *et al.* (2001). Locked patch along plate boundary (green shape) offshore Nicoya after Norabuena *et al.* (2004).

Possible explanations of the nature of anomaly ii were presented in chapter 4. If it consists of underplated material, its buoyancy could locally reduce the plate coupling in this part of the margin by pushing the overriding plate upward, precluding a higher interplate seismic activity, and simultaneously, as interpreted by Pacheco *et al.* (2006), causing deformation through the entire crust above. Those authors determined a slip distribution resembling that of a simple circular rupture with a radius of 8 km, a dimension consistent with the tomographic image of anomaly ii in this sector (profile 5, Figure 5.5). Underplating at depths of 20-30 km has been modelled from gravimetry data and P-wave velocities by Nakada *et al.* (2002) to explain crustal uplift

taking place since the late Pleistocene in the Miyazaki Plain, located opposite to the zone where the Kyushu-Palau Ridge enters the Nankai Trough in Japan. Those authors suggest that the underplated load beneath the forearc seems to weaken the plate coupling by pushing the upper plate upward.

Another possibility is that subduction of thicker, buoyant oceanic crust in this sector causes a locking of the plate interface due to locally increased coupling. But again, subduction of thickened oceanic crust does not preclude interplate seismicity eastward from Quepos Promontory, as manifested recently by the 1999 Quepos and the 1983 Mw 7.4 earthquake landward from the Cocos Ridge.

Comparison with the rupture area of large earthquakes further constrains the extend of the seismogenic zone in a margin. In the sector of the margin covered by the Jacó network, the Mw 7.0 Cóbano took place at the entrance of the Nicoya Gulf (Figures 5.1 and 5.8). As described before, relocation of the aftershocks has been undertaken by Protti *et al.* (1995b) and by Husen *et al.* (2002). In Figure 5.1 the results of the latter are displayed, together with the aftershock areas after 1000 minutes and after 69 days from Protti *et al.* (1995b). Unlike in the Nicoya Peninsula area (DeShon *et al.* 2006), the rupture of the large earthquake, as defined by the aftershocks, coincides with the seismogenic zone deduced from the interplate seismicity. The area of aftershocks after 69 days proposed by Protti *et al.* (1995b) extends until the trench. Nevertheless, the accompanying first-motion focal mechanisms presented by those authors for quakes trenchward from the limits of the seismogenic zone defined by this study do not seem to correspond directly to the rupture area, but to a general increase in intraplate seismicity induced by the main shock.

“Burst”-type swarms

Repeating earthquakes have been identified at transform plate boundaries (Nadeau *et al.* 1995, Templeton *et al.* 2008) and, more recently, at subduction zones (Matsuzawa *et al.* 2002, Igarashi *et al.* 2003). They are thought to be originated by rupture of the same patch of fault repetitively (Nadeau & McEvilly 1999). Currently, models tend to attribute their occurrence to the interaction of continual, aseismic fault slip (creeping) with locked, seismogenic patches of the fault. They have been used to estimate slip rates along creeping fault segments (Nadeau & McEvilly 1999).

Burst-type events, a special case of repeating earthquakes, have been detected along the plate interface and in the upper plate during the Jacó experiment. Burst-type swarms are clusters of events with nearly identically waveforms and similar magnitudes, very short recurrence intervals, repeating within hours or days of each other, and are active for only short periods. They are also found on both tectonic regimes, transform and convergent plate boundaries. Kimura *et al.* (2006) speculate that they are triggered by local increase in stress due to the occurrence of large nearby earthquakes and do not reflect the background creep rate of the fault.

Obana *et al.* (2003) report clusters of earthquakes at the seismogenic zone on the accretionary margin in western Nankai, Japan, offshore Cape Muroto. However, the clusters are located at the updip limit of the interplate seismicity. Since events from the clusters show similar waveforms and their location coincides with the 150°C isotherm, those authors suggest that they are originated at small asperities (few hundred of meters in diameter) in the transition zone from aseismic to seismogenic behaviour. In their model, stress is concentrated on the asperities by steady slip in the surrounding area where interplate coupling is relatively weak. Igarashi *et al.* (2003) and Matsuzawa *et al.* (2002) detected earthquake clusters occurring regularly at the plate boundary in northeast Japan. The repeating earthquakes have the same, low-angle thrust focal mechanisms and similar waveforms. No clusters were detected in the areas of higher moment release during large interplate earthquakes nor in the areas inferred to be strongly coupled from GPS data analysis. The authors associate these events to repeating rupture of small (0.1 to 1 km) asperities surrounded by stable sliding, similar as the scenario described by Nadeau *et al.* (1995) along the San Andreas Fault in Parkfield, California.

The seismic swarms detected along the plate interface in this study coincide with the nucleation area of the Mw 7.0 Cóbano earthquake and, specially, with the western part of anomaly i (Figures 5.1 and 5.6), which has been interpreted as a plateau or seamount (see chapter 4). That is, they seem to be associated to the parts of the plate interface assumed to have stronger coupling and that have generated large earthquakes in the past, at least in the case of the Cóbano seamount (Protti *et al.* 1995b, Husen *et al.* 2002). If the similarity of the waveforms between events belonging to the same swarm indicate the repetitive rupture of the same small asperities, probably they are generated by small-scale seafloor relief of the Cóbano seamount and the plateau or seamount imaged as anomaly i.

Templeton *et al.* (2008), in a study on repeating earthquakes on Central California, found that at the junction of the San Andreas and the Calaveras-Paicines faults they reflect a heterogeneous creep distribution with significant variations in time; burst-type events may be associated to the occurrence of a Mw 5.1 earthquake and a subsequent slow earthquake. At the Coast Range, albeit, in a segment characterized by strike-slip and thrust faults, they found only burst-type events and concluded that they are not produced by steady aseismic creep of the surrounding fault surface. They contemplate the possibility that changes in the lithology along the fault zone hinder creeping and loading of asperities, since burst-type swarms do not seem to repeat in time. Thus, the mechanism of repeating earthquakes in general, appears to be a more complex phenomenon than previously assumed.

For their part, Sage *et al.* (2006) present evidence of “interplate patchiness” in the erosional Ecuadorian margin, where the southern flank of the Carnegie Ridge subducts. High-quality reflection profiles down to depths of 7 km reveal ~600-m thick and several-kilometers wide lenses of underthrusted fluid-rich sediments, supplied by slope mass wasting, along the subduction channel. The contrast between the fluid-rich sediments and the adjacent thinner and dryer sections creates a 3-D patchiness across

the plate boundary, which implies variations in mechanical interplate coupling. The patchiness represents a mechanism of subduction erosion, where the upper plate is weakened by overpressured fluids from the "wet" sediment lenses, and material is removed at the dryer, higher coupled sectors. This configuration may have implications for the deeper subduction processes, such as earthquake nucleation. In a similar scenario, clusters of earthquakes could concentrate around the sediment lenses or similar patches of weaker coupling.

Downdip limit

The transition from seismogenic to aseismic behaviour with depth along the plate interface has been associated to an increased ductility of the subducting plate as temperature and pressure augment (Tichelaar & Ruff 1993). Temperatures of ~350-450°C are commonly cited to mark the transition (Hyndman *et al.* 1997). Alternatively, and specially in the case of cold subduction zones, the termination of stick-slip behaviour could be located around the intersection of the upper-plate Moho with the diving slab and is attributed to stable sliding against a serpentinized forearc mantle wedge (Oleskevich *et al.* 1999).

The interplate seismicity along the portion of the margin studied here extends down to a depth of 25 km (Figures 5.4 and 5.5), with a cluster of events located at ~30 km beneath Parrita coinciding with the more conspicuous part of anomaly ii (profile 5, Figure 5.5). The subducting slab intersects the Moho of the overriding plate at ~30 km depth. Peacock *et al.* (2005) constructed finite-element thermal models of the subduction zone in Nicaragua and Costa Rica, incorporating radiogenic heating within the continental crust and shear heating along the plate interface, as well as a temperature- and stress-dependent olivine rheology for the mantle wedge that focuses hot asthenosphere on its tip. The authors did not use surface heat-flow information along the margin to constrain the rate of shear heating. According to the thermal model of Peacock *et al.* (2005), assuming a shear stress of 10 MPa along the plate interface down to 50 km depth, the temperature at 25-30 km depth along the plate boundary in the Central Costa Rica margin is ~400-450° C. These observations may indicate that the downdip limit of the interplate seismicity is thermally controlled. Moreover, the amount of serpentinization (5-15%) on the tip of the forearc mantle wedge, as estimated in chapter 4 for the area studied here, is relatively low. Nevertheless, the data are not conclusive, given the uncertainties of the thermal model and the uncertainty on the determination of the location of the continental Moho, due to the absence of a strong velocity contrast (see chapter 4).

Comparison with Nicoya and Quepos seismogenic zones

Comparison of the interplate seismicity limits defined in this work shows a good agreement with the previous studies along the margin, as summarized in Figure 5.8. Just southeast from the area studied in this work, DeShon *et al.* (2003) used ~300 aftershocks of the 1999 Mw 6.9 Quepos underthrusting earthquake to investigate the limits of the seismogenic zone on the area off Quepos-Uvita villages (Figure 5.2 for

localities). They imaged a plane dipping 19°, where the majority of events occur below 10 km and above 30 km depth, 30-35 km and 95 km from the trench, respectively. Their observations and those of Bilek *et al.* (2003) support the hypothesis that the Quepos earthquake ruptured specific bathymetric highs on the downgoing plate. DeShon *et al.* (2003) believe that the limits of the seismogenic zone likely change over the earthquake cycle, as physical and chemical parameters influencing the transition from stable sliding to stick-slip behaviour vary. Comparisons with available thermal and mechanical models for the area let them determine the updip limit of the seismogenic zone at 120-185°C and the downdip limit between ~250 and 350°C. This is consistent with proposed temperature-influenced models for the transition aseismic to seismic transition, but the authors point out that further modelling is necessary resolve more clearly the temperature influence on seismicity on this region.

Offshore the Quepos-Uvita region, the seismogenic zone is much wider than offshore the Herradura Promontory, reflecting the presence of thickened, buoyant crust from the trench downward. The downdip limit of the aftershocks distribution from the work of DeShon *et al.* (2003) shows continuity with the limit estimated in this study (Figure 5.8). The seaward limit, like from offshore the Nicoya Gulf entrance to Quepos, closely follows the 150°C isotherm and the border of the continental shelf.

Newman *et al.* (2002) and DeShon *et al.* (2006) analyzed the seismicity recorded in the area of the Nicoya Peninsula by another "amphibian" network, deployed northeast from the Jacó experiment area during 18 months (Figure 5.8). Results from the LET performed by DeShon *et al.* (2006) show that the interplate seismicity extends from 17 to 28 km and from 12 to 26 km depth beneath the northern and southern Nicoya Peninsula, respectively; a 5-km seismicity offset takes place across the suture between oceanic crust created at the EPR and at the CNS. Again, the downdip limit of the interseismic interplate seismicity represents a smooth continuation of the results from this study. The contours of the top of the slab determined by DeShon *et al.* (2006) likewise match very well the geometry derived for the Jacó experiment area (Figure 5.8).

Nevertheless, at the Nicoya Peninsula the picture seems more complicated. Comparison with the geodetic modelling from Norabuena *et al.* (2004) for that sector of the margin revealed that, contrary to expected, the interplate seismicity begins downdip a patch of increased locking along the interface (Figure 5.8). Moreover, in the Nicoya Peninsula the interseismic cycle seismicity does not define the potential rupture size of large earthquakes, as concluded from a large event in 1950, which extended further trenchward, coinciding with the updip limit of the locked patch, and deeper than the limits of the interseismic interplate seismicity (Figure 5.8). The downdip limit of the interplate seismicity in Nicoya determined by DeShon *et al.* (2006) occurs at shallower depths than the intersection between the slab and the continental Moho, which may be attributed to the start of ductile behaviour at 300-350°C according to thermal models for the peninsula. However, those authors remark

that the apparent deeper extension of the rupture of large events and the uncertainties associated to the thermal models preclude a unique interpretation.

Schwartz & DeShon (2007), comparing with thermal models for Nicoya, find that while the shallow locked segment coincides with the 100°C isotherm at the plate boundary, the updip limit of the interplate seismicity matches the 250°C isotherm. At that temperature, most of the sediment diagenetic processes have already concluded. To explain the onset of seismicity, those investigators suggest an increase on pore fluid pressure resulting from dehydration reactions of the oceanic crust and/or decreased permeability in the upper plate. A change in the composition of the upper plate, from basalt to basalt-gabbro, could also modify the frictional stability across the plate interface and account for the onset of seismicity. Alternatively, DeShon *et al.* (2006) consider that local variations along the Nicoya Peninsula could be explained by different degrees of subduction erosion. As proposed by von Huene *et al.* (2004) and Ranero *et al.* (2008), there is an intimate relationship between temperature and the hydrofracturing of the upper plate. Erosion can introduce large amounts of upper-plate material into the subduction channel, whose amount and distribution is influenced by temperature.

Subducted seamounts

The role of seamounts in subduction zones have been studied in different margins of the world, yielding the conclusion that they can act as asperities or barriers for large earthquakes. Scholz & Small (1997) conceived a model where the seamount exerts additional normal stress at the plate interface and its effect in earthquake generation depends on the background state of the plate coupling. A strong coupling would be enhanced by the presence of a seamount, and an increase in magnitude and recurrence time of large subduction earthquake is expected; on the opposite case, where plate coupling is weak, a seamount locally increase the stress and produce seismic activity. According to Cloos (1992), the dimensions of the seamount would determine the size of the subduction earthquake.

Kodaira *et al.* (2000) presented high-quality refraction data from the Nankai Trough, that together with seismic and geodetic modelling of the 1946 Nankaido earthquake indicate a subducted seamount acting as a rupture barrier. The seamount inhibited brittle seismogenic rupture rather stimulating tsunamigenic slow slip. For their part, Abercrombie *et al.* (2001) correlate the 1994 Java earthquake with a seamount serving as an asperity.

The asperity that caused the Cóbano earthquake has been related to a seamount by Protti *et al.* (1995b) and Husen *et al.* (2002). If the interpretation of anomaly i as a seamount or plateau is correct, then due to its location at the seismogenic zone it could be the source of strong earthquakes. The approximate total horizontal area of anomaly i is 800 km^2, an asperity size which could generate an earthquake of magnitude Mw ~6.9 assuming its total rupture. However, the process that causes the decrease on seismic activity offshore the Parrita lowlands could reduce the effective

rupture area to ~500 km^2, diminishing the area capable of nucleating an event of magnitude Mw ~6.7. The zone occupied by anomaly i is bracketed by the aftershocks of the 1990 and the 1999 earthquakes, further stressing the capability of the asperity to generate the next large subduction earthquake of the margin segment.

Protti *et al.* (1995b) point out that the preceding seismic activity showed a large concentration on the same rupture area of the 1990 earthquake. They remark that this indicate a difference between seamounts acting as asperities, and the type of asperities existing in segments where smooth ocean floor subducts. Subduction of seamounts originates significant deformation on the upper plate, but also may suffer intense internal deformation manifested as high seismic rates. Higher seismicity is also coincident with the presence of anomaly i, as inferred from the RSN catalogue and from the Jacó experiment, including the increased swarm activity described before (Figures 5.1, 5.4 and 5.6).

As pointed out by Bilek *et al.* (2003), the frictional behaviour of seamounts is influenced by heterogeneous seafloor morphology, material properties, temperature and fluid pressure, factors that cause the role of the seamounts to change over a seismic cycle.

With data provided by the Jacó experiment and as mentioned above, it could be speculated that in the Central Costa Rican Pacific margin, in addition to their function as asperities when positioned at the seismogenic zone, seamounts beneath the margin slope, i.e. at a shallower stage along the plate boundary, could as well stimulate a local trenchward shifting on the updip limit of the interplate seismicity (Figures 5.4, 5.5 and 5.8). The presence of Jacó seamount at around 10 km depth could enhance the escape of fluids from the plate interface, causing an earlier begin of the stick-slip behaviour. Increased permeability has been observed at the flanks of bathymetric highs on the oceanic plate, favouring focused upward fluid seepage (Giambalvo *et al.* 2000, Fisher *et al.* 2003).

5.2.3 Intraslab seismicity

Profuse seismic activity is generated in the subducting slab, specially beneath or downdip the seismogenic zone, contained in the LVB and for effects of this study referred to as Wadati-Benioff (WBZ) seismicity. But also several events were nucleated between the outer rise and the area of the seismogenic zone, at maximal depths of ~20 km below the top of the slab and in its high-velocity portion (Figure 5.5). In general, intraslab seismic activity is higher toward the east, as observed also in the RSN catalogue (Figure 1.2, 5.1 and 5.4). Several focal mechanisms of variable type were determined for intraslab events, from the trench down to 100 km depth (Figure 5.3b).

In the portion of the slab closer to the trench there seems to be a relatively higher concentration of events beneath the trench, probably associated to slip along the outer-trench faults during increased plate bending (Chapple & Forsyth 1979). Pervasive faulting along the trench have been imaged offshore Middle America by high-resolution seafloor mapping, near-vertical reflection lines and outer-rise seismicity (Hinz *et al.* 1996, von Huene *et al.* 2000, Ranero *et al.* 2003, Grevemeyer *et al.* 2007, Lefeldt & Grevemeyer 2007). In the Central Pacific segment, the thicker oceanic crust promotes a smaller outer rise and a less-developed faulting (von Huene *et al.* 2000). The LVB imaged in this sector supports the existence and continuity of trench faulting landward. Recently, Lefeldt & Grevemeyer (2007) used teleseismic waveform inversion, centroid depths and focal mechanisms of events with magnitudes Mw ~6 from the trench-outer rise offshore Central America. They found that all events occur at depths shallower than 30 km, with ruptures generally propagating downdip and focal mechanisms of subevents of the same earthquake changing from normal faulting to strike-slip or oblique thrusting with time; the depth at which the mechanisms change could represent the transition from tensional to compressional regions on the incoming plate.

The events recorded in this area by the Jacó network show some clustering, for example along cross-section 4 (Figure 5.5) and between cross-sections 2 and 3 (Figure 5.4), at ~20 km depth. Only two focal mechanisms were determined for events originated on this sector (Figure 5.3b), excluding the afore mentioned seismic sequence of April 2002, possibly related to the subducted Jacó seamount, and only one with the best quality (event 21). The hypocenters of the two events are deep (Table 5.1), one of their nodal planes roughly coincide with the trench faulting and their strike-slip component seems to agree with the results from Lefeldt & Grevemeyer (2007).

A few quakes were generated in anomaly i, clearly deeper than the cluster formed by the interplate seismicity (profile 4, Figure 5.5). A thrust-type focal mechanism was determined for one of these events (number 29, Table 5.1), suggesting internal compressive deformation. Further southeastward, DeShon *et al.* (2003), in their study of the aftershocks of the 1999 Quepos earthquake, located some events generated in the oceanic plate beneath the seismogenic zone as well. This spatial and temporal correlation with a strong underthrusting event may indicate that the intraplate events occur also as a response to changes in strain and fluid flow.

In the west of the area studied here, where normal oceanic crust is subducting, the start of the WB seismicity seems to take place ~5 km downdip of the termination of the interplate seismicity and coinciding with the intersection between the slab and the upper-plate mantle (profile 2, Figure 5.5). The WB seismicity is encompassed by the LVB. In the east part of the area, where subduction of anomaly i and the thickened oceanic crust takes place (profile 4, Figure 5.5), abundant intraslab seismicity starts already below the seismogenic zone, ~20 km closer to the trench axis. It takes place over the whole LVB as well, which reaches ~20 km width here.

In their LET, Husen *et al.* (2003a) observed also a widening of the band formed by the WB seismicity eastward from the area crossed by profile 3 of this work. They describe a diffuse, 20-km wide WBZ seismicity extending down to 80 km depth along a cross-section running from the trench over Quepos Promontory to the Irazú-Turrialba volcanoes. In chapter 4, arguments were presented to explain the LVB as crust hydration, at least on the west part of the area. There, low velocities are likely caused by a faulted, hydrated slab. In the east part, though, the notorious widening of the LVB seems to correspond with the subduction of hotspot-modified, thickened oceanic crust.

The mechanism responsible for the WBZ seismicity has been a subject of discussion ever since its existence was revealed. At depths superior than ~30 km the great pressures should prevent brittle or frictional processes. Intermediate-depth seismicity is commonly believed to be enabled by slab dehydration (Kirby *et al.* 1996, Hacker *et al.* 2003). As the slab sinks, metamorphic reactions liberate fluids from hydrous phases. Dehydration increases pore pressure, reducing normal stress enough to bring the system into the brittle regime. Nevertheless, the exact relationship between dehydration and earthquake nucleation is not yet well understood. Earthquakes could be generated by dehydration embrittlement creating new faults (Zhang *et al.* 2004) or reactivating pre-existing weak zones (Peacock 2001), depending on where hydration occurred (Ranero *et al.* 2005).

The 3-D P-wave velocity structure and petrologic modelling from Husen *et al.* (2003a) indicate the existence of a low-velocity hydrous oceanic crust in the subducting plate beneath central Costa Rica. Those authors found a good correlation between the predicted locations of hydrous minerals in the oceanic crust and the hypocenters of intermediate-depth earthquakes, further supporting the hypothesis of the latter being enabled by dehydration. Abers *et al.* (2006) present further evidence of intermediate-depth seismicity triggered by dehydration reactions within the slab. Their results from the Alaska subduction zone using attenuation tomography, receiver function analysis and thermal modelling show the WBZ seismicity descending more steeply than the subducting crust, which is thickened and displays a wide low-velocity zone from 60 to 120 km depth. Thermal modelling shows that seismicity within the subducting crust is distributed in a narrow belt of pressure-temperature conditions, which coincides with the breakdown of high-pressure hydrous minerals such as lawsonite. This suggests that a single set of dehydration reactions may trigger intermediate-depth seismicity.

Recently, Ranero *et al.* (2005) statistically compared the strike of bending-related faults in the oceanic plate with that of the nodal planes of intermediate-depth earthquakes (> 70 km) along different segments of the Middle America and Chile subduction zones. The similarity they found supports previous studies from other subduction zones of the world (e.g. Jiao *et al.* 2000), attributing most of the intraslab seismicity to reactivation of faults rather than formation of new ones at the planes of maximum shear within the slab. The authors also found higher rates of intraslab seismicity associated to segments with more pervasive trench faulting. The conceptual

model of Ranero *et al.* (2005) for intermediate-depth seismicity proposes that it starts between 60-80 km, when dehydration of oceanic crust reactivates the upper segment of bend-faults, which causes concentration of earthquakes on the upper part of slab. Deeper than ~100 km, eclogitization is completed; here or slightly deeper dehydration of slab mantle occurs reactivating bend-faults and generating seismicity within the upper slab mantle. The authors point out that this model may not be applicable to subduction of young lithosphere and broad aseismic ridges.

Warren *et al.* (2008) analyzed the directivity and identified the focal mechanism fault plane of several large (Mw ≥ 5.7) earthquakes between 35 and 220 km depth in the MAT. They concluded that at depths shallower than 85 km, fault planes are consistent with both, reactivation and formation of new faults. Deeper than 85 km, they observed only subhorizontal planes, indicating that trench faults are no longer reactivated. Similar results were found in the colder Tonga-Kermadec subduction zone (Warren *et al.* 2007), suggesting that the mechanism controlling earthquake generation and plane orientation must be related to pressure or other tectonic parameters rather than temperature. The authors speculate that "exclusively subhorizontal faults may result from isobaric rupture propagation or the hindrance of seismic slip on pre-existing weak subvertical planes".

The relatively abundant seismicity generated on the widened LVB (profile 5, Figure 5.5) poses some discrepancy with a model of WBZ seismicity triggered along reactivated outer-rise faults. Thickened oceanic crust displays a reduced ability for bending, and slab hydration at the trench may be consequently decreased. Although some reservations could raise from their quality, good but in general lower than the solutions for shallower events (see appendix), the focal mechanisms obtained in this study for events originated deeper than ~40 km (Figure 5.3b) further complicate the panorama. Most of the nodal planes of the focal mechanisms trend northeast, parallel to the slab direction, and solutions are of all types. Nevertheless, some pattern could be recognised. There is an alignment of inverse and strike-slip focal mechanisms along and beneath the coast (events 8, 24, 26, 28 in Figure 5.3b), at depths varying from 40 to 65 km, at around ~15 km below the top of the slab (profiles 4 and 5, Figure 5.5). Landward, a band of mechanisms of normal type were determined (events 16, 17, 19 in Figure 5.3 b for example), from earthquakes located between 55 and 68 km depth but ~10 km underneath the slab top.

Shiomi *et al.* (2008) studied the inhomogeneous distribution of hypocenter and the variety on focal mechanisms in the intermediate-depth seismicity along the Philippine Sea slab in southwest Japan. To analyze the complex pattern, they constructed a detailed configuration of the oceanic Moho based on receiver function analysis and traveltime tomography. Comparison of Moho structure, seismicity and focal mechanisms led them to the conclusion that the intraslab seismicity is constrained not only by its composition, but also by the interaction between the slab geometry and its motion. In their schema of the relationship between the stress field within the subducting slab and the focal mechanism distribution, they propose that a ridge shape creates tension on the upper part of the slab and compression below, with the

respective P- and T-axes perpendicular to the slab motion. This happens, for example, beneath western Tokai and Shikoku. Although the evidence presented here is inconclusive, maybe something similar takes place beneath this sector of Central Costa Rica. Inverse mechanisms are found deeper than normal mechanisms, and both display nodal planes striking parallel to the slab motion.

5.2.4 Upper-plate seismicity

The seismicity recorded on the overriding plate during the experiment was distributed mainly landward from the edge of the margin wedge, although few events might have occurred on the margin wedge itself, updip of the interplate seismicity. Much of the upper plate activity distributes spatially in clusters, particularly below the Herradura Promontory, at kilometer 140 along profile 3 (lower plot), and around anomaly ii (Figures 5.4 and 5.5). Repeating earthquakes as burst-type swarms, detected at the seismogenic zone as described above, take place also in the overriding plate. Eight small seismic swarms of two and up to nine events with magnitudes from 1.9 to 4.3 M_L were recorded beneath the coast and over the plate interface (Figures 5.5 and 5.6).

There was a higher concentration of events between cross-sections 2 and 4, beneath the coast and the Herradura Promontory, at depths fluctuating around 15 km. This activity is closely delimited seaward by the margin wedge and the plate boundary (Figure 5.5), and upward by a conspicuous, tabular low-velocity anomaly located at 8 km depth underneath the Herradura Promontory (cross-sections 3 and 4, Figure 5.5; Figure 4.16). This feature appears as a landward prolongation of the margin wedge. According to the resolution tests described in chapter 4, this zone is well resolved and no horizontal smearing has been detected. Inversions using a higher damping parameter still show a local decrease in the velocity gradient under the Herradura Promontory. A similar feature was observed by DeShon (2004) beneath the Nicoya Peninsula. The author pointed out that the anomaly could be an artefact. But its presence below Herradura as well may indicate a real characteristic of the margin.

Sallarès & Ranero (2005), on the basis of reflection profiling and CSS tomography modelling, report the presence of a similar low-velocity zone a few kilometers beneath the middle slope and the coastal area on the margin wedge offshore Mejillones Peninsula in North Chile. The upper part of the anomaly coincides with a subhorizontal seismic horizon observed in reflection images, previously interpreted by von Huene & Ranero (2003) as a detachment surface where block-bounding faults cut from the seafloor into the upper plate. Sallarès & Ranero (2005) speculate that the low-velocity anomaly could be either a rheological boundary formed along a pre-faulting contact between two different rock bodies, or a zone of low strength related to the presence of fluids. The latter possibility is not easy to explain, since the rocks above the detachment are fractured; seawater can not percolate down because the faults do not cross the detachment. The authors offer as alternative the migration of fluids from the subduction channel.

Perhaps the low-velocity zone beneath Herradura could be associated with the mechanism of emplacement of the oceanic assemblages that constitute the Herradura Promontory. It could also be attributed to the effect of processes generated by the seismic activity in the continental crust taking place below. Moreover, as mentioned before, the seismic swarms at the plate boundary are often accompanied by events in the upper plate. As suggested by Sallarès & Ranero (2005), this could be related to migration of fluids: movement along the plate boundary causes upward ascend of fluids that does not induce seismicity in the margin wedge, which is not mechanically competent, but may generate earthquakes in the undisturbed part of the upper plate landward from the wedge. In this area, fluids could be accumulating at around 8-10 km depth by the presence of the Herradura Promontory, which may represent a lithological variation.

The focal mechanisms obtained for seismicity in the upper plate (Figure 5.3c), half of which are associated to seismic swarms (Table 5.1, Figure 5.6), are mostly strike-slip, with nodal planes oriented northeast and northwest, corresponding with left- and right-lateral faults, respectively. Several normal-type mechanisms with planes striking northeast were determined at and off the Herradura Promontory.

Crustal deformation in subduction zones is often characterized by trench-parallel motion of slivers located between the trench and the volcanic front due to oblique subduction (Jarrard 1986). DeMets (2001) modelled velocities from GPS sites in the Caribbean, North American and Pacific plates, together with seafloor spreading rates and marine geophysical data, to estimate the present-day Cocos-Caribbean plate motion. Comparing with slip directions of numerous shallow-thrust subduction earthquakes form the MAT between Costa Rica and Guatemala, he concluded that they are deflected 10° clockwise from the plate convergence direction. This supports the hypothesis that the frequent dextral strike-slip earthquake along the Central American volcanic front are the result from partitioning of oblique Cocos-Caribbean convergence.

DeMets (2001) sets the southeastern limit of the sliver at the tip of the Nicoya Peninsula, coincident with the proposed Central Costa Rica Deformed Belt (CCRDB, Marshall *et al.*, 2000), i.e. immediately westward from the area of this study. This diffuse zone of active faulting is believed to represent a deformation front that propagated arcward due to subduction of thickened oceanic crust, i.e. the Cocos Ridge and the flanking seamount segment. Within the inner forearc domain, the CCRDB is expressed in a series of steep, northeast striking faults, 10-20 km long, which accommodate differential uplift of a system of forearc blocks (Marshall *et al.* 2000). It has been proposed that differential uplift is originated by tectonic underplating of seamounts and/or eroded material (Fisher *et al.* 1998). This local uplift is superimposed to the general forearc uplift caused by the subduction of the Cocos Ridge. The forearc domain is bounded arcward by a major, northwest-heading fault separating it from the Miocene volcanic front. Northwest striking dextral and conjugate northeast striking sinistral faults predominate towards the current volcanic

arc. The study of Marshall *et al.* (2000) determined that these fault patterns have been active throughout the Neogene until today.

Another feature of the margin prone to generate seismicity in the upper plate, including strong earthquakes, is anomaly ii. As mentioned in chapter 4, this low-velocity zone seems to be aseismic. No events were located inside of the anomaly either during the recording period of Jacó network or throughout the 2004 Damas sequence, as shown in Figure 5.5 (profile 5). The aftershocks distributed in depth between the top of anomaly ii and the inner-forearc basin. Clusters of events were detected by the Jacó experiment surrounding the anomaly as well; a focal mechanism determined for an event from the cluster (number 3, Table 5.1, Figure 5.3c) displays the strike-slip movement with nodal planes striking northwest and northeast which is predominant in the upper plate in this sector of the margin (Figure 5.3c). The mechanism is similar to that of the 2004 Damas earthquake (Pacheco *et al.* 2006) (Figure 5.1).

As discussed in chapter 4, given its aseismic nature, anomaly ii could be the tomographic image of upward migrating fluids which accumulate there, at the base of the continental crust, or it could be caused by tectonic underplating of seamounts and/or eroded material at the base of the continental crust as mentioned above. A causal relationship between anomaly ii and the Damas earthquake may fit better on the second scenario.

The offshore continuation of several of the inner forearc faults has been interpreted by Barboza *et al.* (1995) based on analysis of seismic reflection data (Figures 1.3 and 5.3c). These faults probably extend only across the continental shelf, since the deformation in the margin slope is dominated by extensional faulting and seamount subduction (Dominguez *et al.* 1998, von Huene *et al.* 2000, Ranero & von Huene 2000). A connection between both systems may follow the structures created in both environments by subduction of seamounts (C. Ranero private communication). In that sector, the slip is being accommodated largely aseismically, since the trenchward boundary of the upper plate seismicity is controlled by the margin wedge, approximately halfway between the border of the continental shelf and the coast.

A cluster of earthquakes was recorded also in the surroundings of Puriscal town, on the Miocene volcanic front, at kilometer 140 along profile 3 (Figure 5.5). This area shows an increased seismicity rate since 1990, after the occurrence of the Cóbano earthquake. Several hours after the mainshock (Protti *et al.* 1995b), a sequence started 60 km inland and lasted for several months in a conjugated system of northeast-striking, left-lateral and northwest-striking, right-lateral faults; it included the 1990 Ms 5.7 Puriscal earthquake (Barquero *et al.* 1991). Such connexion between major events nucleated at the subduction zone and seismicity triggered in the upper plate have been noticed for several historic events in the Central Pacific area of Costa Rica. These cycles may reflect the arcward transfer of convergent stress by shallow subduction (Marshall *et al.* 2000).

Chapter 6

Conclusions and outlook

This study is based on the earthquake database acquired with a combined on- and offshore seismological network, installed during approximately six months at the convergent margin of Central Costa Rica. Almost 2000 events were generated at the target area and the immediate surroundings during this period. The results of the experiment show once more the importance of the combination of on- and offshore, "amphibious", seismological networks in the study of the shallower portion of subduction zones, which normally lie offshore. This is evident when considering earthquake location uncertainties. Reliable, well-constrained hypocenter locations require, in general, more than six P-wave observations with a good azimuthal distribution of stations (GAP < 180°) (Husen *et al*. 2003b).

Following those criteria, a subdataset of 595 earthquakes recorded by the Jacó experiment was selected. Using the P-wave traveltimes from these earthquakes, combined with information provided by controlled-source seismology profiles available for the area, a 3-D tomographic model of the shallow part of the subduction zone (< 70 km) in the Central Costa Rican Pacific margin was obtained. The use of ocean-bottom stations allowed determination of reliable hypocenters from the trench to the coast for the first time in this area. Several tools for model resolution estimation were applied to define the areas of the model well resolved with the available dataset and network configuration. Additionally, first-motion, double-couple focal mechanisms were determined for earthquakes originated at the plate interface, the subducting slab and the overriding plate to better characterize the deformation processes taking place in those scenarios.

The 3-D velocity structure of this sector of the Costa Rican margin, well resolved from the trench down to 60-70 km depth, presents a certain degree of complexity, evidenced by subducted seamounts, the transition from normal to thickened subducted oceanic crust and, possibly, tectonic underplating, taking place along a relatively short distance. This structure also reflects various processes recognised in subduction

zones, invoked in this work to account for the observed anomalies, such as slab hydration through bend faulting, tectonic erosion and slab dehydration.

The subducting slab is imaged down to ~70 km depth, as a high-velocity perturbation with a conspicuous band of low velocities (LVB) on top, which contains the intraslab seismicity deeper than ~30 km. This LVB is the expression of several processes varying in depth and along the margin. From the trench down to 20-25 km depth, the low velocities are found in the first 5-7 km of the slab, originated mainly by the fault system reactivated by bending at the trench and the outer rise and by hydration (Ranero *et al.* 2005). The LVB is locally thickened beneath the continental slope by the presence of the relatively small Jacó and Parrita seamounts, which have been previously identified with high-resolution bathymetry, reflection profiles, gravimetry and magnetic data (von Huene *et al.* 1995, 2000; Barckhausen *et al.* 1998).

The LVB broadens strongly toward the east, where it is preceded by an even sharper widening of the low velocities, interpreted as a big seamount or plateau, both with velocity structure similar to that reported for the Cocos Ridge (Walther 2003, Sallarès *et al.* 2003). This feature have not been recognized before due to its location beneath the continental shelf, an area that was not reached by previous geophysical surveys. The maximal thickness of the LVB imaged in this study concurs with the onset of the Fila Costeña (Coastal Range) onshore, considered as an inverted forearc basin (Kolarsky *et al.* 1995). It is proposed here that this striking change represents the transition from subduction of normal oceanic crust to Galapagos hotspot modified, thickened oceanic crust.

The presence of the thickened crust and the accompanying big seamount or plateau shows spatial reciprocity with an aseismic low-velocity anomaly revealed beneath the inner forearc, at the base of the crust of the upper plate. This anomaly could constitute the first geophysical image of the tectonic underplating of seamounts and material eroded from the upper plate, previously proposed to explain the differential uplift of blocks of the inner forearc in Central Costa Rica (Fisher *et al.* 1998, Marshall *et al.* 2000). Alternatively, its aseismic quality suggests that the anomaly underneath the inner forearc could be caused by accumulation of upward migrating fluids, trapped at the base of the overlying crust by the presence of the seamount or plateau, which locally increases interplate coupling.

To the west and at the center of the area modelled in this study, the interplate seismicity forms a dipping, planar cluster from 15-19 to 25 km depth, distributed between 55 to 80-85 km from the trench axis, beneath the continental shelf. The onset of the interplate seismicity may be controlled by the erosional process and associated distribution of fluids, active along the shallower part of the margin. The updip limit of the seismogenic zone determined in this study is in close agreement with a recently proposed model for the hydrogeological system in erosional margins (Ranero *et al.* 2008), based on late observations from different zones of the world. Early dehydration reactions taking place between 60°C and 150°C in subducted sediments, release fluids at the plate boundary which are overpressured and escape then upward through

fracturing in the upper plate. The sector of the plate boundary where fluids are profuse corresponds to the area where tectonic erosion is evidenced by subsidence and formation of the continental slope. The decreasing in the amount of fluids with depth enables the transition from stable to unstable, seismic behaviour along the plate interface.

To the east, the interplate seismicity becomes abruptly scarce, and forms three clusters at different depths, at least during this experiment: one at the updip limit, and the other two coinciding with the landward edge of the seamount or plateau and the trenchward border of the low-velocity anomaly found beneath the inner forearc. This, together with the landward retreat of the updip limit of the interplate seismicity, could be caused by a reduced thickness and mechanical competence of the upper plate in this sector, coincident with the biggest embayment along the margin slope. Alternatively, this sector could be locked or, to the contrary, the anomaly below the forearc could be pushing the upper plate upward, strongly reducing the coupling (Nakada *et al.* 2002).

Thermal modelling along the Nicaragua-Costa Rica margin (Peacock *et al.* 2005) predicts temperatures of ~400-450° C at 25-30 km depth at the plate interface. These high temperatures and the relatively low amount of serpentinization estimated at the forearc mantle wedge may indicate that the downdip limit of the interplate seismicity is thermally controlled. Nevertheless, the data are not conclusive, given the uncertainties of the thermal model and the uncertainty on the determination of the location of the continental Moho, due to the absence of a strong velocity contrast observed along the Costa Rican margin (e.g. Sallarès *et al.* 2001, DeShon *et al.* 2006).

“Burst”-type swarms, a special case of repeating earthquakes, were detected at the plate interface and in the upper plate. They are clusters of events with nearly identically waveforms and similar magnitudes, very short recurrence intervals, repeating within hours or days of each other, and are active for only short periods. In the area of the experiment, their occurrence coincides with the two larger asperities detected at the plate boundary: the Cóbano seamount and the seamount or plateau imaged by this study. Possibly, they are originated by repetitive rupture of the same relief patches over the seamounts.

The rough-relief ocean floor characteristic of this sector of the margin has profound effects in plate coupling (Protti *et al.* 1994, 1995b), reducing it to patches that break generating moderate earthquakes in contrast to the stronger coupling to the northwest and southeast. Higher small-magnitude seismicity rates and the occurrence of the burst-type episodes coincide with the Cóbano seamount and the big seamount or plateau. Additionally, it is speculated in this study that the presence of seamounts beneath the margin slope could locally shift the updip onset of interplate seismicity by accelerating fluid escape through the disruption structures that they propitiate.

Intraslab earthquakes were detected from the outer rise down to depths greater than 100 km. The highest rates coincide with subduction of thickened crust, where they

distribute all over the width of the LVB. If slab dehydration enables seismicity, as widely accepted, and hydration of thickened oceanic crust at the outer rise-trench area is much reduced due to impaired bending ability (von Huene *et al.* 2000, Ranero *et al.* 2005), then hydration at alternative tectonic scenarios seems to play an important role for seismogenesis.

The margin wedge is imaged as a prominent negative anomaly which ends sharply toward the coast, in concordance with the strong normal faulting and fluid venting detected by previous studies (Ranero & von Huene 2000, Hensen *et al.* 2004), which are the result of the ongoing tectonic-erosion processes underneath (von Huene *et al.* 2004, Ranero *et al.* 2008). The upper plate seismicity is limited trenchward by the margin wedge. The focal mechanisms are in good agreement with previous models of upper plate internal deformation. Burst-type seismic swarms were also detected in the overriding plate. The aseismic low-velocity anomaly at the base of the crust in the inner forearc promotes seismicity in its surroundings by high-friction with the overriding plate, and could be linked to a Mw-6.4 earthquake that caused extensive damage to civil structures along the coast in 2004.

The margin structure and the seismicity presented here are the result of a relatively short recording period. The complex dynamics of subduction zones calls for longer deployment periods in order to more fully understand the processes and their evolution through time. Valuable information from complementing data and techniques, such as attenuation, gravimetry, geodetic modelling and global tomography, could contribute to a better characterization of the rocks physics, stress, deformation and structure, and therefore to gain further insights into the subduction processes. The unfortunate failure of the seismometers deployed offshore decreased the coverage for S-wave traveltimes toward the trench, considerably limiting the resolution of the Vp/Vs model. A better constrained and more extended Vp/Vs model could improve the characterization of the rocks physics, therefore contributing to refine the interpretation.

Finally, the results from this and similar surveys (DeShon *et al.* 2003, DeShon *et al.* 2006) along the margin contribute to obtain an improved image of the configuration of the shallower part of the subduction zone. This knowledge is necessary for reliable and updated seismic hazard studies which constitute the base of seismic codes for construction of civil structures and land regulation.

References

Abers, G.A., Hydrated subducted crust at 100-250 km depth, *Earth Planet. Sci. Lett., 176*, 323-330, 2000.

Abers, G.A., P.E. van Keken, E.A. Kneller, A. Ferris, and J.C. Stachnik, The thermal structure of subduction zones constrained by seismic imaging: Implications for slab dehydration and wedge flow, *Earth Planet. Sci. Lett., 241*, 387-397, 2006.

Abercrombie, R., M. Antolik, K. Felzer, and G. Ekström, The 1994 Java tsunami earthquake: Slip over a subducting seamount, *J. Geophys. Res., 106*, 6595-6607, 2001.

Abratis, G.A. and G. Wörner, Ridge collision, slab-window formation, and the flux of Pacific asthenosphere into the Caribbean realm, *Geology, 29*, 127-130, 2001.

Adamek, S.H., C. Frohlich, and W. Pennington, Seismicity of the Caribbean-Nazca boundary: Constraints on microplate tectonics of the Panama region, *J. Geophys. Res., 93*, 2053-2075, 1988.

Arroyo, I.G., *Sismicidad y Neotectónica en la región de influencia del Proyecto Boruca: hacia una mejor definición sismogénica del sureste de Costa Rica*, Licenciatura Thesis, Universidad de Costa Rica, 2001.

Avants, M., S.Y. Schwartz, A.V. Newman, and H.R. DeShon, Large underthrusting earthquakes beneath the Nicoya Peninsula, *EOS Trans. Am. Geophys. Un., 82*, F1266, 2001.

Barboza, G., J. Barrientos and A. Astorga, Tectonic evolution and sequence stratigraphy of the Central Pacific Margin of Costa Rica, *Rev. Geol. Amér. Central, 18*, 43-63, 1995.

Barckhausen, U., H.A. Roeser, and R. von Huene, Magnetic signature of upper plate structures and subducting seamounts at the convergent margin off Costa Rica, *J. Geophys. Res., 103*, 7079-7094, 1998.

Barckhausen, U., C. Ranero, R. von Huene, S.C. Cande, and H.A. Roeser, Revised tectonics boundaries in the Cocos Plate off Costa Rica: Implications for the segmentation of the convergent margin and for plate tectonic models, *J. Geophys. Res., 106*, 19,207-19,220, 2001.

Barquero, R., I. Boschini, A. Climent, M. Fernández, and W. Rojas, *La crisis sísmica del Golfo de Nicoya y eventos sísmicos relacionados*, 163 pp., internal report, Instituto Costarricense de Electricidad, 1991.

Baumann, M., Three-dimensional modeling of the crust-mantle boundary in the Alpine region, Ph.D. Thesis, ETH Zurich, Switzerland, 1994.

Bialas, J., and E.R. Flueh, A new Ocean Bottom Seismometer (with a new type of datalogger), *Sea Technology, 40*, 41-46, 1999.

Bilek, S.L., S.Y. Schwartz, and H.R. DeShon, Control of seafloor roughness on earthquake rupture behaviour, *Geology, 31*, 455-458, 2003.

Bilek, S.L., and C. Lithgow-Bertelloni, Stress changes in the Costa Rica subduction zone due to the 1999 Mw=6.9 Quepos earthquake, *Earth Planet. Sci. Lett*., *230*, 97-112, 2005.

Brace, W.F., and J.D. Byerlee, Strick slip as a mechanism for earthquakes, *Science, 153*, 990-992, 1966.

Burbach, G.V., C. Frohlich, W.D. Pennington, and T. Matumoto, Seismicity and tectonics of the subducted Cocos Plate, *J. Geophys. Res*., *89*, 7719-7735, 1984.

Byrne, D.E., D.M. Davis, and L.R. Sykes, Loci and maximum size of thrust earthquakes and the mechanics of the shallow region of subduction zones, *Tectonics, 7*, 833-857, 1988.

Carlson, R.L. and D.J. Miller, Mantle wedge water contents estimated from seismic velocities in partially serpentinized peridotites, *Geophys. Res. Lett.*, *30*, 1250, doi:10.1029/2002GL016600, 2003.

Carr, M.J., and R.E. Stoiber, Volcanism, in *The Caribbean Region. The Geology of North America*, edited by G. Dengo and J.E. Case, pp. 375-392, GSA, Boulder, Colorado, 1990.

Chapple, W.M., and D.W. Forsyth, D.W., Earthquakes and bending plates at trenches, *J. Geophys. Res., 84,* 6,729–6,749, 1979.

Christensen, N.I., and W.D. Mooney, Seismic velocity structure and composition of the continental crust: A global view, *J. Geophys. Res*., *100*, 9761-9788, 1995.

Christeson, G.L., K.D. McIntosh, T.H. Shipley, E.R. Flüeh, and H. Goedde, Structure of the Costa Rica convergent margin, offshore Nicoya Peninsula, *J. Geophys. Res.*, *104*, 25,443-25,468, 1999.

Clift, P., and P. Vannucchi, Controls on tectonic accretion versus erosion in subduction zones: Implications for the origin and recycling of the continental crust, *Rev. Geophys*., *42*, doi:10.1029/2003RG000127, 2004.

Clift, P.D., and A.J. Hartley, Slow rates of subduction erosion and coastal underplating along the Andean margin of Chile and Peru, *Geology*, *35*, 503-506, 2007.

Cloos, M., Thrust-type subduction-zone earthquakes and seamount asperities: a physical model for seismic rupture, *Geology*, 20, 601-604, 1992.

Cloos, M., and R.L. Shreve, Shear-zone thickness and the seismicity of Chilean- and Marianas-type subduction zones, *Geology, 24*, 107-110, 1996.

Corrigan, J., P. Mann, and J.C. Ingle, Forearc response to subduction of the Cocos Ridge, Panama-Costa Rica, *Geol. Soc. Am. Bull.*, *102*, 628-652, 1990.

DeMets, C., A new estimate for present-day Cocos-Caribbean plate motion: Implications for slip along the Central American volcanic arc, *Geophys. Res. Lett.*, *28*, 4043-4046, 2001.

DeMets C., R. Gordon, D.F. Argus, and S. Stein, Effect of recent revisions to the geomagnetic reversal timescale on estimates of current plate motions, *Geophys. Res. Lett.*, *21*, 2191-2194, 1994.

Denyer, P., and G.E. Alvarado, *Mapa Geológico de Costa Rica 2007-Escala 1:400000*, Editorial Francesa - Universidad de Costa Rica, San José, Costa Rica, 2007.

Denyer, P., P.O. Baumgartner, and E. Gazel, Characterization and tectonic implications of Mesozoic-Cenozoic oceanic assemblages of Costa Rica and Western Panama, *Geologica Acta*, *4*, 219-223, 2006.

DeShon, H.R., *Seismogenic zone structure along the Middle America subduction zone, Costa Rica*, Ph.D. Thesis, University of California Santa Cruz, 2004.

DeShon, H.R., and S.Y. Schwartz, Evidence for serpentinization of the forearc mantle along the Nicoya Peninsula, Costa Rica, *Geophys. Res. Lett.*, *31*, doi:10.1029/2002JB002294, 2004.

DeShon, H.R., S.Y. Schwartz, S.L. Bilek, L.M. Dorman, V. González, J.M. Protti, E.R. Flueh, and T.H. Dixon, Seismogenic zone structure of the southern Middle America Trench, Costa Rica, *J. Geophys. Res*., *108*, doi:10.1029/2002JB002294, 2003.

DeShon, H.R., S.Y. Schwartz, A.V. Newman, V. González, M. Protti, L.M. Dorman, T.H. Dixon, D.E. Sampson, and E.R. Flueh, Seismogenic zone structure beneath the Nicoya Peninsula, Costa Rica, from three-dimensional local earthquake P- and S-wave tomography, *Geophys. J. Int*., *164*, 109-124, doi:10.1111/j.1365-246X.2005.02809.x, 2006.

Dominguez, S., S.E. Lallemand, J. Malavieille, and R. von Huene, Upper plate deformation associated with seamount subduction, *Tectonophysics*, *293*, 207-224, 1998.

Eberhart-Phillips, D., Three-dimensional velocity structure in Northern California Coast Ranges from inversion of local earthquake arrival times, *Bull. Seism. Soc. Am.*, *76*, 1025-1052, 1986.

Eberhart-Phillips, D., Three-dimensional *P* and *S* velocity structure in the Coalinga region, California, *J. Geophys. Res.*, *95*, 15,343-15,363, 1990.

Eberhart-Phillips, D., Local earthquake tomography: earthquake source regions, in *Seismic Tomography: Theory and Practice*, edited by H.M. Iyer and K. Hirahara, Chapman and Hall, London, United Kingdom, 1993.

Evans, J.R., D. Eberhart-Phillips, and C.H. Thurber, User's manual for SIMULPS12 for imaging Vp and Vp/Vs: a derivative of the Thurber tomographic inversion SIMUL3 for local earthquakes and explosions. *U.S. Geol. Surv. Open-File Report 94-431*, U. S. Government Printing Office, 1994.

Fisher, A.T., C.A. Stein, R.N. Harris, K Wang, E.A. Silver,. M. Pfender, M. Hutnak, A. Cherkaoui, R. Bodzin, and H. Villinger, Abrupt thermal transition reveals hydrothermal boundary and role of seamounts within the Cocos Plate, *Geophys. Res. Lett*., *30*, 1550, doi:10.1029/2002GL016766, 2003.

Fisher, D.M., T.W. Gardner, J.S. Marshall, and W. Montero P., Kinematics associated with late Cenozoic deformation in central Costa Rica: Western boundary of the Panama microplate, *Geology*, *22*, 263-266, 1994.

Fisher, D.M., T.W. Gardner, J.S. Marshall, P.B. Sak, and M. Protti, Effect of subducting sea-floor roughness on fore-arc kinematics, Pacific coast, Costa Rica, *Geology*, *26*, 467-470, 1998.

Fisher, D.M., T.W. Gardner, P.B. Sak, J.D. Sanchez, K. Murphy, and P. Vannucchi, Active thrusting in the inner forearc of an erosive convergent margin, Pacific coast, Costa Rica, *Tectonics, 23*, doi:10.1029/2002TC001464, 2004.

Flores-Hernández, A., *Processing and interpretation of multichannel seismic reflection data on continental and oceanic crust of the Pacific margin of Costa Rica*, Diploma Thesis, Christian-Albrechts-Univ., Kiel, Germany, 1996.

Flueh, E. R., and J. Bialas, A digital, high data capacity ocean bottom recorder for seismic investigations, *Int. Underwater Systems Design*, *18* , 18–20, 1996.

Flueh, E., E. Soeding, and E. Suess, *Cruise Report SO173/1, 3 & 4 Subduction II: The Central American Continental Margin*, 495 pp., ISSN 0936-5788, GEOMAR Report 115, 2003.

Flueh, E.R, and C. Goltz, Report on subproject A2: Coupling and mass transfer between upper and lower plate, in *Report on work in progress and results of Special Research Program 574 Volatiles and Fluids in Subduction Zones: Climate Feedback and Trigger Mechanisms for Natural Disasters*, University Christian Albrecht of Kiel, Germany, 2004.

Gardner, T.W., D. Verdonck, N.M. Pinter, R. Slingerland, K.P. Furlong, T.F. Bullard and S.G. Wells, Quaternary uplift astride the aseismic Cocos Ridge, Pacific coast, Costa Rica, *Geol. Soc. Am. Bull., 104*, 219-232, 1992.

Gardner, T.W., J. Marshall, D. Merritts, M. Protti, B. Bee, R. Burgette, E. Burton, J. Cooke, N. Kehrwald, D. Fisher, and P. Sak, Holocene fore arc block rotation in response to seamount subduction, southeastern Peninsula de Nicoya, Costa Rica, *Geology, 29*, 151-154, 2001.

Giambalvo, E.R., A.T. Fisher, J.T. Martin, L. Darcy, and R.P. Lowell, Origin of elevated sediment permeability in a hydrothermal seepage zone, eastern flank of the Juan de Fuca Ridge, and implications for transport of fluid and heat, *J. Geophys. Res., 105*, 913-928, 2000.

Grevemeyer, I., C.R. Ranero, E.R. Flueh, D. Kläschen, and J.Bialas, Passive and active seismological study of bending-related faulting and mantle serpentinization at the Middle America trench, *Earth planet. Sci. Lett., 258*, 528-542, 2007.

Güendel, F., *Seismotectonics of Costa Rica: An analytical view of the southern terminus of the Middle America Trench*, Ph.D. Thesis, University of California Santa Cruz, 1986.

Hacker, B. R., S. M. Peacock, G. A. Abers, and S. D. Holloway, Subduction factory: 2. Are intermediate-depth earthquakes in subducting slabs linked to metamorphic dehydration reactions?, *J. Geophys. Res.*, *108*(B1), 2030, doi:10.1029/2001JB001129, 2003.

Haslinger, F., *Velocity structure, seismicity and seismotectonics of Northwestern Greece between the Gulf of Arta and Zakynthos*, Ph.D. Thesis, ETH Zurich, Switzerland, 1998.

Haslinger, F., and E. Kissling, Investigating effects of 3-D ray tracing methods in local earthquake tomography, *Phys. Earth Planet. Inter., 123*, 103-114, 2001.

Haslinger, F., E. Kissling, J. Ansorge, E. Hatzfeld, E. Papadimitriou, V. Karakostas, K. Makropoulos, H.-G. Kahle, and Y. Peter, 3D crustal structure from local earthquake tomography around Gulf of Arta (Ionian region, NW Greece), *Tectonophys., 304*, 210-218, 1999.

Hauff, F., K. Hoernle, K., P. van den Bogaard, P., G. Alvarado, G., and D. Garbe-Schoenberg, Age and geochemistry of basaltic complexes in western Costa Rica: Contributions to the geotectonic evolution of Central America, *Geochem. Geophys. Geosyst.***,** *1***,** 1999GC000020, 2000.

Havskov, J., L., and L. Ottemöller, *SEISAN: The Earthquake Analysis Software for Windows, Solaris and LINUX, version 8.1*, University of Bergen, Norway, 2005.

Hensen, C., K. Wallmann, M. Schmidt, C.R. Ranero, and E. Suess, Fluid expulsion related to mud extrusion off Costa Rica-A window to the subducting slab, *Geology, 32,* 201–204, 2004.

Hinz, K., R. von Huene, C.R. Ranero, and the PACOMAR Working Group, Tectonic structure of the convergent margin offshore Costa Rica from multichannel seismic reflection data, *Tectonics, 15*, 54-66, 1996.

Husen, S., *Local earthquake tomography of a convergent margin, north Chile: A combined on- and offshore study*, Ph.D. Thesis, Christian-Albrechts-Univ., Kiel, Germany, 1999.

Husen, S., and R.B. Smith, Probabilistic Earthquake Relocation in Three-Dimensional Velocity Models for the Yellowstone National Park Region, Wyoming, *Bull. Seism. Soc. Am., 94*, 880–896, 2004.

Husen, S., E. Kissling, E.R. Flueh, and G. Asch, Accurate hypocentre determination in the seismogenic zone of the subducting Nazca Plate in northern Chile using a combined on-/offshore network, *Geophys. J. Int., 138*, 687-701, 1999.

Husen, S., E. Kissling, and E.R. Flueh, Local earthquake tomography of shallow subduction in north Chile: A combined onshore and offshore study, *J. Geophys. Res., 105*, 28,183-28,198, 2000.

Husen, S., R. Quintero, and E. Kissling, Tomographic evidence for a subducted seamount beneath the Gulf of Nicoya, Costa Rica: the cause of the 1990 Mw = 7.0 Gulf of Nicoya earthquake, *Geophys. Res. Lett., 29*, doi:10.1029/2001GL014045, 2002.

Husen, S., R. Quintero, E. Kissling, and B. Hacker, Subduction-zone structure and magmatic processes beneath Costa Rica constrained by local earthquake tomography and petrological modeling, *Geophys. J. Int., 155*, 11-32, 2003a.

Husen, S., E. Kissling, N. Deichmann, S. Wiemer, D. Giardini, and M. Baer, Probabilistic earthquake location in complex three-dimensional velocity models: Application to Switzerland, *J. Geophys. Res., 108* (B2), doi:10.1029/2002JB001778, 2003b.

Husen, S., R.B. Smith, and G.P. Waite, Evidence for gas and magmatic sources beneath the Yellowstone volcanic field from seismic tomographic imaging, *J. Volcanol. Geotherm. Res., 131*, 397-410, 2004.

Hyndman, R.D. and S.M. Peacock, Serpentinization of the forearc mantle, *Earth Planet. Sci. Lett., 212*, 417-432, 2003.

Hyndman, R. D., K. Wang, and M. Yamano, Thermal constraints on the seismogenic portion of the southwestern Japan subduction thrust, *J. Geophys. Res., 100*, 15,373–15,392, 1995.

Hyndman, R.D., M. Yamano, and D.A. Oleskevich, The seismogenic zone of subduction thrust faults, *The Island Arc, 6*, 244-260, 1997.

Jarrard, R. D., Terrane motion by strike-slip faulting of forearc slivers, *Geology, 14*, 780-783, 1986.

Jiao, W., P. G. Silver, Y. Fei, and C. T. Prewitt (2000), Do intermediate- and deep-focus earthquakes occur on preexisting weak zones? An examination of the Tonga subduction zone, *J. Geophys. Res., 105*, 28,125– 28,138, 2000.

Johnston, S.T. and D.J. Thorkelson, Cocos-Nazca slab window beneath Central America, *Earth Planet. Sci. Lett*., 27, 425-428, 1997.

Igarashi, T., T. Matsuzawa, and A. Hasegawa, Repeating earthquakes and interplate aseismic slip in the northeastern Japan subduction zone, *J. Geophys. Res., 108*, 2249, doi:10.1029/2002JB001920, 2003.

Kimura, G., E. Silver, and Shipboard Scientific Party, *Proceedings of the Ocean Drilling Program Initial Reports*, vol. 170, Ocean Drill. Program, College Station, Texas, 1997.

Kimura, H., K. Kasahara, T. Igarashi, and N. Hirata, Repeating earthquake activities associated with the Philippine Sea plate subduction in the Kanto district, central Japan: a new plate configuration revealed by interplate aseismic slips, *Tectonophysics*, *417*, 101–118, 2006.

Kirby, S.H., E.R. Engdahl, and R. Denlinger, Intermediate-depth intraslab earthquakes and arc volcanism as physical expressions of crustal and uppermost mantle metamorphism in subducting slabs, in *Subduction: Top to Bottom*, edited by G.E. Bebout et al., *Geophys. Monogr. Ser*., vol. 96, pp.195-214, AGU, Washington D.C., 1996.

Kissling, E., Geotomography with local earthquake data, *Rev. Geophys., 26*, 659-698, 1988.

Kissling, E., W.L. Ellsworth, D. Eberhardt-Phillips, and U. Kradolfer, Initial reference models in local earthquake tomography, *J. Geophys. Res., 99*, 19,635-19,646, 1994.

Kissling, E., U. Kradolfer, and H. Maurer, *VELEST user's guide - short introduction*, Inst. of Geophys. and Swiss Seismol. Serv., ETH, Zurich, 1995.

Kissling, E., J. Ansorge, and M. Baumann, Methodological considerations of 3-D crustal structure modeling by 2-D seismic methods, in *Deep structure of the Swiss Alps: Results of the NRP20*, edited by O.A. Pfiffner, P. Lehner, P. Heitzmann, St. Mueller, and A. Steck, pp. 31-38, Birkhäuser Verlag, Basel, Switzerland, 1997.

Kissling, E., S. Husen, and F. Hasslinger, Model parameterization in seismic tomography: A choice of consequences for the solution quality, *Phys. Earth. Plan. Int., 123*, 89-101, 2001.

Kodaira, S., N. Takahashi, A. Nakanishi, S. Miura, and Y. Kaneda, Subducted seamount imaged in the rupture zone of the 1946 Nankaido earthquake, *Science, 289*, 104-106, 2000.

Kolarsky, R.A., P. Mann, and W. Montero, Island arc response to shallow subduction of the Cocos Ridge, in *Geologic and Tectonic Development of the Caribbean Plate Boundary in Southern Central America*, edited by P. Mann, *Spec. Pap. Geol. Soc. Am. 295*, 235-262, 1995.

La Femina, P.C., T.H. Dixon, and W. Strauch, Bookshelf faulting in Nicaragua, *Geology, 30*, 751-754, 2002.

Lay, T., and T.C. Wallace, *Modern global seismology*, pp. 521, Academic Press, New York, 1995.

Laigle, M., and A. Hirn, Explosion-seismic tomography of a magmatic body beneath Etna: Volatile discharge and tectonic control of volcanism, *Geophys. Res. Lett*., *26*, 2665-2668, 1999.

Lee, W.H.K., and J.C. Lahr, HYPO71 (revised): A computer program for determining hypocenter, magnitude and first motion pattern of local earthquakes. *U.S. Geol. Surv. Open-File Report 75-311*, U. S. Government Printing Office, 1975.

Lefeldt, M., and I. Grevemeyer, Centroid depth and mechanism of trench-outer rise earthquakes, *Geophys. J. Int., 172*, 240-251, doi: 10.1111/j.1365-246X.2007.03616.x, 2007.

Leveque, J.-J., L. Rivera, and G. Wittlinger, On the use of the checkerboard test to asses the resolution of tomographic inversions, *Geophys. J. Int.*, *115*, 313-318, 1993.

Lienert, B.R.E., and J. Havskov, A computer program for locating earthquakes both locally and globally, *Seism. Res. Lett., 66*, 26-36, 1995.

Lin, C., B. Huang, and R. Rau, Seismological evidence for a low-velocity layer within the subducted slab of southern Taiwan, *Earth Planet. Sci. Lett*., *174*, 231-240, 1999.

Marshall, J.S., D.M. Fisher, and T.W. Gardner, Central Costa Rica deformed belt: Kinematics of diffuse faulting across the western Panama Block, *Tectonics*, *19*, 468-492, 2000.

Marshall, J.S., B.D. Idleman, T.W. Gardner, and D.M. Fisher, Landscape evolution within a retreating volcanic arc, Costa Rica, Central America, *Geology*, *31*, 419-422, 2003.

Matumoto, T., M. Ohtake, G. Latham, and J. Umaña, Crustal structure of the Southern Central America, *Bull. Seism. Soc. Am*., *67*, 121-134, 1977.

MacMillan, I., P.B. Gans, and G. Alvarado, Middle Miocene to present plate tectonic history of the southern Central American Volcanic Arc, *Tectonophysics*, *392*, 325-348, 2004.

Matsuzawa, T., T. Igarashi, and A. Hasegawa, Characteristic small-earthquake sequence off Sanriku, northeastern Honshu, Japan, *Geophys. Res. Lett*., *29*, 1543, doi:10.1029/2001GL014632, 2002

McIntosh, K., F. Akbar, C. Calderon, P. Stoffa, S. Operto, G. Christeson, Y. Nakamura, T. Shipley, E. Flueh, A. Stavenhagen, and G. Leandro, Large aperture seismic imaging of a convergent margin: Techniques and results from the Costa Rica seismogenic zone, *Mar. Geophys. Res*., *21*, 451-474, 2000.

Montero, W., El terremoto del 4 de marzo de 1924 (Ms= 7,0): ¿un gran temblor intraplaca relacionado al límite incipiente entre la placa Caribe y la microplaca de Panamá?, *Rev. Geol. Amér. Central*, *22*, 25-62, 1999.

Montero, W., Neotectónica de la región central de Costa Rica: frontera oeste de la microplaca de Panamá, *Rev. Geol. Amér. Central*, *24*, 29-56, 2001.

Montero, W., and A. Climent, Los terremotos de Grecia de 1882 y de Quepos de 1952, Costa Rica: distribución de intensidades y origen tectónico, *Ciencia y Tecnología*, *14*, 81-105, 1990.

Moore, J.C., and D. Saffer, Updip limit of the seismogenic zone beneath the accretionary prism of southwest Japan: An effect of diagenetic to low-grade metamorphic processes and increasing effective stress, *Geology*, 29, 193-186, 2001.

Moore, J.C., C. Rowe and F. Meneghini, How accretionary prisms elucidate seismogenesis in subduction zones, in *The seismogenic zone of subduction thrust faults,* edited by T.H. Dixon and J.C. Moore, Columbia University Press, New York, 2007.

Morales, L.D., Las zonas sísmicas de Costa Rica y alrededores, *Rev. Geol. Amér. Central, 3*, 69-101, 1985.

Nadeau, R. M., W. Foxall, and T.V. McEvilly, Clustering and periodic recurrence of microearthquakes on the San Andreas fault at Parkfield, California, *Science, 267,* 503– 507, 1995.

Nadeau, R., and T.V. McEvilly, Fault slip rates at depth from recurrence intervals of repeating microearthquakes, *Science, 285,* 718-721, 1999.

Newman, A.V., S.Y. Schwartz, V. Gonzales, H.R. DeShon, J.M. Protti, and L. Dorman, Along strike variability in the seismogenic zone below Nicoya Peninsula, Costa Rica, *Geophys. Res. Lett., 29*, doi:10.1029/2002GL015409, 2002.

Norabuena, E., T.H. Dixon, S.Y. Schwartz, H.R. DeShon, M. Protti, L. Dorman, E.R. Flüeh, P. Lundgren, A. Newman, F. Pollitz, and D. Sampson, Geodetic and seismic constraints on some seismogenic zone processes in Costa Rica, *J. Geophys. Res., 109,* B11403, doi:10.1029/2003JB002931, 2004.

Obana, K., S. Kodaira, Y. Kaneda, K. Mochizuki, M. Shinohara, and K. Suyehiro, Microseismicity at the seaward updip limit of the western Nankai Trough seismogenic zone, *J. Geophys. Res., 108,* 2459, doi:10.1029/2002JB002370, 2003.

Oleskevich, D.A., R.D. Hyndman, and K. Wang, The updip and downdip limits to great subduction earthquakes: Thermal and structural models of Cascadia, south Alaska, SW Japan and Chile, *J. Geophys. Res., 104,* 14,965-14,991, 1999.

Pacheco, J.F., R. Quintero, F. Vega, J. Segura, W. Jiménez, and V. González, The Mw 6.4 Damas, Costa Rica, Earthquake of 20 November 2004: Aftershocks and Slip Distribution, *Bull. Seism. Soc. Am., 96*, 1-12, 2006.

Pavlis, G.L., and J.R. Booker, The mixed discrete continuous inverse problem: Application to the simultaneous determination of earthquake hypocenters and velocity structure, *J. Geophys. Res., 85*, 4801-4810, 1980.

Peacock, S., Fluid processes in subduction zones, *Science, 248,* 329–337, 1990.

Peacock, S., Are the lower planes of double seismic zones caused by serpentine dehydration in subducting oceanic mantle?, *Geology, 29*, 299-302, 2001.

Podvin, P., and I. Lecomte, Finite difference computation of travel times in very contrasted velocity models: a massively parallel approach and its associated tools, *Geophys. J. Int., 105*, 271-284, 1991.

Protti, M., F. Güendel, and K. McNally, The geometry of the Wadati-Benioff zone under southern Central America and its tectonic significance: results from a high-resolution local seismographic network, *Phys. Earth Planet. Inter., 84*, 271-287, 1994.

Protti, M., F. Güendel, and K. McNally, Correlation between the age of the subducting Cocos plate and the geometry of the Wadati-Benioff zone under Nicaragua and Costa Rica, in

Geologic and Tectonic Development of the Caribbean Plate Boundary in Southern Central America, edited by P. Mann, *Spec. Pap. Geol. Soc. Am. 295*, 309-326, 1995a.

Protti, M., K. McNally, J. Pacheco, V.González, C. Montero, J. Segura, J. Brenes, V. Barboza, E. Malavassi, F. Güendel, G. Simila, D. Rojas, A. Velasco, A. Mata, and W. Schillinger, The March 25, 1990 (Mw = 7.0, ML = 6.8) earthquake at the entrance of the Nicoya Gulf, Costa Rica, *Geofísica Int.*, *100*, 20,345-20,358, 1995b.

Protti, M., S.Y. Schwartz, and G. Zandt, Simultaneous inversion for earthquake location and velocity structure beneath central Costa Rica, *Bull. Seis. Soc. Am.*, *86*, 19-31, 1996.

Quintero, R., and O. Kulhánek, Pn-wave observations in Costa Rica, *Geofís. Int.*, *37*, 171-182, 1998.

Quintero, R., and E. Kissling, An improved P-wave velocity reference model for Costa Rica, *Geofís. Int*, *40*, 3-19, 2001.

Ranero, C.R., and R. von Huene, Subduction erosion along the Middle America convergent margin, *Nature*, *404*, 748-752, 2000.

Ranero, C.R., R. von Huene, E.R. Flueh, M. Duarte, D. Baca, and K. McIntosh, A cross section of the convergent Pacific margin of Nicaragua, *Tectonics*, *19*, 335-357, 2000.

Ranero, C.R., J. Phipps Morgan, K. McIntosh, and C. Reichert, Bending-related faulting and mantle serpentinization at the Middle America trench, *Nature*, *425*, 367-373, 2003.

Ranero, C.R., A. Villaseñor, J.P. Morgan, and W. Weinrebe, Relationship between bend-faulting at trenches and intermediate-depth seismicity, *Geochem. Geophys. Geosyst.*, *6*, doi:10.1029/2005GC000997, 2005.

Ranero, C.R., I. Grevemeyer, H. Sahling, U. Barckhausen, C. Hensen, K. Wallmann, W. Weinrebe, P. Vannucchi, R. von Huene, and K. McIntosh, Hydrogeological system of erosional convergent margins and its influence on tectonics and interplate seismogenesis, *Geochem. Geophys. Geosyst.*, *9*, doi:10.1029/2007GC001679, 2008.

Reyners, M., D. Eberhart-Phillips, and G. Stuart, A three-dimensional image of shallow subduction: Crustal structure of the Raukumara Peninsula, New Zealand, *Geophys. J. Int.*, *137*, 873-890, 1999.

Rivier, F., Sección geológica del Pacífico al Atlántico a través de Costa Rica, *Rev. Geol. Amér. Central*, *2*, 23-32, 1985.

Ruepke, L.H., J. Phipps Morgan, M. Hort, and J.A.D. Connolly, Are the regional variations in Central American arc lavas due to differing basaltic versus peridotitic slab sources of fluids?, *Geology*, *30*, p. 1035-1038, 2002.

Ruepke, L., J. Phipps Morgan, M. Hort, and J. Connolly, J., Serpentine and the subduction zone water cycle, *Earth Planet. Sci. Lett.*, *223*, 17-34, 2004.

Saffer, D.M., and C. Marone, Comparison of smectite- and illite-rich gouge frictional properties: application to the updip limit of the seismogenic zone along subduction megathrusts, *Earth Planet. Sci. Lett.*, *215*, 219-235, 2003.

Sage, F., J. Y. Collot, and C. R. Ranero, Interplate patchiness and subduction-erosion mechanisms: Evidence from depth-migrated seismic images at the central Ecuador convergent margin, *Geology, 34*, 997–1000, doi:10.1130/G22790A.1, 2006.

Sallarès, V., and C.R. Ranero, Structure and tectonics of the erosional convergent margin off Antofagasta, norh Chile (23°30'S), *J. Geophys. Res., 110,* B06101, doi:10.1029/2004JB003418, 2005.

Sallarès, V., J.J. Dañobeitia, E.R. Flueh, and G. Leandro, Seismic velocity structure across the middle American landbridge in northern Costa Rica, *J. Geodyn., 27*, 327-344, 1999.

Sallarès, V., J.J. Dañobeitia, and E.R. Flueh, Lithospheric structure of the Costa Rican Isthmus: Effects of subduction zone magmatism on an oceanic plateau, *J. Geophys. Res., 106*, 621-643, 2001.

Sallarès, V., P. Charvis, E.R. Flueh, and J. Bialas, Seismic structure of Cocos and Malpelo Volcanic Ridges and implications for hot spot-ridge interaction, *J. Geophys. Res., 108*(B12), 2564, doi:10.1029/2003JB002431, 2003.

Scholz, C. H., Earthquakes and friction laws, *Nature, 391*, 37–42, 1998.

Scholz, C.H., and C. Small, The effect of seamount subduction on seismic coupling, *Geology, 25*, 487-490, 1997.

Schwartz, S.Y., and H.R. DeShon, Distinct up-dip limits to geodetic locking and microseismicity at the northern Costa Rica Seismogenic Zone: evidence for two mechanical transitions, in *The seismogenic zone of subduction thrust faults*, edited by T.H. Dixon and J.C. Moore, Columbia University Press, New York, 2007.

Schwartz, S.Y., and J. Rokosky, Slow slip events and seismic tremor at Circum-Pacific subduction zones, *Rev. Geophys., 45*, doi:10.1029/2006RG000208, 2007.

Seno, T., Variation of downdip limit of the seismogenic zone near the Japanese islands: Implications for the serpentinization mechanism of the forearc mantle wedge, *Earth Planet. Sci. Lett., 231*, 249-262, 2005.

Seno, T., and Y. Yamanaka, Double seismic zones, compressional deep trench-outer rise events, and superplumes, in *Subduction Top to Bottom*, edited by G.E. Bebout, D.W. Scholl, S.H. Kirby and J.P. Platt, *Geophys. Monogr. Ser*., 96, 347-355, 1996.

Shiomi, K., M. Matsubara, Y. Ito, and K. Obara, Simple relationship between seismic activity along Philippine Sea slab and geometry of oceanic Moho beneath southwest Japan, *Geophys. J. Int., 173*, 1018–1029, doi: 10.1111/j.1365-246X.2008.03786.x, 2008.

Shipley, T.H., K.D. McIntosh, E.A. Silver, and P.L. Stoffa, Three-dimensional seismic imaging of the Costa Rica accretionary prism: Structural diversity in a small volume of the lower slope, *J. Geophys. Res., 97*, 4439-4459, 1992.

Smith, W. H. F., and D. T. Sandwell, Global seafloor topography from satellite altimetry and ship depth soundings, *Science, 277,* 1957-1962, 1997.

Soeding, E., K. Wallmann, E. Suess, and E. Flueh, *Cruise Report M54/2 + M54/3 Fluids and Subduction Costa Rica 2002*, 366 pp., GEOMAR Report 111, 2003.

Snoke, J.A., FOCMEC: Focal MEChanism Determinations, in *International Handbook of Earthquake and Engineering Seismology*, edited by W.H.K. Leem, H. Kanamori, P.C. Jennings, and C. Kisslinger, Academic Press, San Diego, 2003.

Snoke, J.A., J. W. Munsey, A.C. Teague, and G.A. Bollinger, A program for focal mechanism determination by combined use of polarity and SV -P amplitude ratio data, *Earthquake Notes, 55*, 15, 1984.

Spinelli, G.A., and D.M. Saffer, Along-strike variations in underthrust sediment dewatering on the Nicoya margin, Costa Rica related to the updip limit of seismicity, *Geophys. Res. Lett.*, *31*, L04613, doi:10.1029/2003GL018863, 2004.

Spinelli, G.A., and M.B. Underwood, Character of sediments entering the Costa Rica subduction zone: Implications for partitioning of water along the plate interface, *Island Arc*, *13*, 432–451, 2004.

Stavenhagen, A., Refraktionsseimische Untersuchungen des akkretionären ozeanischen Kontinentalschelfes der Pazifikküste Costa Ricas, Diploma Thesis, Christian-Albrechts-Univ., Kiel, Germany, 1994.

Stavenhagen, A.U., *Refraktionsseismische Untersuchungen on- und offshore Costa Rica*, Ph.D. Thesis, Christian-Albrechts-Univ., Kiel, Germany, 1998.

Stavenhagen, A.U., E.R. Flueh, C. Ranero, K.D. McIntosh, T. Shipley, G. Leandro, A. Schultze, and J.J. Dañobeitia, Seismic wide-angle investigations in Costa Rica - A crustal velocity model from the Pacific to the Caribbean, *Zbl. Geol. Palaont., Teill. 1*, *3 (6)*, 393-408, 1998.

Stern, R.J., Subduction zones, *Rev. Geophys*., *40*, 1012, doi:10.1029/2001RG000108, 2002.

Templeton, D.C., R.M. Nadeau, and R. Bürgmann, Behavior of Repeating Earthquake Sequences in Central California and the Implications for Subsurface Fault Creep, *Bull. Seism. Soc. Am.*, *98*, 52-65, doi: 10.1785/0120070026, 2008.

Thurber, C.H., Earthquake locations and three-dimensional crustal structure in the Coyote Lake area, central California, *J. Geophys. Res.*, *88*, 8226-8236, 1983.

Tichelaar, B.W. and L.J. Ruff, Depth of seismic coupling along subduction zones, *J. Geophys. Res.*, *98*, 2017-2037, 1993.

Toomey, D.R. and G.R, Foulger, Tomographic inversion of local earthquake data from the Hengill-Grensdalur central volcano complex, Iceland, *J. Geophys. Res.*, *94*, 17,497-17,510, 1989.

Tournon, J., and G.E. Alvarado, *Mapa geológico de Costa Rica: folleto explicativo*, 79 pp., Ed. Tecnológica de C.R., Costa Rica, 1997.

Um, J., and C. Thurber, A fast algorithm for two point seismic ray tracing, *Bull. Seis. Soc. Am.*, *77*, 972-986, 1987.

Utheim, T., and J. Havskov, *The SEISLOG Data Acquisition System - PC version - Guide to installation, maintenance and daily operation of the system*, Institute of Solid Earth Physics, University of Bergen, Norway, 2002.

Vanucchi, P., D.W. Scholl, M. Meschede, and K. McDougall-Reid, Tectonic erosion and consequent collapse of the Pacific margin of Costa Rica: Combined implications from ODP Leg 170, seismic offshore data, and regional geology of the Nicoya Peninsula, *Tectonics*, *20*, 649-668, 2001.

Vannucchi, P., C.R. Ranero, S. Galeotti, S.M. Straub, D.W. Scholl, and K. McDougall-Ried, Fast rates of subduction erosion along the Costa Rica Pacific margin: Implications for nonsteady rates of crustal recycling at subduction zones, *J. Geophys. Res*., *108*(B11), 2511, doi:10.1029/2002JB002207, 2003.

Virieux, J., and V. Farra, Ray tracing in 3-D complex isotropic media: an analysis of the problem, *Geophysics*, *56*, 2057-2069, 1991.

von Huene, R., and D. Scholl, Observations at convergent margins concerning sediment subduction, subduction erosion, and the growth of continental crust, *Rev. Geophys*., *29*, 279–316, 1991.

von Huene, R. and E.R. Flueh, A review of marine geophysical studies along the Middle America Trench off Costa Rica and the problematic seaward terminus of continental crust, in *Profil*, *Band 7*, edited by H. Seyfried and W. Hellmann, pp. 143-159, Inst. Geol. Palaeont., Univ. Stuttgart, Germany, 1994.

von Huene, R., and C.R. Ranero, Subduction erosion and basal friction along the sediment-starved convergent margin off Antofagasta, Chile, *J. Geophys. Res*., *108*(B2), 2079, doi:10.1029/2001JB001569, 2003.

von Huene, R., D. Klaeschen, and B. Cropp, Tectonic structure across the accretionary and erosional parts of the Japan Trench margin, *J. Geophys. Res*., *99*, 349–361, 1994.

von Huene, R. and 16 others, Morphotectonics of the Pacific convergent margin of Costa Rica, in *Geologic and Tectonic Development of the Caribbean Plate Boundary in Southern Central America*, edited by P. Mann, *Spec. Pap. Geol. Soc. Am. 295*, 291-307, 1995.

von Huene, R., C. Ranero, W. Weinrebe, and K. Hinz, Quaternary convergent margin tectonics of Costa Rica, segmentation of the Cocos Plate, and Central American volcanism, *Tectonics*, *19*, 314-334, 2000.

von Huene, R., C. Ranero, and P. Vannucchi, Generic model of subduction erosion, *Geology*, *32*, doi:10.1130/G20563.1, 913-919, 2004a.

von Huene, R., R. Ranero, and P. Watts, Tsunamigenic slope failure along the Middle America Trench on two tectonic settings, *Marine Geology*, *203*, 303-317, 2004b.

Vrolijk, P., On the mechanical role of smectite in subduction zones, *Geology*, *18*, 703-707, 1990.

Waldhauser, F., *A parametrized three-dimensional Alpine crustal model and its application to teleseismic wavefront scattering*, Ph.D. Thesis, ETH Zurich, Switzerland, 1996.

Waldhauser, F., and L. Ellsworth, A double-difference location algorithm: method and application to the Northern Hayward Fault, California, *Bull. Seism. Soc. Am*., *90*, 1353-1368, 2000.

Waldhauser, F., E. Kissling, J. Ansorge, and S. Mueller, Three-dimensional interface modelling with two-dimensional seismic data: The Alpine crust-mantle boundary, *Geophys. J. Int*., *135*, 264-278, 1998.

Walther, C.H.E., The crustal structure of Cocos Ridge off Costa Rica, *J. Geophys. Res.*, *108*(B3), 2136, doi:10.1029/2001JB000888, 2003.

Walther, C., and E.R. Flueh, Remnant of the ancient Farallon Plate breakup: a low-velocity body in the lower oceanic crust off Nicoya Peninsula, Costa Rica - evidence from wide-angle seismics, *Geophys. Res. Lett., 29*, 1939, doi:10.1029/2002GL015026, 2002.

Warren, L. M., A. N. Hughes, and P. G. Silver, Earthquake mechanics and deformation in the Tonga-Kermadec subduction zone from fault-plane orientations of intermediate- and deep-focus earthquakes, *J. Geophys. Res.*, *112*, B05314, doi:10.1029/2006JB004677, 2007.

Warren, L.M., M.A. Langstaff, and P.G. Silver, Fault plane orientations of intermediate-depth earthquakes in the Middle America Trench, *J. Geophys. Res.*, *113*, B01304, doi:10.1029/2007JB005028, 2008.

Weinrebe, W., and E. Flueh, *Cruise Report SO163 Subduction I Multi-system analysis of fluid recycling and geodynamics at the continental margin off Costa Rica*, 547 pp., ISSN 0936-5788, GEOMAR Report 106, 2002.

Werner, R., K. Hoernle, P. van den Bogaard, C.R. Ranero, R. von Huene, and D. Korich, Drowned 14 m.y. old Galapagos archipielago off the coast of Costa Rica: Implications for tectonic and evolutionary models, *Geology*, *27*, 499-502, 1999.

Wessel, P. and W. H. F. Smith, New, improved version of the Generic Mapping Tools released, *EOS Trans. Amer. Geophys. U.*, *79*, 579, 1998

Ye, S., J. Bialas, E.R. Flueh, A. Stavenhagen, R. von Huene, G. Leandro, and K. Hinz, Crustal strucure of the Middle America Trench off Costa Rica from wide-angle seismic data, *Tectonics*, *15*, 1006-1021, 1996.

Zhang, J., H. W. Green II, K. Bozhilov, and Z. Jim, Faulting induced by precipitation of water at grain boundaries in hot subducting oceanic crust, *Nature*, *428*, 633– 636, 2004.

Appendix

Focal mechanism solutions

Next pages: Lower-hemisphere stereographic projections of the focal mechanisms shown in Figure 5.3 and Table 5.1. Compressional first P-wave onsets shown in red and dilatational in blue. P and T axes as indicated. Date and number of inconsistent polarities (inc) given for each event.

Interplate earthquakes

1) May 10, 2002 09:06 inc=0

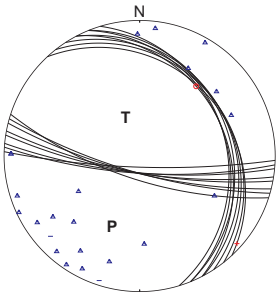

6) June 6, 2002 20:33 inc=2

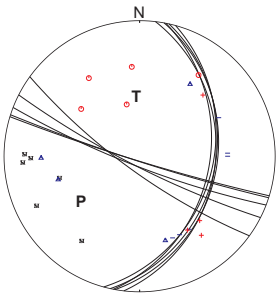

11) July 6, 2002 20:09 inc=0

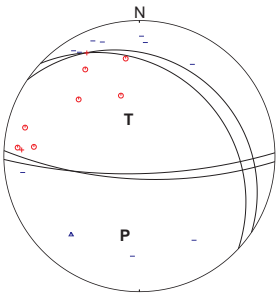

2) May 19, 2002 14:32 inc=0

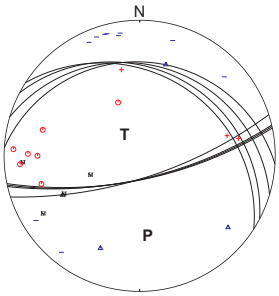

7) June 11, 2002 23:44 inc=0

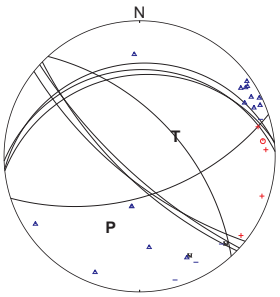

12) Aug. 2, 2002 05:16 inc=1

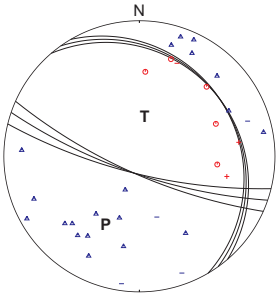

3) May 20, 2002 12:23 inc=1

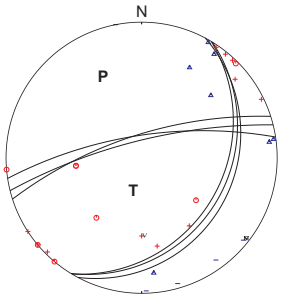

8) June 23, 2002 19:50 inc=1

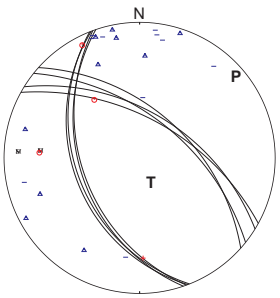

13) Aug. 2, 2002 07:28 inc=0

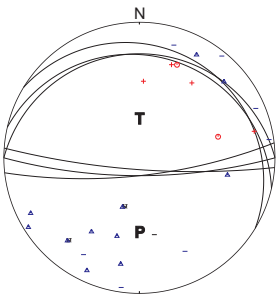

4) May 23, 2002 09:30 inc=2

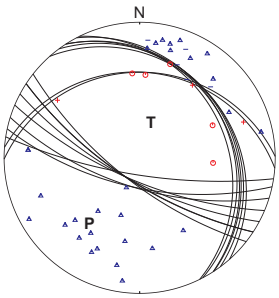

9) July 3, 2002 22:07 inc=0

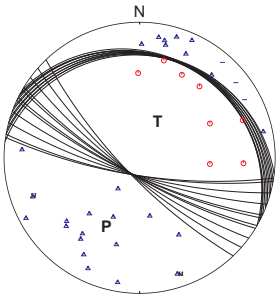

14) Aug. 7, 2002 00:08 inc=2

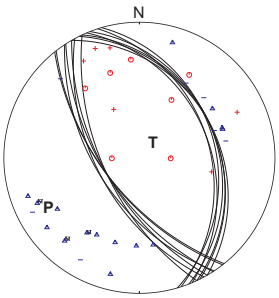

5) May 23, 2002 21:22 inc=2

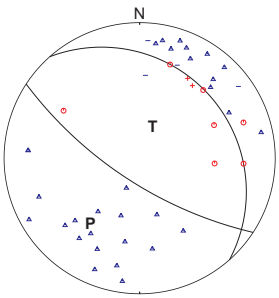

10) July 6, 2002 18:00 inc=1

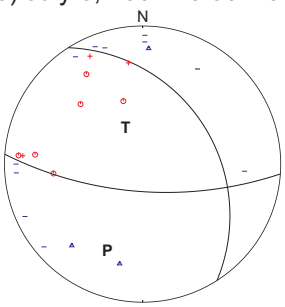

15) Aug. 14, 2002 05:34 inc=0

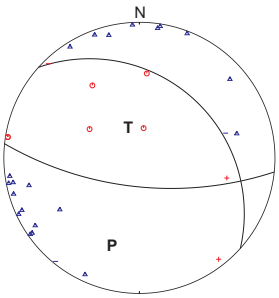

16) Aug. 14, 2002 19:53 inc=0

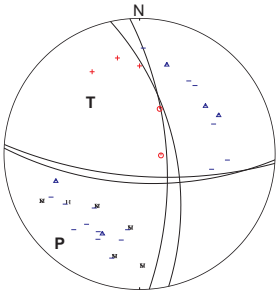

17) Aug. 18, 2002 18:38 inc=1

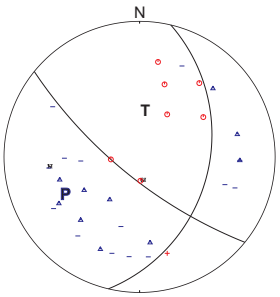

18) Aug. 31, 2002 13:04 inc=0

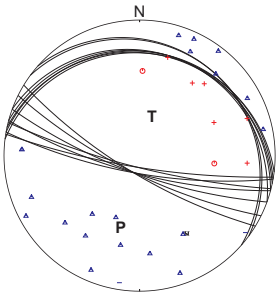

19) Aug. 31, 2002 17:28 inc=2

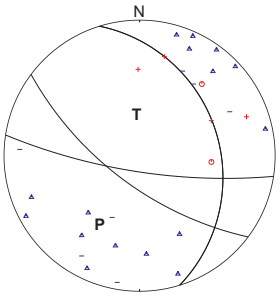

20) Sept. 8, 2002 08:12 inc=0

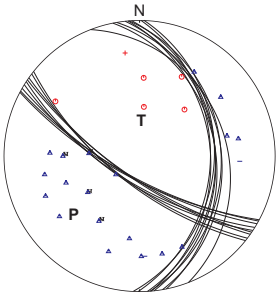

Intraslab earthquakes

1) Apr. 13, 2002 02:59 inc=1

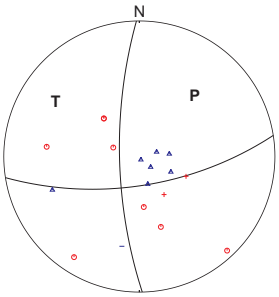

2) Apr. 26, 2002 22:27 inc=2

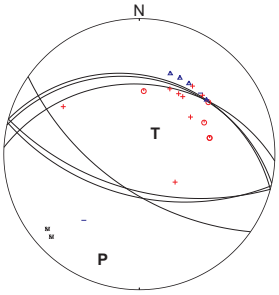

3) Apr. 28, 2002 13:55 inc=1

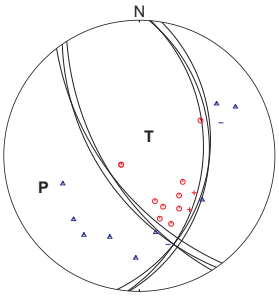

4) May 5, 2002 07:42 inc=0

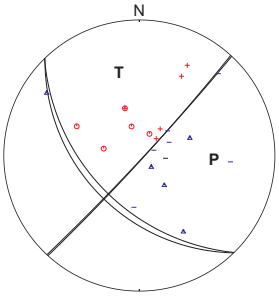

5) May 14, 2002 22:19 inc=0

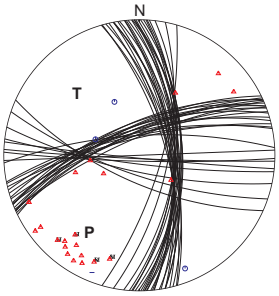

6) May 24, 2002 04:25 inc=1

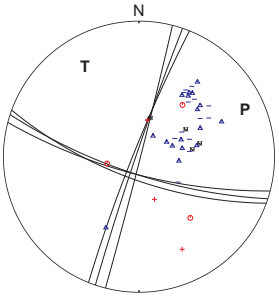

7) May 26, 2002 00:38 inc=0

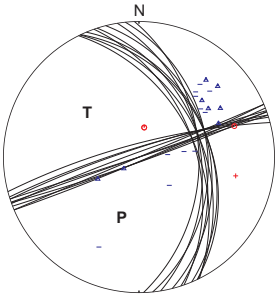

8) May 29, 2002 08:19 inc=0

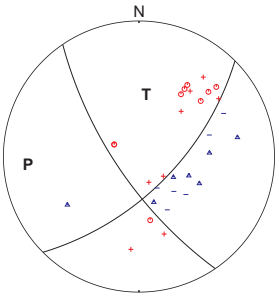

9) May 31, 2002 11:46 inc=0

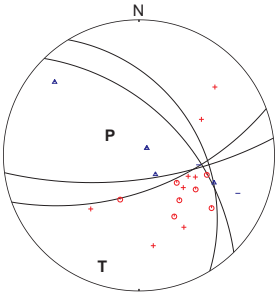

10) June 6, 2002 09:47 inc=0

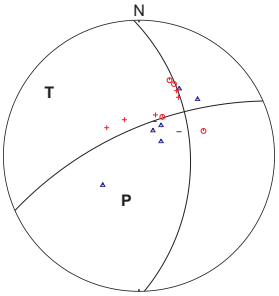

11) June 7, 2002 04:00 inc=0

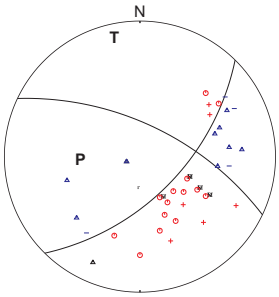

12) June 14, 2002 05:49 inc=1

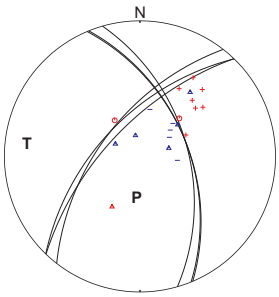

13) June 16, 2002 18:04 inc=0

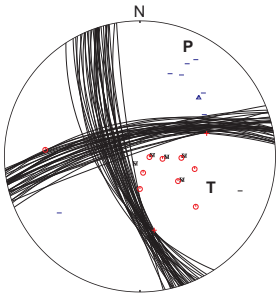

14) July 1, 2002 14:32 inc=0

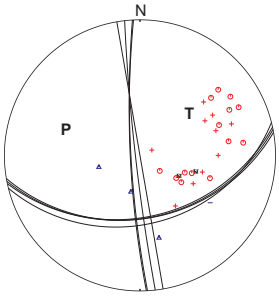

15) July 4, 2002 02:46 inc=1

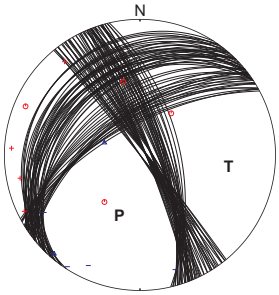

16) July 5, 2002 07:34 inc=0

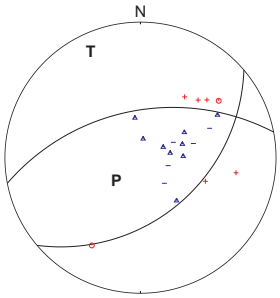

17) July 11, 2002 19:30 inc=1

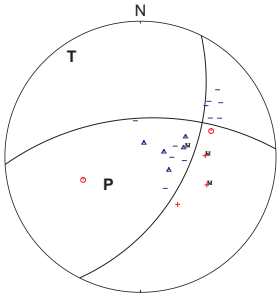

18) July 12, 2002 12:44 inc=0

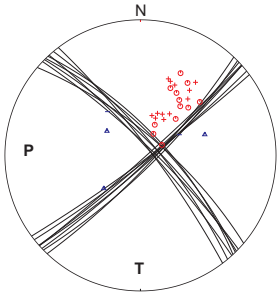

19) July 29, 2002 15:11 inc=1

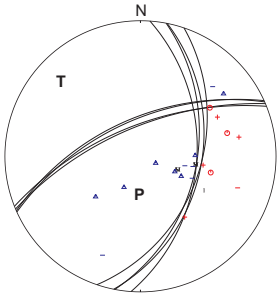

20) Aug. 6, 2002 00:34 inc=1

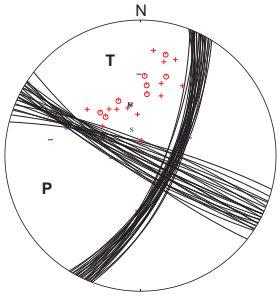

21) Aug. 10, 2002 04:32 inc=0

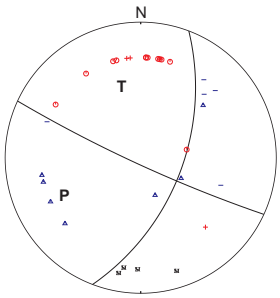

22) Aug. 10, 2002 09:14 inc=0

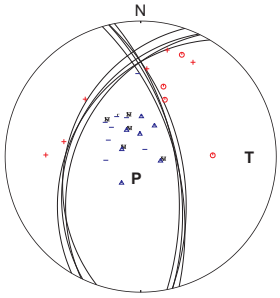

23) Aug. 15, 2002 16:09 inc=1

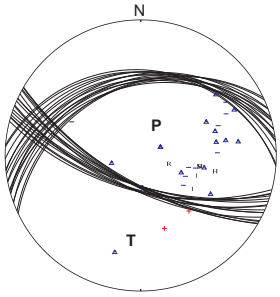

24) Aug. 23, 2002 16:57 inc=1

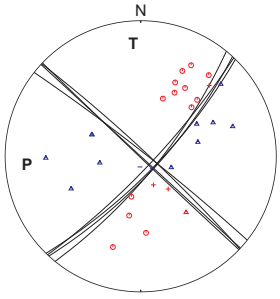

25) Sept. 6, 2002 07:34 inc=3

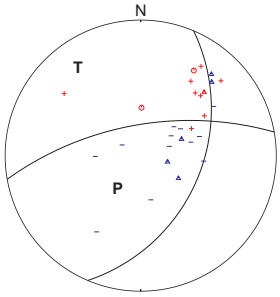

26) Sept. 17, 2002 13:46 inc=0

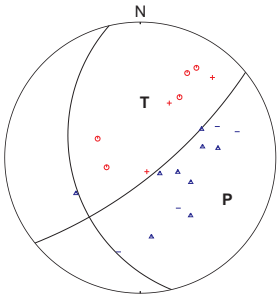

27) Sept. 24, 2002 11:41 inc=0

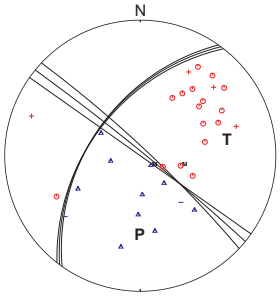

28) Sept. 30, 2002 00:34 inc=1

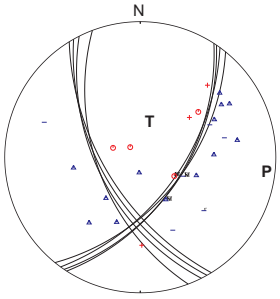

29) Oct. 1, 2002 13:56 inc=0

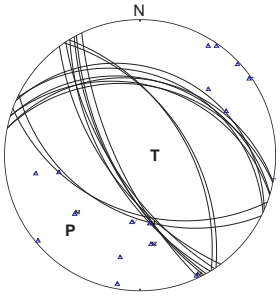

Upper plate earthquakes

1) Apr. 20, 2002 23:42 inc=0

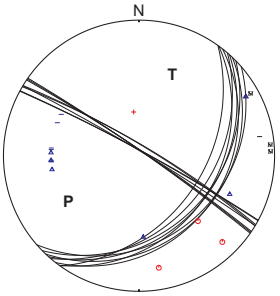

2) Apr. 23, 2002 02:31 inc=0

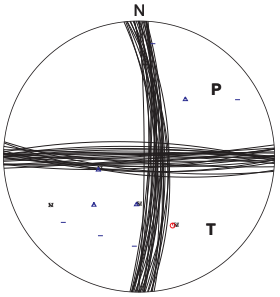

3) Apr. 25, 2002 07:01 inc=0

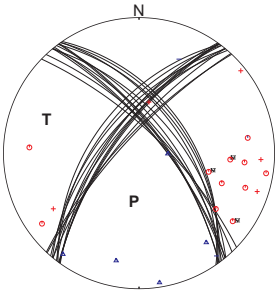

4) Apr. 26, 2002 07:21 inc=1

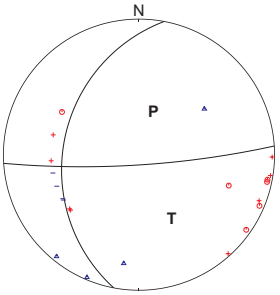

5) Apr. 26, 2002 23:55 inc=3

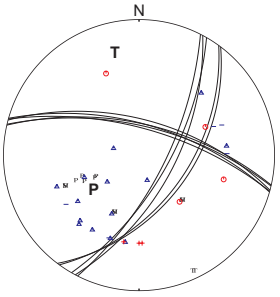

6) July 2, 2002 06:50 inc=1

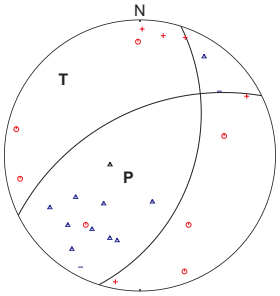

7) July 15, 2002 14:13 inc=2

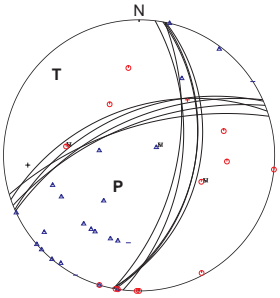

8) July 15, 2002 17:32 inc=2

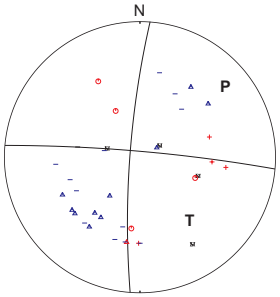

9) July. 15, 2002 21:08 inc=0

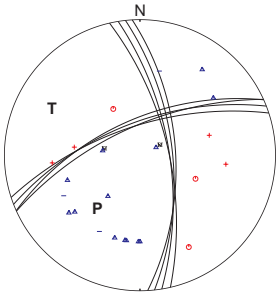

10) July 18, 2002 03:37 inc=1

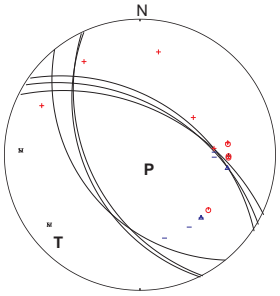

11) July 19, 2002 14:15 inc=0

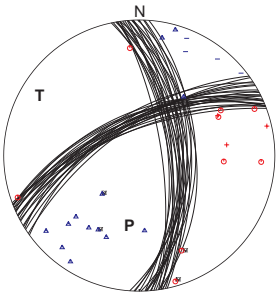

12) July 21, 2002 21:31 inc=0

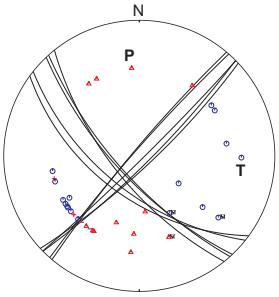

13) July 21, 2002 22:56 inc=0

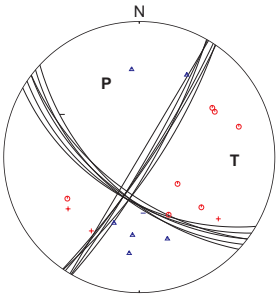

14) July 22, 2002 06:24 inc=0

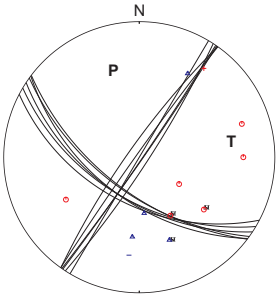

15) July 22, 2002 06:25 inc=0

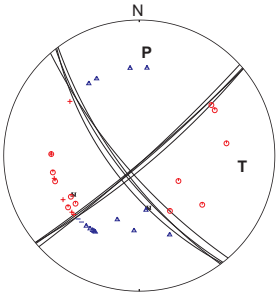

16) July 22, 2002 06:28 inc=0

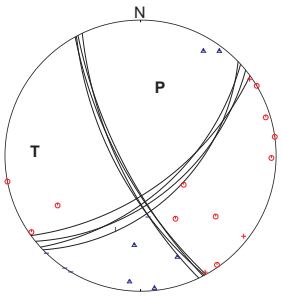

21) Aug. 29, 2002 05:03 inc=2

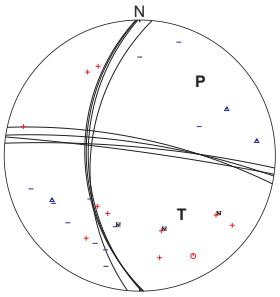

26) Sept. 25, 2002 09:22 inc=1

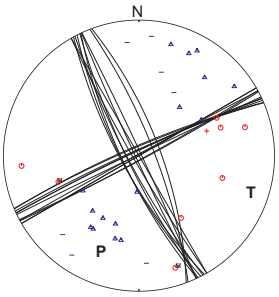

17) July 22, 2002 19:10 inc=0

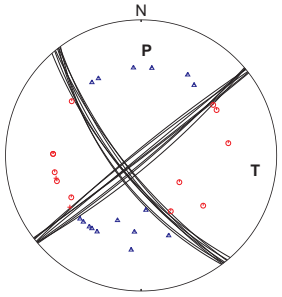

22) Sept. 9, 2002 15:07 inc=0

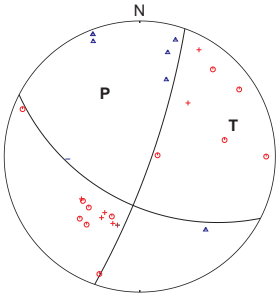

27) Sept. 25, 2002 21:58 inc=0

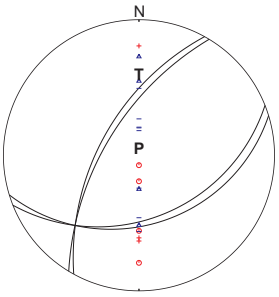

18) July 31, 2002 21:53 inc=1

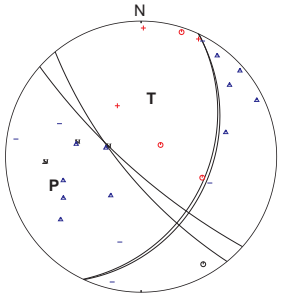

23) Sept. 8, 2002 15:18 inc=0

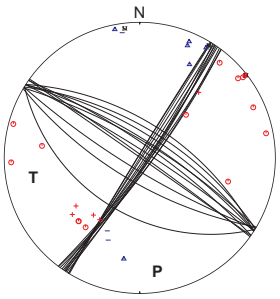

28) Sept. 26, 2002 09:57 inc=0

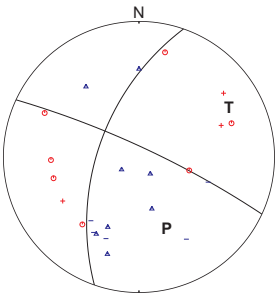

19) Aug. 16, 2002 06:48 inc=0

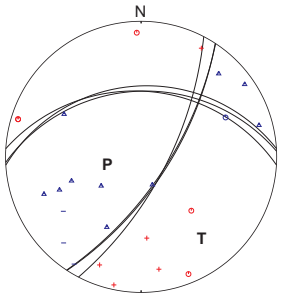

24) Sept. 14, 2002 19:20 inc=0

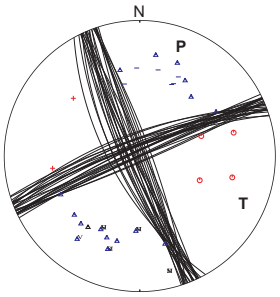

20) Aug. 28, 2002 11:33 inc=0

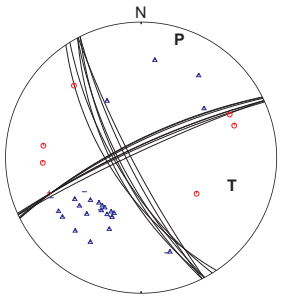

25) Sept. 17, 2002 04:37 inc=0

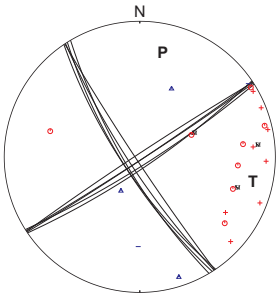

Acknowledgements

I am very much obliged to the *Deutscher Akademischer Austauschdienst* (DAAD), which provided the funding for most of my time at IFM-GEOMAR. Of course, this work would not have been possible without the collaboration in different ways from many persons, most of which I would like to mention here…

I would like to express first my gratitude to my advisors. To Ernst Flüh, for his support and helpful suggestions, for producing extra funds for my attendance to meetings and of course, for infecting me with his passion for seafaring. And to Stephan Husen, for introducing and guiding me to the "tomographic world", for the expertise he shared so generously, his encouragement and patience… and even for setting an unmovable deadline for the defense!

I thank also Prof. Dr. Jan Behrmann for agreeing to be the co-referee on a very short notice.

Many thanks undoubtedly to Guillermo Alvarado, who is certainly responsible for the whole idea, and whose passion for science has always been an inspiration.

To Jürgen Goßler, for the good memories *unterwegs* in the Costa Rican jungles carrying our barrels through the dusty roads, and the useful data-processing coaching along many nautical miles aboard the Old Lady, and for good-needed help on my first months at GEOMAR.

Special thanks to the staff from the Department of Seismology and Volcanology of the Instituto Costarricense de Electricidad (ICE). Their expertise, enthusiasm and commitment to the work were the key of a successful survey, not to speak of their jolliness and camaraderie, that made the survey a merry one as well. To the people that trusted us to enter their properties to install "suspicious" equipment, because their warmness and generosity make me proud of my country. And to the *Seebären* from RV Sonne for their excellent work and for making me feel welcome in such a convivial fraternity.

To the personnel of the Red Sismológica Nacional (RSN), and specially Carlos Redondo at the Universidad de Costa Rica, for providing their data and for the ready response to all those many emails requiring all kind of infos. And to Rafael Barquero from ICE, whose constant stream of reports and bulletins I have highly appreciated through the years.

Thanks to the members, present and past, of the Marine Geodynamics Department at GEOMAR and the SFB574. To César Ranero and Roland von Huene, for their interest and encouragement. And specially to Lars Planert, Anne Krabbenhöft, Cord Papenberg, Anke Dannowski, Jörg Petersen, Dietmar Bürk, Kristin Garofalo and Martin Scherwath for all the agreeable *Mensa* lunches, cruises, meetings, grills and parties shared through these years. And again to Anne K. and Annemarie Sticher, excellent office-mate, for providing patient ears to my stress-babbling, taking care of the office greenery and keeping me updated about the going-ons in Kiel during my frequent absences.

To my "four-wheel" friends, Yenory Morales, Wendy Pérez and Lepolt Linkimer. It is not possible to express in words what it means for me that you are always there, unconditionally. And to Illeana, Natalia, Pedro and Roberto for good vibras from the other side of the Atlantic. To Lars, on this side, our "official" and superb English-German translator, moving-up driver, source of black humour and good friend. To Cristian Agurto, for his friendship and endless discussions about life in general, besprinkled with Chilean wine, beer, pisco... To Daniel Heugas for helping me to stay relatively whole and sound through my late personal and academic ordeals.

Hearty extra-thanks to Wendy, with whom I have shared –among others along our lives since childhood– this adventure of living in Germany and trying to integrate without losing the lucidity –most of the time at least– during the attempt. Even more, without her skills in CorelDraw, elephant memory, good humour and her pushing me forward, I would probably still be writing chapter 1. It has been certainly great with her around!

To my big affectionate family, particularly my aunts, for sending always their love, prayers and much-missed Costa Rican commodities. And to the Adens, my German family, who made me felt at home since the beginning.

To my father, who I couldn't embrace once again. Wherever his souls is, it certainly gave me –gives me– strength. *Mi tata*, this one is of course for you, for lots of reasons, including the inherited passion for books… it sent me to discover the wide world. And it is also for my mother and sister, simply wonderful, always and in all ways, with their blind love and support that have taken me this far.

And finally I want to thank my life-mate, Nils Aden, for his amazing ability to make me laugh in all situations, for sharing that laugh as well as the sorrow, for believing in me all the time, and for making me travel all around the world to meet him.

Hiermit erkläre ich, dass die vorliegende Abhandlung, abgesehen von der Beratung der Betreuer nach Inhalt und Form, meine eigene Arbeit ist. Bisher ist die Arbeit noch nicht an anderer Stelle im Rahmen eines Prüfungsverfahrens vorgelegt worden.

Ivonne Aden-Arroyo